FACULDADE DA ENGENHARIA DA UNIVERSIDADE DO PORTO

Modelling and analysis of polymers at different scales

Seyed Mohsen Mirkhalaf Valashani

Supervisors: Prof. Francisco Pires
Prof. Ricardo Simões

A thesis submitted for the degree of
Doctor of Philosophy
February 2015

Dedicated to my wife

Acknowledgements

The work presented in this thesis was accomplished between 2010 and 2015. This period of time was thoroughly different form the rest of my life both personally and professionally. I am writing these lines to express my gratitude to those whose supports were undeniably holding my back to resist the hard challenging path throughout the last five years.

First of all, I would like to thank Professor Pires, my supervisor, who helped me to start my career from the very beginning and provided me a great scientific supervision during the whole period. His interesting ideas were always encouraging me to keep looking for solutions and whenever I felt down, his effort to keep me motivated was truly effective. His deep knowledge in computational mechanics has been shedding light on the dark parts of the path. Besides, bureaucratic issues I faced through these years were kindly helped by Prof. Pires to be resolved. The first year of my work was funded by a project form IDMEC (Instituto de engenharia Mecânica) referenced as "PTDC/EMEPME/108859/2008" and the rest by FCT (Fundação para a Ciência e a Tecnologia) under a PhD grant with reference "SFRH/ BD/74027/2010" within POPH/FSE. The financial supports are gratefully acknowledged.

I was also receiving interesting comments and references from Professor Simões, my thesis co-supervisor. He also provided me the opportunity to have some fruitful collaboration with his research group at university of Minho. I wish to express my thanks for his support and the collaboration opportunity.

I was lucky to enter a very strong research group of PhD students of

Prof. Pires. I had very constructive discussions with my colleagues and they were kindly helpful to me to resolve the issues I confronted during the accomplishment of my work. I am particularly thankful to Dr. Fábio Reis who helped me to get started with micromechanical and multiscale simulations.

During my stay at Porto, my friends' company helped me not to be emotionally affected by being so far from homeland. I could not name them all here but I thank all of them for their friendship and sense of humor and responsibility.

Finally, I express my deepest thanks to my wife and parents for their unconditional support through the last years. My wife adjusted her professional life according to my conditions and she always considered my academic situation and choices as the driving parameter of our life together. My parents, even though in another continent, constantly motivated me and helped me keep thinking there is no effort not to be awarded. Without the aforementioned supports, the PhD road could be much harder to go through and I sincerely acknowledge them all.

Abstract

Polymers have become an important and highly applicable branch of materials due to their interesting chemical, optical, thermal and mechanical properties. Because of highly demanded advanced performance and due to the inherent hierarchical heterogeneous structure of polymers, multi-scale simulations have become more and more interesting particularly for the academic community. The objective of this thesis is to investigate and model the behavior of polymers, more specifically amorphous polymeric materials, at different scales. Phenomenological, micromechanical and coupled multi-scale constitutive modelling approaches are used to characterize the mechanical behavior of amorphous polymers. Having provided, in Chapter 1, some introductory information and a global overview of the thesis, Chapter 2 summarizes the main concepts of Continuum Mechanics and Finite Element Method. A constitutive model is developed based on single mode Leonov model in Chapter 3. The integration algorithm of the model, reduced to a single non-linear scalar equation, is presented in the same chapter. Chapter 4 presents an elasto-viscoplastic model based on the model presented in Chapter 3, in order to predict the deformation behavior of polymeric materials under different loading conditions more accurately. Lode angle parameter is used in order to modify the function for the evolution of the post-yield softening and also the final hardening regime of the deformation. Micro-structural analysis on rubber toughened amorphous polymers are performed in Chapter 5. Some statistical analyses are performed and two criteria and an algorithm are proposed in order to determine the size of

the RVE. The next contribution of this work is to develop a continuum level constitutive model taking into account the effect of rubbery particles, taken as porosity, on the overall deformation behavior of polymers. To this end, the model presented in Chapter 3 is combined with Gurson model in Chapter 6. Chapter 6 also presents coupled multi-scale analyses of heterogeneous amorphous polymers together with some comparisons between the two approaches. The conclusions, taken from this work, as well as some suggestions for the potential paths of the future research are given in the final chapter.

Resumo

Os polímeros têm-se tornado num ramo importante e de elevada aplicação dos materiais, devido principalmente às suas propriedades químicas, óticas, térmicas e mecânicas. Devido à necessidade recomendada de desempenho avançado e devido à estrutura heterogénea hierárquica inerente aos polímeros, as simulações multiescala têm-se tornado cada vez mais interessantes, nomeadamente para a comunidade académica. O objetivo desta tese passa pela investigação e modelação do comportamento dos polímeros, mais especificamente dos materiais poliméricos amorfos, a diferentes escalas. Modelos constitutivos com bases fenomenológicas, micromecânicas e multiescala acoplada, são usados para caracterizar o comportamento mecânico de polímeros amorfos. Tendo fornecido, no Capítulo 1, alguma informação introdutória e uma visão global da tese, o Capítulo 2 sumariza os principais conceitos da Mecânica dos Meios Contínuos e do Método dos Elementos Finitos. No Capítulo 3 é desenvolvido um modelo constitutivo baseado no modelo de Leonov de modo singular. O algoritmo de integração do modelo, reduzido a uma única equação escalar não-linear, é apresentado no mesmo capítulo. O Capítulo 4 apresenta um modelo elasto-viscoplástico baseado no modelo apresentado no Capítulo 3, com o intuito de prever o comportamento à deformação dos materiais poliméricos sob diferentes condições de carregamento. O ângulo de Lode é usado com o objetivo de modificar a função para a evolução do amaciamento pós-cedência e também do regime de endurecimento final da deformação. A análise microestrutural dos polímeros amorfos em borracha endurecida é efetuada no Capítulo 5. Algumas análises estatísticas são realizadas e são propostos dois critérios e um algoritmo com o intuito de

determinar o tamanho do *Elemento de Volume Representativo* (RVE). A contribuição seguinte deste trabalho passa pelo desenvolvimento de um modelo constitutivo de nível contínuo tendo em conta o efeito das partículas de borracha, tidas em conta como porosidades, no comportamento geral à deformação dos polímeros. Com esta finalidade, o modelo apresentado no Capítulo 3 é combinado com o modelo de Gurson no Capítulo 6. O Capítulo 6 também apresenta as análises multiescala acoplada dos polímeros amorfos heterogéneos juntamente com algumas comparações entre as duas abordagens. As conclusões, retiradas deste trabalho, tal como algumas sugestões de trajetos potenciais em investigação futura, são apresentadas no capítulo final.

Contents

Nomenclature **xix**

1 Introduction **1**
1.1 Polymers . . . 1
1.2 Modelling . . . 3
1.3 Motivation . . . 8
1.4 Scope and outline . . . 10

2 Continuum mechanics and Finite Element Method **15**
2.1 Continuum Mechanics . . . 15
2.1.1 Kinematics of deformation . . . 16
2.1.1.1 The deformation gradient . . . 17
2.1.1.2 The velocity gradient . . . 20
2.1.1.3 Strain measures . . . 21
2.1.2 Stress measures . . . 21
2.1.3 Fundamental laws of thermodynamics . . . 22
2.1.3.1 Conservation of mass . . . 23
2.1.3.2 Momentum balance . . . 23
2.1.3.3 The first and second principles of thermodynamics 23
2.1.3.4 The Clausius-Duhem inequality . . . 24
2.1.4 The quasi-static IBVP . . . 25
2.2 Displacement-based finite elements . . . 27
2.2.1 Spatial discretisation . . . 27
2.2.2 Temporal discretization . . . 30
2.2.3 The non-linear incremental finite element equation . . . 31

2.2.4 Numerical integration of $\mathbf{f}^{int}$ and $\mathbf{f}^{ext}$ . . . 32
2.2.5 Newton-Raphson method . . . 33
2.3 Conclusions . . . 34

3 Leonov based model **37**
3.1 Introduction . . . 38
3.2 Formulation . . . 39
3.2.1 Multiplicative kinematics . . . 40
3.2.2 Logarithmic strain measure . . . 41
3.2.3 Free energy potential . . . 41
3.2.4 Dissipation potential . . . 43
3.2.5 Additive decomposition of total stress . . . 47
3.3 Integration algorithm . . . 48
3.3.1 The state update procedure . . . 49
3.3.1.1 Return mapping . . . 50
3.3.2 Consistent tangent operator . . . 55
3.4 Numerical examples . . . 56
3.4.1 Cylinder upsetting-strain rate effect . . . 57
3.4.2 Compression on a cube . . . 58
3.4.3 Cylinder upsetting-temperature effect . . . 60
3.4.4 Cylinder upsetting-effect of superimposed hydrostatic pressure . . . 61
3.4.5 Necking of a cylindrical bar . . . 61
3.4.6 Compression of a notched round bar . . . 62
3.5 Conclusions . . . 64

4 An elasto-viscoplastic model for polymers under different stress states **67**
4.1 Introduction . . . 68
4.2 Material properties and initial simulations . . . 69
4.2.1 Material properties . . . 70
4.2.1.1 Eyring properties . . . 71
4.2.1.2 Softening properties . . . 73
4.2.1.3 Hardening parameter . . . 73

4.2.2 Simulations . . . 74
4.2.2.1 Cylinder upsetting . . . 74
4.2.2.2 Cube compression . . . 75
4.2.2.3 Tension on dumbbell shape specimen . . . 76
4.2.2.4 Butterfly specimen . . . 79
4.3 Modified constitutive model . . . 82
4.3.1 Required enhancements . . . 82
4.3.1.1 Plateau like behaviour in plane strain compression 83
4.3.1.2 Hardening underestimation in plane strain compression . . . 84
4.3.1.3 Softening overestimation in tension on dumbbell shape specimen . . . 84
4.3.1.4 Hardening underestimation in tension on dumbbell shape specimen . . . 84
4.3.2 Modifications proposed . . . 84
4.3.2.1 Softening . . . 88
4.3.2.2 Hardening . . . 89
4.4 Integration algorithm . . . 91
4.4.1 State update . . . 91
4.4.2 Tangent operator . . . 93
4.5 Evaluating the modified model . . . 94
4.6 Conclusions . . . 98

5 Micro-structural analysis 100
5.1 Introduction . . . 100
5.2 Kinematical description of the micro-scale problem . . . 101
5.2.1 Periodic boundary condition . . . 105
5.2.2 Spatial discretization of the Microscopic problem . . . 105
5.3 Numerical examples . . . 107
5.4 RVE size . . . 111
5.4.1 RT-PS with 10% of rubbery particles . . . 113
5.4.2 RT-PS with 15% of rubbery particles . . . 120
5.5 Conclusions . . . 126

6 Continuum and coupled multi-scale modelling of porous polymers **128**
6.1 Introduction . . . 129
6.2 Continuum modelling . . . 131
6.2.1 Formulation . . . 132
6.2.2 Integration algorithm . . . 137
6.2.2.1 State update . . . 137
6.2.2.2 Tangent operator . . . 140
6.2.3 Numerical examples . . . 141
6.2.3.1 Evolution of stress and porosity . . . 142
6.2.3.2 Boundary value problem . . . 144
6.3 Coupled Multi-scale . . . 145
6.3.1 Coupled Multi-scale for polymers . . . 149
6.3.2 Numerical examples . . . 151
6.4 Comparison . . . 154
6.5 Conclusions . . . 157

7 Conclusions and suggestions **159**
7.1 Objectives and achievements . . . 159
7.2 Suggestions for future research . . . 162

A Softening evolution function for Leonov based model **165**

B Derivation of tangent operator for Leonov based model **167**

C Tangent operator for different stress states model **171**

D Details of the state update for Porous model **176**

E Tangent operator for the Porous model **185**

F Relevant publications **189**

References **207**

List of Figures

1.1 Schematic representation of coupled multi-scale problem. 7
1.2 Hierarchical length scales for polymeric materials, adapted from [Li et al. (2013)]. 9
1.3 Spatial and Temporal scales associated with different simulation approaches, adapted from [Araujo et al. (2014)]. 10

2.1 Deformation. Initial and deformed configuration (adapted from Figure (3.1) of [De Souza Neto et al. (2008)]). 16
2.2 Polar decomposition of the deformation gradient (adapted from Figure (3.8) of [De Souza Neto et al. (2008)]) 18
2.3 Multiplicative kinematics (adapted from Figure (14.1) of [De Souza Neto et al. (2008)]) 19
2.4 Numerical approximation. The initial boundary value problem is reduced to a set of incremental finite element equations, reproduced from Figure (4.1) of [De Souza Neto et al. (2008)] 28
2.5 Finite element interpolation. The element shape function, adapted from Figure (4.2) of [De Souza Neto et al. (2008)]. 29
2.6 Finite element interpolation. The global shape function adapted from Figure (4.2) of [De Souza Neto et al. (2008)] 29
2.7 The Newton-Raphson algorithm for the incremental finite element equilibrium equation 34

3.1 Rheological representation of the model 40
3.2 Stress-strain curves of cylinder upsetting for four different polymeric materials. yellow: PS, red: PC, blue: PA-6 and green: PET. 58

3.3 The effect of strain rate on the stress-strain curve of axisymmetric compression on PS: dashed line: $\dot{\varepsilon} = -0.0001(1/s)$; solid line: $\dot{\varepsilon} = -0.0005(1/s)$ and dotted line: $\dot{\varepsilon} = -0.001(1/s)$ 59
3.4 stress-strain curves of cylinder and cube compression on PA-6 under strain rate $\dot{\varepsilon} = -0.001(1/s)$: dashed line: cube and solid line: cylinder 60
3.5 Stress-strain curves for cylinder compression tests using PS at different temperatures: dashed line: $T = 60^{oc}$; solid line:$T = 40^{oc}$ and dotted line: $T = 20^{oc}$ 62
3.6 Stress-strain curves for cylinder compression tests using PET under different superimposed hydrostatic pressures: solid line: $p_0 = 0.1MPa$ and dashed line: $p_0 = 300MPa$ 63
3.7 Geometry and mesh of the necking problem 64
3.8 accumulated plastic strain of the cylinder under tensile deformation 65
3.9 Geometry and mesh of the notched bar compression example . . . 65
3.10 Accumulated plastic strain for the compression simulation on the notched round bar 66

4.1 Eyring plot: Yield stress over temperature as a function of logarithm of train rate; circles: $T = 296°$K; squares: $T = 323°$K 72
4.2 The geometry and mesh of the cylinder upsetting simulations . . . 75
4.3 True stress-true strain for the uniaxial compression test on PC at room temperature, solid line: simulation; circles: experiment; horizontal axis: true compressive strain; vertical axis: True compressive stress (Pa); (a): $\dot{\varepsilon} = -0.001(1/s)$; (b): $\dot{\varepsilon} = -0.0005(1/s)$; (c): $\dot{\varepsilon} = -0.0001(1/s)$. 76
4.4 True stress-true strain for the plane strain compression test on PC at room temperature, solid line: simulation; squares: experiment; horizontal axis: true compressive strain; vertical axis: True compressive stress (Pa); (a): $\dot{\varepsilon} = -0.001(1/s)$; (b): $\dot{\varepsilon} = -0.0005(1/s)$; (c): $\dot{\varepsilon} = -0.0001(1/s)$ 77
4.5 The geometry and mesh of the 3D tensile test on a dumbbell shape specimen. 78

4.6 Force-displacement curve of tensile test on dumbbell shape specimen under deformation speed $\dot{u} = 2\frac{mm}{min}$. Circles: experimental results and solid line: simulation 78
4.7 The details of the geometry of the butterfly specimen. Adapted from [Bai and Wierzbicki (2007)]. 79
4.8 The spatial discretization of the butterfly specimen. 80
4.9 Schematic representation of pure shear and combined shear tension loading conditions on the butterfly specimen, adapted from [Malcher (2012)]. 80
4.10 The force displacement curve for butterfly specimen under pure shear stress state. 81
4.11 The normalized force-normalized displacement curve for butterfly specimen under combined shear-tension stress state. 81
4.12 Plateau-like behaviour in plane strain compression tests under three different strain rates. Solid line: simulation; circles: experiment; horizontal axis: true compressive strain; vertical axis: True compressive stress (Pa); (a): $\dot{\varepsilon} = -0.001(1/s)$; (b): $\dot{\varepsilon} = -0.0005(1/s)$; (c): $\dot{\varepsilon} = -0.0001(1/s)$. 83
4.13 Hardening comparison between simulations and experiments in plane strain compression tests under three different strain rates. Solid line: simulation; circles: experiment; horizontal axis: true compressive strain; vertical axis: True compressive stress (Pa); (a): $\dot{\varepsilon} = -0.001(1/s)$; (b): $\dot{\varepsilon} = -0.0005(1/s)$; (c): $\dot{\varepsilon} = -0.0001(1/s)$. 85
4.14 Force-displacement curve of tensile test on dumbbell shape specimen under deformation speed $\dot{u} = 2\frac{mm}{min}$: The post-yield softening prediction of the model compared to experiments. 86
4.15 Force-displacement curve of tensile test on dumbbell shape specimen under deformation speed $\dot{u} = 2\frac{mm}{min}$: Difference in the post-yield hardening prediction of the model compared to experiments. 86
4.16 How softening modification function, $g(\bar{\theta})$, evolves. 89
4.17 How hardening modification function, $l(\bar{\theta})$, evolves. 90

4.18 True stress-true strain for the uniaxial compression test on PC at room temperature, black solid line: simulations with original model; filled blue circles: experiment; unfilled red circles: simulations with modified model; horizontal axis: true compressive strain; vertical axis: True compressive stress (Pa); (a): $\dot{\varepsilon} = -0.001(1/s)$; (b): $\dot{\varepsilon} = -0.0005(1/s)$; (c): $\dot{\varepsilon} = -0.0001(1/s)$. 95
4.19 True stress-true strain for the plane strain compression test on PC at room temperature, black solid line: simulations with original model; filled blue squares: experiment; unfilled red squares: simulations with modified model; horizontal axis: true compressive strain; vertical axis: True compressive stress (Pa); (a): $\dot{\varepsilon} = -0.001(1/s)$; (b): $\dot{\varepsilon} = -0.0005(1/s)$; (c): $\dot{\varepsilon} = -0.0001(1/s)$. 96
4.20 Force-displacement curve of tensile test on dumbbell shape specimen, black solid line: simulations with original model; filled blue squares: experiment; unfilled red squares: simulations with modified model. 97
4.21 Force-displacement curve of shear loading on butterfly specimen, black solid line: simulations with original model; unfilled red squares: simulations with modified model. 97
4.22 The normalized force-normalized displacement curve for butterfly specimen under combined shear-tension stress state using the original and modified models, black solid line: simulations with original model; unfilled red squares: simulations with modified model. . . 98

5.1 Two different samples with size of $20\mu m$ and volume fraction of inclusions equal to (a): 10% and (b): 15%. 108
5.2 Stress-deformation of the samples shown in Figure (5.1), solid line: 10% and dashed line: 15%. 109
5.3 Second morphologies of the samples with size of $20\mu m$ and volume fraction of inclusions equal to (a): 10% and (b): 15%. 109
5.4 Stress-deformation of the samples shown in Figure (5.3), solid line: 10% and dashed line: 15% 110

5.5 Stress-deformation of the samples shown in Figures (5.1a) and (5.3a), both with IVF equal to 10%. 110
5.6 Stress-deformation of the samples shown in Figures (5.1b) and (5.3b), both with IVF equal to 15%. 111
5.7 Flow chart for RVES determination. 114
5.8 Different realizations for IVF equal to 10% and VES equal to 20μm. 115
5.9 Stress-deformation of the samples shown in Figure (5.8). 115
5.10 Average stress-deformation of the samples shown in Figure (5.8) with shaded bounds of standard deviation. 116
5.11 Different realizations for IVF equal to 10% and VES equal to 30μm. 116
5.12 Stress-deformation of the samples shown in Figure (5.11). 117
5.13 Average stress-deformation of the samples shown in Figure (5.11) with shaded bounds of standard deviation. 117
5.14 Different realizations for IVF equal to 10% and VES equal to 40μm. 118
5.15 Stress-deformation of the samples shown in Figure (5.14). 119
5.16 Average stress-deformation of the samples shown in Figure (5.14) with shaded bounds of standard deviation. 119
5.17 Average stress-deformation of the samples shown in Figures (5.11) and (5.14). Solid line: VES=40μm and dashed line: VES=30μm. 120
5.18 Different realizations for IVF equal to 15% and VES equal to 20μm. 121
5.19 Stress-deformation of the samples shown in Figure (5.18). 121
5.20 Average stress-deformation of the samples shown in Figure (5.18) with shaded bounds of standard deviation. 122
5.21 Different realizations for IVF equal to 15% and VES equal to 30μm. 122
5.22 Stress-deformation of the samples shown in Figure (5.21). 123
5.23 Average stress-deformation of the samples shown in Figure (5.21) with shaded bounds of standard deviation. 123
5.24 Different realizations for IVF equal to 15% and VES equal to 40μm. 124
5.25 Stress-deformation of the samples shown in Figure (5.24). 125
5.26 Average stress-deformation of the samples shown in Figure (5.24) with shaded bounds of standard deviation. 125
5.27 Average stress-deformation of the samples shown in Figures (5.11) and (5.14). Solid line: VES=40μm and dashed line: VES=30μm. 126

6.1 Evolution of stress and porosity against strain for RT-PS at strain rate equal to $\dot{\varepsilon} = 0.0001(1/s)$, right vertical axis: stress (Pa); horizontal axis: strain; right vertical axis: porosity; black line: evolution of stress; blue line: evolution of viscosity; (a): $f_0 = 0$; (b): $f_0 = 5\%$; (c): $f_0 = 10\%$; (d): $f_0 = 20\%$. 143
6.2 Stress-strain curves of RT-PS under different strain rates, vertical axis: stress (Pa); horizontal axis: strain; (a): $\dot{\varepsilon} = 0.0001(1/s)$; (b): $\dot{\varepsilon} = 0.0005(1/s)$; (c): $\dot{\varepsilon} = 0.001(1/s)$; (d): $\dot{\varepsilon} = 0.005(1/s)$; black line: $f_0 = 0$; red line: $f_0 = 5\%$; green line: $f_0 = 15\%$; blue line: $f_0 = 20\%$. 144
6.3 Comparison of the post-yield softening and hardening of PS and RT-PS with initial 20% of porosity. 145
6.4 The evolution of volumetric strain versus axial strain for RT-PS under different strain rates, vertical axis: volumetric strain; horizontal axis: axial strain; (a): $\dot{\varepsilon} = 0.0001(1/s)$; (b): $\dot{\varepsilon} = 0.0005(1/s)$; (c): $\dot{\varepsilon} = 0.001(1/s)$; (d): $\dot{\varepsilon} = 0.005(1/s)$; black line: $f_0 = 0$; red line: $f_0 = 5\%$; green line: $f_0 = 15\%$; blue line: $f_0 = 20\%$. 146
6.5 Mesh of the dog-bone specimen. 146
6.6 The level of porosity in the dog-bone specimen after deformation considering different levels of initial porosity (a): 2.5%; (b):5%; (c):10% and (d): 15%. 147
6.7 Schematic representation of an RVE 147
6.8 Separation of scales 148
6.9 Schematic representation of coupled multi-scale problem 149
6.10 Finite element discretization of the coupled multi-scale simulation of a flat grooved specimen; (a): spatial discretization of the macro structure; (b): Spatial discretization of the micro-structural sample. 151
6.11 The force-displacement curves for heterogeneous and homogeneous material, solid line: homogeneous material and dashed line: heterogeneous material. 152
6.12 The contour plot of the effective stress at macro level using macro and coupled analyses when $u = 0.25mm$, (a):macro analysis; (b): coupled analysis. 153

6.13 The contour plot of the effective stress at macro level using macro and coupled analyses when $u = 0.5mm$, (a):macro analysis; (b): coupled analysis. 153
6.14 The contour plot of the effective stress at both macro level and micro level when $u = 0.25mm$, (a):macro structure; (b): micro-structural sample (1); (c):micro-structural sample (2) and (d): micro-structural sample (3). 154
6.15 The contour plot of the effective stress at both macro level and micro level when $u = 0.5mm$, (a):macro structure; (b): micro-structural sample (1); (c):micro-structural sample (2) and (d): micro-structural sample (3). 155
6.16 The force-displacement curves for Rubber Toughened Polystyrene (RT-PS), dotted line: continuum model; dashed line: coupled multi-scale. 156
6.17 The contour plot of the effective stress for RT-PS at macro level using continuum model and coupled analyses when $u = 0.25mm$, (a):continuum model; (b): coupled analysis. 156

List of Tables

2.1 The incremental non-linear finite element scheme - implicit solution. 32
2.2 Newton-Raphson scheme for the solution of the incremental non-linear finite element equilibrium equation (implicit solution). . . . 35

3.1 Material properties for the constitutive model 57
3.2 Global convergence table for cylinder upsetting simulations 59
3.3 Equilibrium convergence table for necking of a cylindrical bar and compression of a notched round bar 64

4.1 Material properties for Makrolon 2607 74

Chapter 1

Introduction

1.1 Polymers

Polymers are a broad class of materials, either natural or synthetic (man-made), composed of very large molecules [Mackerle (2003)]. The molecules comprise hundreds or thousands of atoms linked together in chain or network structures. The concept of polymer could be considered as one of the great ideas of chemistry in twentieth century. The acceptance of polymer in the scientific community is mainly attributed to Hermann Staudinger who received the Nobel Prize in 1953 [Hall (1989)].

The history of polymeric materials dates back to the 1500's when British explorers found out the ancient Mayan civilization in Central America. Many years later, in 1839, vulcanization was discovered by Charles Goodyear through the combination of natural rubber and sulfur and by heating the compound to 270°F. Vulcanized rubber, currently being used in automobile tires, is a polymeric substance which is remarkably more durable than its natural counterpart. Bakelite in 1907 fabricated the oldest recorded synthetic plastic. In 1917, the X-ray crystallography was invented and it was possible to prove the fact that polymer unit cells contain long chain of molecules rather than small molecular species. Staudinger by publishing the paper entitled as "Uber polymerization" in 1920 presented the development of modern polymer theory. Producing Vinyl-chloride resins in large scale started in 1927. Three years later, Polystyrene, which is used in videocassettes, was invented. Nylon which is one of the most well-known polymeric materials was

produced by Wallace Carothers at Dupont company in 1938. In the second year of the 1940's, Polyethylene, another widespread polymer, was introduced. One of the moldable high temperature polymers was developed by James Economy in the beginning of the 1970's. In the subsequent year, S. Kwolek, who was awarded more than 37 patents in polymer science developed Kevlar (which is a commercial brand name for an aramid synthetic fiber). The year 1976 was the first year in which the polymer/plastic industry exceeded steel as the most widely used material in US [Rosato and Rosato (2003)].
There are different ways of classification of polymers based on different factors. Some of them are provided below:

- Based on source: natural and synthetic;
- Based on structure: linear, branched chain and cross linked or network;
- Based on molecular (inter-particle) forces: Elastomers, thermosets and thermoplastics .

There are more ways of classifications of polymers, which are not really in the scope of this work. According to the morphology, thermoplastic polymers can be divided into two main subcategories:

1. Amorphous polymers (Polycarbonate, Polystyrene, ...);
2. Semi-crystalline polymers (Polyamide, Polyethylene, ...).

Both natural science and technology are affected by the concept of polymer (macromolecule) [Hall (1989)]. Molecular biology emerged through the study of some natural macromolecular substances like proteins. Successful polymer synthesizes created a new sector in the engineering industry to produce different polymeric materials with different characteristics e.g. Plastics, rubbers, coatings and adhesives, to name a few. Polymers have a wide range of physical, chemical and mechanical properties [Mackerle (2003)]. Some of the most important properties of polymers are:

- ▶ They are good thermal and electrical insulators.

- They have lower density in comparison to metals.
- They have lower elastic modulus than metals but they usually exhibit higher yield strain compared to metals.

Besides the properties mentioned above, one of the most interesting characteristics of polymers is that complicated shapes can be easily fabricated using polymers within processes such as extrusion, molding and casting. Polymers are rheologically characterized as viscoelastic materials. Polymers have a variety of applications that are far more than any other class of materials. Some of the areas for the applications of polymers are [Mackerle (2003)]:

- Electronic products (insulators, waveguides, sensors, actuators, membranes, transducers, electronic packaging, etc);
- Automotive engineering (under hood components, side-view mirrors, instrument panels, seating foams, etc);
- Biomechanics (knee prostheses, inserts, heart valve prostheses, micro catheters, helmets, femoral stems, etc);
- Civil and building engineering (bridges, polymer concrete structures, pipes, tubes, fittings, etc);
- Other fields (marine engineering, pressure vessels, containers, compressor valves, packaging materials, etc).

1.2 Modelling

Through the last decades, both scientific and industrial communities have been working on the optimization and design of structures. In order to have efficient and optimized design, the necessity of predicting the behavior of different kinds of materials is undeniable. Therefore, to avoid expensive and time consuming experiments, simulation tools are required to be developed and used for predicting the behavior, and probably the failure, of different structures. Developing new simulation tools and material models is facilitated by the remarkable increased

computational capacity, new powerful fast CPUs and RAMs, for desktops and laptops.

Over the last century, a considerable effort has been devoted to the development of new material models capable of reproducing experimentally observed data. The approaches for material modelling could be classified into two main categories: discrete methods and continuum methods. Discrete methods such as molecular dynamics, Brownian dynamics, monte carlo, ab-initio, quantum simulations are mainly used at the molecular level. Continuum models are either phenomenological or micro-mechanical based. Phenomenological constitutive equations are developed based on phenomenological assumptions. Tresca (1864), Huber (1904), von Mises (1913) and Hencky (1924) are some of the Pioneers. In micromechanical approach, the constitutive equations are developed considering micromechanical assumptions e.g. the Gurson model [Gurson (1977)]. In order to fill the gap between the two above mentioned constitutive modeling frameworks, the coupled multi-scale approach has been developed. The basic concepts and principles of coupled multi-scale analysis were presented by Suquet (1985), Guedes and Kikuchi (1990), Terada and Kikuchi (1995), Ghosh et al. (1995) and Ghosh et al. (1996). In this thesis, all the above mentioned modelling approaches, phenomenological, micromechanical and coupled multi-scale, are used and explained.

It can be said that the initiation of the efforts to determine the behavior of polymers dates back to 1930's. Eyring (1936) proposed a molecular theory for the yield stress of amorphous polymers, considering the yield behavior as a thermally activated process. Temperature and strain rate effect is accounted for in the theory. Mooney (1940) proposed a strain energy function for rubber elastic materials. Haward and Tackray (1968) developed a 1 dimensional constitutive model for glassy polymers. The work could be considered as the initial constitutive model proposed for predicting the deformation behavior of glassy polymers. According to this work, the post yield behavior of glassy polymers includes two different phases: First, a rate dependent plastic flow, modelled by an Eyring dashpot, and second, a rate independent contribution of the entanglement, modelled by a Langevin spring. The three dimensional version of Haward and Tackray model was proposed by Boyce et al. (1988). An alternative constitutive model which is able to predict the typical deformation behavior of polymeric materials is

the generalised compressible Leonov model, which has been proposed by Baaijens (1991) and extended by Tervoort et al. (1998) and Govaert et al. (2000). For a review on finite element simulation of polymers, the reader is referred to [Mackerle (1997), Mackerle (2003)]. The phenomenologiacl constitutive models developed for amorphous polymers could be, in many cases, used for semi-crystalline polymers as well [Rojek et al. (2004)]. The molecular orientation of polymers evolves during large deformations and the corresponding strengthening is, for some polymers, greatly dependent on the strain state. Time dependent deformation and failure of polymers have been studied using linear and non-linear visco-elastic and visco-plastic FEM models [Mackerle (1997), Mackerle (2003)].

Analytical and computational modeling approaches describing the mechanics of materials on different scales ranging from atomistic, microstructural or transitional to continuum level have received more attention in recent papers and are advancing rapidly. Ghonimet et al. (2003) have explained in detail the issues related to the links between atomistic, nano, micro and macro scales. They have also identified the parameters necessary for transferring data from one scale to an upper one. Computational modeling of materials behavior has become an important and reliable tool and serves as complement to theoretical and experimental approaches. Although the research conducted to understand the behavior of a material at different length scales, continuum at large scale and discrete at atomic level, is needed, multiscale approaches are required to complement and link the existing continuum and atomistic analyses. Introducing multiscale material modeling approaches also helps to understand the interdependencies of different length scales. Despite the remarkable contributions obtained from the micromechanical approach, a considerable gap between macrostructure behavior and micromechanical results, specifically when a specimen is under very large deformation, can be observed. Recently, a lot of effort has been dedicated to a numerical strategy called coupled multiscale modeling. In this approach, a coupled analysis between macro scale and transitional (micro) scale is performed. Continuum mechanics rules and relations are assumed valid on the transitional scale as well. In the coupled multiscale approach, the characteristics of the microstructure are affecting the deformation behavior of the macrostructure. For example,

the deformation behavior after the elastic regime is usually characterized by appropriate constitutive relations. The constitutive relations, within the framework of continuum mechanics, assume that the material properties vary continuously through the solid. The existing heterogeneities in the microstructure, however, cannot be characterized within the continuum mechanics framework. In coupled multiscale analysis, the heterogeneities and other specifications of the microstructure simultaneously affects pre-yield, yield and post-yield behaviour at the macro level.

The history of coupled multi-scale model dates back to 1980's and 1990's when the basic ideas behind the multi-scale theory were introduced by Suquet (1985), Guedes and Kikuchi (1990), Terada and Kikuchi (1995), Ghosh et al. (1995) and Ghosh et al. (1996). The modeling approach introduces a stress-strain relationship at each macroscopic point as the homogenization of stresses and strains of microscopic points (transitional or RVE level) associated to the macroscopic point under study. Using the finite element approximation to continuum mechanics, coupled multi-scale approach solves two boundary value problems, namely macroscopic and microscopic, at the same time. The microscopic, or transitional or RVE, problem is actually solved for each macroscopic integration Gauss point. The procedure of coupled multi-scale problem is schematically shown in Figure (1.1). The coupled multi-scale approach has the following advantages:

- At the RVE level, arbitrary geometries can be used;
- Time dependent and non-linear problems could be solved;
- The possible interactions between different constituents and other eventual phenomena such as phase transformation could be modelled using appropriate algorithms [Kouznetsova and Geers (2008)];
- Large deformations are applicable at both macro and micro level;
- In case just the behaviour of the material at macro scale is of interest, regardless of RVE behaviour, it is possible to consider only the macro structure behaviour which is a consequence of the RVE characteristics.

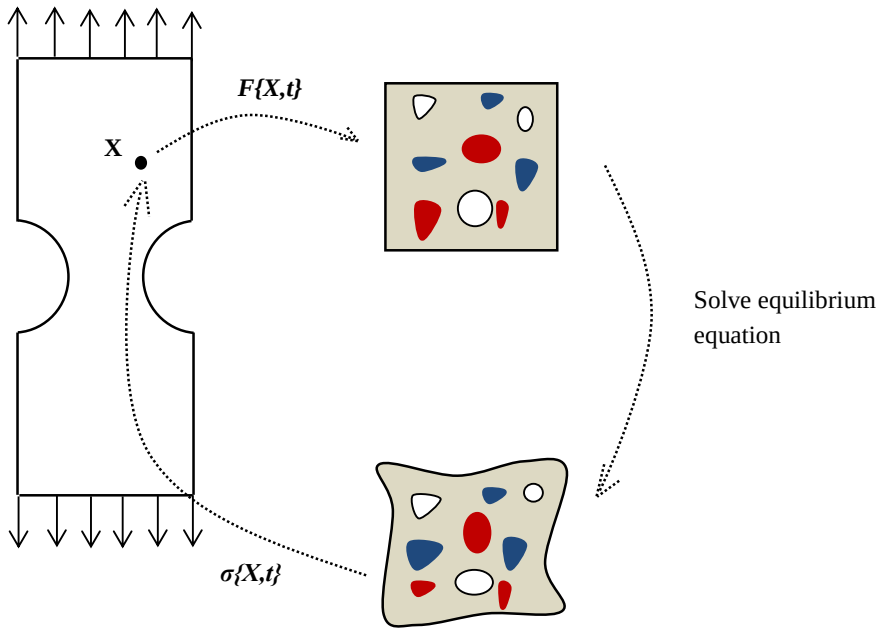

Figure 1.1: Schematic representation of coupled multi-scale problem.

During the last decade, several authors have contributed to the progress of the coupled multi-scale approach. Miehe et al. (1999) and Miehe and Koch (2002) have established crystal plasticity framework at small and finite strains. Second order multi-scale scheme was introduced by Kouznetsova et al. (2004). An enhancement of the coupled multi-scale was proposed by Ozdemir et al. (2008 a,b) in order to take into account the thermal effects. There are more recent studies within the frame work of multi-scale analysis, such as, to name a few, Mercatoris et al. (2009), Coenen et al. (2010), Speirs et al. (2008), Hettich et al. (2008), Ghanbari and Naghdabadi (2008) and Takano et al. (2010). Despite the above mentioned advantages of coupled multi-scale approach, it should be emphasized that this approach is computationally expensive. Some authors have proposed methods to minimize the required computation time and memory, e.g. parallel computing [Feyel and Chaboche (2000), Matsui et al. (2004)] and selective usage [Ghosh et al. (2001)]. In the later, in some parts of the specimen when

the deformation and stress state are not critical, continuum constitutive laws are used instead of multi-scale analysis.
Multi-scale constitutive models are particularly relevant and applicable for materials which have heterogeneous micro-structure. Semi-crystalline polymers often have spherulitic structure which consists of radial assembly of crystalline lamellae separated by amorphous layers [Ghorbel (2008)]. In view of existing different phases into the structure of these materials, using multi-scale approach seems really useful and applicable. Parks and Azhi (1990), Dahoun (1992), lee et al. (1993) and van Dommelin et al. (2003) proposed multi-scale models to describe the behaviour of semi-crystalline polymers at large strains. Modelling small deformation of semi-crystalline polymers using multi-scale approach has been accomplished by some authors, e.g. Nikolov and Doghri (2000), Nikolov et al. (2002), Drozdov and Gupta (2003) and Drozdov and Christiansen (2003). Contrary to semi-crystalline polymers, no crystalline phase in observed in the structure of amorphous polymers. Smit et al. (1998) used multi-level finite element modelling, the so-called coupled multi-scale strategy, in order to predict the deformation behaviour of heterogeneous polymeric materials. One may consider this work as one of the first applications of coupled multi-scale models for polymeric materials available in the literature. Smit et al. (1999) predicted the mechanical behaviour of voided polycarbonate by spatial discretization of the microstructure of the material. They used Leonov model for characterizing the behaviour of the glassy matrix material. Later, Smit et al. (2000) performed coupled multi-scale simulations on rubber modified notched and hour-glass-shaped polycarbonate and polystyrene tensile specimen with different volume fraction of rubbery particles.

1.3 Motivation

Polymeric materials have become a reference material for high reliability and performance applications. However, their performance in service conditions is difficult to predict, due in large part to their inherent complex morphology, which leads to non-linear behaviour observed [Araujo et al. (2014)]. In order to improve the mechanical properties of polymers, microstructural adaptations are common

procedures. For example, suitable scattering of low modulus rubber particles into the microstructure of amorphous and semi-crystalline polymers remarkably improves toughness and impact resistance [Smit (1998)]. Performing experimental studies has been a way to observe the behaviour of different materials including polymeric materials. There is a large number of experimental studies conducted on polymers in order to understand different features and aspects of deformation behaviour of polymers such as mechanical behaviour e.g. [Raha and Bowden (1972), Boyce and Arruda (1990), Buckley et al. (1996), Khan and Zhang (2001), Khan (2002), Drozdov and Christiansen (2003), Wu and Buckley (2004), Dupaix and Boyce (2005), Diez (2010), Srivastava et al. (2010), Del Piero and Pampolini (2012), Balieu et al. (2013), Senden et al. (2013), Hachour et al. (2014), Mathiesen (2014)] to name a few. In order to minimize expensive, time wise and cost wise, experimental procedures, powerful simulation tools are required to characterize the behaviour of polymers.

Undoubtedly, the design and analyzing polymeric materials are becoming more and more difficult due to advanced required performance for technological applications and also increasing demand for shorter implementation time. Hence, it is of great interest to predict the behaviour of polymeric materials from its molecular constituents. Figure (1.2) shows different length scales in polymeric materials. Establishing a rigorous link between molecular and macroscale behaviour is

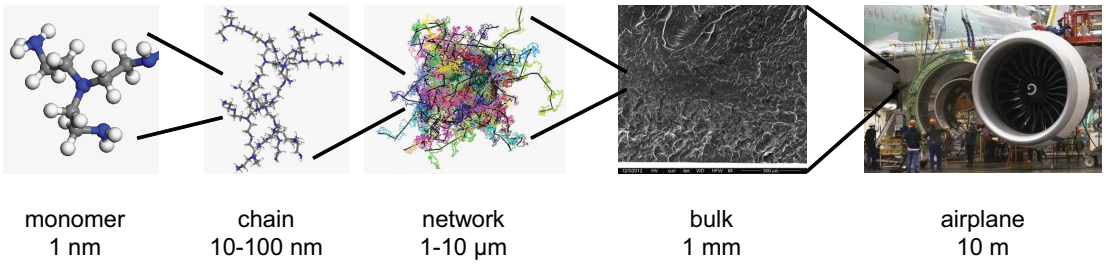

Figure 1.2: Hierarchical length scales for polymeric materials, adapted from [Li et al. (2013)].

greatly desired but not fully achieved yet due to the fact that characterization of polymers involves different spatial and also temporal scales. Figure (1.3) depicts length and time scales associated with different simulations methods. According

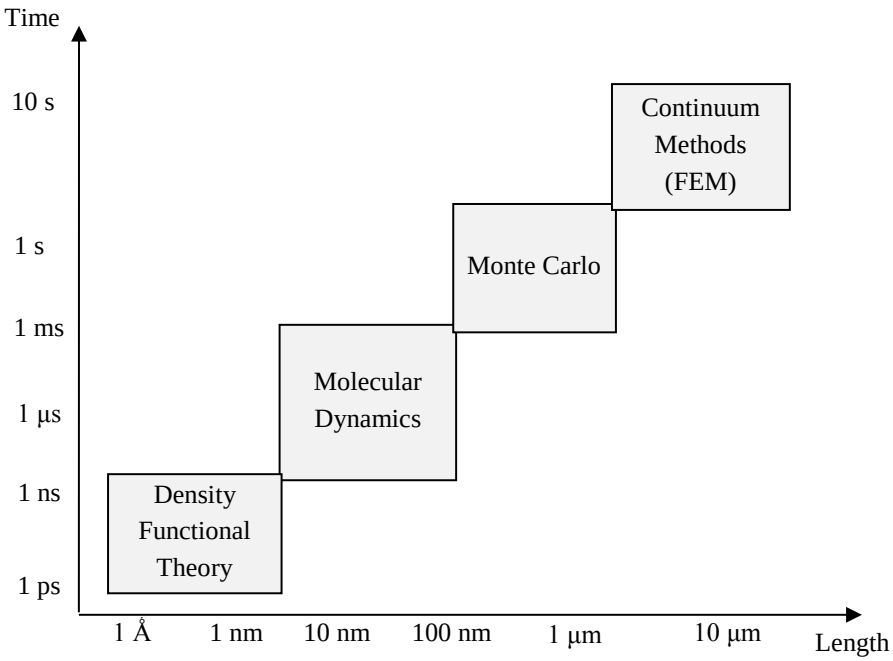

Figure 1.3: Spatial and Temporal scales associated with different simulation approaches, adapted from [Araujo et al. (2014)].

to the aforementioned issues, the necessity and importance of multi-scale modelling, particularly for the case of polymers is undoubtedly obvious. In this work, purely phenomenological, micromechanical and coupled multi-scale modelling approach are used in order to characterize the mechanical behaviour of amorphous polymers.

1.4 Scope and outline

The goal of the thesis is to develop new constitutive models to capture the mechanical behaviour of polymers using finite element method. Both macro structure (e.g. a dumbbell shape tensile specimen) and micro structure (e.g. dispersed rubbery particles in glassy matrix) are considered in order to predict the defor-

mation behavior at both scales and the effect of micro structure on the overall macro structure behavior. The main tools for the aforementioned objective are:

- An elasto-viscoplastic constitutive model to describe the deformation behaviour of the polymer under study at the macro level or the polymeric matrix at the RVE level;
- Finite element discretization of macro structure as well as micro structure;
- A finite strain micro-macro homogenization method;
- A coupled multi-scale model in order to solve equilibrium problem at both macro scale and micro scale simultaneously;
- A continuum level porous elasto-viscoplastic model to characterize mechanical behaviour of heterogeneous polymers which presents volumetric plastic deformation.

For the readers' convenience, the structure of the thesis is provided below.

Chapter 2

In this chapter, the main concepts of continuum mechanics and finite element method in quasi-static non-linear solid mechanics are reviewed [De Souza Neto et al. (2008)]. This is by no means a comprehensive presentation of the subjects and an attempt is made to provide the most important concepts of the subjects used in this work.

Chapter 3

In this chapter a three dimensional finite strain elasto-viscoplastic constitutive model is developed based on the single mode compressible Leonov model [Timmermans (1998), Govaert et al. (2000)]. The model is composed by the Maxwell model and a spring in a parallel assemblage. The Maxwell model is characterized by an initial elastic response and the Eyring viscosity which describes yielding and viscoplastic behavior. The Eyring flow relation is extended to include intrinsic softening behavior. The spring parallel to the Maxwell element describes the hardening behavior. The elasto-viscoplastic constitutive model predicts an

initial linear elastic behavior; strain rate, temperature and pressure dependent yield; post yield softening and hardening. The integration algorithm of the model, reduced to a single non-linear scalar equation, is presented and some simple examples and benchmark problems are provided in order to show the predictive capability of the model and also to assess the efficiency and robustness of the finite element implementation. An efficient integration algorithm which can dramatically decrease the computational cost when analyzing real life structures specially using explicit Finite Element algorithms, is proposed.

Chapter 4

This chapter describes a modified version of an already developed constitutive model, introduced in chapter 3, in order to predict the behaviour of polymers under different stress states. One of the important issues raised in material constitutive modelling and material parameters identification is that, the material properties obtained from one specific stress state (e.g. uniaxial compression or tension) do not provide good estimation of material behaviour in other stress states. In other words, in order to have good estimation of material behaviour under different stress states, one set of material properties may, most likely, not suffice. Some experimental results for a specific commercial grade of Bisphenol, a polycarbonate called Makrolon 2607, under three different stress states: uniaxial compression, plane strain compression and tensile test on a dumbbell shape specimen, are taken from [Diez (2010)]. Material properties are quantified and calibrated for uniaxial compression. The material parameters obtained are then used for plane strain compression and for the tensile test on the dumbbell shape specimen. It is realized that the prediction of the model (using properties obtained for uniaxial compression) for the later stress states should be modified. Based on the comparisons between simulations and experimental results, some modifications, using lode angle parameter, are proposed to improve the prediction of the model for the softening and hardening regimes of deformation.

Chapter 5

In this chapter, a statistical analysis of numerical experiments is proposed in order

to determine the size of the Representative Volume Element (RVE) for heterogeneous amorphous polymers subjected to finite deformation. The Finite Element Method (FEM) is used in combination with mathematical homogenization to obtain the macrostructure stress-strain behavior. Rubber Toughened Polystyrene (RT-PS) with two different fractions of rubbery particles is considered as the driving material of this chapter. The Leonov based model, presented in Chapter 3, is used for the matrix material and the rubbery particles are modelled as voids inside the micro-structure. First, the necessity of determination of the size of RVE is shown. Then, two criteria and an associated algorithm are proposed to be used for the RVE size determination. By performing a statistical-numerical analysis, following the proposed criteria and algorithm, the size of the Representative Volume Element (RVES) is determined for RT-PS for Inclusion Volume Fraction (IVF) equal to 10% and 15%.

Chapter 6

In this chapter, a continuum level constitutive model is developed in order to predict the behaviour of heterogeneous polymeric materials. While assuming homogeneous polymers, Chapters 3 and 4, the plastic deformation of the material is assumed incompressible. In other words, the flow rule of homogeneous material is totally deviatoric. This chapter presents a continuum constitutive model with a flow potential representing both deviatoric and volumetric plastic deformations. To this end, the model presented in Chapter 3 is used and Gurson yield surface is used to modify the flow rule of the model in order to account for the porosity effect on the overall deformation behaviour. Besides, coupled Multi-scale (micro-macro) analysis is used in this chapter in order to characterize the behaviour of heterogeneous polymeric materials. RT-PS is used as the driving material of this chapter. The model presented in Chapter 3 is used for Polystyrene matrix and the rubbery particles, which toughen the polymeric matrix, are modelled as voids. Using coupled micro-macro simulations, the macro structure behaviour as well as micro structure behaviour is characterized. Some comparisons are made between homogeneous and heterogeneous materials behaviour at macro level. Some more comparisons are also made between both previously introduced approaches.

Chapter 7

In this final chapter, achievements of the thesis are summarized. Conclusions drawn from different stages of the work are presented and finally, according to development of different stages of the work, some suggestions for future work are provided.

Chapter 2

Continuum mechanics and Finite Element Method

With the objective of modelling the mechanical behaviour of polymers, it is required to understand the constitutive models available in the literature for polymers and recognize their limitations, which can lead to the development of a new constitutive model. Becoming familiar with fundamental concepts of continuum mechanics is absolutely necessary. In order to solve the equilibrium equation obtained from continuum mechanics, a numerical method should be used. The Finite Element Method is the numerical approach used in this thesis. In this chapter, both continuum mechanics and Finite Element Method are briefly presented.

2.1 Continuum Mechanics

This section of this chapter provides some fundamental concepts of continuum mechanics. It is worth noting that since detailed and comprehensive textbooks such as [Holzapfel (2000), Criesfield (2000), Bertram (2005), Bonet and Wood (2008) and Shabana (2008)] explain continuum mechanics theory, this subject is just briefly reviewed here. First, kinematics of deformation is explained in Section 2.1.1. Then, the fundamental thermodynamic laws are introduced in Section 2.1.3. Finally, Section 2.1.4 derives the quasi-static initial boundary value problem.

2.1.1 Kinematics of deformation

A body which has occupied the region Ω_0 with the boundary $\partial\Omega_0$ is under a deformation represented as $\boldsymbol{\varphi}$. Particle $\mathbf{p}$ is located either in the body or on its boundary. During the deformation, after passing a specific time t, the particle will have another position $\mathbf{x}$.

$$\mathbf{x} = \boldsymbol{\varphi}(\mathbf{p}, t). \tag{2.1}$$

Displacement vector, $\mathbf{u}$, is defined as follows:

$$\mathbf{u}(\mathbf{p}, t) = \boldsymbol{\varphi}(\mathbf{p}, t) - \mathbf{p}. \tag{2.2}$$

Figure (2.1) shows the initial and final configuration together with the displacement vector. Inverting relation (2.1) gives:

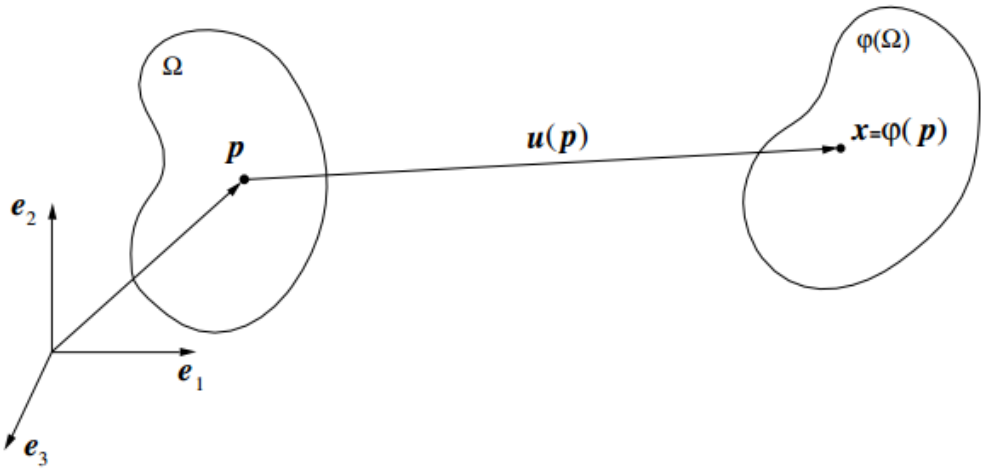

Figure 2.1: Deformation. Initial and deformed configuration (adapted from Figure (3.1) of [De Souza Neto et al. (2008)]).

$$\mathbf{p} = \boldsymbol{\varphi}^{-1}(\mathbf{x}, t). \tag{2.3}$$

It should be emphasized that in relation (2.3), it is assumed that the deformation $\boldsymbol{\varphi}$ is reversible.

In the above mentioned relations, two different configurations exist. The first one is the initial (undeformed or material) configuration and the second one is the

current (deformed or spatial) configuration. Particle $\mathbf{p}$ is in the initial one and the material particle $\mathbf{x}$ is in the current one. The velocity of particle $\mathbf{p}$ is given by:

$$\dot{\mathbf{x}} = \frac{\partial \boldsymbol{\varphi}(\mathbf{p}, t)}{\partial t} \tag{2.4}$$

Using relation (2.3), the velocity of the material particle $\mathbf{x}$ at time t is given by:

$$\boldsymbol{\upsilon}(\mathbf{x}, t) = \dot{\mathbf{x}}(\boldsymbol{\varphi}^{-1}(\mathbf{x}, t), t). \tag{2.5}$$

2.1.1.1 The deformation gradient

the deformation gradient is defined by:

$$\mathbf{F}(\mathbf{p}, t) = \nabla_p \boldsymbol{\varphi}(\mathbf{p}, t) = \frac{\partial \mathbf{x}_t}{\partial \mathbf{p}}. \tag{2.6}$$

Substituting relation (2.2) in relation (2.6), results in:

$$\mathbf{F} = \mathbf{I} + \nabla_p \mathbf{u}, \tag{2.7}$$

in relation (2.7), the second order identity tensor is represented as $\mathbf{I}$. The term ∇_p in relations (2.6) and (2.7) is a material gradient operator and the deformation gradient is defined in the reference configuration. The deformation gradient in the deformed configuration is given by:

$$\mathbf{F}(\mathbf{x}, t) = [\nabla_x \boldsymbol{\varphi}^{-1}(\boldsymbol{x}, t)]^{-1} = [\mathbf{I} - \nabla_x \mathbf{u}]^{-1}, \tag{2.8}$$

where, ∇_x is a spatial gradient operator. Determinant of the deformation gradient, represented as J, is the volume change during deformation. Determinant of the deformation gradient J, is also called deformation Jacobian.

$$J = \det \mathbf{F}. \tag{2.9}$$

Polar decomposition

Polar decomposition of the deformation gradient results in:

$$\mathbf{F} = \mathbf{RU} = \mathbf{VR}, \tag{2.10}$$

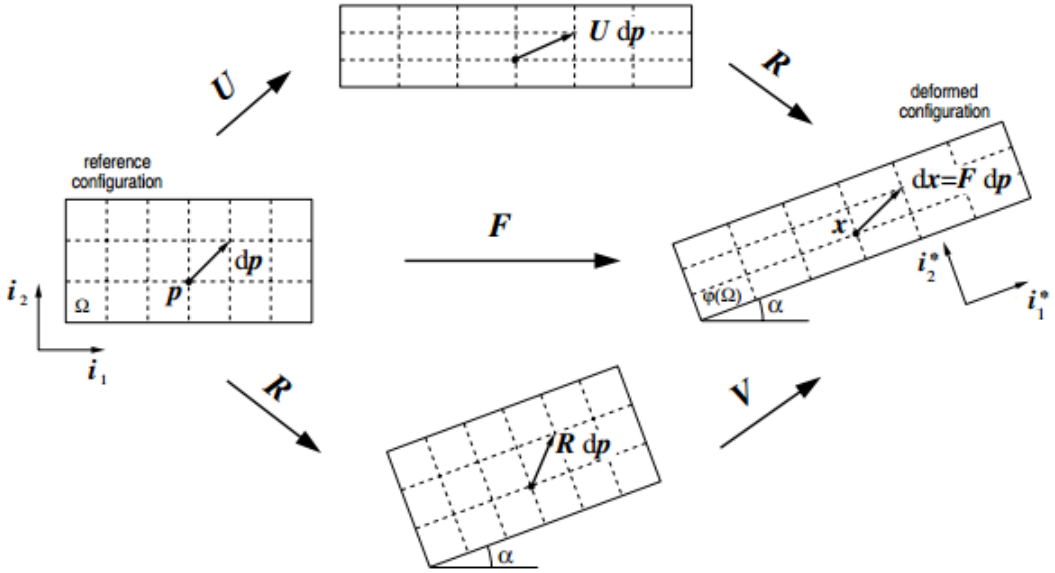

Figure 2.2: Polar decomposition of the deformation gradient (adapted from Figure (3.8) of [De Souza Neto et al. (2008)])

where $\mathbf{R}$ is called rotation tensor and it is a proper orthogonal tensor. The tensors $\mathbf{U}$ and $\mathbf{V}$ are symmetric positive definite tensors and called right and left stretch tensors, respectively. Figure (2.2) depicts the polar decomposition of the deformation gradient and the corresponding stretches and rotation. The right and left stretch tensors could be represented as:

$$\mathbf{U} = \sqrt{\mathbf{C}}, \quad \mathbf{V} = \sqrt{\mathbf{B}}, \tag{2.11}$$

where $\mathbf{C}$ and $\mathbf{B}$ are right and left Cauchy-Green strain tensors, respectively.

$$\mathbf{C} = \mathbf{U}^2 = \mathbf{F}^T\mathbf{F}, \quad \mathbf{B} = \mathbf{V}^2 = \mathbf{F}\mathbf{F}^T. \tag{2.12}$$

Multiplicative kinematics

The main assumption behind the finite strain constitutive framework, adopted in this work, is the multiplicative decomposition of the deformation gradient. Based on this assumption, the deformation gradient, $\mathbf{F}$, is multiplicatively composed of the elastic deformation gradient, $\mathbf{F}^e$, and the plastic deformation gradient, $\mathbf{F}^p$,

[Lee (1969)].

$$\mathbf{F} = \mathbf{F}^e \, \mathbf{F}^p \tag{2.13}$$

In fact, the decomposition, relation (2.13), introduces a local unstressed intermediate configuration obtained by elastic unloading from the final deformed configuration. Figure (2.3) schematically represents the multiplicative deformation gradient. Polar decomposition of the elastic and plastic deformation gradient

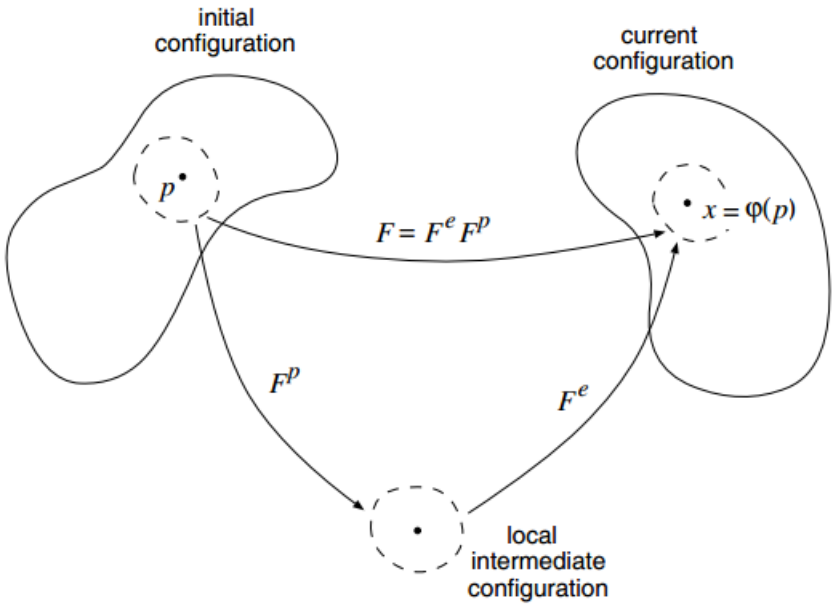

Figure 2.3: Multiplicative kinematics (adapted from Figure (14.1) of [De Souza Neto et al. (2008)])

results in:

$$\mathbf{F}^e = \mathbf{R}^e\mathbf{U}^e = \mathbf{V}^e\mathbf{R}^e, \tag{2.14}$$

$$\mathbf{F}^p = \mathbf{R}^p\mathbf{U}^p = \mathbf{V}^p\mathbf{R}^p, \tag{2.15}$$

where, $\mathbf{R}^e, \mathbf{U}^e$ and $\mathbf{V}^e$ are the elastic rotation tensor, elastic right stretch tensor and elastic left stretch tensor, respectively. The terms in relation (2.15) are the corresponding plastic terms.

2.1.1.2 The velocity gradient

The velocity gradient is defined by:

$$\mathbf{L} = \nabla_x \boldsymbol{\upsilon}, \tag{2.16}$$

or, alternatively by

$$\mathbf{L} = \dot{\mathbf{F}}\mathbf{F}^{-1}. \tag{2.17}$$

The velocity gradient is additively composed of symmetric and skew part:

$$\mathbf{L} = \mathbf{D} + \mathbf{W}. \tag{2.18}$$

The stretching tensor (or rate of deformation tensor) is represented by $\mathbf{D}$ and is the symmetric part of the velocity gradient.

$$\mathbf{D} = sym(\mathbf{L}) = \frac{1}{2}\left(\mathbf{L} + \mathbf{L}^T\right) \tag{2.19}$$

where, the superscript T denotes the transpose of the tensor. The spin tensor is represented by $\mathbf{W}$ and is the skew part of the velocity gradient.

$$\mathbf{W} = skew(\mathbf{L}) = \frac{1}{2}\left(\mathbf{L} - \mathbf{L}^T\right). \tag{2.20}$$

The velocity gradient could be represented as:

$$\mathbf{L} = \mathbf{L}^e + \mathbf{F}^e\mathbf{L}^p(\mathbf{F}^e)^{-1}, \tag{2.21}$$

where, the elastic velocity gradient, $\mathbf{L}^e$, and plastic velocity gradient, $\mathbf{L}^p$, are defined by:

$$\mathbf{L}^e \equiv \dot{\mathbf{F}}^e(\mathbf{F}^e)^{-1}, \tag{2.22}$$

$$\mathbf{L}^p \equiv \dot{\mathbf{F}}^p(\mathbf{F}^p)^{-1}. \tag{2.23}$$

Based on the plastic velocity gradient, the rate of plastic deformation (plastic stretching tensor), $\mathbf{D}^p$, and plastic spin tensor, $\mathbf{W}^p$, are defined by:

$$\mathbf{D}^p \equiv sym\left(\mathbf{L}^p\right) = \frac{1}{2}\left[\mathbf{L}^p + \left(\mathbf{L}^p\right)^T\right], \tag{2.24}$$

$$\mathbf{W}^p \equiv skew\left(\mathbf{L}^p\right) = \frac{1}{2}\left[\mathbf{L}^p - \left(\mathbf{L}^p\right)^T\right]. \tag{2.25}$$

2.1.1.3 Strain measures

The material particles are strained when their relative position changes after deformation. In order to measure the amount of straining, different relations could be introduced and used. Lagrangian and Eulerian strain measures are two important class of strain measures. The Lagrangian strain tensor is given by:

$$\mathbf{E}^{(m)} = \begin{cases} \frac{1}{m}(\mathbf{U}^m - \mathbf{I}), & m \neq 0 \\ \ln[\mathbf{U}], & m = 0 \end{cases} \tag{2.26}$$

where m is a real number and $\ln[\bullet]$ represents the logarithm of a tensor. The Eulerian strain tensor is given by:

$$\varepsilon^{(m)} = \begin{cases} \frac{1}{m}(\mathbf{V}^m - \mathbf{I}), & m \neq 0 \\ \ln[\mathbf{V}], & m = 0 \end{cases} \tag{2.27}$$

In this thesis, the logarithmic strain tensor ($m = 0$) is used.

2.1.2 Stress measures

There are different definitions in order to measure the stress. In this thesis the Kirchhof stress, $\boldsymbol{\tau}$, and Cauchy stress, $\boldsymbol{\sigma}$, are used and they are defined in this section. The Cauchy stress tensor or true stress is given by:

$$\mathbf{t} = \boldsymbol{\sigma}\mathbf{n}, \tag{2.28}$$

where $\mathbf{t}$ is the surface traction force and $\mathbf{n}$ is its associated normal vector. The Cauchy stress tensor can be additively composed of hydrostatic term and deviatoric part.

$$\boldsymbol{\sigma} = \mathbf{s} - p\mathbf{I}, \tag{2.29}$$

where, $\mathbf{s}$ is the deviatoric stress and p is hydrostatic pressure:

$$\mathbf{s} = dev\,(\boldsymbol{\sigma}) = \mathsf{I}_d : \boldsymbol{\sigma}, \tag{2.30}$$

where, I_d is the deviatoric fourth order identity tensor:

$$\mathsf{I}_d = \mathsf{I}_s - \frac{1}{3}\left(\mathbf{I} \otimes \mathbf{I}\right), \tag{2.31}$$

where, I_s is the symmetric fourth order identity and $\mathbf{I}$ is the second order identity. The tensors I_s and $\mathbf{I}$ in component form can be expressed by:

$$\mathsf{I}_{ijkl} = \frac{1}{2}\left[\delta_{ik}\delta_{jl} + \delta_{il}\delta_{jk}\right], \tag{2.32}$$

$$\mathbf{I}_{ij} = \delta_{ij}, \tag{2.33}$$

where, δ is the Kronecker delta. The hydrostatic pressure is given by:

$$p = -\frac{1}{3}tr\left(\boldsymbol{\sigma}\right). \tag{2.34}$$

The second stress measure is the Kirchhoff stress tensor denoted by $\boldsymbol{\tau}$, defined as

$$\boldsymbol{\tau} = J\boldsymbol{\sigma}. \tag{2.35}$$

The Kirchhoff stress tensor, similarly to the Cauchy stress, can be additively composed of deviatoric and hydrostatic components.

$$\boldsymbol{\tau} = \boldsymbol{\tau}_d - \tau_h\mathbf{I}, \tag{2.36}$$

where the deviatoric Kirchhof stress is given by:

$$\boldsymbol{\tau}_d = dev[\boldsymbol{\tau}] = \mathsf{I}_d : \boldsymbol{\tau}, \tag{2.37}$$

and the hydrostatic Kirchhof stress is defined by:

$$\tau_h = -\frac{1}{3}tr[\boldsymbol{\tau}]. \tag{2.38}$$

2.1.3 Fundamental laws of thermodynamics

In this section, the fundamental laws of thermodynamics, which are necessary to derive the equilibrium equations will be presented. Conservation of mass, momentum balance, the first and second principles of thermodynamics and Clausius-Duhem inequality are explained.

2.1.3.1 Conservation of mass

The Postulate of the conservation of mass implies that:

$$\dot{\rho} + \rho \; div_x \; \dot{\mathbf{u}} = 0, \tag{2.39}$$

where the density of the material at deformed configuration is represented by ρ.

2.1.3.2 Momentum balance

The strong form of the equilibrium equation, also referred to as momentum balance, is given by:

$$div_x \boldsymbol{\sigma} + \mathbf{b} = \rho \ddot{\mathbf{u}}, \tag{2.40}$$

where $\mathbf{b}$ denotes the body force vector in the deformed configuration. The equilibrium equation (2.40) needs to fulfill the following boundary condition:

$$\mathbf{t} = \boldsymbol{\sigma} \mathbf{n}, \tag{2.41}$$

where $\mathbf{t}$ is a traction vector applied on the boundary of the body.

2.1.3.3 The first and second principles of thermodynamics

The first principle of thermodynamics implies the conservation of energy. The first principle of thermodynamics can be mathematically represented by:

$$\rho \dot{e} = \boldsymbol{\sigma} : \mathbf{D} + \rho r - div_x \mathbf{q}, \tag{2.42}$$

where e, r and $\mathbf{q}$ are, respectively, the specific internal energy, the density of heat production and the heat flux. In this thesis, only isothermal process are considered, i.e. it is assumed the temperature during deformation is not altered. For constant temperature deformation processes, the first principle of thermodynamics reduces to:

$$\rho \dot{e} = \boldsymbol{\sigma} : \mathbf{D}. \tag{2.43}$$

The equation above states that the rate of internal energy per unit of deformed volume must equal the stress power, $\boldsymbol{\sigma} : \mathbf{D}$, per unit of deformed volume. The

relation between the density at initial configuration and final configuration is given by:

$$\bar{\rho} = J\rho, \tag{2.44}$$

where $\bar{\rho}$ denotes the reference density. Using equations (2.43) and (2.44), the following relation could be written.

$$\bar{\rho}\dot{e} = \boldsymbol{\tau} : \mathbf{D}. \tag{2.45}$$

The second principle of thermodynamics states that the entropy production is irreversible. The following relation is the mathematical expression for the second principle of thermodynamics:

$$\rho T\dot{s} + div_x\mathbf{q} - \rho r \geq 0, \tag{2.46}$$

where s represents the entropy and temperature is denoted by T. Similarly to the first principle of thermodynamics, in case of constant temperature processes, Equation (2.46) could be simplified to:

$$\rho T\dot{s} \geq 0. \tag{2.47}$$

Using relation (2.44), Equation (2.47) could be rewritten as:

$$\bar{\rho} T\dot{s} \geq 0. \tag{2.48}$$

2.1.3.4 The Clausius-Duhem inequality

The specific free energy (Helmholtz free energy), ψ, is given by:

$$\psi = e - Ts \tag{2.49}$$

Re-arranging Equation (2.49) and performing time derivation results in:

$$T\dot{s} = \dot{e} - \dot{\psi}. \tag{2.50}$$

It should be emphasized that the process is postulated under constant temperature conditions and thus the derivation of temperature in order to time is zero, $\dot{T} = 0$. Using relation (2.45), it could be written:

$$\bar{\rho} T\dot{s} = \boldsymbol{\tau} : \mathbf{D} - \bar{\rho}\dot{\psi}. \tag{2.51}$$

Finally, substituting equation (2.48) gives.

$$\boldsymbol{\tau} : \mathbf{D} - \bar{\rho}\dot{\psi} \geq 0. \tag{2.52}$$

The inequality (2.52) is called Clausius-Duhem inequality.

2.1.4 The quasi-static IBVP

The formalism of constitutive equations to describe the deformation behavior of polymers in this work adopts an internal variable approach. Therefore, the generic constitutive problem reduce to the solution of an initial value problem. In order to derive the initial boundary value problem, the fundamental laws of thermodynamics will be used. Solving the initial boundary value problem, gives the mechanical behaviour of the solid under the specific boundary conditions and loads. It should be emphasized that this work is concerned with quasi-static problems i.e. the inertia effects are neglected. Relation (2.40), which expresses the equilibrium equation in strong form, is re-written as follows:

$$div_x \boldsymbol{\sigma} = 0. \tag{2.53}$$

Mathematical manipulation of relation (2.53), multiplying with virtual displacement $\boldsymbol{\eta}$ and volume integrating, results in:

$$\int_{\varphi(\Omega)} (div_x \boldsymbol{\sigma})^T \boldsymbol{\eta} dV = 0. \tag{2.54}$$

Application of some straightforward mathematical operations to relation (2.54) yields to:

$$\int_{\varphi(\Omega)} [\boldsymbol{\sigma} : \nabla_x \boldsymbol{\eta} - (div_x \boldsymbol{\sigma} \cdot \boldsymbol{\eta})] dV = 0. \tag{2.55}$$

Using the divergence theorem results in:

$$\int_{\varphi(\Omega)} \boldsymbol{\sigma} : \nabla_x \boldsymbol{\eta} dV - \int_{\varphi(\partial\Omega)} (\boldsymbol{\sigma} \cdot \mathbf{n})^T \boldsymbol{\eta} dA = 0. \tag{2.56}$$

Finally, substituting relation (2.41) into relation (2.56) leads to:

$$\int_{\varphi(\Omega)} \boldsymbol{\sigma} : \nabla_x \boldsymbol{\eta} dV - \int_{\varphi(\partial\Omega)} \mathbf{t} \cdot \boldsymbol{\eta} dA = 0. \tag{2.57}$$

Equation (2.57) is the so-called weak form of the equilibrium equation at final configuration. In other words, Equation (2.57) is the spatial version of the initial boundary value problem. Using the weak form of the equilibrium equation allows using numerical methods for solving the initial value problem.

Problem 2.1
Given a prescribed deformation gradient history

$$\mathbf{F}(t) = \mathbf{I} + \nabla_p \mathbf{u}(\mathbf{p}, t) \tag{2.58}$$

and the Cauchy stress, at each point of the body expressed as

$$\boldsymbol{\sigma}(t) = \boldsymbol{\sigma}(\mathbf{F}(t, \boldsymbol{\alpha}(t)) \tag{2.59}$$

obtained from the solution of the constitutive initial boundary value problem where $\boldsymbol{\alpha}$ is the set of internal variables associated with the material, find a kinematically admissible displacement function, $\mathbf{u} \in \mathcal{K}$ such that the equation

$$\int_{\varphi(\Omega)} \boldsymbol{\sigma}(t) : \nabla_x \boldsymbol{\eta} dV - \int_{\varphi(\partial\Omega)} \mathbf{t}(t) \cdot \boldsymbol{\eta} dA = 0, \tag{2.60}$$

is satisfied for all $t \in [t_0, t_n]$ and for all $\boldsymbol{\eta} \in \nu_t$. The set of kinematically admissible displacements, $\mathcal{K}$, and the space of virtual displacements at time t, ν_t, are respectively given by

$$\mathcal{K} = \{\mathbf{u} : \Omega \to \mathcal{U} | \boldsymbol{u}(\boldsymbol{p}, t) = \bar{\boldsymbol{u}}(\boldsymbol{p}, t), t \in [t_0, t_n], \boldsymbol{p} \in \partial\varphi_u\}, \tag{2.61}$$

$$\nu_t = \{\eta : \varphi \to \mathcal{U} | \eta = 0 \in \partial\varphi_u(t)\}. \tag{2.62}$$

Unfortunately, analytical solutions for the problem defined above exist only for a restricted set of special cases. For accurate predictions of the mechanical behavior of solids in the general case, the use of numerical methods is therefore indispensable.

Material version of the initial boundary value problem
For reference, the material version of the weak form of the equilibrium equation is also herein provided, which reads

$$\int_{\varphi} \mathbf{P} : \nabla_p \boldsymbol{\eta} dV - \int_{\partial\varphi} \bar{\boldsymbol{t}} \cdot \boldsymbol{\eta} dA = 0, \tag{2.63}$$

where, $\mathbf{P}$ is the first Piola Kirchhof stress and $\bar{\boldsymbol{t}}$ is the surface traction per unit reference area.

2.2 Displacement-based finite elements

This section briefly describes the displacement based finite element which is used in this work for solving the equilibrium equation. It is essential to bear in mind, before proceeding further, that in the finite element solution of the generic initial boundary value problem, two main numerical approximations, which are schematically represented in Figure (2.4), are required. The numerical approximation steps are:

1. A time discretization of the underlying constitutive initial value problem.
2. A spatial discretization.

Introducing the aforementioned approximations reduces the original initial boundary value problem to an incremental (generally nonlinear) set of algebraic finite element equations, which should be solved at each time station of the considered time interval. Furthermore, the solution of the corresponding system of equations is described later in this chapter. The Newton-Raphson method is the one which is particularly emphasized, due to the asymptotic quadratic rate of the convergence of the method. In Figure (2.4), IVP refers to "Initial Value Problem" and PVW is an acronym for "Principal of Virtual Work".

2.2.1 Spatial discretisation

A numerical strategy is required for solving problem 2.1 for a generic case. In finite element framework, the so-called interpolation or shape functions are used for discretization of the field variables. In displacement-based finite elements, the field variable to be interpolated is displacement. For a given element e, displacement is interpolated as follows:

$$\mathbf{u}(\boldsymbol{x}) \equiv \sum_{i=1}^{n_{node}} N_i^{(e)}(\boldsymbol{x})\mathbf{u}_i, \tag{2.64}$$

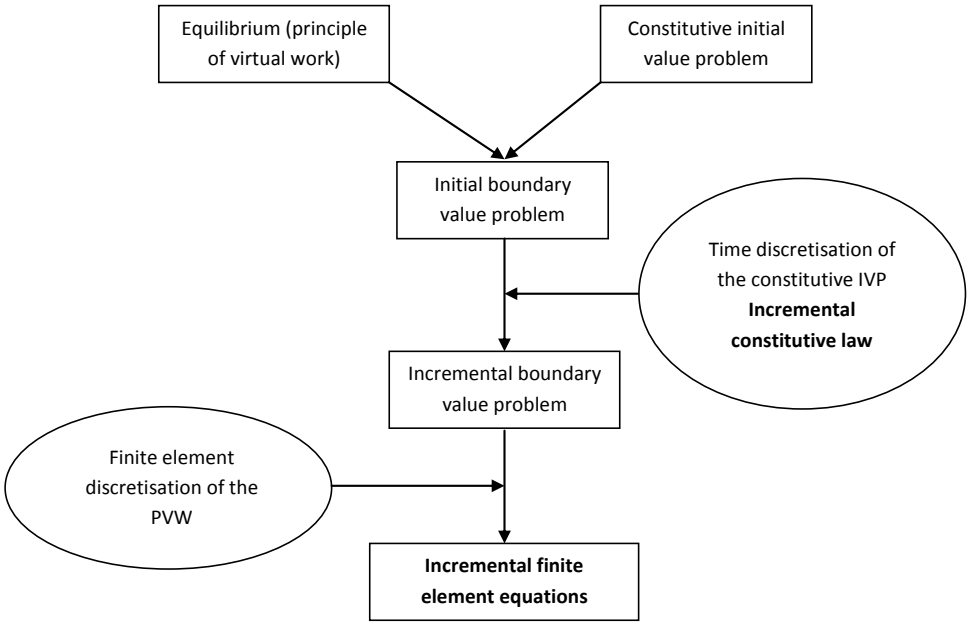

Figure 2.4: Numerical approximation. The initial boundary value problem is reduced to a set of incremental finite element equations, reproduced from Figure (4.1) of [De Souza Neto et al. (2008)]

where $N_i^{(e)}(\boldsymbol{x})$ is the shape function associated with node i (evaluated at $\boldsymbol{x}$) and n_{node} is the number of nodes of the element. In Figure (2.5), a three noded triangular element with linear shape function is depicted. A global interpolation function could be introduced:

$$\mathbf{u}(\boldsymbol{x}) \equiv \sum_{i=1}^{n_{poin}} N_i^g(\boldsymbol{x})\mathbf{u}_i, \tag{2.65}$$

where n_{poin} is the total number of nodes of the finite element mesh and $N_i^g(\boldsymbol{x})$ is the global interpolation matrix given by:

$$\mathbf{N}^g(\boldsymbol{x}) = [diag[N_1^g(\boldsymbol{x})] \;\; diag[N_2^g(\boldsymbol{x})] \;\; \cdots \;\; diag[N_{n_{poin}}^g(\boldsymbol{x})]] \tag{2.66}$$

where $diag[N_i^g]$ denotes a $n_{dim} \times n_{dim}$ diagonal matrix defined by:

$$diag[N_i^g] = \begin{pmatrix} N_i^g & 0 & \cdots & 0 \\ 0 & N_i^g & \cdots & 0 \\ \vdots & \vdots & \ddots & \vdots \\ 0 & 0 & \cdots & N_i^g \end{pmatrix}. \tag{2.67}$$

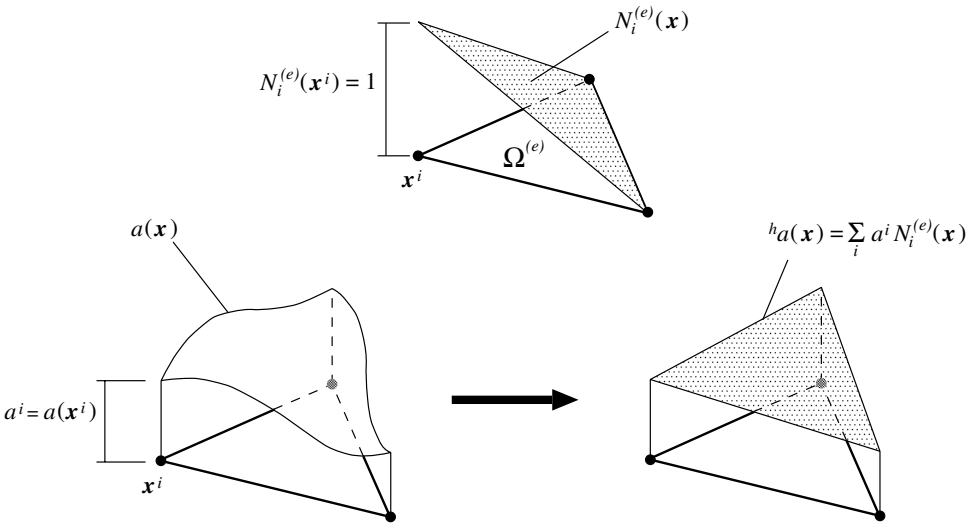

Figure 2.5: Finite element interpolation. The element shape function, adapted from Figure (4.2) of [De Souza Neto et al. (2008)].

A typical case, where a plane domain has been discretised by a mesh of triangular finite elements, is illustrated in Figure (2.6). For the sake of convenience, the

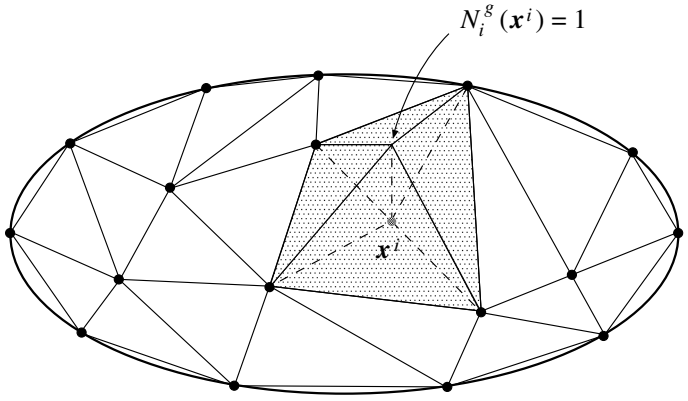

Figure 2.6: Finite element interpolation. The global shape function adapted from Figure (4.2) of [De Souza Neto et al. (2008)]

global vector of nodal displacements is defined as:

$$\mathbf{u} = [u_1^1, \cdots u_1^{n_{dim}}, \cdots\cdots u_{n_{poin}}^1, \cdots u_{n_{dim}}^{n_{poin}}]^T. \tag{2.68}$$

Using the above introduced matrices, Equation (2.64) could be represented by:

$$\boldsymbol{u}(\boldsymbol{x}) = \mathbf{N}^g(\boldsymbol{x})\mathbf{u}, \tag{2.69}$$

Equation (2.69) is displacement field interpolated by discrete functions. By the same token, virtual displacements could be given by:

$$\boldsymbol{\eta}(\boldsymbol{x}) = \mathbf{N}^g(\boldsymbol{x})\boldsymbol{\eta}. \tag{2.70}$$

It is also convenient to define the global discrete symmetric gradient matrix, $\mathbf{B}^g$. In plane stress and plane strain problems has the form:

$$\mathbf{B}^g = \begin{pmatrix} N^g_{1,1} & 0 & N^g_{2,1} & 0 & \cdots & N^g_{n_{poin},1} & 0 \\ 0 & N^g_{1,2} & 0 & N^g_{2,2} & \cdots & 0 & N^g_{n_{poin},2} \\ N^g_{1,2} & N^g_{1,1} & N^g_{2,2} & N^g_{2,1} & \cdots & N^g_{n_{poin},2} & N^g_{n_{poin},1} \end{pmatrix}, \tag{2.71}$$

The following notation has been used:

$$(\cdot)_{i,j} = \frac{\partial(\cdot)_i}{\partial x_j}. \tag{2.72}$$

For the sake of completeness, the *global discrete full gradient operator*, $\mathbf{G}^g$, is also defined. It is, in plane stress and plane strain analyses, given by:

$$\mathbf{G}^g = \begin{pmatrix} N^g_{1,1} & 0 & N^g_{2,1} & 0 & \cdots & N^g_{n_{poin},1} & 0 \\ 0 & N^g_{1,1} & 0 & N^g_{2,1} & \cdots & 0 & N^g_{n_{poin},1} \\ N^g_{1,2} & 0 & N^g_{2,2} & 0 & \cdots & N^g_{n_{poin},2} & 0 \\ 0 & N^g_{1,2} & 0 & N^g_{2,2} & \cdots & 0 & N^g_{n_{poin},2} \end{pmatrix}. \tag{2.73}$$

2.2.2 Temporal discretization

The non-linear incremental finite element procedure is briefly presented. In most of the materials used in practical engineering applications, it is required to take into account the deformation history in the modelling of the behaviour of the material. The materials whose deformation is dependent on deformation history are called path dependent materials. For these kinds of materials, it is required to apply time discretization to the constitutive equations. In this work, a (pseudo-) time discretization of the constitutive equations within the time increment $[t_n, t_{n+1}]$ will be performed.

Generally, an incremental constitutive function for a path dependent material could be represented by:

$$\boldsymbol{\sigma}_{n+1} = \hat{\boldsymbol{\sigma}}(\mathbf{F}_{n+1}, \boldsymbol{\alpha}_n). \tag{2.74}$$

It should be emphasized that the numerical constitutive law is generally non-linear and path-independent within one increment. Similarly, the integration algorithm defines an incremental constitutive function for the internal variables:

$$\boldsymbol{\alpha}_{n+1} = \hat{\boldsymbol{\alpha}}(\mathbf{F}_{n+1}, \boldsymbol{\alpha}_n). \tag{2.75}$$

Up to this point, it suffices to leave the incremental constitutive functions $\hat{\boldsymbol{\sigma}}$ and $\hat{\boldsymbol{\alpha}}$ unspecified for the sake of generality.

2.2.3 The non-linear incremental finite element equation

Incremental finite element equilibrium equation is obtained from Equation (2.60) using the definition of the incremental constitutive function, presented in Section 2.2.2, and the spatial discretization, presented in Section 2.2.1:

$$\mathbf{r}(\mathbf{u}_{n+1}) \equiv \mathbf{f}^{int}(\mathbf{u}_{n+1}) - \mathbf{f}^{ext} = 0, \tag{2.76}$$

where $\mathbf{f}^{int}$ and $\mathbf{f}^{ext}$ are the internal and external force vectors. For a given element e the internal and external force vectors are given by:

$$\mathbf{f}^{int} = \int_{\varphi_{n+1}(\varphi^{(e)})} \mathbf{B}^T \hat{\boldsymbol{\sigma}}(\mathbf{F}_{n+1}, \boldsymbol{\alpha})\, dV, \tag{2.77}$$

$$\mathbf{f}^{ext} = \int_{\varphi_{n+1}(\partial\varphi^{(e)})} \mathbf{N}^T \boldsymbol{t}_{n+1}\, dA, \tag{2.78}$$

Generally, Equation (2.76) is non-linear and thus it is required to use an appropriate (numerical) method to solve it. An incremental scheme is adopted in this work where the external load is applied in different (pseudo) time increments. In each time increment a specific fraction of the external load is applied. In this thesis, in order to keep the strain rate constant, the load increments are not the same for all increments and it will be explained in the subsequent chapter, how the strain rate is kept constant by applying different load increments in different

Table 2.1: The incremental non-linear finite element scheme - implicit solution.

1.Assemble the global external force vector,$\bar{\mathbf{f}}^{ext}$
2.Initialize increment counter $i = 1$
3.Set load factor ,λ_i
4.Solve the non-linear equilibrium equation $\mathbf{r}(\mathbf{u}_{n+1}) = \mathbf{f}^{int}(\mathbf{u}_{n+1}) - \lambda_i \bar{\mathbf{f}}^{ext} = 0$
5.Update increment counter $i = i + 1$
6.Check if prescribed number of increments has been achieved

increments. Table (2.1) summarizes how Equation (2.76) is solve in an incremental non-linear finite element scheme.
It should be mentioned that practically, the external force is computed by:

$$\mathbf{f}_{n+1}^{ext} = \lambda_{n+1} \bar{\mathbf{f}}^{ext}, \tag{2.79}$$

where λ_{n+1} is the prescribed load factor at time t_{n+1} and $\bar{\mathbf{f}}^{ext}$ is computed only once at the first iteration of the incremental procedure through the expression

$$\bar{\mathbf{f}}^{ext} = \int_{\varphi_{n+1}(\partial\Omega^{(e)})} \mathbf{N}^T \bar{\boldsymbol{t}} dA \tag{2.80}$$

where $\bar{\mathbf{t}}$ is a prescribed field, which remains constant through the incremental procedure.

2.2.4 Numerical integration of $\mathbf{f}^{int}$ and $\mathbf{f}^{ext}$

In finite element solution, some numerical approximation is used to the exact integrals for computing the internal and external force vectors introduced in relations (2.77) and (2.78). Standard Gaussian quadratures is used to integrate both the internal and external force vectors. The internal force vector, $\mathbf{f}^{int}$ is approximated by the following expression:

$$\mathbf{f}_{(e)}^{int} = \int_{\varphi_{n+1}(\Omega^{(e)})} \mathbf{B}^T \hat{\boldsymbol{\sigma}} dV \approx \sum_{i=1}^{ngp} w_i J_i \mathbf{B}_i^T \hat{\boldsymbol{\sigma}}_i \tag{2.81}$$

where w_i and J_i are, respectively, the Gaussian weight and the Jacobian at the i^{th} integration point. A similar procedure is carried out for the external force vector.

2.2.5 Newton-Raphson method

As mentioned before, Equation (2.76) which is the finite element equilibrium equation is generally non-linear and an appropriate solution approach is required to be used for solving the equation. In this work, the Newton-Raphson method is used as the numerical method to solve the equation. It is worth mentioning that the Newton-Raphson method is particularly attractive due to its quadratic rate of convergence. Using the Newton-Raphson method and considering the finite element framework, the displacements are updated as:

$$\mathbf{u}_{n+1}^{k+1} = \mathbf{u}_{n+1}^{k} - \left(\frac{\partial \mathbf{r}}{\partial \mathbf{u}_{n+1}} \bigg|_{\mathbf{u}_{n+1}^{k}} \right)^{-1} \mathbf{r}\left(\mathbf{u}_{n+1}^{k}\right) \tag{2.82}$$

Equation (2.82) is rewritten as:

$$\mathbf{K}_T \delta \mathbf{u} = -\mathbf{r}(\mathbf{u}_{n+1}^{k}), \tag{2.83}$$

where

$$\delta \mathbf{u} = \mathbf{u}_{n+1}^{k+1} - \mathbf{u}_{n+1}^{k}, \tag{2.84}$$

and $\mathbf{K}_T$ is called global tangent stiffness matrix, given by

$$\mathbf{K}_T = \frac{\partial \mathbf{r}}{\partial \mathbf{u}_{n+1}} \bigg|_{\mathbf{u}_{n+1}^{k}} . \tag{2.85}$$

A schematic representation of the method is provided in Figure (2.7). To obtain the quadratic rate of convergence of the Newton-Raphson method, it is crucial to derive the tangent stiffness correctly. In the case of finite strains within a spatial description, the expression for Equation (2.85) arises quite naturally from the linearisation of the equilibrium equation in its weak form. Recalling that the internal force vector is integrated using a Gaussian quadrature (Equation 2.81), the element stiffness matrix is then given by:

$$\mathbf{K}_T^{(e)} = \sum_{i=1}^{ngp} w_i J_i \mathbf{B}_i^T \hat{\mathbf{a}}_i \mathbf{G}_i, \tag{2.86}$$

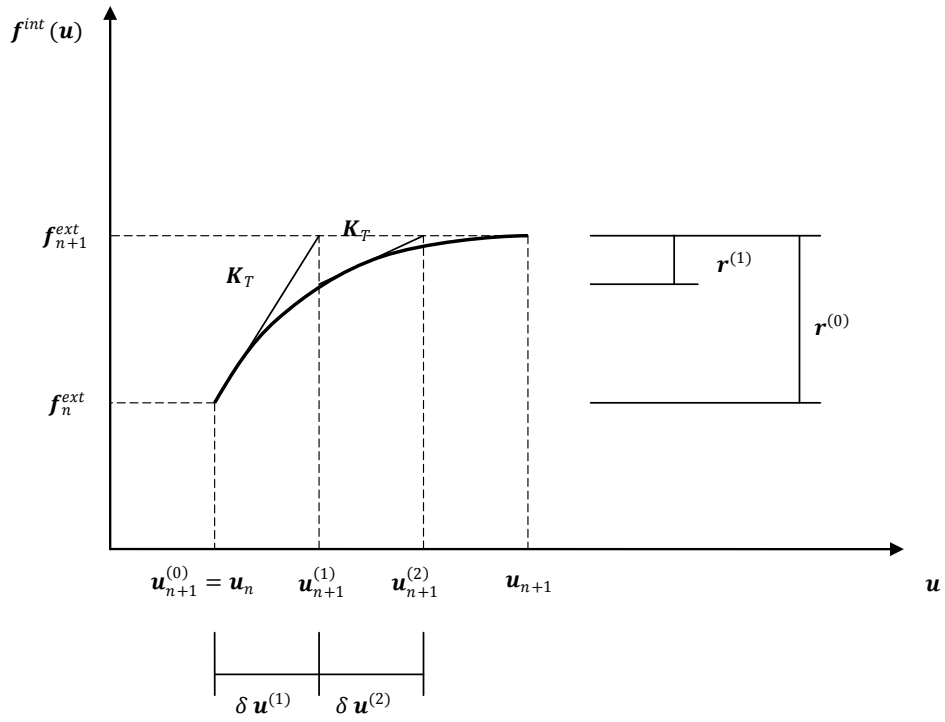

Figure 2.7: The Newton-Raphson algorithm for the incremental finite element equilibrium equation

where $\mathbf{a}_i$ is the spatial tangent modulus whose components are given by

$$\mathbf{a}^{ijkl} = \frac{1}{J}\frac{\partial \tau^{ij}}{\partial F^{km}} F^{lm} - \sigma^{il}\delta^{jk}. \tag{2.87}$$

Table (2.2) summarizes the full Newton-Raphson procedure associated with the present finite element framework at finite strains.

2.3 Conclusions

In this section, the main concepts of continuum mechanics and displacement based finite elements, which are used in this work, were briefly presented. It is worth emphasizing that all the concepts provided in this chapter are well-established and they are widely accepted by both academic community and industry. One may say that the Finite Element Method is now one of most applicable and

Table 2.2: Newton-Raphson scheme for the solution of the incremental non-linear finite element equilibrium equation (implicit solution).

1. Set $k = 1$, initial guess and residual function array
$$\mathbf{u}_{n+1}^{k} = \mathbf{u}_n; \;\; \mathbf{r}^k = \mathbf{f}^{int}(\mathbf{u}_n) - \lambda_{n+1}\bar{\mathbf{f}}^{ext}$$

2. Compute the consistent spatial tangent moduli
$$\mathbf{a}^{ijkl} = \frac{1}{J}\frac{\partial \tau^{ij}}{\partial F^{km}}F^{lm} - \sigma^{il}\delta^{jk}.$$

3. Assemble element tangent stiffness matrices
$$\mathbf{K}_T^{(e)} = \sum_{i=1}^{ngp} w_i J_i \mathbf{B}_i^T \hat{\mathbf{a}}_i \mathbf{G}_i,$$

4. Assemble global stiffness and solve for $\delta\mathbf{u}^{k+1}$
$$\mathbf{K}_T \delta\mathbf{u}^{k+1} = -\mathbf{r}^k$$

5. Update displacements
$$\mathbf{u}_{n+1}^{k+1} = \mathbf{u}_{n+1}^{k} + \delta\mathbf{u}^{k+1}$$

6. Update the deformation gradient
$$\mathbf{F}_{n+1}^{k+1} = \left(I + \nabla_x \mathbf{u}_{n+1}^{k+1}\right)^{-1}$$

7. Update stresses and internal variables
$$\boldsymbol{\sigma}_{n+1}^{k+1} = \hat{\boldsymbol{\sigma}}(\mathbf{F}_{n+1}^{k+1}, \boldsymbol{\alpha}_n); \;\; , \;\; \boldsymbol{\alpha}_{n+1}^{k+1} = \hat{\boldsymbol{\alpha}}(\mathbf{F}_{n+1}^{k+1}, \boldsymbol{\alpha}_n)$$

8. Compute element internal force
$$\mathbf{f}_{(e)}^{int} = \sum_{i=1}^{ngp} w_i J_i \mathbf{B}_i^T \hat{\boldsymbol{\sigma}}_{n+1}^{k+1}$$

9. Assemble the global internal force array and re-compute the residual function
$$\mathbf{r}^{k+1} = \mathbf{f}^{int} - \lambda_{n+1}\bar{\mathbf{f}}^{ext}$$

10. Check convergence
$$\textbf{IF} \;\; \|\mathbf{r}^{k+1}\| < TOL \;\; \textbf{EXIT}$$

11. Set $k = k + 1$ and go to (2).

most used methods in different industries from design to manufacturing. The problem formulation at the continuum level and application of the finite element

were presented for the macroscopic problem. For micro-structural problem and coupled multi-scale analysis, the kinematics of the deformation and finite element solution will be given in the subsequent chapters.

Chapter 3

Leonov based model

Over the last decades, a considerable effort has been made by the academic community to develop constitutive models that are able to describe the deformation behavior of polymeric based materials [Mackerle (1997), Mackerle (2003)]. The use of these materials is steadily increasing due to their ability to fulfill requirements for a large number of applications ranging from automotive, medical and electronic sectors. Their mechanical behavior is usually highly nonlinear and it is extremely important to understand how their mechanical performance is affected by the molecular structure, the processing conditions and the geometry of the micro constituents.

This chapter describes a finite strain elasto-viscoplastic constitutive model capable of predicting the behaviour of polymeric based materials. An efficient numerical integration algorithm for the model is provided through a one equation return mapping procedure. The theoretical basis of the material model and the computational treatment, within the framework of finite element solution procedure, are presented. The operator split methodology and the Newton-Raphson method are used to derive the state update algorithm and to obtain the numerical solution of the discretized evolution equations. The integration algorithm reduces to the solution of only one scalar non-linear equation and generalizes the standard return mapping procedure of the infinitesimal theory. For the sake of completeness, a closed formula for the corresponding consistent tangent operator, which results from the exact linearization of the discretized evolution equations, is presented. Different aspects of the constitutive model and its integration algorithm

are investigated through numerical examples.

3.1 Introduction

The model presented is this chapter is inspired on the single mode compressible Leonov model [Tervoort (1996)] which has been extensively used by a large number of authors, see e.g.[Govaert et al. (2000), Smit et al. (2000), Smit et al. (1999), Smit et al. (2000), Timmermans (1998), Van der Aa (1999)], in the prediction of the deformation behaviour of polymeric materials. The first compressible version of the Leonov model [Leonov (1976)] was proposed by Baaijens (1991) to predict flow-induced residual stresses in injection molded products. Later, the model was derived within a thermodynamically consistent framework by Tervoort (1996). The rate of plastic strain was constitutively described by the stress-activated Eyring flow. This model was later extended by Timmermans (1998) and Govaert et al. (2000) to capture the typical characteristics of the post-yield behaviour of glassy polymers, namely the phenomenon of intrinsic strain softening and strain hardening. We use the same rheological model as Timmermans (1998) and also Eyring equation for the plastic flow.
The numerical solution of the constitutive equations of a material model, usually defined by a set of evolution equations, in the context of finite element simulations has been thoroughly investigated by a large number of authors [De Souza Neto et al. (2008),Ortiz et al. (1983),Owen and Hinton (1980),Simo and Hughes (1998),Simo et al. (1998),Zienkiewicz and Taylor (1991)]. This numerical integration is carried out locally at each quadrature point in typical finite element implementations. This process has a strain driven structure where the stresses and updated internal variables, which characterize the inelastic response of the material, are pursued for a given strain increment and the previous values of the internal variables. The consistent linearization of the resulting discrete equations is crucial for the successful solution of the global boundary value problem with the Newton-Raphson scheme due to its asymptotic quadratic rate of convergence. The use of operator split techniques, which result in the classical elastic predictor/plastic corrector format of the time-discrete evolution problem, is widely accepted and has become standard nowadays. Integration algorithm of the model

including state update and consistent tangent operator is provided through a system of algebraic equations. The efficiency of the integration algorithm is proven by some global (equilibrium) and local (stress update) convergence table of some representative examples.
The numerical integration of the model by means of a return mapping-type scheme requires, in the three-dimensional stress state, the solution of seven coupled non-linear equations. This large number of equations on the stress update algorithm, which is solved at each Gauss point of the finite element mesh, makes the simulation with this model rather expensive. Therefore, in this chapter, we show that a constitutive integration algorithm can be derived where the return mapping procedure, under any stress state, is reduced to the solution of only one single non-linear equation. Consequently, the computational burden of the model is significantly reduced.
The chapter is structured as follows. In Section 3.2, the elasto-viscoplastic model is formulated. Section 3.3 describes in detail the algorithm for numerical integration of the model. For convenience, the closed form of the associated consistent tangent operator is presented. The performance of the model and the efficiency of the integration algorithm are assessed through a representative set of numerical examples in Section 3.4. Based on the obtained results, we present some concluding remarks in Section 3.5. Appendices A and B are provided to describe some algebraic operations that were removed from the body text for the readers' convenience. This should be useful for those interested in the implementation of the algorithm within an implicit finite element environment.

3.2 Formulation

In this section, a multiplicative model is described. The mechanical model is provided in Figure (3.1). The elastic behaviour is characterized by the linear spring in the Maxwell model (the linear spring together with the dashpot is called Maxwell model); the dashpot characterizes the rate dependent yield behaviour and the non-linear viscoplastic material response; and the spring parallel to the Maxwell model represents the strain hardening response.
The followings are the backbone of the presented model:

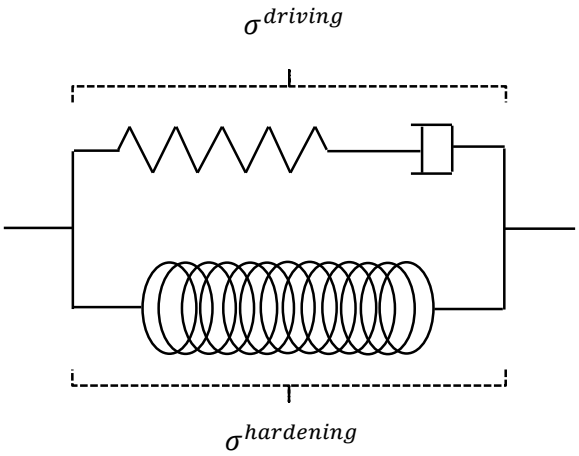

Figure 3.1: Rheological representation of the model

- The multiplicative kinematic,
- The logarithmic strain measure,
- A free energy potential, from which the hyper-elastic law is derived,
- A dissipation potential, from which the plastic flow rule is obtained,
- Additive decomposition of the total stress to driving and hardening stresses.

3.2.1 Multiplicative kinematics

The main assumption behind the finite strain constitutive framework adopted here is the multiplicative decomposition of the deformation gradient. Based on this assumption, the deformation gradient, $\mathbf{F}$, is multiplicatively composed of the elastic deformation gradient, $\mathbf{F}^e$, and the plastic deformation gradient, $\mathbf{F}^p$, [Lee (1969)].

$$\mathbf{F} = \mathbf{F}^e \ \mathbf{F}^p \tag{3.1}$$

It can be said that the elastic deformation gradient, $\mathbf{F}^e$, is acting on the elastic spring, the plastic deformation gradient, $\mathbf{F}^p$, is the component of the total deformation gradient, $\mathbf{F}$, which is effective on the Eyring dashpot (viscoplastic element) and the non-linear spring is affected by the total deformation gradient.

The plastic spin tensor, introduced by relation (2.25), is assumed null, $\mathbf{W}^p = 0$. It is worth mentioning that there are different choices regarding the plastic spin tensor and this issue is detailed by Boyce et al. (1989) and Timmermans (1998). According to the mentioned references, choosing different plastic spin tensors, does not remarkably affect the overall stress-strain curves.

3.2.2 Logarithmic strain measure

In the finite strain model, presented in this contribution, the logarithmic (or natural) Eulerian (or spatial) strain is adopted to measure elastic deformations. The use of logarithmic strain is motivated not only by its physical meaning, but also by the fact that using this strain measure provides remarkably simplified stress integration algorithm of the finite strain model in a way that the infinitesimal elastic predictor/return mapping algorithms can be naturally extended to finite strain. This simplification will be explained more in the next section. The Eulerian logarithmic elastic strain tensor is defined by:

$$\boldsymbol{\varepsilon}^e \equiv \ln \mathbf{V}^e = \frac{1}{2} \ln \mathbf{B}^e \tag{3.2}$$

where, $\ln(\cdot)$ denotes the tensorial logarithm of $(\cdot)$ and the left elastic Cauchy-Green deformation tensor is given by:

$$\mathbf{B}^e \equiv \mathbf{F}^e [\mathbf{F}^e]^T = [\mathbf{V}^e]^2. \tag{3.3}$$

3.2.3 Free energy potential

The thermodynamic formalism which is used in this study is according to the local state of the material. In order to know the local state of the material, we should have knowledge of the state variables of the material. The state variables are categorized to two groups: observable variables which are total strain and temperature, and internal variables describing current state of the material. It should be emphasized that in this study, constant temperature is considered and as a result, observable variables reduce to strain. The thermodynamic formalism

assumes existence of a free energy potential ψ. Assuming the existence of a free energy potential with the following form:

$$\psi = \psi(\boldsymbol{\varepsilon}^e, \boldsymbol{\alpha}), \tag{3.4}$$

where, $\boldsymbol{\varepsilon}^e$ is elastic logarithmic strain and $\boldsymbol{\alpha}$ is a set of internal variables, the following constitutive law for the Kirchhof stress tensor is obtained:

$$\boldsymbol{\tau} = \overline{\rho}\frac{\partial\psi(\boldsymbol{\varepsilon}^e, \boldsymbol{\alpha})}{\partial\boldsymbol{\varepsilon}^e}. \tag{3.5}$$

We know that the relation between Kirchhof stress tensor, $\boldsymbol{\tau}$, and Cauchy stress tensor, $\boldsymbol{\sigma}$, is given by:

$$\boldsymbol{\tau} = J\boldsymbol{\sigma}, \tag{3.6}$$

where, J is the determinant of the deformation gradient, $J = det(\mathbf{F})$. Different free energy potentials, available in the literature and used for different kind of materials, can be used to derive the constitutive law for the stress as a function of strain. In this work, we are using the so-called Hencky strain energy function (logarithmic strain-based hyper-elasticity law), which is generally accepted for a wide range of applications. The Hencky strain energy function, in terms of principal stretches, is given by:

$$\overline{\rho}\psi\left(\lambda_1^e, \lambda_2^e, \lambda_3^e\right) = G\Big[\left(\ln\lambda_1^e\right)^2 + \left(\ln\lambda_2^e\right)^2 + \left(\ln\lambda_3^e\right)^2\Big]$$

$$+\frac{1}{2}\left(K - \frac{2}{3}G\right)\left[\ln\left(\lambda_1^e\lambda_2^e\lambda_3^e\right)\right]^2, \tag{3.7}$$

where, $\overline{\rho}$ is the reference density; $\lambda_1^e, \lambda_2^e, \lambda_3^e$ are the principal stretches in principal directions; K is the bulk modulus and G is the shear modulus of the material. Using the strain energy function introduced in relation (3.7) and also equation (3.5) results in the following relation between Kirchhof stress and Eulerian logarithmic strain:

$$\boldsymbol{\tau} = \mathsf{D}^e : \boldsymbol{\varepsilon}^e, \tag{3.8}$$

where, D^e denotes the fourth order isotropic constant elastic tensor:

$$\mathsf{D}^e \equiv 2G\mathsf{I}_s + \left(K - \frac{2}{3}G\right)(\mathbf{I}\otimes\mathbf{I}). \tag{3.9}$$

I_s is the fourth order symmetric identity tensor and $\mathbf{I}$ is the second order identity tensor. The tensors I_s and $\mathbf{I}$ in component form can be expressed as:

$$\mathsf{I}_{ijkl} = \frac{1}{2}\left[\delta_{ik}\delta_{jl} + \delta_{il}\delta_{jk}\right], \tag{3.10}$$

$$\mathbf{I}_{ij} = \delta_{ij}, \tag{3.11}$$

where, δ is the Kronecker delta.

3.2.4 Dissipation potential

The flow rule in the Leonov model is characterized by the Eyring equation. The Eyring flow model in one dimension is depicted as follows [Tervoort (1996)]:

$$\dot{\gamma}^p = \frac{1}{A}\sinh\left(\frac{\tau}{\tau_0}\right), \tag{3.12}$$

where, τ is the shear stress; $\dot{\gamma}^p$ is the plastic rate of shear; A and τ_0(a characteristic stress) are the material constants at constant temperature:

$$A = A_0 \exp\left(\frac{\Delta H}{RT}\right), \tag{3.13}$$

$$\tau_0 = \frac{RT}{V^*}, \tag{3.14}$$

where, ΔH and V^* are the activation energy and the shear activation volume, respectively. A_0 is a constant or pre-exponential factor involving the fundamental vibration energy; R is the universal gas constant and T is the absolute temperature. Performing an inversion on equation (3.12) results in:

$$\dot{\gamma}^p = \frac{\tau}{\left(\tau_0\ arcsinh(A\dot{\gamma}^p)/\dot{\gamma}^p\right)}. \tag{3.15}$$

From equation (3.15), a viscosity function can be defined:

$$\eta(\dot{\gamma}^p) = \tau_0\ arcsinh(A\dot{\gamma}^p)/\dot{\gamma}^p. \tag{3.16}$$

Using relation (3.16), the one dimensional Eyring flow equation, equation (3.15), can be rewritten as follows:

$$\dot{\gamma}^p = \frac{\tau}{\eta(\dot{\gamma}^p)}. \tag{3.17}$$

The flow model in three dimensions can be introduced by the following relation for the equivalent rate of shear strain:

$$\dot{\gamma}^{eq} = \frac{1}{A}\sinh\left(\frac{\tau^{eq}}{\tau_0}\right), \tag{3.18}$$

where, τ^{eq} is an equivalent stress defined by:

$$\tau^{eq} = \sqrt{\frac{1}{2}\,tr(\mathbf{s})} = \sqrt{\frac{1}{2}\mathbf{s}:\mathbf{s}}, \tag{3.19}$$

where, $\mathbf{s}$ is the deviatoric part of stress:

$$\mathbf{s} = \mathsf{I}_d : \boldsymbol{\tau}. \tag{3.20}$$

The fourth order deviatoric identity tensor, I_d, is given by:

$$\mathsf{I}_d = \mathsf{I}_s - \frac{1}{3}\big(\mathbf{I}\otimes\mathbf{I}\big). \tag{3.21}$$

Note that relations (3.19) and (3.18) for equivalent stress, τ^{eq}, and equivalent rate of shear strain, $\dot{\gamma}^{eq}$, are defined such that in case of having a shear stress state, they reduce to the shear stress, τ, and plastic rate of shear, $\dot{\gamma}^{p}$, respectively. It should be emphasized that relations (3.12) and (3.18), only determine the magnitude of the plastic strain in 1-D and 3-D cases. As opposed to the one dimensional flow, in order to fully characterize the flow behaviour of the material in a generic 3-D case, the flow vector, $\mathbf{N}$, should also be determined. As mentioned in the beginning of this section, there should be a dissipation potential, Ψ, from which the flow vector would be determined. The existence of a continuous and convex scalar function as the dissipation potential is necessary and useful to define the complementary relations for the flow potential. The plastic flow rule of the model presented here, is given by:

$$\mathbf{d}^p = \dot{\gamma}^{eq}\frac{\partial\Psi}{\partial\boldsymbol{\sigma}} = \dot{\gamma}^{eq}\mathbf{N}, \tag{3.22}$$

where, Ψ is a dissipation potential, $\mathbf{N}$ is a flow vector and $\mathbf{d}^p$ is the spatial plastic stretching tensor:

$$\mathbf{d}^p \equiv \mathbf{R}^e\mathbf{D}^p\mathbf{R}^{eT}. \tag{3.23}$$

Spatial plastic stretching tensor, $\mathbf{d}^p$, is the plastic stretching tensor, $\mathbf{D}^p$, rotated to the current (spatial) configuration by elastic rotation, $\mathbf{R}^e$. In order to determine the flow vector, $\mathbf{N}$, we need to define the dissipation potential, Ψ, from which we can derive the flow vector. The dissipation potential is postulated to have the following definition:

$$\Psi = \sqrt{\frac{1}{2}\mathbf{s} : \mathbf{s}}. \tag{3.24}$$

As a result, the flow vector is obtained:

$$\mathbf{N} = \frac{\partial \Psi}{\partial \boldsymbol{\tau}} = \sqrt{\frac{1}{2}}\frac{\mathbf{s}}{||\mathbf{s}||}, \tag{3.25}$$

where, $||\mathbf{s}||$ is the norm of $\mathbf{s}$ defined by:

$$||\mathbf{s}|| = \sqrt{\mathbf{s} : \mathbf{s}}. \tag{3.26}$$

Combining relations (3.22) and (3.25), the multi-dimensional plastic flow rule of the model is obtained as:

$$\mathbf{d}^p = \dot{\gamma}^{eq}\sqrt{\frac{1}{2}}\frac{\mathbf{s}}{||\mathbf{s}||}. \tag{3.27}$$

Using relation (3.18) and also equation (3.19), the plastic flow rule is written in another form:

$$\mathbf{d}^p = \frac{1}{A}\sinh\left(\frac{\tau^{eq}}{\tau_0}\right)\left(\frac{\mathbf{s}}{2\tau^{eq}}\right), \tag{3.28}$$

or equivalently,

$$\mathbf{d}^p = \frac{\mathbf{s}}{2A\left[\frac{\tau^{eq}}{\sinh\left(\tau^{eq}/\tau_0\right)}\right]}, \tag{3.29}$$

which can be represented as:

$$\mathbf{d}^p = \frac{\mathbf{s}}{2\eta(\tau^{eq})}, \tag{3.30}$$

where, the viscosity function, $\eta(\tau^{eq})$, is given by:

$$\eta(\tau^{eq}) = A\left[\frac{\tau^{eq}}{\sinh\left(\tau^{eq}/\tau_0\right)}\right]. \tag{3.31}$$

Equation (3.30) is the extension of the one dimensional non-Newtonian fluid relationship, Equation (3.17), to the multi-dimensional case. Hence, it can be

mentioned that, the plastic flow rule in this model is characterized by the generalized Eyring equation. The rate of equivalent plastic shear can be written in terms of the multi-dimensional plastic flow rule:

$$\dot{\gamma}^{eq} = \sqrt{2\mathbf{d}^p : \mathbf{d}^p}. \tag{3.32}$$

The parameter A is already introduced in Equation (3.13). In order to account for the pressure dependence behaviour and also the softening behaviour of the material, the parameter A can be generalized to the following relation [Govaert et al. (2000), Timmermans (1998)]:

$$A = A_0 \exp\left[\frac{\Delta H}{RT} + \frac{\mu P}{\tau_0} - D\right]. \tag{3.33}$$

The parameter μ is a pressure coefficient related to the shear activation volume, V^*, and the pressure activation volume, Ω, according to:

$$\mu = \frac{\Omega}{V^*}. \tag{3.34}$$

In relation (3.33), P is the total hydrostatic pressure:

$$P = p_0 + p, \tag{3.35}$$

where, the scalar p is the hydrostatic pressure defined by:

$$p = -\frac{1}{3} tr(\boldsymbol{\tau}), \tag{3.36}$$

and the scalar p_0 is the superimposed hydrostatic pressure of the analysis and D is the softening parameter. The evolution of the softening parameter is modelled according to [Hasan et al. (1993)]:

$$\dot{D} = h\left(1 - \frac{D}{D_\infty}\right)\dot{\bar{\gamma}}^p, \tag{3.37}$$

where, D_∞ is the saturation value of the softening parameter with the initial condition $D = 0$. The scalar quantity h influences the softening slope and $\dot{\bar{\gamma}}^p$ is an equivalent plastic strain rate defined by [Govaert et al. (2000)]:

$$\dot{\bar{\gamma}}^p = \sqrt{\mathbf{d}^p : \mathbf{d}^p}. \tag{3.38}$$

Using relations (3.19), (3.31), (3.32), (3.33) and (3.37) together with some algebric manipulations, provided in Appendix A, results in the following viscosity function:

$$\eta = A_0 \exp\left[\frac{\Delta H}{RT} + \frac{\mu P}{\tau_0} - D_\infty + D_\infty \exp\left(\frac{-h\sqrt{3}\,\bar{\varepsilon}^p}{\sqrt{2}D_\infty}\right)\right] \left[\tau^{eq}/\sinh\left(\frac{\tau^{eq}}{\tau_0}\right)\right], \tag{3.39}$$

where, $\bar{\varepsilon}^p$ is an accumulated plastic strain. The rate of accumulated plastic strain rate is given by:

$$\dot{\bar{\varepsilon}}^p = \sqrt{\frac{2}{3}\mathbf{d}^p : \mathbf{d}^p}. \tag{3.40}$$

It should be emphasized that in this model, we do not use any explicit yield function i.e. at any time of the deformation and in any point of the structure, the total strain is assumed additively composed of elastic strain (or reversible strain) and inelastic strain (or non-instantaneously reversible or non-reversible strain). In order to facilitate the notation, the latter is referred to by superscript p standing for "plastic". In fact, this decomposition of strain is consistent with the physical phenomena happening during the deformation. Bending and stretching of strong chain covalent bonds and also small displacement of adjacent molecules which is resisted by the presence of van der Waals and hydrogen secondary bonds contribute to the elastic deformation. At small deformations (less than 5%), viscoplastic strain should be considered in terms of a cooperative movement of molecular chain segments. Chain entanglements have remarkable contributions in resistance of polymers to visco-plastic flow [Ghorbel (2008)].

3.2.5 Additive decomposition of total stress

The total stress, $\boldsymbol{\tau}^{total}$, in the model, is additively composed, in a parallel assemblage, of driving stress and hardening stress:

$$\boldsymbol{\tau}^{total} = \boldsymbol{\tau}^{driving} + \boldsymbol{\tau}^{hardening}. \tag{3.41}$$

Two different kind of hardening could be considered: isotropic hardening and kinematic hardening. Physically, isotropic hardening could be associated with increasing the covalent bonds, with the entanglements density and with the change

of the conformation of molecular links inside the amorphous phase. Kinematic hardening could be physically related to the existence of structural defects in the amorphous phase such as the existence of free radicals or chain scission points [Ghorbel (2008)]. In this study, isotropic hardening is considered. The hardening stress in this model is characterized by the following relation:

$$\boldsymbol{\tau}^{hardening} = H\ \boldsymbol{\varepsilon}_d, \tag{3.42}$$

where, H is the hardening modulus (one of the material properties) and $\boldsymbol{\varepsilon}_d$ is the deviatoric part of the total strain:

$$\boldsymbol{\varepsilon}_d = \mathsf{I}_d : \boldsymbol{\varepsilon}. \tag{3.43}$$

3.3 Integration algorithm

Operator split algorithms are widely used for numerical integration of constitutive equations in the context of elasto-plasticity and elasto-viscoplasticity [Criesfield (1997), Simo and Hughes (1998)]. Numerical implementation of constitutive models into finite element codes basically requires the appropriate derivative of the state update procedure for the specific model and the computation of the consistent tangent operator. Here, we shall focus on the particularization of the fully implicit elastic predictor/return mapping method to the finite strain model introduced in the previous section.

It must be emphasized that the derivation of the state update procedure and consistent tangent operator will be performed on the small strain format of the constitutive equations and they will be extended to finite strain counterparts with a finite strain extension described in the following. The finite strain extension used in this study keeps the most important features of the small strain formulation [De Souza Neto et al. (2008)]. In particular, it preserves the volumetric plastic deformation, finite plastic incompressibility, and associativity and maximum plastic dissipation at large strain [De Souza Neto et al. (2008)]. This kind of extension has been, due to its suitable features, widely used by different authors [De Souza Neto et al. (1994), Peric et al. (1992), Rouinia and Peric (1998)].

In this section, the particularization of fully implicit elastic predictor/return mapping method to the finite strain model introduced in the previous section is presented. It is shown how to reduce the system of return mapping equations to a single non-linear scalar equation.

3.3.1 The state update procedure

The derivation of the state update procedure and consistent tangent operator will be performed on the small strain format of the constitutive equations. For the time interval $[t_n, t_{n+1}]$, the set of variables $\{\boldsymbol{\sigma}_n,\ \boldsymbol{\varepsilon}^e_n, \boldsymbol{\varepsilon}^p_n, \bar{\varepsilon}^p_n\}$ is known at time t_n and the main problem is to determine the same set $\left\{\boldsymbol{\sigma}_{n+1},\ \boldsymbol{\varepsilon}^e_{n+1}, \boldsymbol{\varepsilon}^p_{n+1}, \bar{\varepsilon}^p_{n+1}\right\}$ at time t_{n+1}.
Assuming that the incremental displacement, Δu, is known, we should update the deformation gradient. The incremental deformation gradient, $\mathbf{F}_\Delta$, is obtained by [De Souza Neto et al. (2008)]:

$$\mathbf{F}_\Delta = \mathbf{I} + \bigtriangledown_n(\Delta u), \tag{3.44}$$

where, $\bigtriangledown_n(\Delta u)$ is the gradient of the incremental displacement. Having known the incremental deformation gradient, we can update the deformation gradient at time step t_{n+1}:

$$\mathbf{F}_{n+1} = \mathbf{F}_\Delta \mathbf{F}_n. \tag{3.45}$$

Now, it is the turn to evaluate the elastic trial state. Assuming that the total elastic strain, $\boldsymbol{\varepsilon}^e_n$, at t_n is known, the elastic left Cauchy-Green deformation tensor is given by:

$$\mathbf{B}^e_n = \exp[2\ \boldsymbol{\varepsilon}^e_n]. \tag{3.46}$$

The elastic trial left Cauchy-Green deformation tensor at t_{n+1} ia obtained by:

$$\mathbf{B}^{e\ trial}_{n+1} = \mathbf{F}_\Delta \mathbf{B}^e_n (\mathbf{F}_\Delta)^T. \tag{3.47}$$

The elastic trial strain, which is in fact the driving parameter in the computational implementation of the model under study, at t_{n+1} is computed by:

$$\boldsymbol{\varepsilon}^{e\ trial}_{n+1} = \ln\left[\mathbf{V}^{e\ trial}_{n+1}\right] = \frac{1}{2}\ln\left[\mathbf{B}^{e\ trial}_{n+1}\right]. \tag{3.48}$$

It must be noted that so far, everything is done at the kinematical level i.e. it is completely independent of the material model. At this point, we should update stress and the state variables based on the constitutive relations of the model.

3.3.1.1 Return mapping

We know that the total strain is additively composed of elastic strain and plastic strain:

$$\boldsymbol{\varepsilon}^{tot}_{n+1} = \boldsymbol{\varepsilon}^{e}_{n+1} + \boldsymbol{\varepsilon}^{p}_{n+1}. \tag{3.49}$$

As mentioned before, we present the integration algorithm of the model within the context of infinitesimal theory and the finite strain algorithm adopted in this study preserves the format of the state update algorithm and also the tangent operator derived within the infinitesimal strain formulation. Hence, we shall adopt the small strain counterpart of relation (3.30) to work with:

$$\dot{\boldsymbol{\varepsilon}}^{p} = \frac{\mathbf{s}}{2\eta}. \tag{3.50}$$

Integrating relation (3.50) during the time step $[t_n, t_{n+1}]$ leads to the following:

$$\boldsymbol{\varepsilon}^{p}_{d\ n+1} = \boldsymbol{\varepsilon}^{p}_{d\ n} + \frac{\Delta t}{2\eta_{n+1}}\mathbf{s}_{n+1}. \tag{3.51}$$

The subscript d in relation (3.51) stands for the deviatoric part of the plastic strain and from relation (3.50), it is obvious that the plastic strain is totally deviatoric and there is no volumetric plastic strain. The rate of accumulated plastic strain is defined by:

$$\dot{\bar{\varepsilon}}^{p} = \sqrt{\frac{2}{3}\dot{\boldsymbol{\varepsilon}}^{p} : \dot{\boldsymbol{\varepsilon}}^{p}}. \tag{3.52}$$

Integrating equation (3.52) over the time step $[t_n, t_{n+1}]$ and using relation (3.50) results in:

$$\bar{\varepsilon}^{p}_{n+1} = \bar{\varepsilon}^{p}_{n} + \frac{\sqrt{3}\Delta t}{3\eta_{n+1}}\tau^{eq}_{n+1}, \tag{3.53}$$

where, the effective stress at t_{n+1} is given by:

$$\tau^{eq}_{n+1} = \sqrt{\frac{1}{2}\mathbf{s}_{n+1} : \mathbf{s}_{n+1}}, \tag{3.54}$$

and the discretized expression for the viscosity is given by:

$$\eta_{n+1} = A_0 \exp\left[\frac{\Delta H}{RT} + \frac{\mu P_{n+1}}{\tau_0} - D_\infty + D_\infty \exp\left(\frac{-h\sqrt{3}\bar{\varepsilon}^p_{n+1}}{\sqrt{2}D_\infty}\right)\right] \left[\tau^{eq}_{n+1} \Big/ \sinh\left(\frac{\tau^{eq}_{n+1}}{\tau_0}\right)\right]. \tag{3.55}$$

The relations (3.49),(3.51) and (3.53) are a particularization of the standard return mapping procedure for the present model. The aforementioned system of equations needs to be solved for the unknowns $\boldsymbol{\varepsilon}^e_{n+1}$, $\boldsymbol{\varepsilon}^p_{d\ n+1}$ and $\bar{\varepsilon}^p_{n+1}$. Nevertheless we will show that the return mapping can be reduced, through algebraic manipulations, to a single non-linear scalar equation. Since the total strain, $\boldsymbol{\varepsilon}_{n+1}$, is known:

$$\boldsymbol{\varepsilon}_{n+1} = \boldsymbol{\varepsilon}^{e\ trial}_{n+1}, \tag{3.56}$$

and we can express the total strain split, relation (3.49), on the deviatoric space as:

$$\boldsymbol{\varepsilon}^{tot}_{d\ n+1} = \boldsymbol{\varepsilon}^e_{d\ n+1} + \boldsymbol{\varepsilon}^p_{d\ n+1}, \tag{3.57}$$

where, the elastic deviatoric strain, $\boldsymbol{\varepsilon}^e_{d\ n+1}$, can be obtained from the determination of the plastic strain, $\boldsymbol{\varepsilon}^p_{d\ n+1}$. Consequently, the problem is reduced to the determination of the plastic strain, $\boldsymbol{\varepsilon}^p_{d\ n+1}$, and accumulated plastic strain, $\bar{\varepsilon}^p_{n+1}$. This means that for a generic 3D problem, we would have to solve a system of seven coupled equations: six for plastic strain components and one for the accumulated plastic strain. In the following, it will be shown how to manipulate the relations such that the integration algorithm turns out to be significantly more efficient. The stress deviator, $\mathbf{s}_{n+1}$, is given by:

$$\mathbf{s}_{n+1} = 2G\ \boldsymbol{\varepsilon}^e_{d\ n+1} = 2G(\boldsymbol{\varepsilon}^{tot}_{d\ n+1} - \boldsymbol{\varepsilon}^p_{d\ n+1}). \tag{3.58}$$

Substitution of equation (3.51) in equation (3.58) gives:

$$\mathbf{s}_{n+1} = 2G(\boldsymbol{\varepsilon}^{tot}_{d\ n+1} - \boldsymbol{\varepsilon}^p_{d\ n} - \triangle t\ \frac{\mathbf{s}_{n+1}}{2\eta_{n+1}}). \tag{3.59}$$

Rearranging relation (3.59) results in:

$$\mathbf{s}_{n+1} = \frac{2G}{1 + (\Delta t\ G/\eta_{n+1})}(\boldsymbol{\varepsilon}^{tot}_{d\ n+1} - \boldsymbol{\varepsilon}^p_{d\ n}). \tag{3.60}$$

The deviatoric strain at t_{n+1}, is equal to the deviatoric strain at t_n plus incremental deviatoric strain:

$$\boldsymbol{\varepsilon}_{d\ n+1}^{tot} = \boldsymbol{\varepsilon}_{d\ n} + (\Delta\boldsymbol{\varepsilon})_d. \tag{3.61}$$

Substituting relation (3.61) in relation (3.60) yields to:

$$\mathbf{s}_{n+1} = \frac{2G}{1 + (\Delta t\ G/\eta_{n+1})}(\boldsymbol{\varepsilon}_{d\ n} + \Delta\boldsymbol{\varepsilon}_d - \boldsymbol{\varepsilon}_{d\ n}^{p}). \tag{3.62}$$

Since the total deviatoric strain, $\boldsymbol{\varepsilon}_{d\ n}$, is composed of the elastic deviatoric strain, $\boldsymbol{\varepsilon}_{d\ n}^{e}$, and plastic deviatoric strain, $\boldsymbol{\varepsilon}_{d\ n}^{p}$, relation (3.62) is rewritten as follows:

$$\mathbf{s}_{n+1} = \frac{2G}{1 + (\Delta t\ G/\eta_{n+1})}(\boldsymbol{\varepsilon}_{d\ n}^{e} + \Delta\boldsymbol{\varepsilon}_d). \tag{3.63}$$

Finally, the deviatoric stress tensor can be expressed by:

$$\mathbf{s}_{n+1} = \frac{2G}{1 + (\Delta t\ G/\eta_{n+1})}(\boldsymbol{\varepsilon}_{d\ n+1}^{e\ trial}), \tag{3.64}$$

or equivalently,

$$\mathbf{s}_{n+1} = \frac{1}{1 + \ (\Delta t\ G/\eta_{n+1})}\left(\mathbf{s}_{n+1}^{trial}\right), \tag{3.65}$$

where,

$$\mathbf{s}_{n+1}^{trial} = 2G(\boldsymbol{\varepsilon}_{d\ n+1}^{e\ trial}). \tag{3.66}$$

Substituting relation (3.65) in relation (3.54) leads to:

$$\tau_{n+1}^{eq} = \frac{\eta_{n+1}}{\eta_{n+1} + \Delta t\ G}\ \sqrt{\frac{1}{2}}\ ||\mathbf{s}_{n+1}^{trial}||, \tag{3.67}$$

where, norm of the trial deviatoric stress is given by:

$$||\mathbf{s}_{n+1}^{trial}|| = \sqrt{\mathbf{s}_{n+1}^{trial} : \mathbf{s}_{n+1}^{trial}}. \tag{3.68}$$

Inserting relation (3.67) in relation (3.53) gives:

$$\bar{\varepsilon}_{n+1}^{p} = \bar{\varepsilon}_{n}^{p} + \frac{\Delta t}{3(\eta_{n+1} + \Delta t\ G)}\ \sqrt{\frac{3}{2}}\ ||\mathbf{s}_{n+1}^{trial}||. \tag{3.69}$$

With the above relations at hand, it can be clearly observed that both the effective stress, τ_{n+1}^{eq}, and the accumulated plastic strain, $\bar{\varepsilon}_{n+1}^{p}$, are functions of

the viscosity, η_{n+1}. Therefore, it is possible to substitute relations (3.67) and (3.69) into the discretized expression for the viscosity, relation (3.55), reducing the problem to the solution of only one scalar non-linear residual equation:

$$R(\eta_{n+1}) = \eta_{n+1} - C_1(\eta_{n+1})\frac{C_2(\eta_{n+1})}{C_3(\eta_{n+1})} = 0. \tag{3.70}$$

The factors $C_1(\eta_{n+1})$,$C_2(\eta_{n+1})$ and $C_3(\eta_{n+1})$ are given by:

$$C_1(\eta_{n+1}) = A_0 \exp\left[\frac{\Delta H}{R\,T} + \frac{\mu P_{n+1}}{\tau_0} - D_\infty + D_\infty \exp\left(-\frac{h\sqrt{3}C_4}{\sqrt{2}D_\infty}\right)\right], \tag{3.71}$$

$$C_2(\eta_{n+1}) = \frac{\eta_{n+1}}{\eta_{n+1} + \Delta t G}\sqrt{\frac{1}{2}}\,||\mathbf{s}_{n+1}^{trial}||, \tag{3.72}$$

$$C_3(\eta_{n+1}) = \sinh(\frac{C_2}{\tau_0}), \tag{3.73}$$

where,

$$C_4(\eta_{n+1}) = \bar{\varepsilon}_n^p + \frac{\Delta t}{3(\eta_{n+1} + \Delta t G)}\sqrt{\frac{3}{2}}||\mathbf{s}_{n+1}^{trial}||. \tag{3.74}$$

where Δt is the time interval between two consecutive time steps. We will use the well-known Newton-Raphson iterative procedure to solve the residual equation (3.70). To do so, we need to compute the derivative of the residual, $R(\eta_{n+1})$, in order to the viscosity, η_{n+1},. Performing the derivations together with some algebraic manipulations leads to:

$$\frac{dR(\eta_{n+1})}{d\eta_{n+1}} = 1 - \left[K_1(\eta_{n+1})\left(\frac{C_2(\eta_{n+1})}{C_3(\eta_{n+1})}\right) + \right.$$

$$\left. + C_1\left(\frac{C_3(\eta_{n+1})K_2(\eta_{n+1}) - C_2(\eta_{n+1})K_3(\eta_{n+1})}{(C_3(\eta_{n+1}))^2}\right)\right], \tag{3.75}$$

where,

$$K_1(\eta_{n+1}) = \frac{dC_1}{d\eta_{n+1}} = C_1 \exp\left(\frac{-h\sqrt{3}C_4}{\sqrt{2}D_\infty}\right)\left[\frac{h\Delta t||\mathbf{s}_{n+1}^{trial}||}{2\left(\eta_{n+1} + \Delta t G\right)^2}\right], \tag{3.76}$$

$$K_2(\eta_{n+1}) = \frac{dC_2}{d\eta_{n+1}} = \sqrt{\frac{1}{2}}\left[\frac{\Delta t G||\mathbf{s}_{n+1}^{trial}||}{(\eta_{n+1} + \Delta t G)^2}\right], \tag{3.77}$$

$$K_3(\eta_{n+1}) = \frac{dC_3}{d\eta_{n+1}} = \sqrt{\frac{1}{2}} \left[\frac{\Delta t G ||\mathbf{s}^{trial}_{n+1}||}{\tau_0 \left(\eta_{n+1} + \Delta t G\right)^2} \right] \left(\cosh \frac{C_2}{\tau_0} \right). \tag{3.78}$$

Having computed the aforementioned factors, we can apply the Newton-Raphson method to solve the residual equation in an iterative fashion:

$$\eta^k_{n+1} = \eta^{k-1}_{n+1} - \frac{R(\eta^{k-1}_{n+1})}{\frac{dR}{d\eta_{n+1}}(\eta^{k-1}_{n+1})}, \tag{3.79}$$

where, the superscript (k) and $(k-1)$ stand for two consecutive Newton-Raphson iterations. Once the iterations on the viscosity functions, $R(\eta_{n+1})$, converge, we can update all the other variables through relations (3.80)-(3.83).

$$\mathbf{s}_{n+1} = \frac{\eta_{n+1}}{\eta_{n+1} + \Delta t G} \mathbf{s}^{trial}_{n+1}. \tag{3.80}$$

$$\boldsymbol{\varepsilon}^e_{d\ n+1} = \frac{\eta_{n+1}}{\eta_{n+1} + \Delta t G} \frac{\mathbf{s}^{trial}_{n+1}}{2G} \tag{3.81}$$

$$\boldsymbol{\varepsilon}^p_{d\ n+1} = \boldsymbol{\varepsilon}^p_{d\ n} + \frac{\Delta t}{2(\eta_{n+1} + \Delta t G)} \mathbf{s}^{trial}_{n+1} \tag{3.82}$$

$$\bar{\varepsilon}^p_{n+1} = \bar{\varepsilon}^p_n + \frac{\Delta t}{3(\eta_{n+1} + \Delta t\ G)} \sqrt{\frac{3}{2}}\ ||\mathbf{s}^{trial}_{n+1}||. \tag{3.83}$$

The discretized form of the hardening stress, relation (3.42), is given by:

$$\boldsymbol{\sigma}^{hardening}_{n+1} = H \boldsymbol{\varepsilon}_{d\ n+1} \tag{3.84}$$

Relation (3.65) is the key relation to condense the system of equations to only one scalar equation. Using relation (3.65) in relations (3.67) and (3.69) results in having effective stress and accumulated plastic strain as functions of viscosity. By inserting the resulting functions of viscosity in relation (3.55), the system of equations reduces to one single equation.

3.3.2 Consistent tangent operator

In order to complete the numerical treatment of the model within an implicit quasi-static integration scheme, we need to obtain the consistent tangent operator. The global tangent stiffness matrix is assembled using the tangent operators, which are derived by consistently linearizing the integration scheme. The spatial tangent modulus is given by [De Souza Neto et al. (2008)]:

$$\mathsf{a}_{ijkl} = \frac{1}{2J}[\mathsf{D} : \mathsf{L} : \mathsf{B}]_{ijkl} - \boldsymbol{\sigma}_{il}\, \delta_{jk}, \tag{3.85}$$

where, δ is the Kronecker delta, D is the small strain, either elastic or viscoplastic, consistent tangent operator. The fourth order tensor L is defined by:

$$\mathsf{L} = \frac{\partial \ln [\mathbf{B}^{e\ trial}_{n+1}]}{\partial [\mathbf{B}^{e\ trial}_{n+1}]}, \tag{3.86}$$

and the fourth order tensor B is defined by the cartesian components:

$$\mathsf{B}_{ijkl} = \delta_{ik} \left(\mathbf{B}^{e\ trial}_{n+1}\right)_{jl} + \delta_{jk} \left(\mathbf{B}^{e\ trial}_{n+1}\right)_{il}. \tag{3.87}$$

It should be emphasized here that the only material related term in relation (3.85) is D and the other contributions of the spatial tangent module are thoroughly independent of the material model, i.e. all the components taking part in relation (3.85), other than D, are purely related to the kinematic level. As a matter of fact, the perfect separation of the finite strain kinematics and the material related contributions to the integration algorithm, previously observed, is also possible through the assemblage of the spatial tangent module, as shown in relations (3.85)-(3.87).

The perfect separation of the finite strain kinematics and the material related contributions is possible through the assemblage of the spatial tangent module, as explained in relations (3.85)-(3.87). The exact linearization of the constitutive relations together with some algebraic manipulations, described in detail in Appendix B, result in the following closed form relation for the tangent operator.

$$\mathsf{D}^p = \left(\frac{2G\eta_{n+1}}{\eta_{n+1} + \Delta t G} + H\right)\left[\mathsf{I}_s - \frac{1}{3}\left(\mathbf{I} \otimes \mathbf{I}\right)\right] + K\left(\mathbf{I} \otimes \mathbf{I}\right)$$

$$+\left(\frac{\Delta tG}{\eta_{n+1}^2 X}\right)\left[F_1\left(1-F_2-F_3\right)\right]\left(\mathbf{s}_{n+1}\otimes\mathbf{s}_{n+1}\right) \tag{3.88}$$

$$-\left[\frac{\Delta tGKC_1\mu\left(1+C_2\right)}{\eta_{n+1}\left(\eta_{n+1}+\Delta tG\right)C_3\tau_0 X}\right]\left(\mathbf{s}_{n+1}\otimes\mathbf{I}\right),$$

where,

$$F_1=\frac{\sqrt{2}GC_1\eta_{n+1}}{C_3(\eta_{n+1}+\Delta tG)||\mathbf{s}_{n+1}^{trial}||}, \tag{3.89}$$

$$F_2=\frac{c_2h\Delta t}{\eta_{n+1}}\exp\left(\frac{-h\sqrt{3}C_4}{Q_\infty}\right), \tag{3.90}$$

$$F_3=\frac{C_2}{C_3\tau_0}\cosh\left(\frac{C_2}{\tau_0}\right), \tag{3.91}$$

$$X=1-\left[K_1\left(\frac{C_2}{C_3}\right)+C_1\left(\frac{K_2C_3-C_2K_3}{C_3^2}\right)\right]. \tag{3.92}$$

3.4 Numerical examples

In this section, the performance and accuracy of the numerical implementation are, with some numerical examples, evaluated. The material properties, for the materials used in this section, are provided in Table (3.1). The materials used for doing the numerical examples are PET copolyester 9921W, Polystyrene-N5000, Lexan 101^R , which is a commercial grade of Polycarbonate, and Nylon-6. The mentioned materials are referred to as PET, PS, PC and PA-6 in Table (3.1) and in what follows, respectively. It should be noted that in this contribution, we do not aim to compare the results obtained from numerical examples with experimental results available in the literature because we are just using the properties obtained and calibrated by other researchers. Since, the model presented in this contribution is not exactly what the references of this work used, the determination and calibration of the material properties should be done in order to make a comparison to experimental results. The material properties for PET, PS, PC and PA-6 are taken from [Van der Aa (1999)], [Van Melic et al. (2003)], [Van Melic et al. (2003)] and [Timmermans (1998)], respectively.

Table 3.1: Material properties for the constitutive model

	E(MPa)	ν	$\Delta H(J/mol)$	$A_0(s)$	τ_0(MPa)	D_∞	h	μ	R	H(MPa)
PET	2211	0.4	2.3E+5	8.1E-26	0.9	27.3	205	0.047	8.3143	26
PS	3300	0.37	1.7E+5	1.11E-20	2.559	9	60	0.14	8.3143	11
PC	2400	0.4	2.9E+5	3.6E-25	0.717	26	200	0.07	8.3143	29
PA-6	2800	0.4	2.8E+5	9.1E-42	2.3	1.2	120	0.05	8.3143	16

3.4.1 Cylinder upsetting-strain rate effect

In this subsection, uniaxial compression tests are performed on cylinders using all aforementioned materials and a comparison is made between stress-strain curves. In order to keep the strain rate constant during loading, the following relation is used for the displacement applied [Diez (2010)]:

$$u(t) = l_0(\exp(\dot{\varepsilon}t) - 1), \tag{3.93}$$

where, $u(t)$ is the total displacement, $\dot{\varepsilon}$ is the strain rate, l_0 is the initial length of the specimen and t is the total time. The simulations are performed under strain rate $\dot{\varepsilon} = -0.001(1/s)$. The time interval between load steps is $\Delta t = 5s$. The simulations are done assuming room temperature, $T = 20^c$, and atmospheric superimposed hydrostatic pressure, $p_0 = 0.1E + 06\ Pa$. The height of the specimen and also the diameter is considered 6 mm. The test is approximated as a 2D axisymmetric problem. A rectangular with 6 mm height and 3 mm width is spatially discretized with 72 eight noded quadrilaterial elements. The total displacement is $u = 3.8\ mm$ and it is applied in 200 load increments. In Figure (3.2), the stress-strain curves of four different materials under aforementioned simulation conditions are provided. One of the most important features of the numerical implementation is the convergence rate of the algorithm. Consequently, it is necessary to investigate the convergence rate of the implementation. In Table (3.2), the convergence of the problem at the global level at increment 150 is shown by providing the values of relative residual norm for four different materials. It should be mentioned that Table (3.2) could be considered as a typical increment convergence table for all four materials. In order to observe the effect of strain rate on the deformation behaviour of polymers, the cylinder upsetting is done under three different strain rates, $\dot{\varepsilon} = -0.0001(1/s), \dot{\varepsilon} = -0.0005(1/s)$ and

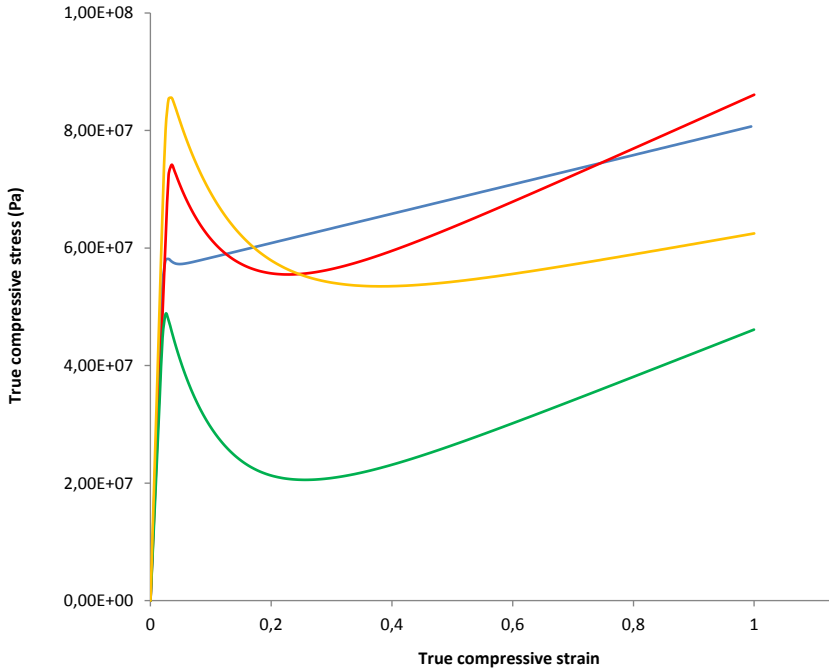

Figure 3.2: Stress-strain curves of cylinder upsetting for four different polymeric materials. yellow: PS, red: PC, blue: PA-6 and green: PET.

$\dot{\varepsilon} = -0.001(1/s)$, on PS. Figure (3.3) depicts stress-strain curves of PS cylinder upsetting under different strain rates. As expected, it can be seen that by increasing the strain rate, despite almost the same deformation pattern for all strain rates, the level of stress is increased. It should be emphasized that the strain rates are kept very low because increasing strain rate causes thermo-mechanical effects [Diez (2010)] which is not included in the model used in this contribution.

3.4.2 Compression on a cube

In this subsection, cube compression simulations, modelled as plane strain compression, are performed at room temperature, atmospheric superimposed hydrostatic pressure and strain rate $\dot{\varepsilon} = -0.001(1/s)$ on PC. In Figure (3.4), both cylinder upsetting (axisymmetric) and cube compression (plane strain) results are shown. According to Aruuda and Boyce (1993), chains are uniaxially ori-

Table 3.2: Global convergence table for cylinder upsetting simulations

	Relative residual norm (%) at increment 150			
Iteration number	PA-6	PET	PC	PS
1	0.854515	0.817685	0.341777	1.20778
2	0.291957E-03	0.146578E-03	0.480991E-04	0.865578E-03
3	0.347145E-10	0.139360E-08	0.843004E-10	0.425418E-08

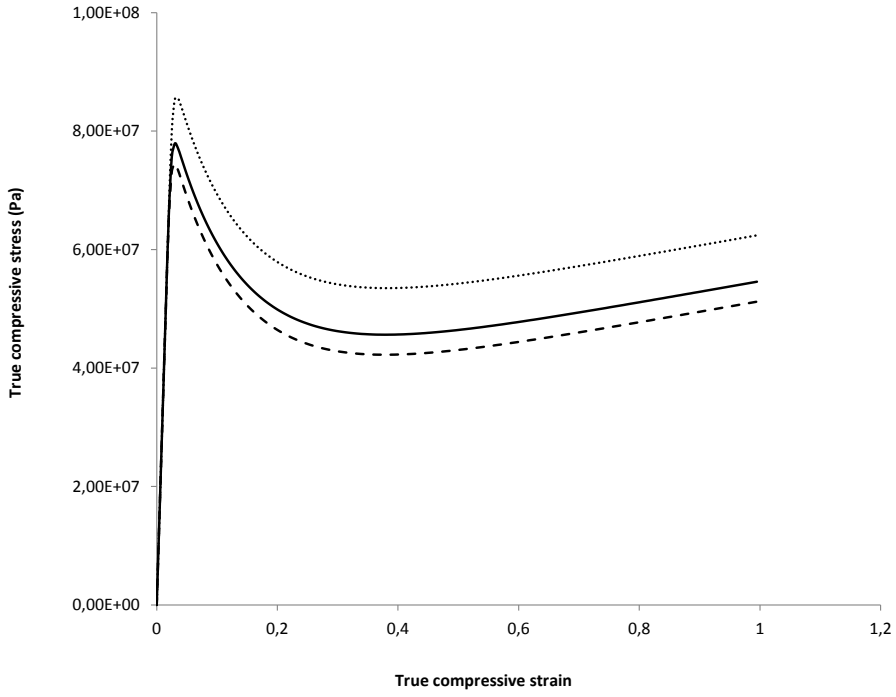

Figure 3.3: The effect of strain rate on the stress-strain curve of axisymmetric compression on PS: dashed line: $\dot{\varepsilon} = -0.0001(1/s)$; solid line: $\dot{\varepsilon} = -0.0005(1/s)$ and dotted line: $\dot{\varepsilon} = -0.001(1/s)$

ented in plane strain compression; in contrast, under uniaxial compression chains have planar orientation. Since under axisymmetric compression, chains have additional paths for deformation, larger strain are allowed under lower stresses whereas under plane strain compression, stress increases at higher speed due to

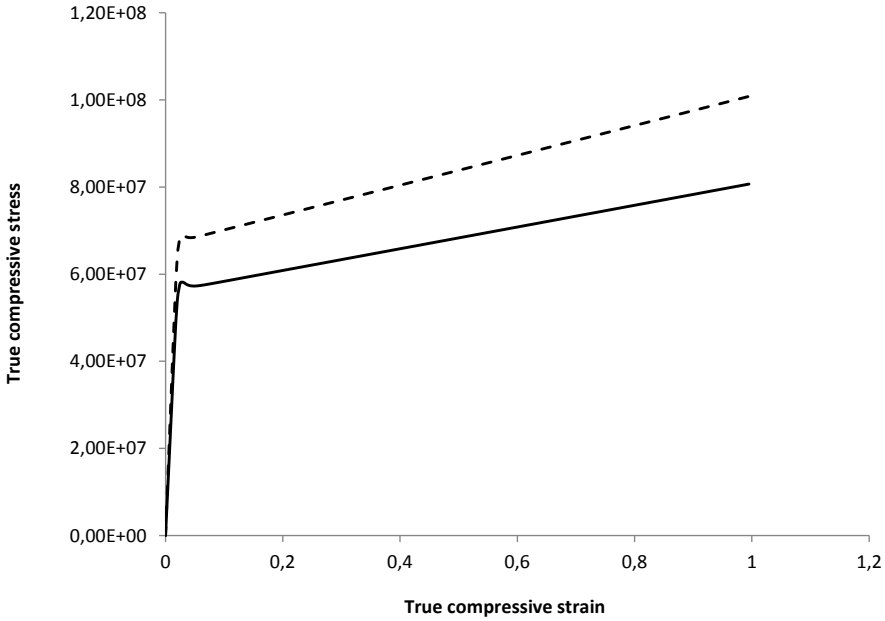

Figure 3.4: stress-strain curves of cylinder and cube compression on PA-6 under strain rate $\dot{\varepsilon} = -0.001(1/s)$: dashed line: cube and solid line: cylinder

the same paths of the chain deformations. Thus, the stress-strain behavior, shown in Figure (3.4), seems to be well captured.

3.4.3 Cylinder upsetting-temperature effect

To make clear how temperature affects stress-strain curves in polymers, Axisymmetric compression test has been simulated, using PS material properties, at three different temperatures, $T = 20^{oc}, 40^{oc}, 60^{oc}$ and under plane strain conditions. The superimposed hydrostatic pressure is assumed to be $p_0 = 0.1MPa$ and the strain rate is $\dot{\varepsilon} = -0.001s^{-1}$. It must be emphasized that since some properties of the polymeric based materials are highly dependent on the temperature, relations 3.94, taken from [Van Melic et al. (2003)] , are used to update

some properties in temperatures other than room temperature.

$$E(T) = E_0(-0.002696T + 1.79)$$

$$D_\infty(T) = D_{\infty,0}(-0.012T + 4.516) \tag{3.94}$$

$$H(T) = H_0(-0.01334T + 4.91)$$

In relations (3.94), E_0, $D_{\infty,0}$ and H_0 are the reference values for the Young modules, saturation value of the softening parameter and hardening modules obtained at room temperature, $T = 20^{oc}$, and the strain rate of $\dot{\varepsilon} = -0.001s^{-1}$. It is illustrated, in Figure (3.5), that if the analysing temperature is increased, the level of stress would considerably decrease.

3.4.4 Cylinder upsetting-effect of superimposed hydrostatic pressure

In order to show the influence of superimposed hydrostatic pressure on deformation behaviour of polymers, axisymmetric compression tests, assuming PET material properties, have been numerically done under two different superimposed hydrostatic pressures, $p_0 = 0.1, 300MPa$. The strain rate is $\dot{\varepsilon} = -0.001$ and room temperature, $T = 20^{oC}$, is assumed for the test. In Figure (3.6), it is clearly depicted that by increasing the superimposed hydrostatic pressure, the stress level will be raised.

3.4.5 Necking of a cylindrical bar

In order to explore more the efficiency and robustness of the implemented algorithm, more examples are provided. In this subsection, necking of a cylindrical bar assuming PC material properties, room temperature and atmospheric superimposed hydrostatic pressure is given. The geometry and mesh of the example is given in Figure (3.7). As can be seen in Figure (3.7), the problem is approximated as an axisymmetric tensile test and the specimen is spatially discretized with 1800 eight noded quadrilateral elements with reduced four integration Gauss

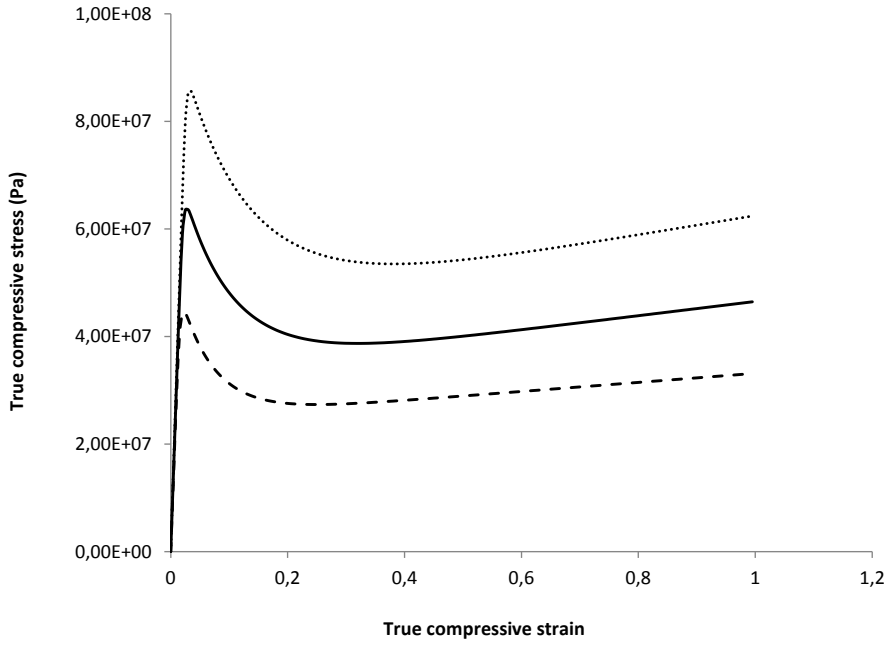

Figure 3.5: Stress-strain curves for cylinder compression tests using PS at different temperatures: dashed line: $T = 60^{oc}$; solid line:$T = 40^{oc}$ and dotted line: $T = 20^{oc}$

points. Total displacement of $u = 2\ mm$ is applied within 100 increments and the displacement rate is $\dot{u} = 0.6\ mm/min$. In order to trigger necking, a very small reduction in the area, almost one percent, is applied. In Figure (3.8), the accumulated plastic strain on the deformed cylinder at the end of deformation is shown.

3.4.6 Compression of a notched round bar

The next example is a notched bar under uniaxial compression. The geometry and mesh of the problem is shown in Figure (3.9). The specimen is spatially discretized with 350 eight noded quadrilateral elements with reduced four integration Gauss

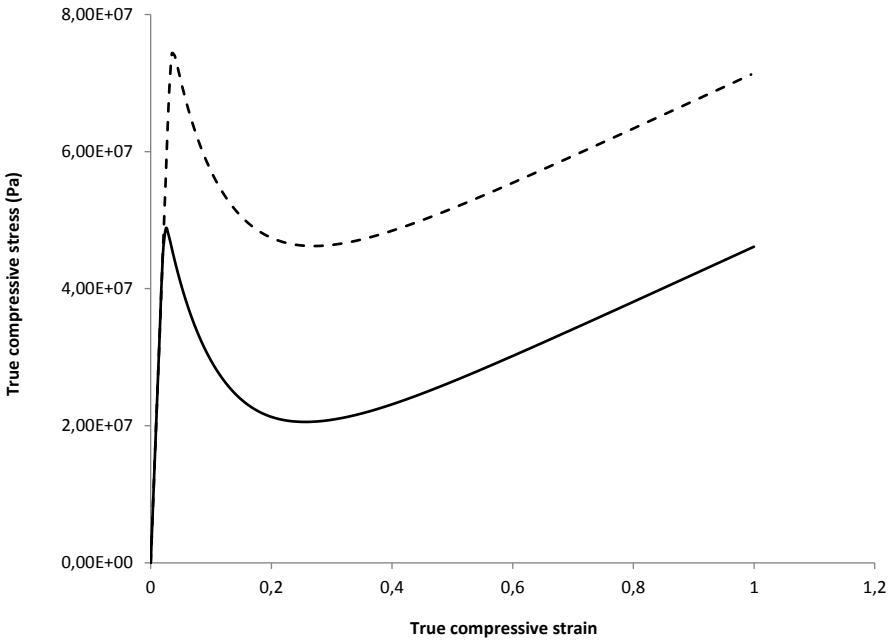

Figure 3.6: Stress-strain curves for cylinder compression tests using PET under different superimposed hydrostatic pressures: solid line: $p_0 = 0.1MPa$ and dashed line: $p_0 = 300MPa$

points. The specimen is assumed to be made of PS and is subjected to a total displacement of 2 mm in 100 increments under atmospheric condition and room temperature. The deformation speed is $\dot{u} = 0.6\ mm/min$. In Figure (3.10), the contour plot of accumulated plastic strain at the end of deformation is shown. In order to show the numerical robustness of derived and implemented algorithm, the equilibrium convergence of the later boundary value problems, necking of a cylindrical bar and compression of a notched round bar, are presented in Table (3.3).

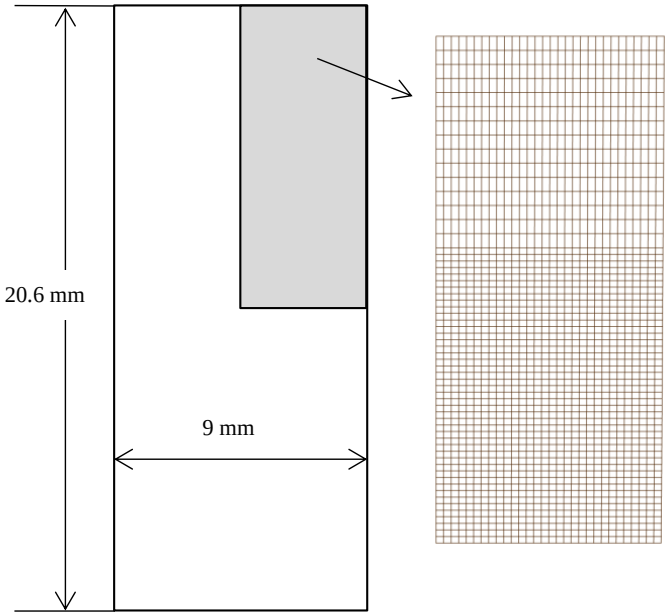

Figure 3.7: Geometry and mesh of the necking problem

Table 3.3: Equilibrium convergence table for necking of a cylindrical bar and compression of a notched round bar

	Relative residual norm (%)			
	Necking of a cylindrical bar		Compression of a notched round bar	
Iteration number	Increment (45)	Increment (90)	Increment (50)	Increment (100)
1	10.2200	12.6694	9.50544	8.69701
2	0.755383	0.613833	0.755592	0.851280
3	0.464948E-02	0.221951E-02	0.206673E-01	0.389391E-01
4	0.672957E-05	0.350794E-06	0.890494E-04	0.133873E-03
5	0.280901E-07		0.474970E-06	0.486659E-06

3.5 Conclusions

An elasto-viscoplastic model based on single model Leonov model was presented. A fast robust one equation implementation for the return mapping process of the numerical integration algorithm of the model was provided. The ability of the model, with the integration algorithm presented, to capture the effect of strain rate, hydrostatic pressure and temperature on the deformation behaviour of poly-

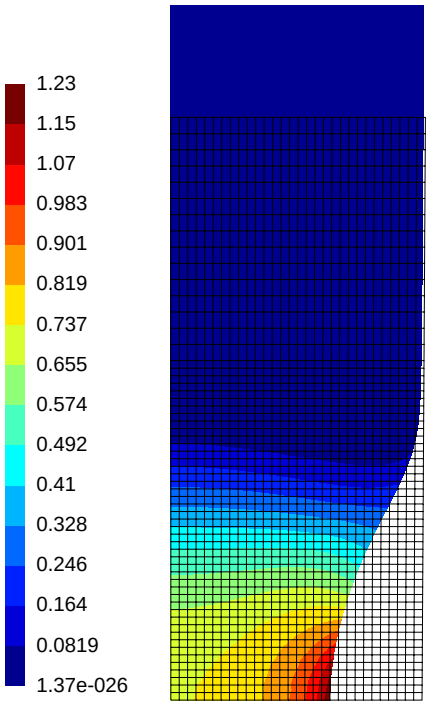

Figure 3.8: accumulated plastic strain of the cylinder under tensile deformation

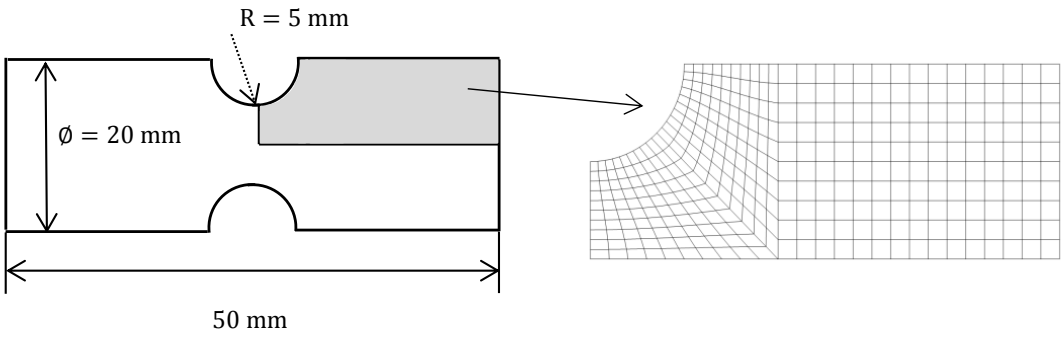

Figure 3.9: Geometry and mesh of the notched bar compression example

mers is shown through some numerical examples. The efficiency of the integration algorithm was investigated by showing the global convergence rates for different numerical examples. In summary and in view of the aforementioned issues, it can be concluded that the constitutive relations of the elasto-viscoplastic model has

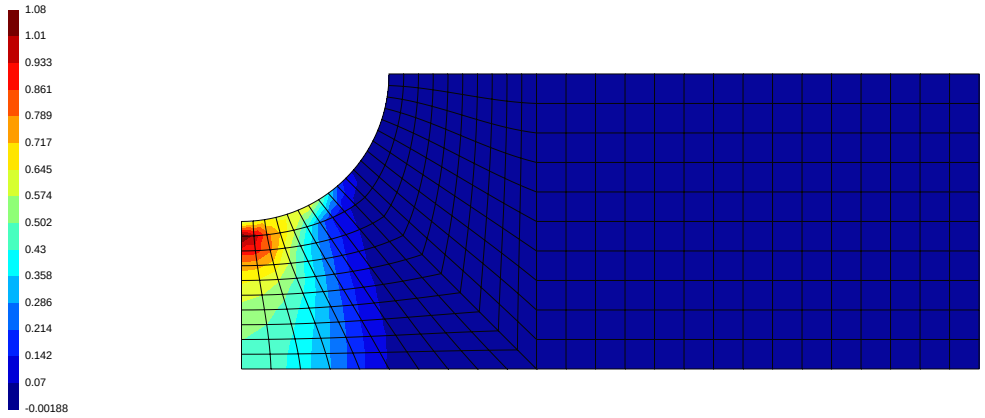

Figure 3.10: Accumulated plastic strain for the compression simulation on the notched round bar

been successfully implemented through finite element with only one equation for the return mapping of the state update procedure. The ability to capture reasonable results, efficiency and robustness of the numerical implementation were validated through some examples.

Chapter 4

An elasto-viscoplastic model for polymers under different stress states

In this Chapter, a modified version of the Leonov based constitutive model, presented in Chapter 3, is proposed in order to predict the behavior of polymers under different stress states. Although the model could be used for different polymeric materials, the driving material of this study is a specific commercial grade of Bisphenol, a polycarbonate called Makrolon 2607, for which there were experimental results for uniaxial compression, plane strain compression and tensile test on a dumbbell shape specimen available in open literature. The material properties are determined and calibrated for uniaxial compression loading. Then, the constitutive relation for the hardening stress is modified to be a function dependent on accumulated plastic strain. Simulations are performed, using the properties obtained for cylinder upsetting, under different stress states, and those for which there are experimental results, compared to experiments. According to differences observed between the simulations and experiments, some modifications are proposed, using lode angle parameter, to modify the predictions of the model under different loading conditions.

4.1 Introduction

Over the last decades, a considerable effort has been made by the academic community to develop constitutive models that are able to describe the deformation behaviour of polymeric based materials such as Boyce et al. (1988), Tervoort (1996) and Aruuda and Boyce (1993). A large number of authors have also performed experimental studies on polymers, e.g. Senden et al. (2013), Hachour et al. (2014) and Mathiesen (2014). Modified version of Von-mises, Tresca and Drucker-Prager yield criteria are used by different authors such as Bowden and Jukes (1972), Raghava et al. (1973), Fasce et al. (2008), Farrokh and Khan (2010), Ghorbel (2008) and Epee et al. (2011), in order to describe the yield behaviour of different polymers. For a detailed discussion about modified yield functions to account for yield behaviour of polymeric materials, the reader is referred to Ghorbel (2008). Nevertheless, the open literature lacks of studies on modification of constitutive models in order to better capture the post-yield behaviour of polymers. As opposed to metallic materials which show hardening behaviour after the yield point, polymers (most of thermoplastics and thermosetting polymers) show pronounced post yield softening and then hardening behaviour. The softening behaviour causes deformation localization and hence, it is very important to capture it properly. Besides, if the softening behaviour is not characterized well, the final hardening regime will not be captured properly either.

The objective of this study is to modify the constitutive equations of the model presented in Chapter 3, using lode angle parameter, in order to characterize the post-yield behaviour of polymeric materials namely post-yield softening and hardening regimes under different stress states.

One of the important issues raised in material constitutive modelling and material parameters identification is that, the material properties obtained from one specific stress state (e.g. uniaxial compression or tension) do not provide good estimation of material behaviour under arbitrary stress states. In other words, in order to have good estimation of material behaviour under different stress states, one set of material properties may, most likely, not suffice. For metallic materials, there are studies conducted on this issue. For instance Bai and Wierzbicki

(2007) used stress triaxiality and lode angle (to include the effects of hydrostatic pressure and shear effects, respectively) to modify the constitutive description of the material.
In contrast to a significant amont of work conducted on metallic material to modify the constitutive formulations using hydrostatic pressure and shear effects, open literature lacks of studies for polymers on this issue. In this chapter, the elasto-viscoplastic model presented in the previous chapter developed based on single mode Leonov model is used as a starting model. Experimental results for Makrolon 2607, under three different stress states: uniaxial compression, plane strain compression and tensile test on a dumbbell shape specimen, are taken from [Diez (2010)]. Material properties are quantified and calibrated for uniaxial compression. The material parameters obtained are then used for plane strain compression and the tensile test on the dumbbell shape specimen and it is realized that the prediction of the model (using properties obtained for uniaxial compression) for the later stress states should be modified. Based on the observations of the comparisons between the simulations and experimental results, some modifications are proposed to improve the prediction of the model for softening and hardening regimes of deformation.
Section 4.2 describes how to quantify the material parameters required by the constitutive model used in this study. In addition, some simulations, uniaxial compression, plane strain compression and tensile test on a dumbbell shape specimen, are performed using the properties. In Section 4.3, the propositions to modify the predictions of the model for softening and hardening are provided. Section 4.3 also provides the integration algorithm and finite element implementation of the enhanced model. Evaluation of the predictions of the enhanced model and also the efficiency and robustness of the integration algorithm are made in section 4.5. Finally, some concluding remarks are provided in section 4.6.

4.2 Material properties and initial simulations

The objective of this section is to obtain the properties required for the Leonov based constitutive model and conduct some simulations, using the quantified

parameters, in order to evaluate the initial model and realize the modifications required in the model. Uniaxial compression tests are chosen to be the reference to determine the properties. The material parameters required for the model presented in the previous section, are grouped in four different categories:

- Elastic properties;
- Eyring (Yielding) properties;
- Softening properties;
- Hardening properties.

4.2.1 Material properties

Diez (2010) performed extensive experiments on a specific commercial grade of Bisphenol, a Polycarbonate called Makrolon 2607, under uniaxial compression, plane strain compression and a dumbbell shape specimen under tensile condition. The material properties for Makrolon 2607 are quantified. The elastic properties are taken from [Diez (2010)]. In this contribution, the cylinder upsetting experiments are used to determine the yielding properties. Compression experiments are chosen to determine the material properties due to the following reasons:

- The deformation in compression simulations is uniform as opposed to the tensile experiments;
- In order to determine the Eyring properties, a relation between the yield stress and Eyring properties is required (which will be given in Section 4.2.1.1) and Diez (2010) provided experimental stress-strain curves for compression experiments;
- In order to calibrate the softening properties (explained in Section 4.2.1.2), using stress-strain curves is more convenient than force-displacement curves;
- Similarly to the softening properties, hardening parameter (explained in Section 4.2.1.3) is more conveniently obtained from stress-strain curve than a force-displacement curve.

It should also be mentioned that axisymmetric compression is chosen over plane strain compression because deriving a relation between the yield stress and yielding properties, which is given by Equation (4.1), for axisymmetric condition is easier than plane strain compression.

4.2.1.1 Eyring properties

The Eyring parameters are determined by measuring the true stress at yield at different strain rates. Relation (4.1) is used to obtain the yield properties.

$$\frac{|\sigma_y|}{T} = \frac{3R}{\sqrt{3}V + a\Omega}\Big[\ln(A_0|\dot{\varepsilon}|) + \frac{\Delta H}{RT} + \ln\left(\sqrt{3}\right)\Big], \tag{4.1}$$

Relation (4.1) could be rewritten as follows:

$$\frac{|\sigma_y|}{T} = \frac{3R}{\sqrt{3}V + a\Omega}\Big[\ln(|\dot{\varepsilon}|)\Big] + \frac{3R}{\sqrt{3}V + a\Omega}\Big[\ln(A_0) + \frac{\Delta H}{RT} + \ln\left(\sqrt{3}\right)\Big];\ \ a = sign(\sigma_y) \tag{4.2}$$

In relations (4.1) and (4.2), the parameter a is the sign of yield stress i.e. in case of compression it is equal to $a = -1$ and in case of tension it is $a = +1$. The yield stress over temperature as a function of logarithm of strain rate is plotted for two different temperatures and three different strain rates. The plot, Figure (4.1), of the function is called Eyring plot [Tervoort (1996)]. By approximating the yield behaviour by strain rate as a linear function, we could have the functions (4.3) for the Eyring plots. It should be mentioned that the linear approximations are taken using a Microsoft Excel tool, trend line.

$$T = 296^K : \frac{|\sigma_y|}{T} = 5620.4\Big[\ln(|\dot{\varepsilon}|)\Big] + 286022,$$

$$T = 323^K : \frac{|\sigma_y|}{T} = 5811.9\Big[\ln(|\dot{\varepsilon}|)\Big] + 239000. \tag{4.3}$$

According to relations (4.2) and (4.3), the following system of equations could be written:

$$T = 296^K : 5620.4\Big[\ln(A_0) + \frac{\Delta H}{RT} + \ln\left(\sqrt{3}\right)\Big] = 286002,$$

$$T = 323^K : 5811.9\Big[\ln(A_0) + \frac{\Delta H}{RT} + \ln\left(\sqrt{3}\right)\Big] = 239000. \tag{4.4}$$

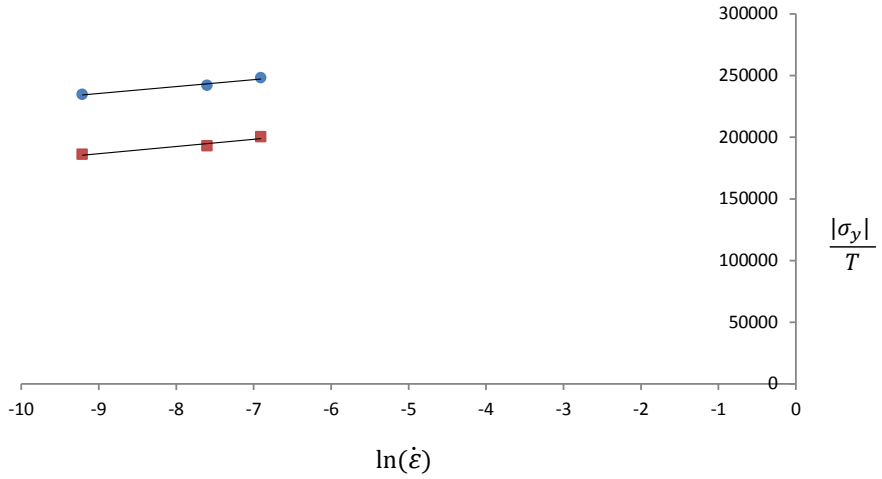

Figure 4.1: Eyring plot: Yield stress over temperature as a function of logarithm of train rate; circles: $T = 296°\text{K}$; squares: $T = 323°\text{K}$

By solving the system of equations (4.4) the activations energy and pre-exponential factor are obtained: $\Delta H = 2.87461E + 5, A_0 = 4.16564E - 30$. Now, the other two parameters should be obtained: τ_0 and μ. We have:

$$\tau_0 = \frac{RT}{V}, \mu = \frac{\Omega}{V}. \tag{4.5}$$

In order to achieve the values of τ_0 and μ the following trial and error procedure is followed:

- ▷ We guess a value for V;
- ▷ The value of Ω is obtained form the slope of the Eyring plot $\frac{3R}{\sqrt{3}V-\Omega}$;
- ▷ τ_0 and μ are obtained form relations (4.5);
- ▷ Using the values of Eyring parameters, simulations are performed to obtain the yield stress of simulations;
- ▷ The yield stress obtained in the previous stage is compared to measured yield stress. If the values are close enough, V and Ω and consequently, τ_0 and μ are obtained. In case the obtained yield stress and measured one are

not close together, the procedure should be repeated. This trial and error procedure is continued until desired values are obtained.

it should be emphasized that the parameters Ω and V were obtained at the temperature $T = 296°\text{K}$. The pressure coefficient and pressure parameter are quantified: $\tau_0 = 0.91149E + 06$ and $\mu = 8.8E - 02$.

4.2.1.2 Softening properties

The softening parameters, D_∞, h, are non dimensional factors. We know that the property h affects the slope of the softening regime of the deformation and the parameter D_∞ determines the ultimate amount of softening behaviour [Timmermans (1998)]. A trial and error procedure is adopted to determine the mentioned properties such that the softening regime is captured best. The softening properties are obtained: $h = 67$ and $D_\infty = 22$.

4.2.1.3 Hardening parameter

The final parameter to be specified is the hardening parameter, H. Timmermans (1998) obtained hardening parameter for different polymeric materials. The hardening module for Polycarbonate (PC) was obtained by a tensile test after mechanical rejuvenation by torsion. For Polypropylene and Nylon-6, an expression derived by Haward (1987) was used to determine the hardening module. Haward (1987) derived the expression originally for a non-intrinsic softening material such as Polypropylene. In this contribution, since the material under study shows remarkable post-yield softening behaviour and we do not have any results from a mechanically rejuvenated specimen, a different hardening parameter is introduced called initial hardening module, H_{ini}. We measure this parameter from the initial slope of the hardening regime of the stress-strain curve in axisymmetric compression. Having defined the new hardening parameter, initial hardening module, H_{ini}, a relation for the total hardening, H, is introduced which is not constant any more and it changes as deformation proceeds.

$$H = (a\bar{\varepsilon}^p)H_{ini}, \tag{4.6}$$

where, H_{ini} is the initial hardening parameter determined from the initial slope of the hardening regime of the deformation; $\overline{\varepsilon}^p$ is the accumulated plastic strain and a is new dimensionless parameter to be calibrated and is called constant hardening coefficient. With the aforementioned hardening factor, relation (4.6), the hardening property is not constant during deformation. Haward and Tackray (1968), Argon (1973) and Boyce and Arruda (1990) considered strain hardening as a result of evolving resistance to chain alignment. Having an evolving hardening property could be associated to evolving resistance to chain alignment. The physical phenomenon is incorporated in relation (4.6). With the above mentioned processes of determination of material properties, the following set of material properties, tabulated in Table (4.1), is obtained for axisymmetric compression test at room temperature.

Table 4.1: Material properties for Makrolon 2607

E(MPa)	ν	$\Delta H(J/mol)$	$A_0(s)$	τ_0(MPa)	D_∞	h	μ	R	H_{ini}(MPa)	a
2347.8	0.304	2.87461E+05	4.16564E-30	0.91149	22	67	0.088	8.3143	26	2.2

4.2.2 Simulations

In this section, some simulations are performed, using the material properties obtained in the previous section, under axisymmetric compression, plane strain compression and tensile test on a dumbbell shape specimen. The objective is to realize if the material parameters obtained and calibrated using cylinder upsetting work well for other stress states and if not, how different are the simulations from the experimental results. It should be mentioned that determining the material properties is done for the strain of $\dot{\varepsilon} = -0.001(1/s)$ and room temperature, $T = 23^C$. Contrary to the remarkable dependence of some of the material properties to the temperature, strain rate does not affect the material parameters.

4.2.2.1 Cylinder upsetting

Axisymmetric compression simulations are performed under three different strain rates, $\dot{\varepsilon} = -0.001(1/s), \dot{\varepsilon} = -0.0005(1/s)$ and $\dot{\varepsilon} = -0.0001(1/s)$. In Fig-

ure (4.2), the geometry and mesh of the cylinder upsetting simulation can be seen. The specimen is spatially discretized with 128 quadrilateral eight noded

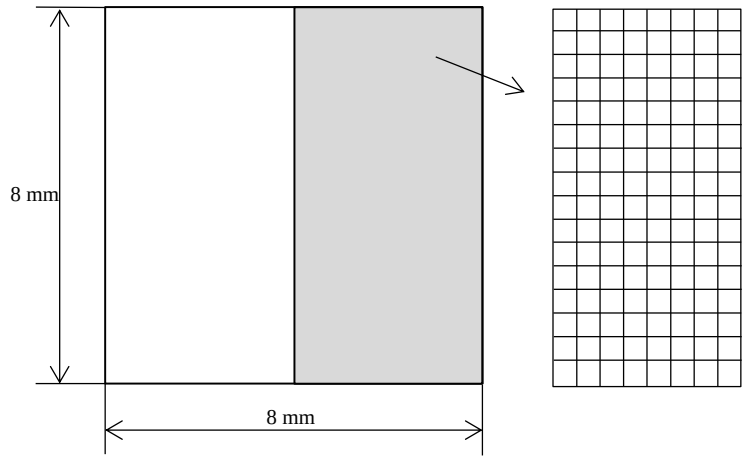

Figure 4.2: The geometry and mesh of the cylinder upsetting simulations

elements with reduced four integration Gauss points. Figure (4.3) shows simulations and experimental results for axisymmetric compression under three strain rates, $\dot{\varepsilon} = -0.001(1/s), -0.0005(1/s), -0.0001(1/s)$. It can be seen the obtained and calibrated properties could precisely provide approximation to experimental results under axisymmetric compression stress state. Yield stress, softening and hardening regimes have a good agreement. The difference observed at the yield strain stems from visco-elastic effects which are not considered because a single mode model is used [Tervoort (1996), Timmermans (1998)]. Using multi relaxation time could help to capture the pre-yield non-linear behaviour [Tervoort (1996), Timmermans (1998)].

4.2.2.2 Cube compression

In this subsection, the assessment of the predictive ability of the original model and properties will be conducted under plane strain compression. The mesh used for axisymmetric compression, shown in Figure (4.2), is also used for plane strain compressions. Compressive simulations under three different strain rates are performed. Figure (4.4) depicts simulations and experimental results for

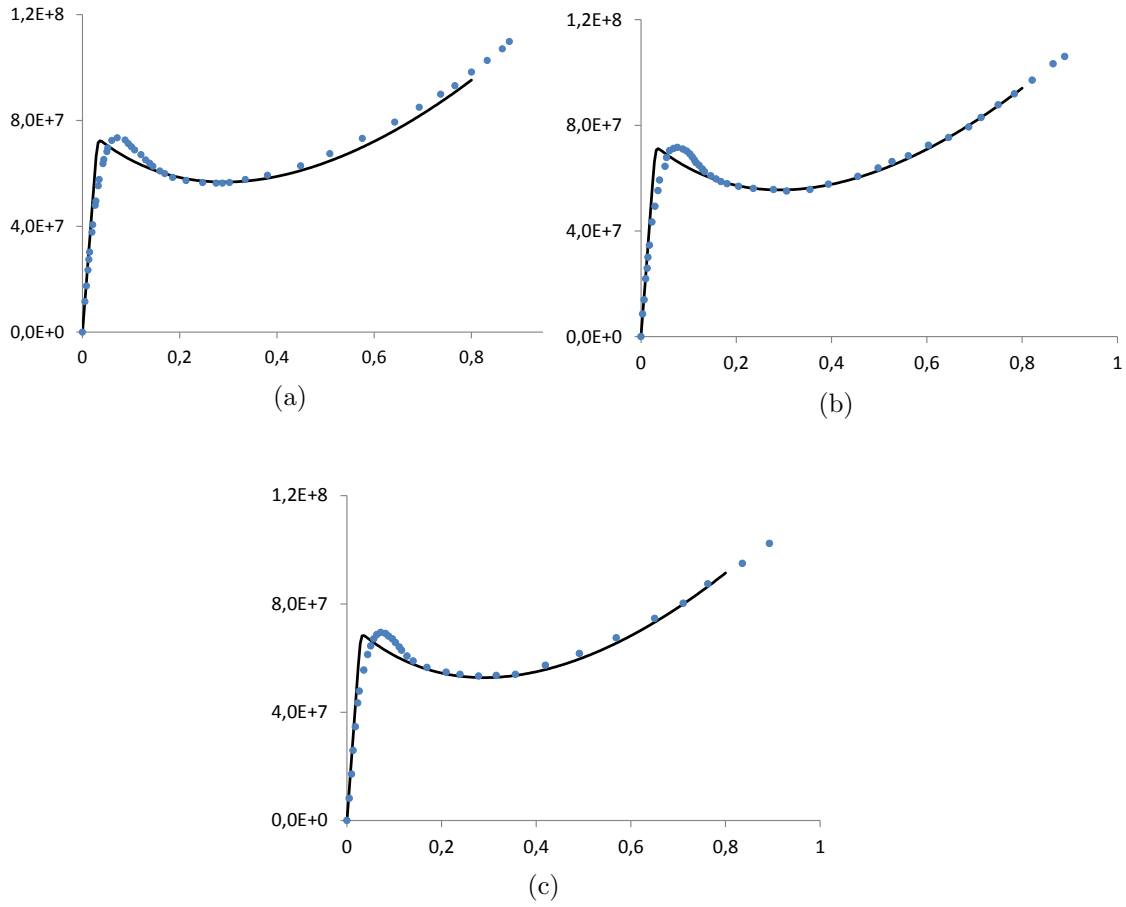

Figure 4.3: True stress-true strain for the uniaxial compression test on PC at room temperature, solid line: simulation; circles: experiment; horizontal axis: true compressive strain; vertical axis: True compressive stress (Pa); (a): $\dot{\varepsilon} = -0.001(1/s)$; (b): $\dot{\varepsilon} = -0.0005(1/s)$; (c): $\dot{\varepsilon} = -0.0001(1/s)$.

three compressive strain rates. In contrast to the yield stress, which is well captured under all three different strain rates, softening and hardening regimes of deformation under plane strain compression are not characterized properly.

4.2.2.3 Tension on dumbbell shape specimen

The next test to be examined is a 3D tensile test on a dumbbell shape specimen. The geometry and mesh of the example is depicted in Figure (4.5). The specimen is discretized with 1100 eight noded elements with eight integration Gauss points.

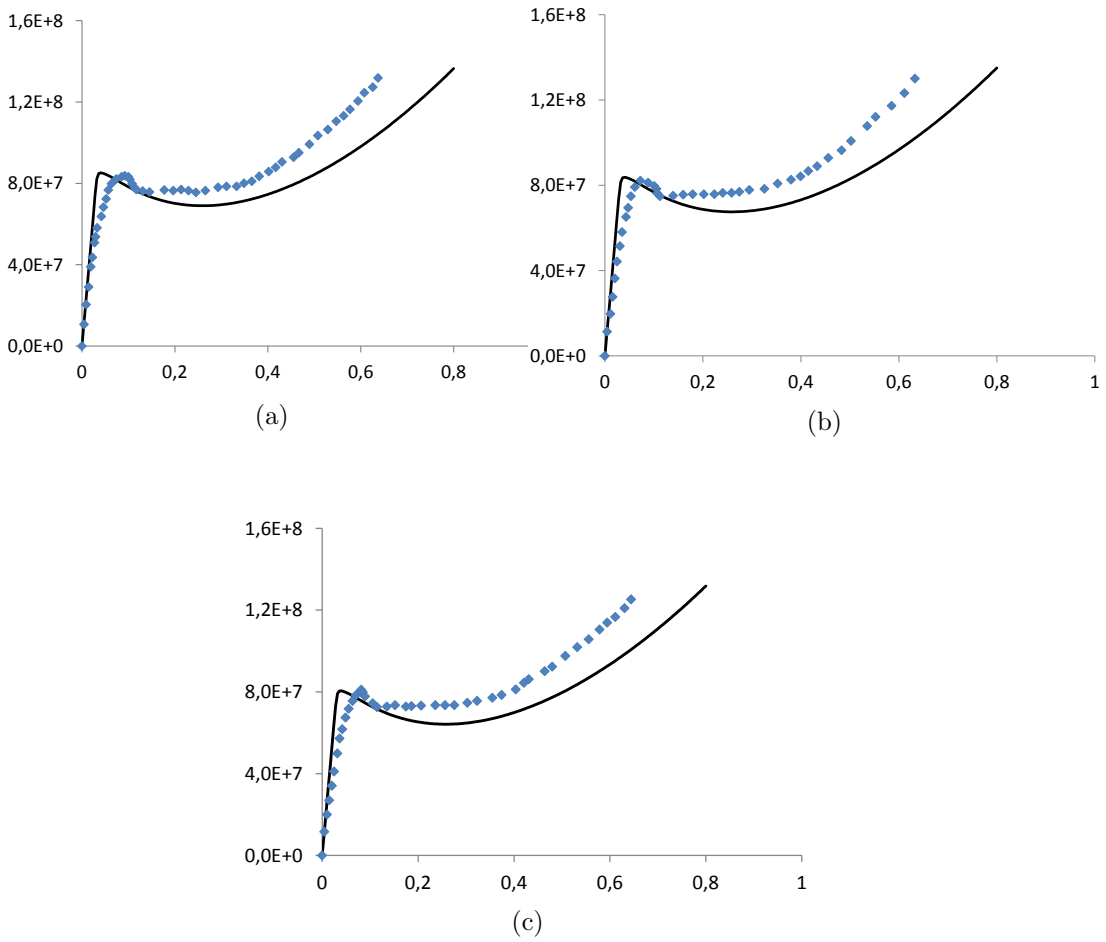

Figure 4.4: True stress-true strain for the plane strain compression test on PC at room temperature, solid line: simulation; squares: experiment; horizontal axis: true compressive strain; vertical axis: True compressive stress (Pa); (a): $\dot{\varepsilon} = -0.001(1/s)$; (b): $\dot{\varepsilon} = -0.0005(1/s)$; (c): $\dot{\varepsilon} = -0.0001(1/s)$

The displacement rate is $\dot{u} = 2\frac{mm}{min}$. The force-displacement curve of the specimen is shown in Figure (4.6). Again, it is possible to conclude that although the yield behaviour is well predicted by the model, both softening and hardening regimes of the deformation are not in agreement with the experimental results.

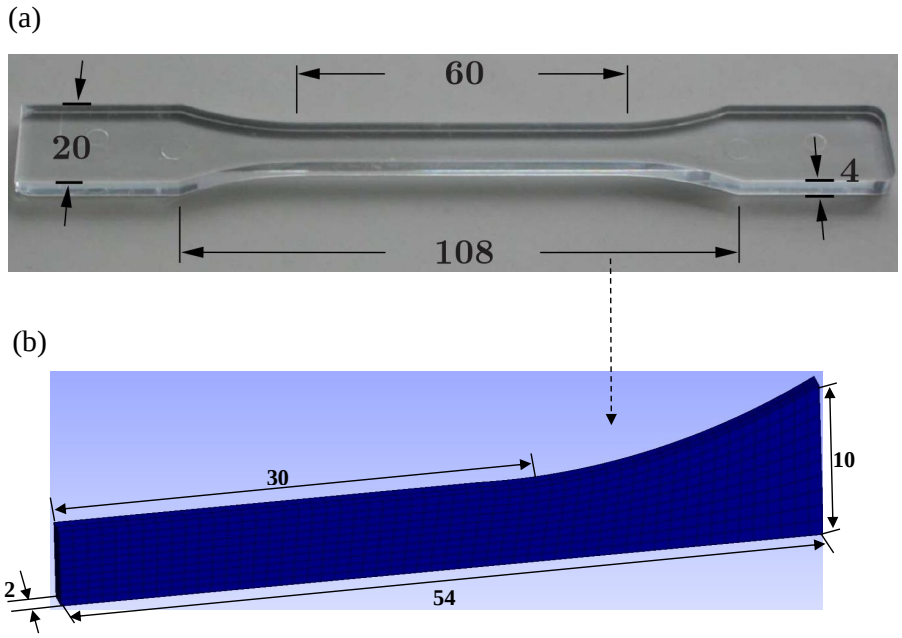

Figure 4.5: The geometry and mesh of the 3D tensile test on a dumbbell shape specimen.

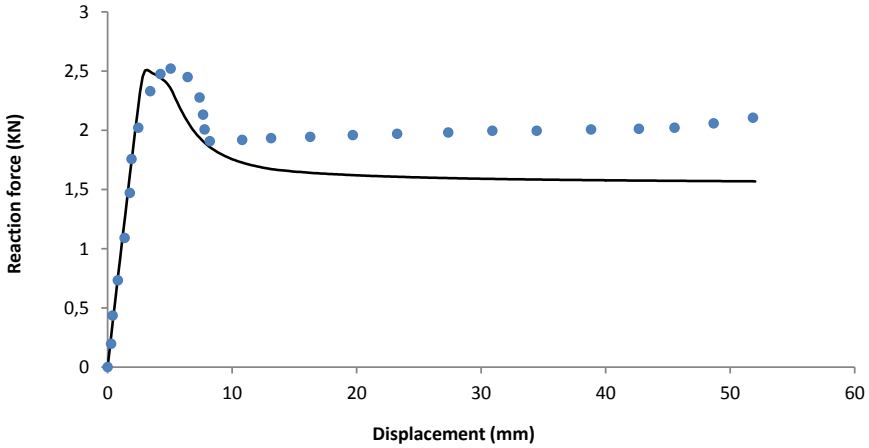

Figure 4.6: Force-displacement curve of tensile test on dumbbell shape specimen under deformation speed $\dot{u} = 2\frac{mm}{min}$. Circles: experimental results and solid line: simulation

4.2.2.4 Butterfly specimen

The last example examined in this chapter is a butterfly specimen under different loading conditions. Using this example, it is intended to cover loading conditions from pure shear to combined shear-tensile conditions. The specimen geometry is taken from [Bai and Wierzbicki (2007)]. Figure (4.7) depicts the details of the geometry of the specimen. The 3D butterfly specimen is spatially discretized

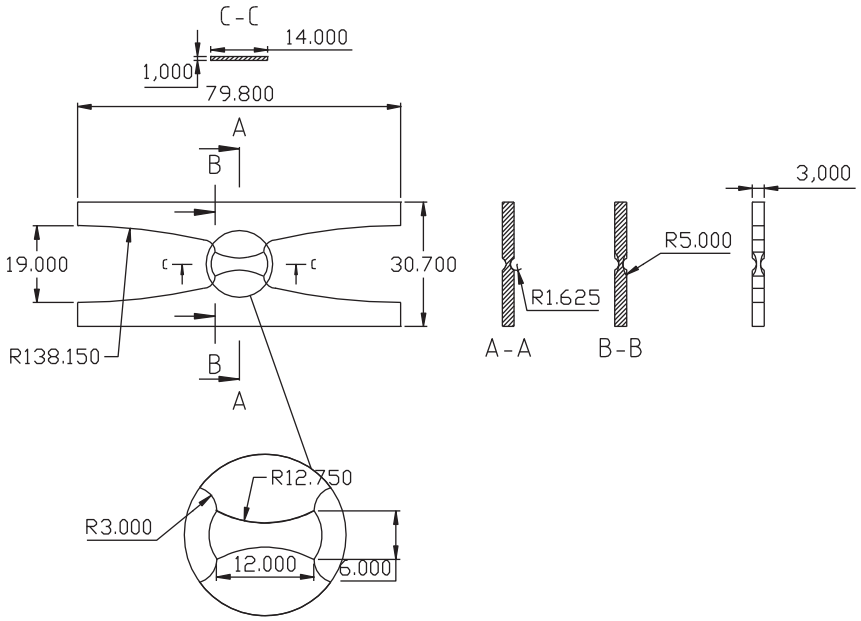

Figure 4.7: The details of the geometry of the butterfly specimen. Adapted from [Bai and Wierzbicki (2007)].

with 3392 twenty noded finite elements with eight integration Gauss points resulting in a mesh with 17465 nodes in the finite element mesh. The mesh of the specimen is shown in Figure (4.8). The butterfly specimen is loaded under different stress states, namely pure shear, combined shear tension, tension and compression. Schematic representation of pure shear and combined shear tension loading conditions is provided in Figure (4.9). The first simulation on the butterfly specimen is pure shear, represented in Figure (4.9a). The total displacement is equal to $8mm$ and is applied in 200 increments with the displacement speed of $\dot{u} = 2.4mm/min$. The load displacement curve is shown in Figure (4.10). When

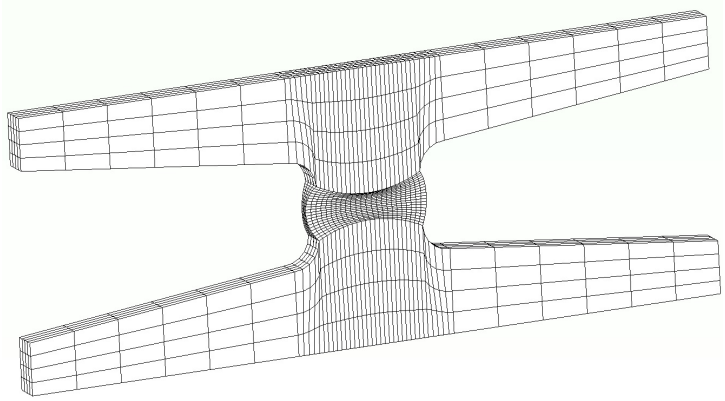

Figure 4.8: The spatial discretization of the butterfly specimen.

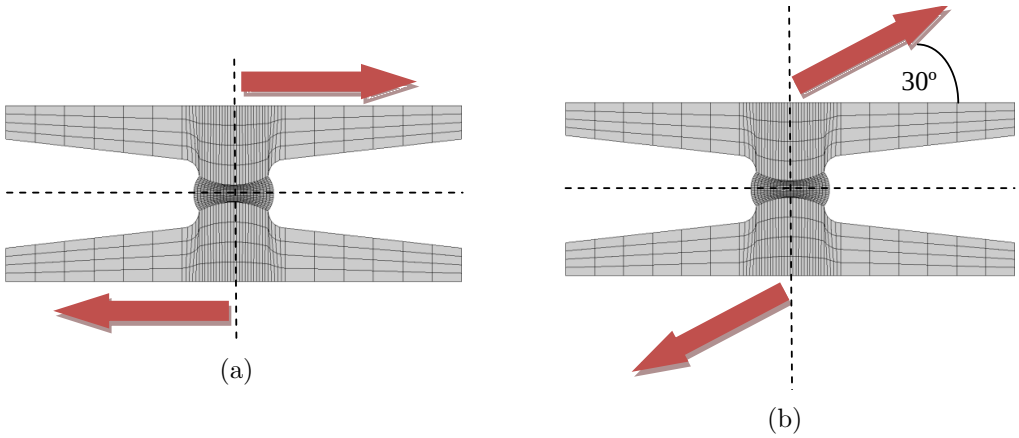

Figure 4.9: Schematic representation of pure shear and combined shear tension loading conditions on the butterfly specimen, adapted from [Malcher (2012)].

the butterfly specimen is subjected to pure shear loading, no load softening is observed which is expected. Hachour et al. (2014) also observed no load softening in pure shear experiment on a butterfly specimen made from HDPE. The next simulation on the butterfly specimen is the combined shear tension stress state, shown in Figure (4.9b). The total displacement of $5mm$ is applied in 500 increments. The load speed is equal to $\dot{u} = 3mm/min$. The normalized force-normalized displacement curve is shown in Figure (4.11). Similarly to the tensile test on the dumbbell shape specimen and the corresponding force-displacement curve, shown in Figure (4.6), the force-displacement curve for the combined shear-tensile loading has a load softening after the initial elastic behaviour. Taking into

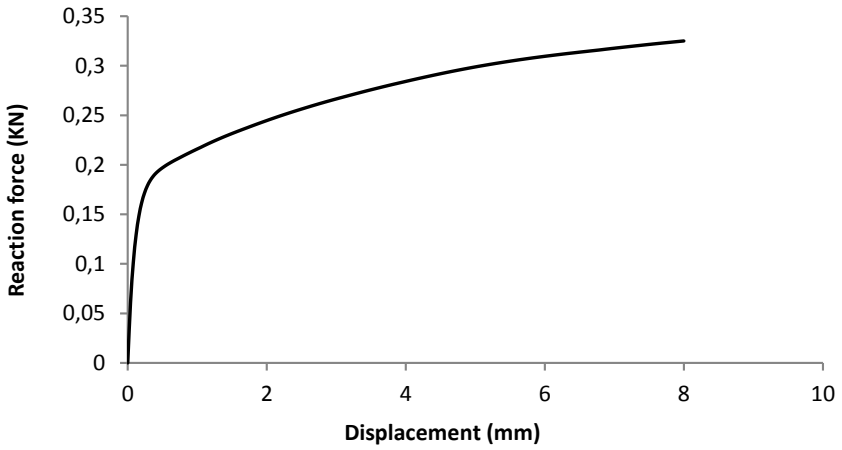

Figure 4.10: The force displacement curve for butterfly specimen under pure shear stress state.

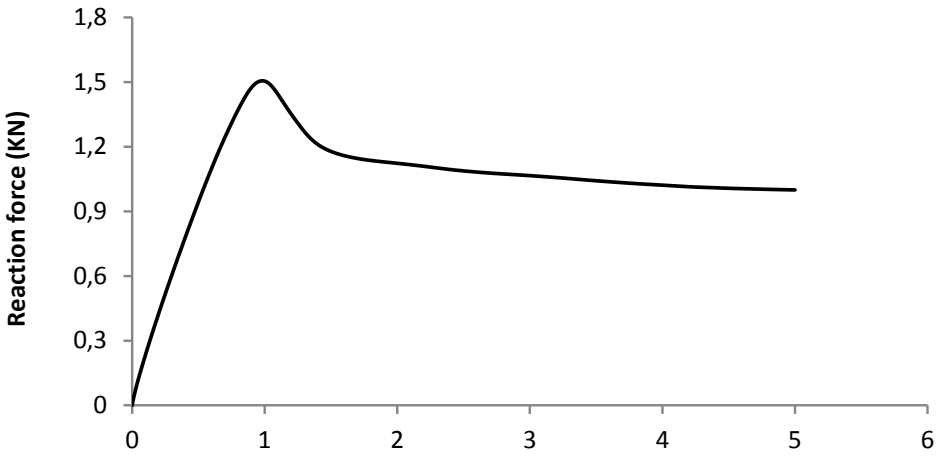

Figure 4.11: The normalized force-normalized displacement curve for butterfly specimen under combined shear-tension stress state.

account no load drop in the pure shear stress state, one could say that in the combined shear-tensile loading, presented in Figure (4.9b), the tensile resistance to deformation is dominant compared to the shear resistance.

4.3 Modified constitutive model

In the previous section, it was presented that in contrast to axisymmetric compression, the model could not capture the behaviour of Makrolon 2607 under plane strain compression and tensile test on a dumbbell shape specimen, with the material properties obtained for axisymmetric compression. Therefore, improvements in the model are required to capture the behaviour of the material under arbitrary stress states. Three possible approaches could be followed as provided below:

- Introducing additional material parameters obtained for different stress states into the model;
- Attributing different values to the same set of material properties for different stress states;
- Modifying the constitutive equations to promote different deformation evolution under different stress states.

The third approach is favoured because if it is possible to have a generic constitutive model for different stress states with only a single set of material properties, it would be highly desired. Hence, in this work, the third approach is followed. The goal is to use the lode angle parameter, which has been successfully used in metallic materials, inside the material constitutive relations such that the predictions of the model in stress states other than axisymmetric compression improve.

4.3.1 Required enhancements

In this section, a detailed discussion of the enhancements required by the original model is undertaken by comparing the experimental results with the predictions of the model. As shown previously, for plane strain compression and a tensile test on the dumbbell shape specimen, the post-yield behaviour including softening and hardening were not well captured. In the following, it is explained how the model could be improved in order to have better agreements for all stress states.

4.3.1.1 Plateau like behaviour in plane strain compression

For plane strain compression, the yield stress prediction is reasonably good; the difference in yield strain, as mentioned before, is due to using single mode model and therefore is not going to be dealt with in this study; softening slope is overestimated and the plateau-like behaviour during softening, shown in Figure (4.12), is not captured. The softening evolution function should be modified in a way to

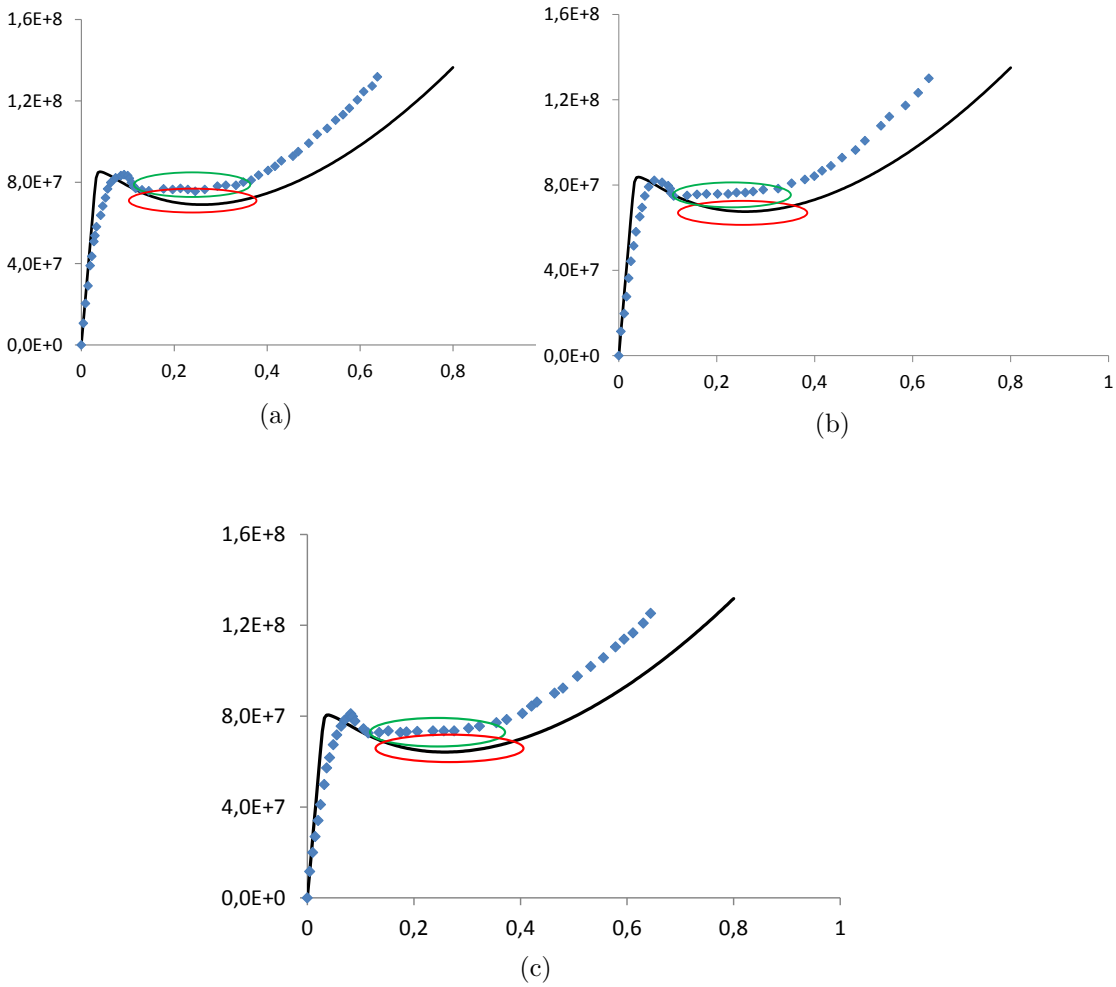

Figure 4.12: Plateau-like behaviour in plane strain compression tests under three different strain rates. Solid line: simulation; circles: experiment; horizontal axis: true compressive strain; vertical axis: True compressive stress (Pa); (a): $\dot{\varepsilon} = -0.001(1/s)$; (b): $\dot{\varepsilon} = -0.0005(1/s)$; (c): $\dot{\varepsilon} = -0.0001(1/s)$.

remove, or at least minimize, this discrepancy.

4.3.1.2 Hardening underestimation in plane strain compression

Under plane strain compression state, as it can be observed in Figure (4.13), the slope of the hardening regime is under estimated in the simulations when it is compared to the experiments. The hardening stress should be enhanced in a way to make the hardening regime of the deformation predicted by simulations closer to experiments.

4.3.1.3 Softening overestimation in tension on dumbbell shape specimen

Having investigated the required enhancements in plane strain compression, now, comparison between simulations and experiments should be done for the 3D tensile test in order to see in which way the results should be improved. As it can be seen in Figure (4.6), the elastic regime of the deformation and also the yield behaviour under tensile condition is captured reasonably well. In contrast, the post-yield softening and also the final hardening regimes of deformation are not well-predicted. It is graphically shown in Figure (4.14), that the softening is overestimated.

4.3.1.4 Hardening underestimation in tension on dumbbell shape specimen

Under tensile stress state, the model prediction in the hardening phase of the deformation is underestimated in comparison to experimental results. Figure (4.15) shows the difference between the simulations and the experiments.

4.3.2 Modifications proposed

In this section, the lode angle definition is given. Besides, two functions of lode angle are proposed to be included in the constitutive relations in order to improve the predictions of the model.
For any isotropic material, the stress state of each point could be defined in

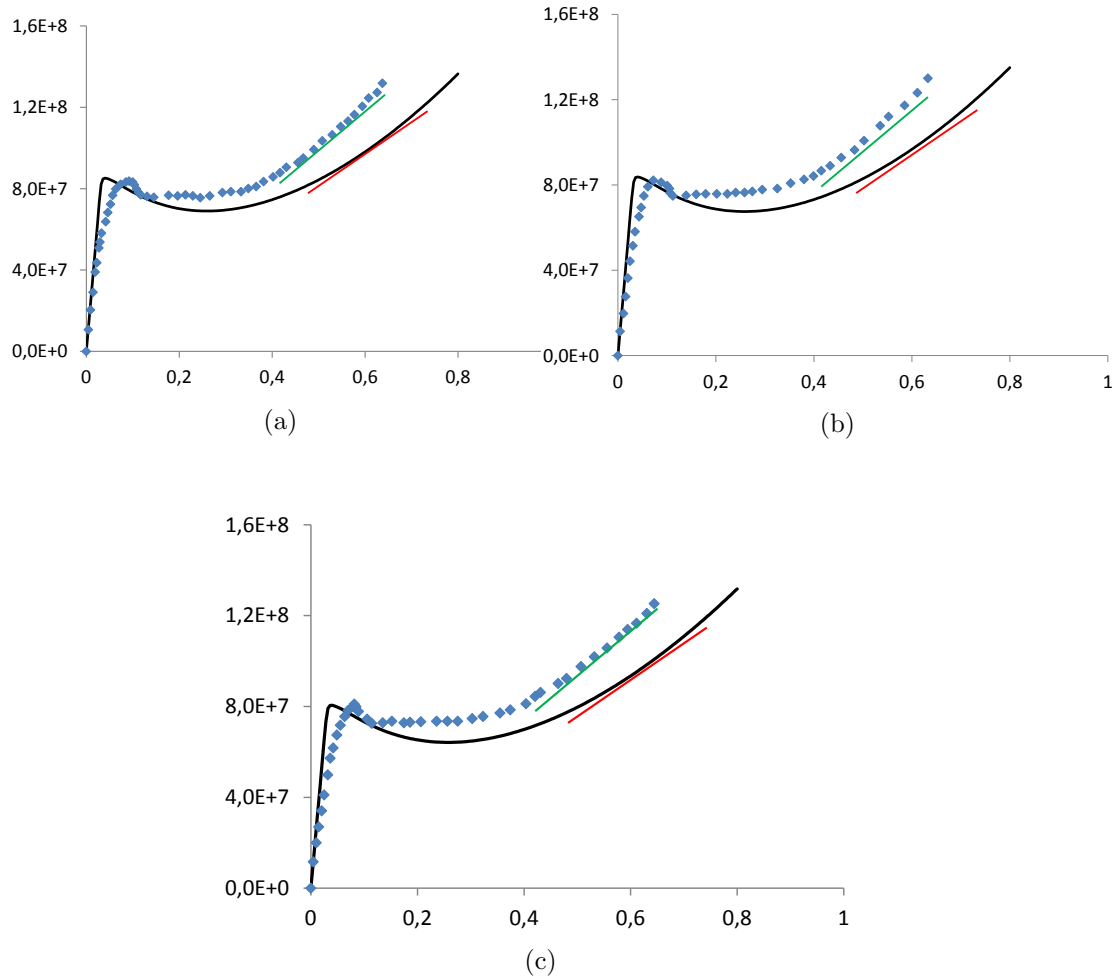

Figure 4.13: Hardening comparison between simulations and experiments in plane strain compression tests under three different strain rates. Solid line: simulation; circles: experiment; horizontal axis: true compressive strain; vertical axis: True compressive stress (Pa); (a): $\dot{\varepsilon} = -0.001(1/s)$; (b): $\dot{\varepsilon} = -0.0005(1/s)$; (c): $\dot{\varepsilon} = -0.0001(1/s)$.

Cartesian principal stress space $(\sigma_1, \sigma_2, \sigma_3)$. The second possible choice for the stress state of an isotropic material is a cylindrical coordinate system $(\sigma_m, \overline{\sigma}, \theta)$. In the later, σ_m is hydrostatic pressure, $\overline{\sigma}$ is von-mises effective stress and θ is lode angle parameter. The lode angle parameter, θ, is related to the normalized

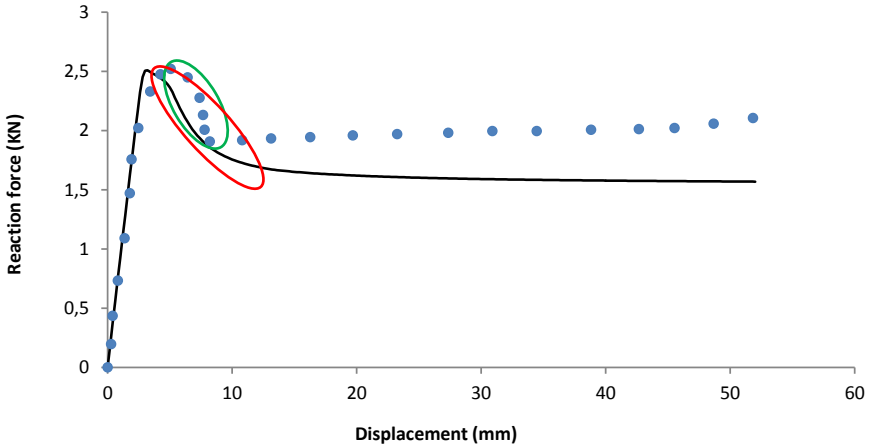

Figure 4.14: Force-displacement curve of tensile test on dumbbell shape specimen under deformation speed $\dot{u} = 2\frac{mm}{min}$: The post-yield softening prediction of the model compared to experiments.

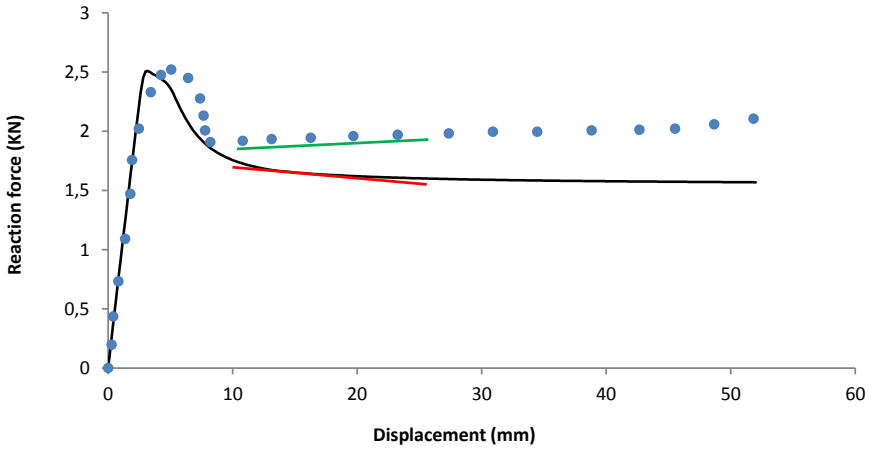

Figure 4.15: Force-displacement curve of tensile test on dumbbell shape specimen under deformation speed $\dot{u} = 2\frac{mm}{min}$: Difference in the post-yield hardening prediction of the model compared to experiments.

third deviatoric stress invariant, ξ, with the following relation:

$$\xi = \left(\frac{r}{q}\right)^3 = \cos(3\theta), \tag{4.7}$$

where,

$$r = \left[\frac{27}{2} det(\mathbf{s})\right]^{(1/3)}, \tag{4.8}$$

and

$$q = \overline{\sigma} = \sqrt{\frac{3}{2}\mathbf{s} : \mathbf{s}}, \tag{4.9}$$

where, $\mathbf{s}$ is the deviatoric stress. The lode angle varies between 0 and $\pi/3$, see [Bai and Wierzbicki (2007)] ($0 \leq \theta \leq \pi/3$); hence, the range for ξ is: $-1 \leq \xi \leq 1$. The lode angle parameter is normalized with relation (4.10).

$$\overline{\theta} = 1 - \frac{6\theta}{\pi} = 1 - \frac{2}{\pi}\arccos(\xi) \tag{4.10}$$

The range of normalized lode angle is $-1 \leq \overline{\theta} \leq +1$. It should be emphasized that lode angle parameter is geometry and loading dependent and it does not depend on the material under study. Both geometry and loading conditions promote different lode angle values. When polymer chains are subjected to shear, they start to deform i.e. the main mechanism of deformation in polymers is shear stress applied to polymer chains. According to the formulation of the model, presented in Chapter 3, the flow potential of the model is characterized with shear stress in one dimensional case and deviatoric stress in generic three dimensional case. We know that lode angle is representative of shear stress. Due to the aforementioned facts, it is physically meaningful to incorporate lode angle parameter for improving the constitutive equations. It is also worth emphasizing that the value of the lode angle under most of stress states is $\overline{\theta} = -1$, $\overline{\theta} = 0$ or $\overline{\theta} = 1$. Hence, In addition to the physical appropriateness of the lode angle parameter to be included in the constitutive equations of homogeneous polymers, it is mathematically and computationally convenient to be used. Normalized lode angle, $\overline{\theta}$, is used to modify the constitutive relations.

As can be seen in Figures (4.3), (4.4) and (4.6), the yield behaviour of the material under axisymmetric compression, plane strain compression and also tensile test on the dumbbell shape specimen are captured well. As mentioned before, most of studies on modification of constitutive models for polymers are concerned about better prediction of the yield behaviour. Since, we were able to capture the yield behaviour properly, and also the importance of characterizing the post-yield

softening and hardening behaviour, in the next sections, constitutive equations characterizing the softening and final hardening behaviour will be improved using two functions of lode angle parameter.

4.3.2.1 Softening

It is known that plastic strain localization in glassy polymers is induced by intrinsic strain softening [Govaert et al. (2000), Van Breemen et al. (2012)]. It should be mentioned that the stress drop after that yield point, local maximum stress after elastic regime in the typical stress-strain curve of glassy polymers, is referred as softening behaviour. As previously explained, the slope of the post-yield softening in the plane strain compression simulations is overestimated by the model and the plateau like behaviour is not captured. In order to include shear effects in the softening behaviour, the relation for the evolution of the softening parameter, relation (3.37), is changed as follows:

$$\dot{D} = h g(\overline{\theta}) \left(1 - \frac{D}{D_\infty}\right) \dot{\overline{\gamma}}^p, \tag{4.11}$$

where, $g(\overline{\theta})$ is defined as:

$$g(\overline{\theta}) = \frac{1}{2}\left(\overline{\theta}^2 + 1\right). \tag{4.12}$$

Using relation (4.11), the following viscosity function is obtained.

$$\eta = A_0 \exp\left[\frac{\Delta H}{RT} + \frac{\mu P}{\tau_0} - D_\infty + D_\infty \exp\left(\frac{-h g(\overline{\theta})\sqrt{3}\ \overline{\varepsilon}^p}{\sqrt{2} D_\infty}\right)\right] \cdot \left[\tau^{eq} / \sinh\left(\frac{\tau^{eq}}{\tau_0}\right)\right], \tag{4.13}$$

As mentioned before, the lode angle parameter varies between -1 and $+1$: $-1 \leq \overline{\theta} \leq +1$. Figure (4.16) depicts how $g(\overline{\theta})$ evolves through the domain of lode angle parameter. For axisymmetric compression, compression test on cylinders, the lode angle parameter is equal to $\overline{\theta} = -1$, [Bai and Wierzbicki (2007)], hence the value of the function is equal to unity. As a result, this function does not affect the softening prediction of the model, as wanted, since the original model gave good predictions of the model for the cylinders upsetting. The function reduces to $g(\overline{\theta}) = 0.5$ for plastic plane strain compression. We know that the softening parameter h affects the softening slope [Timmermans (1998)], and

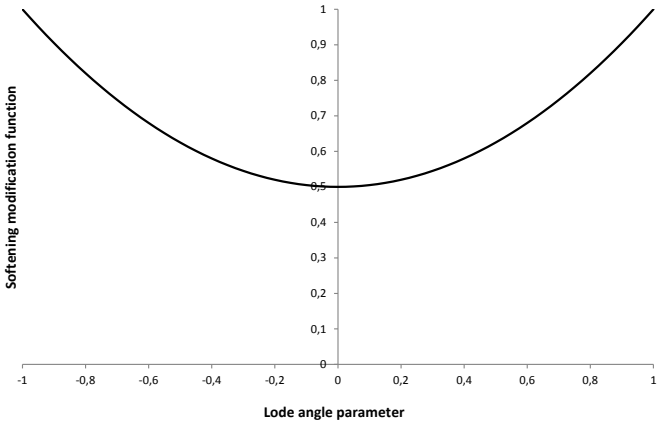

Figure 4.16: How softening modification function, $g(\overline{\theta})$, evolves.

as it increases, the softening slope rises. Consequently, application of softening modification function results in decreasing the softening slope in plane strain compression state. For stress states which have the lode angle parameter equal to unity, $\overline{\theta} = 1$, such as tensile tests on smooth round bars, the function does not influence the softening prediction of the model. It will be shown in section (4.5) that the introduction of the function (4.12) will considerably improve the prediction ability of the model in the softening regime.

4.3.2.2 Hardening

The hardening regime of the deformation, characterized by the increasing stress after the post-yield stress drop, was not precisely predicted under both plane strain compression and tensile test on the dumbbell shape specimen. Similarly to strain softening, strain hardening strongly depends on the stress state. The strain hardening response of the material increases at higher rate under plane strain compression compared to axisymmetric compression. Aruuda and Boyce (1993) justified the difference in strain hardening by different chain orientations in different stress states. They mentioned that chains are uniaxially oriented in plane strain compression; in contrast, under uniaxial compression chains have planar

orientation. Since under axisymmetric compression, chains have additional paths for deformation, larger strains are allowed under lower stresses, whereas under plane strain compression, stress increases at higher speed due to the same paths of the chain deformations. Substituting relation (4.6) in relation (3.42) gives:

$$\boldsymbol{\tau}^{hardening} = a\bar{\varepsilon}^{p} H_{ini}\ \boldsymbol{\varepsilon}_{d}. \tag{4.14}$$

In order to take into account the effect of different stress states on the hardening behaviour of the material, the hardening function is extended with relation (4.15):

$$l(\overline{\theta}) = \frac{1}{4}\Big(\overline{\theta} + 5\Big). \tag{4.15}$$

Using relations (4.14) and (4.15) results in relation (4.16) for hardening stress:

$$\boldsymbol{\tau}^{hardening} = a\bar{\varepsilon}^{p} l(\overline{\theta}) H_{ini}\ \boldsymbol{\varepsilon}_{d}. \tag{4.16}$$

The evolution of the hardening modification function, $l(\theta)$, is depicted in Figure (4.17). For cylinder upsetting, $\overline{\theta} = -1$, the functions takes the value of unity

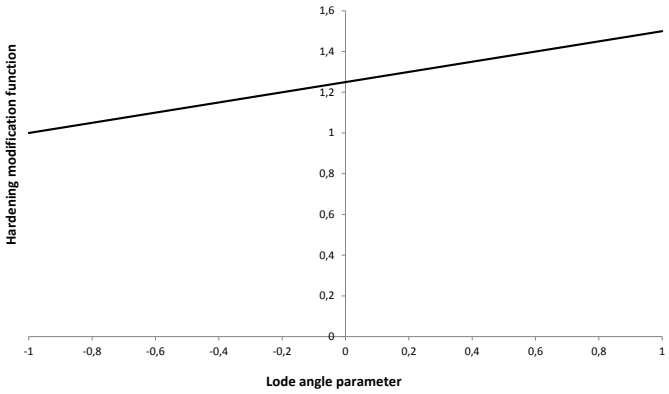

Figure 4.17: How hardening modification function, $l(\overline{\theta})$, evolves.

and since it is multiplied by the previous hardening function, it has no effect on the hardening prediction of the model. The function increases as the lode angle parameter increases. For plastic plane strain compression, $\overline{\theta} = 0$, the hardening

modification function is $l(\overline{\theta}) = 1.25$. It helps to compensate the difference between the hardening slope predicted by the model and the experimental results explained in Figure (4.13).

4.4 Integration algorithm

Since this model, is a modified version of the model presented in Chapter 3, the same approach for deriving the integration algorithm and finite element implementation of the model is followed. In other words, the system of evolutionary equations is reduced to a single scalar equation similar to relation (3.70) in Chapter 3.

4.4.1 State update

In this chapter, the finite strain extension and some details of the implementation are not included and the reader is directed to Chapter 3 for more details. The system of equations to be solved iteratively at the state update level is reduced to the following single scalar equation.

$$R(\eta_{n+1}) = \eta_{n+1} - M_1(\eta_{n+1})\frac{M_2(\eta_{n+1})}{M_3(\eta_{n+1})} = 0, \tag{4.17}$$

where,

$$M_1(\eta_{n+1}) = A_0 \exp\left[\frac{\Delta H}{R\,T} + \frac{\mu P_{n+1}}{\tau_0} - D_\infty + D_\infty \exp\left(M_5(\eta_{n+1})\right)\right], \tag{4.18}$$

$$M_2(\eta_{n+1}) = \frac{\eta_{n+1}}{\eta_{n+1} + \Delta t G}\sqrt{\frac{1}{2}}\,||\mathbf{s}_{n+1}^{trial}||, \tag{4.19}$$

$$M_3(\eta_{n+1}) = \sinh(\frac{M_2}{\tau_0}). \tag{4.20}$$

Where, $M_5\left(\eta_{n+1}\right)$ is given by:

$$M_5\left(\eta_{n+1}\right) = -\frac{hg\left(\overline{\theta}_{n+1}\right)\sqrt{3}M_6\left(\eta_{n+1}\right)}{\sqrt{2}\eta_{n+1}}, \tag{4.21}$$

where,

$$M_6\left(\eta_{n+1}\right) = \overline{\varepsilon}_n^p + \frac{\Delta t}{3(\eta_{n+1} + \Delta t G)} \sqrt{\frac{3}{2}} ||\mathbf{s}_{n+1}^{trial}||. \tag{4.22}$$

Where Δt is the time interval between two consecutive time steps. We will use the well-known Newton-Raphson iterative procedure to solve the residual equation (4.17). To do so, we need to compute the derivative of the residual, $R(\eta_{n+1})$, in order to the viscosity, η_{n+1}. Performing the derivations together with some algebraic manipulations leads to:

$$\frac{dR(\eta_{n+1})}{d\eta_{n+1}} = 1 - \left[N_1(\eta_{n+1}) \left(\frac{M_2(\eta_{n+1})}{M_3(\eta_{n+1})} \right) + \right.$$

$$\left. M_1 \left(\frac{M_3(\eta_{n+1}) N_2(\eta_{n+1}) - N_2(\eta_{n+1}) N_3(\eta_{n+1})}{\left(M_3(\eta_{n+1})\right)^2} \right) \right] \tag{4.23}$$

where,

$$N_1\left(\eta_{n+1}\right) = \frac{dM_1}{d\eta_{n+1}} = M_1 D_\infty \exp\left(M_5\right) N_5 \tag{4.24}$$

$$N_2(\eta_{n+1}) = \frac{dM_2}{d\eta_{n+1}} = \sqrt{\frac{1}{2}} \left[\frac{\Delta t G ||\mathbf{s}_{n+1}^{trial}||}{\left(\eta_{n+1} + \Delta t G\right)^2} \right], \tag{4.25}$$

$$N_3(\eta_{n+1}) = \frac{dM_3}{d\eta_{n+1}} = \sqrt{\frac{1}{2}} \left[\frac{\Delta t G ||\mathbf{s}_{n+1}^{trial}||}{\tau_0 \left(\eta_{n+1} + \Delta t G\right)^2} \right] \left(\cosh \frac{M_2}{\tau_0} \right). \tag{4.26}$$

where, N_5 is given by:

$$N_5(\eta_{n+1}) = \frac{dM_5}{d\eta_{n+1}} = \frac{-h\sqrt{3}}{2\sqrt{2} D_\infty} \left(\overline{\theta}_{n+1}^2 + 1 \right) N_6\left(\eta_{n+1}\right) \tag{4.27}$$

where,

$$N_6(\eta_{n+1}) = \frac{dM_6}{d\eta_{n+1}} = -\frac{\Delta t \sqrt{\frac{3}{2}} ||\mathbf{s}_{n+1}^{trial}||}{3\left(\eta_{n+1} + \Delta t G\right)^2}. \tag{4.28}$$

Having computed the aforementioned factors, we can apply the Newton-Raphson method to solve the residual equation in an iterative fashion:

$$\eta_{n+1}^k = \eta_{n+1}^{k-1} - \frac{R(\eta_{n+1}^{k-1})}{\frac{dR}{d\eta_{n+1}}(\eta_{n+1}^{k-1})}, \tag{4.29}$$

where, the superscript (k) and $(k-1)$ stand for two consecutive Newton-Raphson iterations. Once the iterations on the viscosity functions, $R(\eta_{n+1})$, are converged, we can update all the other variables through relations (4.30)-(4.33).

$$\mathbf{s}_{n+1} = \frac{\eta_{n+1}}{\eta_{n+1} + \Delta t G} \mathbf{s}^{trial}_{n+1} \tag{4.30}$$

$$\boldsymbol{\varepsilon}^{e}_{d\ n+1} = \frac{\eta_{n+1}}{\eta_{n+1} + \Delta t G} \frac{\mathbf{s}^{trial}_{n+1}}{2G} \tag{4.31}$$

$$\boldsymbol{\varepsilon}^{p}_{d\ n+1} = \boldsymbol{\varepsilon}^{p}_{d\ n} + \frac{\Delta t}{2(\eta_{n+1} + \Delta t G)} \mathbf{s}^{trial}_{n+1} \tag{4.32}$$

$$\bar{\varepsilon}^{p}_{n+1} = \bar{\varepsilon}^{p}_{n} + \frac{\Delta t}{3(\eta_{n+1} + \Delta t\ G)} \sqrt{\frac{3}{2}}\ ||\mathbf{s}^{trial}_{n+1}||. \tag{4.33}$$

4.4.2 Tangent operator

Similarly to the model presented in Chapter 3, in order to fully implement the model within an implicit quasi-static finite element code, it is required to obtain the tangent operator consistent with the state update algorithm. In the spatial tangent module, relation (3.85), the material related term, D, is the tangent operator consistent with the state update algorithm.

Following the procedure explained in Appendix B, relations (B.1) to (B.12), the tangent operator consistent with the state update, is obtained as follows.

$$\mathsf{D}^{p} = K\left(\mathbf{I}\otimes\mathbf{I}\right) + \left(F_1 + F_5\right)\mathsf{I}_d + F_2\left(\mathbf{s}_{n+1}\otimes\mathbf{I}\right) + F_3\left(\mathbf{s}_{n+1}\otimes\mathbf{z}_{n+1}\right) + F_4\left(\mathbf{s}_{n+1}\otimes\mathbf{s}_{n+1}\right) +$$

$$F_6\left(\boldsymbol{\varepsilon}^{tot}_{d\ n+1}\otimes\mathbf{z}_{n+1}\right) + F_7\left(\boldsymbol{\varepsilon}^{tot}_{d\ n+1}\otimes\mathbf{s}_{n+1}\right) + F_8\left(\boldsymbol{\varepsilon}^{tot}_{d\ n+1}\otimes\mathbf{I}\right) \tag{4.34}$$

Where, K is the bulk modulus of the material, I_d is the deviatoric fourth order identity tensor.

$$\mathsf{I}_d = \left[\mathsf{I}_s - \frac{1}{3}\left(\mathbf{I}\otimes\mathbf{I}\right)\right], \tag{4.35}$$

where, I_s and $\mathbf{I}$ are the symmetric fourth order identity and second order identity tensors, repectively. The tensor $\mathbf{z}_{n+1}$ is given by:

$$\mathbf{z}_{n+1} = \frac{\partial \det(\boldsymbol{\varepsilon}^{e\ trial}_{n+1})}{\boldsymbol{\varepsilon}_{n+1}}. \tag{4.36}$$

The components of tensor $\mathbf{z}_{n+1}$ in 2D and 3D spaces are given in Appendix C.

4.5 Evaluating the modified model

In order to observe how the applied modifications, introduced in the section 4.3.2, affect the predictions of the model, the simulations in section 4.2.2 are performed again using the model with the lode angle modifications.
In Figure (4.18), uniaxial compression simulations with the original model and the modified model, under strain rates $\dot{\varepsilon} = -0.0001(1/s)$, $\dot{\varepsilon} = -0.0005(1/s)$ and $\dot{\varepsilon} = -0.001(1/s)$, together with the experimental results are provided. Since the predictions of the model were good under axisymmetric compression condition, as previously seen in Figure (4.3), the same agreement under this stress state using the modified model was expected. Figure (4.18) proves that this expectation is satisfied and the close agreement between experiments and simulations is retained using the enhanced model.
Figure (4.19) depicts the plane strain compression results, obtained from the original model and the improved one, under strain rates $\dot{\varepsilon} = -0.0001(1/s)$, $\dot{\varepsilon} = -0.0005(1/s)$ and $\dot{\varepsilon} = -0.001(1/s)$ with experimental results.
Plane strain compression results improved noticeably by the applied lode angle changes to the constitutive relations. The softening slope, plateau-like behaviour and the final hardening response of the material are better captured.
The 3D tensile test on the dumbbell shape specimen is performed again in order to check if lode angle inclusion in the model could also improve the prediction of the model in this stress state. Figure (4.20) shows the force-displacement curve using original and improved models together with experimental results. Figure (4.20) simply shows that overestimation of the softening regime under tensile stress state is not seen anymore and the underestimation of the hardening behaviour is relatively improved.
The shear stress state on the butterfly specimen is numerically performed using the modified model as well. The force-displacement curve of the shear stress state on the butterfly specimen, with the same loading condition as mentioned before, is depicted in Figure (4.21). As mentioned before, in Section 4.2.2.4, in pure shear stress state on the butterfly specimen, no load drop is observed after the elastic regime of the deformation and thus, no difference was expected between the simulations of the original model and the modified model. This could be seen

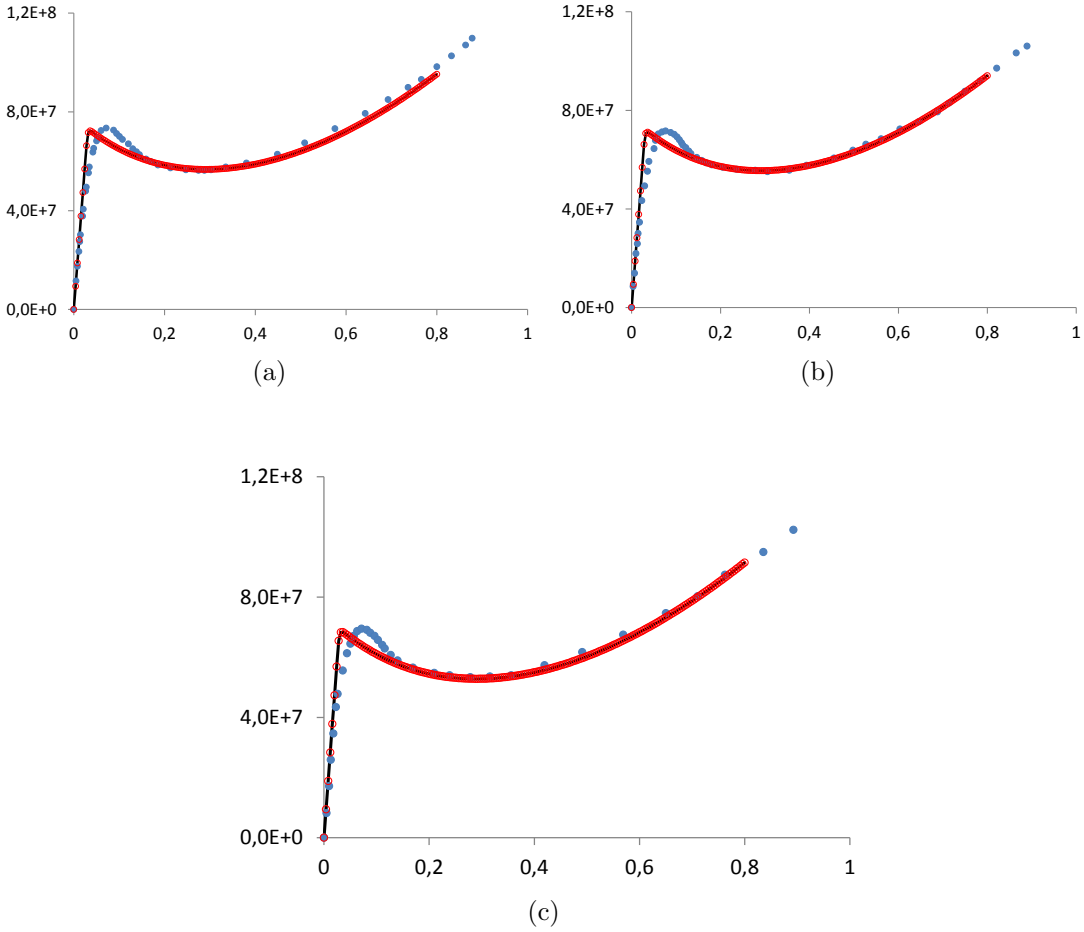

Figure 4.18: True stress-true strain for the uniaxial compression test on PC at room temperature, black solid line: simulations with original model; filled blue circles: experiment; unfilled red circles: simulations with modified model; horizontal axis: true compressive strain; vertical axis: True compressive stress (Pa); (a): $\dot{\varepsilon} = -0.001(1/s)$; (b): $\dot{\varepsilon} = -0.0005(1/s)$; (c): $\dot{\varepsilon} = -0.0001(1/s)$.

in Figure (4.21).

Figure (4.22) shows the normalized force versus normalized displacement for the butterfly specimen under combined shear-tension stress state using the original model and the modified one. In Section 4.2.2.4, it was mentioned that in the combined shear-tensile loading, presented in this chapter, the tensile resistance to the deformation is dominant compared to the shear resistance. This could also

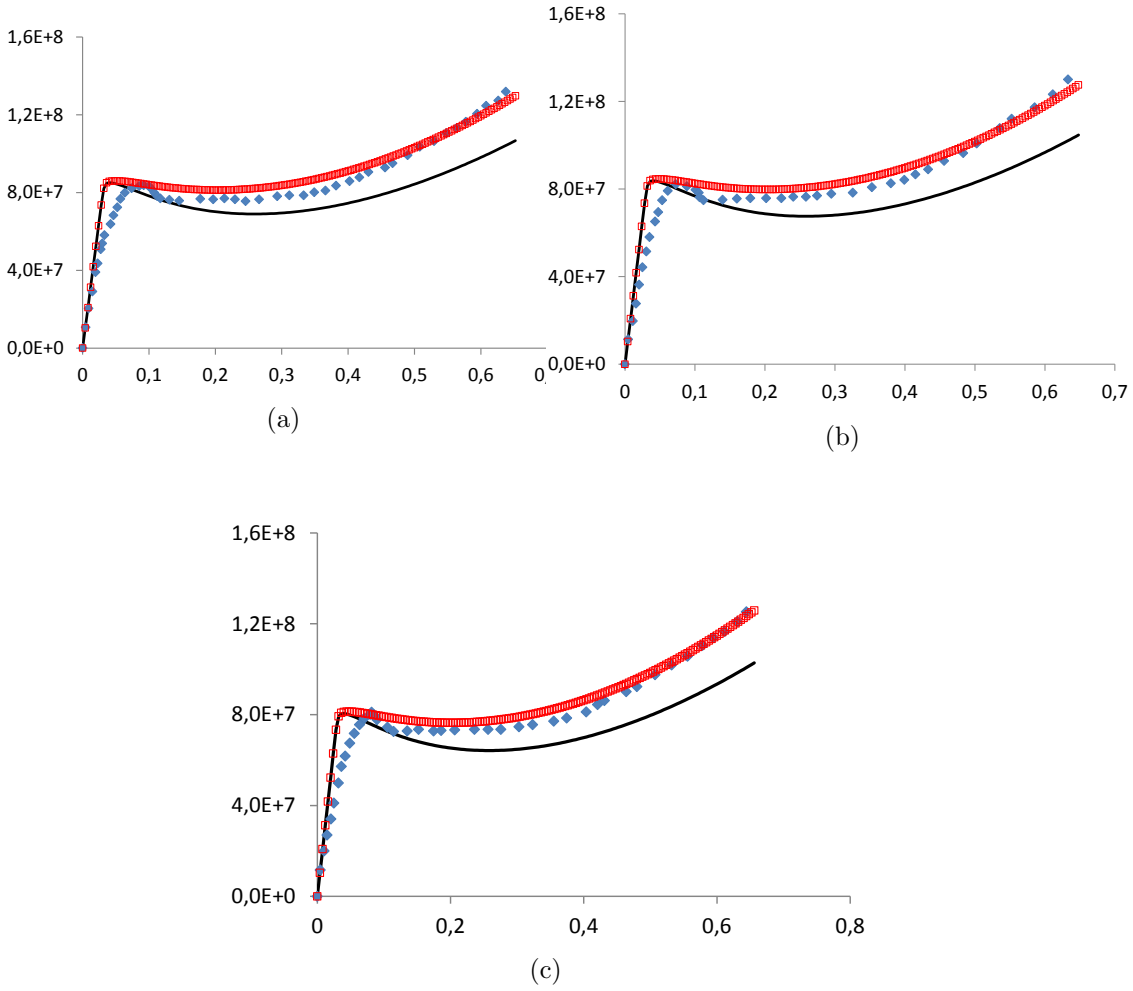

Figure 4.19: True stress-true strain for the plane strain compression test on PC at room temperature, black solid line: simulations with original model; filled blue squares: experiment; unfilled red squares: simulations with modified model; horizontal axis: true compressive strain; vertical axis: True compressive stress (Pa); (a): $\dot{\varepsilon} = -0.001(1/s)$; (b): $\dot{\varepsilon} = -0.0005(1/s)$; (c): $\dot{\varepsilon} = -0.0001(1/s)$.

be observed in Figure (4.22), where, the softening prediction with the modified model is reduced compared to predictions of the original model which is similar to the tensile test of the dumbbell shape specimen as shown in Figure (4.20).

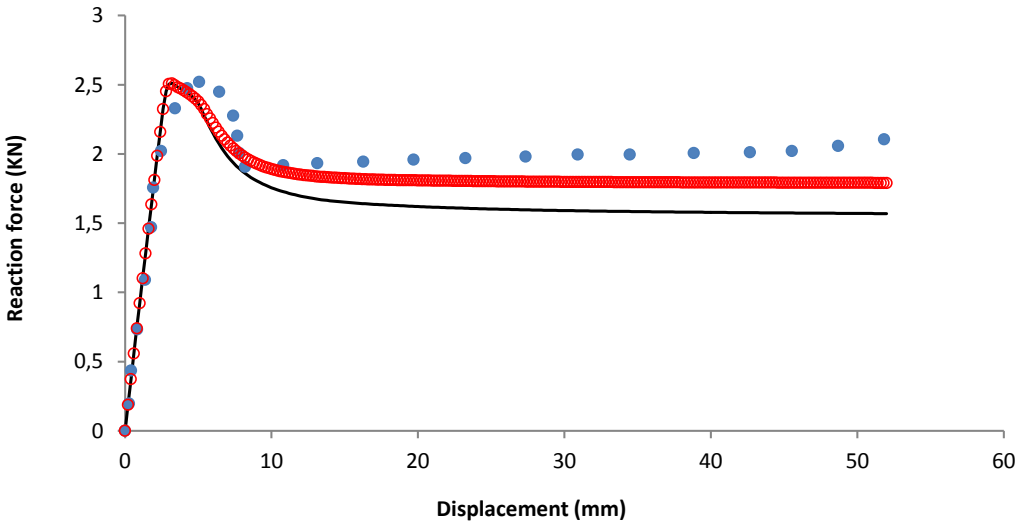

Figure 4.20: Force-displacement curve of tensile test on dumbbell shape specimen, black solid line: simulations with original model; filled blue squares: experiment; unfilled red squares: simulations with modified model.

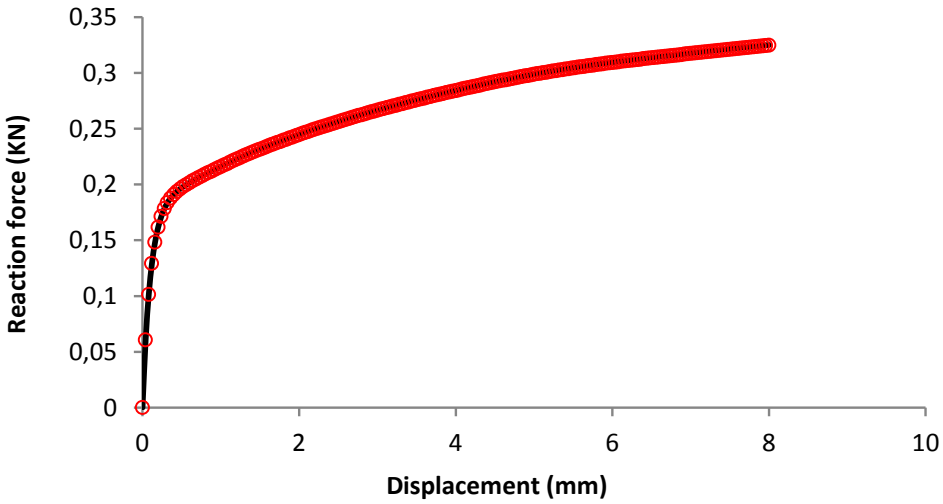

Figure 4.21: Force-displacement curve of shear loading on butterfly specimen, black solid line: simulations with original model; unfilled red squares: simulations with modified model.

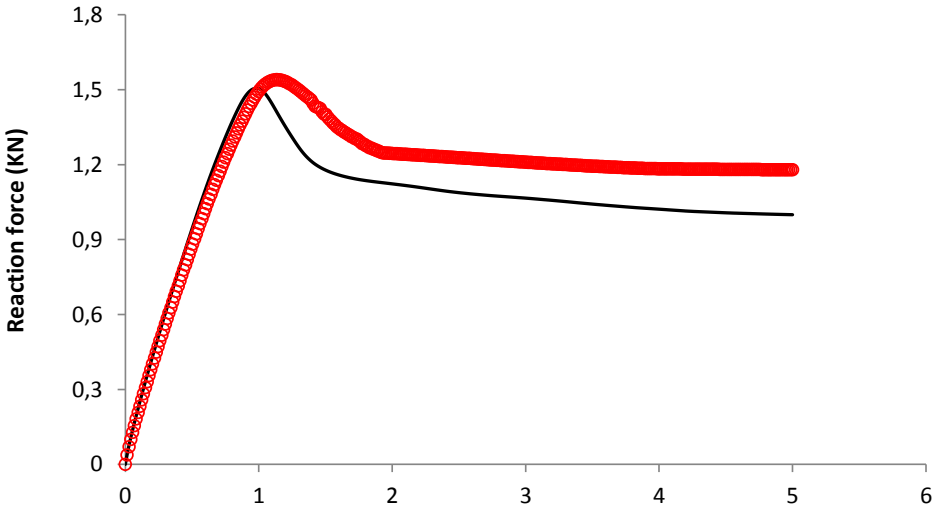

Figure 4.22: The normalized force-normalized displacement curve for butterfly specimen under combined shear-tension stress state using the original and modified models, black solid line: simulations with original model; unfilled red squares: simulations with modified model.

4.6 Conclusions

In this chapter, an elasto-viscoplastic model, introduced in Chapter 3, was improved to characterize the behavior of polymeric materials under different loading conditions. Despite the fact that the model could be utilized for different polymeric materials, more specifically thermoplastics, Makrolon 2607, which is a commercial grade of Polycarbonate, is the driving parameter of the study. First, the hardening module which was, in the initial model, a constant factor through the whole deformation was changed to a factor dependent on the accumulated plastic strain meaning the hardening factor was not constant anymore and it became dependent on deformation via relation (4.6). After parameter identification of the model for the specific material, using uniaxial compression tests, it was realized that in order to have better prediction for plane strain compression and 3D tensile test on a dumbbell shape specimen, there should be either other sets of material properties or improved constitutive model. Lode angle parameter was used to enhance the constitutive relations in order to have the improved results for plane strain compression and tensile test on the dumbbell shape specimen.

An effort was made to improve the model such that the predictions for uniaxial compression remain as they were with the initial model and the other two aforementioned stress states would be better captured.

Chapter 5

Micro-structural analysis

In this chapter, Rubber Toughened Polystyrene (RT-PS) is numerically analysed at the micro level. Different micro-structural samples with different percentages of rubbery particles inside the micro-structure are studied. Periodic boundary condition is applied on the boundaries of the samples. The Finite Element Method (FEM) is used in combination with mathematical homogenization to obtain the macro stress. After performing some numerical examples and getting the conclusion of the necessity of determination of the size for the Representative Volume Element (RVE), a statistical analysis of the numerical experiments is proposed in order to determine the size for heterogeneous amorphous polymers subjected to finite deformation. Two criteria are proposed to be used for the RVE size determination. RT-PS with two different levels of Inclusion Volume Fraction (IVF) of rubbery particles, namely 10% and 15% are considered. The proposed criteria are checked for the mentioned material and the Size of the Representative Volume Element (RVES) is obtained.

5.1 Introduction

In order to work within the framework of coupled multi-scale model, it is required to have the Representative Volume Element (RVE) of the heterogeneous material defined. In the published literature, there are different definitions for the RVE [Hill (1963), Drugan and Willis (1996), Hashin (1983), van Mier (1996),

Evesque (2000), Freudenthal (1950), Ostoja-Starzewski (2002)]. What is common in the variety of definitions is that the RVE should accommodate enough information about the microstructure while its dimensions are smaller than the macroscopic dimensions so that the concept of separation of scales is satisfied.
In this chapter, a statistical-numerical approach is proposed to determine the size of RVE for heterogeneous amorphous polymers subjected to finite strain deformation. Polystyrene (PS) is used as the matrix material toughened with rubbery particles. Two different volume fraction of inclusions are considered. The model presented in chapter 3, is used for the matrix material and the material properties for PS introduced in Chapter 3 are used for the numerical simulations. The rubbery particles are modelled as voids.
The chapter will be presented as follows. In Section 5.2, the Kinematical description of the micro-scale problem is provided. Section 5.3 presents some numerical examples at the micro-structural level with different percentage of inclusion volume fraction of rubbery particles. Section 5.4 details the proposed statistical-numerical approach for determination of the RVES and presents some more numerical examples. Finally, Section 5.5 is devoted to some conclusions and concluding remarks.

5.2 Kinematical description of the micro-scale problem

In this Section, the main assumptions and mathematical formulation governing this study will be introduced. If $\mathbf{x}$ is an infinitesimal point at the macro-scale and $\mathbf{y}$ is an infinitesimal point on the RVE domain and $\mathbf{T}(\mathbf{y})$ is a generic field defined over the RVE domain, the homogenized response of the mentioned generic field, $\mathbf{T}$, for the macroscopic point to which the RVE is linked, is obtained by the following volume average relation:

$$\mathbf{T}(\mathbf{x}) = \frac{1}{V_\mu} \int_{\Omega_\mu} \mathbf{T}(\mathbf{y}) dV \tag{5.1}$$

It must be emphasized that the above relation can be applied to both undeformed and deformed configurations of the RVE. In this study, all the homogenized vari-

ables are defined as the volume average of the respective quantities over the initial configuration of the RVE. The first Piola-Kircchof stress is defined as follows:

$$\mathbf{P}(\mathbf{y},t) = \boldsymbol{\beta}(\mathbf{F}(\mathbf{y},t)), \tag{5.2}$$

where, $\boldsymbol{\beta}$ is a tensor valued functional and $\mathbf{F}(\mathbf{y},t)$ is the deformation gradient at the fine scale defined by:

$$\mathbf{F}_p(\mathbf{y},t) = \mathbf{I} + \bigtriangledown_p \mathbf{u}(\mathbf{y},t), \tag{5.3}$$

where, $\mathbf{I}$ is the second order identity tensor and $\bigtriangledown_p(*)$ is the material gradient operator. The deformation of the RVE is driven by the macroscopic deformation gradient, which is the volume average of the microscopic deformation gradient:

$$\mathbf{F}(\mathbf{x}) = \frac{1}{V_\mu}\int_{\Omega_\mu} \mathbf{F}(\mathbf{y})dV, \tag{5.4}$$

or equally,

$$\mathbf{F}(\mathbf{x}) = \mathbf{I} + \frac{1}{V_\mu}\int_{\Omega_\mu} \bigtriangledown_p \mathbf{u}(\mathbf{y},t)dV. \tag{5.5}$$

The displacement field can be split to two terms as follows:

$$\mathbf{u}(\mathbf{y},t) = [\mathbf{F}(\mathbf{x},t) - \mathbf{I}]\mathbf{Y} + \widetilde{\mathbf{u}}(\mathbf{y},t), \tag{5.6}$$

where the first term is the linear displacement varying linearly with $\mathbf{Y}$, which represents the RVE coordinates in the reference configuration, and the second term denoted by $\widetilde{\mathbf{u}}(\mathbf{y},t)$ is the displacement fluctuation field. So, the microscopic deformation gradient, $\mathbf{F}(\mathbf{y},t)$, can be written as:

$$\mathbf{F}(\mathbf{y},t) = \mathbf{F}(\mathbf{x},t) + \bigtriangledown_p \widetilde{\mathbf{u}}(\mathbf{y},t). \tag{5.7}$$

Doing some algebraic manipulations, using divergence theorem and relations (5.4) and (5.7), result in the following relation:

$$\int_{\partial\Omega_\mu} \widetilde{\mathbf{u}}(y,t) \otimes \mathbf{N}(\mathbf{Y})dA = 0, \tag{5.8}$$

where, $\mathbf{N}(\mathbf{Y})$ denotes the outward unit vector to the undeformed boundary of the RVE. From the above relation, the minimally constrained vector set of kinematically admissible fluctuation displacement of the RVE, is obtained as:

$$\widetilde{K}_\mu \equiv \left[\mathbf{u}, sufficiently \;\; regular | \int_{\partial\Omega_\mu} \widetilde{\mathbf{u}}(y,t) \otimes \mathbf{N}(\mathbf{Y})dA = 0\right]. \tag{5.9}$$

The first Piola-Kirchhof stress of the infinitesimal point at the macro-scale is, as previously mentioned, the volume average of corresponding stress at the micro-scale:

$$\mathbf{P}(\mathbf{x},t) = \frac{1}{V_\mu}\int_{\Omega_\mu^s} \mathbf{P}(\mathbf{y},t)dV. \tag{5.10}$$

The relation between the Cauchy stress and the first Piola-Kircchof stress is the following:

$$\boldsymbol{\sigma} = \frac{1}{\det(\mathbf{F})}\mathbf{P}[\mathbf{F}]^T. \tag{5.11}$$

Consequently, at the macro-scale, the Cauchy stress is derived based on the following relation:

$$\boldsymbol{\sigma}(\mathbf{x},t) = \frac{1}{\det(\mathbf{F}(\mathbf{x},t))}\mathbf{P}(\mathbf{x},t)[\mathbf{F}(\mathbf{x},t)]^T. \tag{5.12}$$

In order to relate the micro-scale and macro-scale, the Hill-Mandel principle is used. This principle is expressed as follows:

$$\mathbf{P}(\mathbf{x},t) : \dot{\mathbf{F}}(\mathbf{x},t) = \frac{1}{V_\mu}\int_{\Omega_\mu} \mathbf{P}(\mathbf{y},t) : \dot{\mathbf{F}}(\mathbf{y},t)dV. \tag{5.13}$$

The above relation must be verified for all the admissible microscopic deformation gradient rate fields, $\dot{\mathbf{F}}(y,t)$,

$$\dot{\mathbf{F}}(y,t) = \bigtriangledown\dot{\mathbf{u}}(y,t) = \dot{\mathbf{F}}(\mathbf{x},t) + \bigtriangledown\ \tilde{\dot{\mathbf{u}}}(y,t), \tag{5.14}$$

and also microscopic stress field, $\mathbf{P}(y,t)$, in equilibrium. Performing some mathematical manipulations and simplifications results in:

$$\int_{\partial\Omega_\mu} \mathbf{T}_{ref}(\mathbf{y},t)\cdot\tilde{\dot{\mathbf{u}}}(\mathbf{y},t)dA = 0, \tag{5.15}$$

$$\int_{\Omega_\mu^s} \mathbf{B}_{ref}(\mathbf{y},t)\cdot\tilde{\dot{\mathbf{u}}}(\mathbf{y},t)dV = 0. \tag{5.16}$$

The basic concepts of the variational framework for the large strain models are summarized in the following box:

- Homogenized deformation gradient

$$\mathbf{F}(\mathbf{x},t) = \mathbf{I} + \frac{1}{V_\mu}\int_{\partial\Omega_\mu} \mathbf{u}(\mathbf{y},t) \otimes \mathbf{N}(\mathbf{Y}) dA$$

- Homogenized first Piola-Kircchof stress tensor

$$\mathbf{P} = \frac{1}{V_\mu}\left[\int_{\partial\Omega_\mu} \mathbf{T}_{ref}(\mathbf{y},t) \otimes \mathbf{Y} dA - \int_{\Omega_\mu^s} \mathbf{B}_{ref}(\mathbf{y},t) \otimes Y dV\right]$$

- Split decomposition of the microscopic deformation gradient

$$\mathbf{F}(\mathbf{y},t) = \mathbf{F}(\mathbf{x},t) + \bigtriangledown_p \widetilde{\mathbf{u}}(\mathbf{y},t)$$

- Hill-Mandel principle

$$\int_{\partial\Omega_\mu} \mathbf{T}_{ref}(\mathbf{y},t) \cdot \eta \; dA = 0 \quad \forall \eta \in \nu_\mu$$

$$\int_{\Omega_\mu^s} \mathbf{B}_{ref}(\mathbf{y},t) \cdot \eta \; dV = 0 \quad \forall \eta \in \nu_\mu$$

Considering the Hill-Mandel principle, the terms associated with tractions and also body forces vanish from the variational equation governing the equilibrium at the micro-scale. Hence, the problem at the micro-scale can be defined as:
For a given macroscopic deformation gradient, $\mathbf{F}(\mathbf{x},t)$*, and assuming the history of the internal variables known at macroscopic point x, find a kinematically admissible microscopic displacement field,* $\widetilde{\mathbf{u}}(\mathbf{y},t)$*, such that:*

$$\int_{\Omega_\mu} \mathbf{P}(\mathbf{y},t) : \nabla\eta dV - \int_{\partial\Omega_\mu^v} \mathbf{T}_{ref}(\mathbf{y},t) \cdot \eta dA = 0. \tag{5.17}$$

Four different boundary conditions, which can be applied to RVE under study, are well established in the literature: Taylor assumption; Linear boundary condition; Periodic boundary condition and uniform traction on the boundary. Since in this study, the periodic boundary conditions would be applied to the RVEs under study, this boundary condition is presented in what follows.

5.2.1 Periodic boundary condition

The periodic boundary condition is one of the most used boundary conditions within the scientific community. This boundary condition is particularly suitable for the analysis of the mechanical behavior of materials with periodic or even quasi-periodic microstructure. This boundary condition imposes the following condition: the frontier defining the limits of the RVE can always be devided into d equal groups:

$$\partial V_\mu = (\Gamma_i^- \cup \Gamma_i^+). \tag{5.18}$$

It should be emphasized that each point $y^+ \in \Gamma_i^+$ has it counterpart point $y^- \in \Gamma_i^-$. Furthermore, the following condition must be satisfied:

$$n^+ = -n^-, \tag{5.19}$$

where, n^+ and n^- are the unit normal vectors of Γ_i^+ and Γ_i^- at points y^+ and y^-, respectively. Due to the fact that the boundary is composed of d equal groups, we have:

$$\int_{\partial\Omega_\mu} \widetilde{\mathbf{u}}(\mathbf{y},t) \otimes \mathbf{N}(\mathbf{Y}) dA = \sum_{i=1}^{d} \int_{\partial\Omega_{\mu,i}} \widetilde{\mathbf{u}}_i(\mathbf{y},t) \otimes \mathbf{N}_i(\mathbf{y}) dA_i$$

$$= \sum_{i=1}^{d} \left[\int_{\Gamma_i^+} \widetilde{\mathbf{u}}_i(\mathbf{y}^+,t) \otimes \mathbf{N}_i^+(\mathbf{y}^+) d\Gamma^+ + \int_{\Gamma_i^-} \widetilde{\mathbf{u}}_i(\mathbf{y}^-,t) \otimes \mathbf{N}_i^-(\mathbf{y}^-) d\Gamma^- \right]$$

$$= 0 \tag{5.20}$$

The above relation is satisfied, if and only if, the fluctuation displacement vectors over Γ^+ and Γ^- are equal:

$$\widetilde{\mathbf{u}}(\mathbf{y}^+,t) = \widetilde{\mathbf{u}}(\mathbf{y}^-,t) \tag{5.21}$$

5.2.2 Spatial discretization of the Microscopic problem

The main goal of this section is to introduce a strategy, composed by several algorithmic steps, for solving the microscopic boundary value problem. The equation

governing the equilibrium of the micro-structure in discretized form, assuming that the voids are completely empty, is given by:

$$\left[\int_{\Omega_\mu^d} (\mathbf{G}^g)^T \mathbf{P}(\mathbf{y},t)dV\right]^T \boldsymbol{\eta} = 0 \quad \forall \boldsymbol{\eta} \in \nu_\mu \tag{5.22}$$

As the virtual displacement field, η, is not zero and in order to satisfy the equilibrium of the RVE, we can conclude:

$$\int_{\Omega_\mu^d} (\mathbf{G}^g)^T \mathbf{P}(\mathbf{y},t)dV = 0 \quad \forall \boldsymbol{\eta} \in \nu_\mu \tag{5.23}$$

The FEM is complete by solving the aforementioned equation. The Newton-Raphson method is used to solve the equation and in order to use the method, the linearization of the microscopic discretized variational equilibrium equation would be required. Following well established FEM concepts, we can write:

$$[\mathbf{f}_{int}(\mathbf{y},t) + \mathbf{K}(\mathbf{y},t)\widetilde{\mathbf{u}}(\mathbf{y},t)] \cdot \boldsymbol{\eta} = 0 \quad \forall \boldsymbol{\eta} \in \nu_\mu, \tag{5.24}$$

where, $\mathbf{f}_{int}(\mathbf{y},t)$ is the internal force vector defined as:

$$\mathbf{f}_{int}(\mathbf{y},t) = \mathbf{ASSEMB}_{e=1}^{n_{elem}} \int_{\Omega_\mu^e} \mathbf{G}^T \mathbf{P}(\mathbf{y},t)dV, \tag{5.25}$$

and, $[\mathbf{K}(\mathbf{y},t)]$ is the global stiffness matrix for the RVE under study defined by:

$$[\mathbf{K}(\mathbf{y},t)] = \mathbf{ASSEMB}_{e=1}^{n_{elem}} \int_{\Omega_\mu^e} \mathbf{G}^T \mathrm{A} \mathbf{G} \mathrm{dV}. \tag{5.26}$$

In the last equation, the fourth order tensor A is called material tangent modulus and is given by:

$$\mathrm{A} = \frac{\partial \mathbf{P}(\mathbf{y},\mathrm{t})}{\partial \mathbf{F}(\mathbf{y},\mathrm{t})} \tag{5.27}$$

It must be mentioned that relation (5.24) is the generic FEM relation without considering the effects of boundary conditions.
Relation (5.24) considering periodic boundary conditions is explained. Kinematically, the Periodic boundary condition is governed by the following space:

$$\widetilde{K}_\mu^{per} \equiv \{\boldsymbol{\eta}, sufficiently\ regular | \boldsymbol{\eta}(\mathbf{y}^+,t) = \boldsymbol{\eta}(\mathbf{y}^-,t) \ \ \forall pairs\{y^+,y^-\}\} \tag{5.28}$$

The above space of kinematically admissible displacement filed means that the adjacent sides of the RVE must have the same fluctuation, $\widetilde{\mathbf{u}}(\mathbf{y},t)$. The fluctuation displacement field can be expressed in the following form of sub-sets:

$$\widetilde{\mathbf{u}}(\mathbf{y},t)=\begin{Bmatrix}\widetilde{\mathbf{u}}^{i}\\ \widetilde{\mathbf{u}}^{+}\\ \widetilde{\mathbf{u}}^{-}\end{Bmatrix} \tag{5.29}$$

Based on the aforementioned decomposition, relation (5.24) can be written as follows:

$$\left\{\begin{Bmatrix}\mathbf{f}^{i}\\ \mathbf{f}^{+}\\ \mathbf{f}^{-}\end{Bmatrix}+\begin{bmatrix}\mathbf{k}^{ii} & \mathbf{k}^{i+} & \mathbf{k}^{i-}\\ \mathbf{k}^{+i} & \mathbf{k}^{++} & \mathbf{k}^{+-}\\ \mathbf{k}^{-i} & \mathbf{k}^{-+} & \mathbf{k}^{--}\end{bmatrix}\begin{Bmatrix}\delta\widetilde{\mathbf{u}}^{i}\\ \delta\widetilde{\mathbf{u}}^{+}\\ \delta\widetilde{\mathbf{u}}^{-}\end{Bmatrix}\right\}\cdot\begin{Bmatrix}\eta^{i}\\ \eta^{+}\\ \eta^{-}\end{Bmatrix}=0 \tag{5.30}$$

According to the admissible space of periodic boundary condition, the following relation must be satisfied:

$$\widetilde{\mathbf{u}}^{+}=\widetilde{\mathbf{u}}^{-}. \tag{5.31}$$

Consequently, relation (5.30) can be simplified as follows:

$$\left\{\begin{Bmatrix}\mathbf{f}^{i}\\ \mathbf{f}^{+}+\mathbf{f}^{-}\end{Bmatrix}+\begin{bmatrix}\mathbf{k}^{ii} & \mathbf{k}^{i+}+\mathbf{k}^{i-}\\ \mathbf{k}^{+i}+\mathbf{k}^{-i} & \mathbf{k}^{++}+\mathbf{k}^{-+}+\mathbf{k}^{+-}+\mathbf{k}^{--}\end{bmatrix}\begin{Bmatrix}\delta\widetilde{\mathbf{u}}^{i}\\ \delta\widetilde{\mathbf{u}}^{+}\end{Bmatrix}\right\}\cdot\begin{Bmatrix}\eta^{i}\\ \eta^{+}\end{Bmatrix}=0 \tag{5.32}$$

Finally, the FEM relation is given by:

$$\begin{bmatrix}\mathbf{k}^{ii} & \mathbf{k}^{i+}+\mathbf{k}^{i-}\\ \mathbf{k}^{+i}+\mathbf{k}^{-i} & \mathbf{k}^{++}+\mathbf{k}^{-+}+\mathbf{k}^{+-}+\mathbf{k}^{--}\end{bmatrix}\begin{Bmatrix}\delta\widetilde{\mathbf{u}}^{i}\\ \delta\widetilde{\mathbf{u}}^{+}\end{Bmatrix}=-\begin{Bmatrix}\mathbf{f}^{i}\\ \mathbf{f}^{+}+\mathbf{f}^{-}\end{Bmatrix} \tag{5.33}$$

Since the microscopic equilibrium is explained, computation of the homogenized first piola-Kirchhof stress is required:

$$\mathbf{P}(\mathbf{x},t)=\frac{1}{V_{\mu}}\int_{\partial\Omega_{\mu}}\mathbf{t}(\mathbf{y},t)\otimes\mathbf{Y}da \tag{5.34}$$

5.3 Numerical examples

In this section, some numerical examples are performed on samples with two levels of Inclusion Volume Fraction (IVF), namely 10% and 15%. The inclusions size range (ISR) is assumed to be from $1.4\mu m$ to $2\mu m$. The first sample size is

$20\mu m$. The numerical examples are performed under tensile condition with the following deformation gradient.

$$\mathbf{F} = \begin{bmatrix} 1.15 & 0 \\ 0 & 1 \end{bmatrix} \tag{5.35}$$

Figure (5.1) shows two samples with dimension of $20\mu m$ and volume fraction of inclusions equal to 10% and 15%. Both samples are examined under the ten-

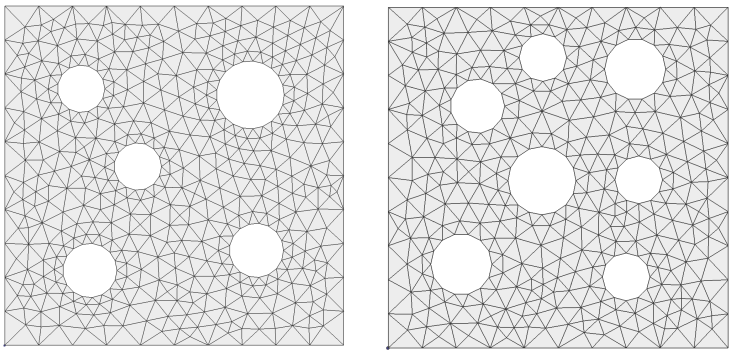

(a) (b)

Figure 5.1: Two different samples with size of $20\mu m$ and volume fraction of inclusions equal to (a): 10% and (b): 15%.

sile conditions applied by the deformation gradient presented in equation (5.35). Figure (5.2) shows the stress deformation for both samples subjected to tensile loading under periodic boundary condition. In order to check whether changing the morphology of the micro-structure significantly affects the overall deformation behaviour, one more sample of each IVF (Inclusion Volume Fraction) is generated. The samples are shown in Figure (5.3). Figure (5.4) depicts the stress-deformation graph for the samples shown in Figure (5.3). In order to appreciate the difference between different realizations of the same IVF, the stress-deformation graph for samples of the size of $20\mu m$ and IVF of 10%, shown in Figures (5.1a) and (5.3a), is shown in Figure (5.5). Similarly to Figure (5.5), the stress-deformation graph for samples of the size of $20\mu m$ and IVF of 15%, depicted in Figures (5.1b) and (5.3b), is presented in Figure (5.6). As can be seen in Figures (5.5) and (5.6), changing the morphology of the micro-structure, significantly affects the overall behaviour of the micro-structural samples. Therefore, in order to converge to a

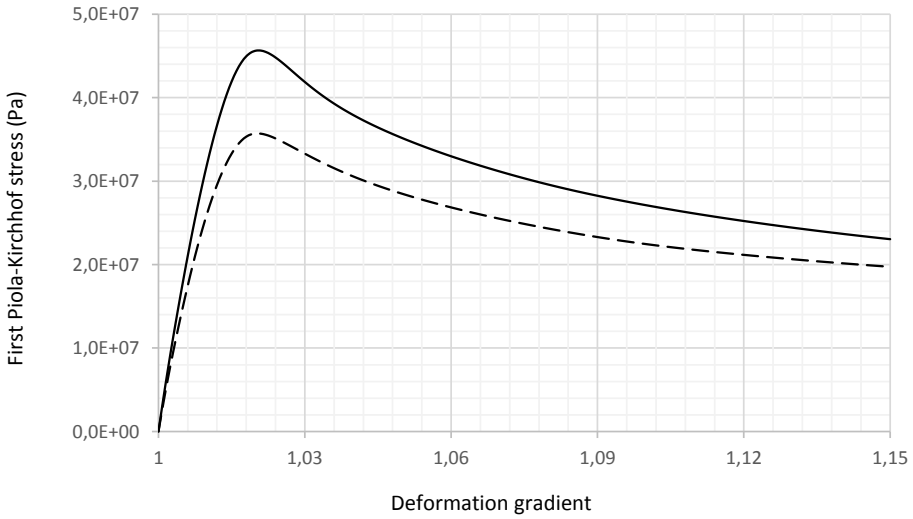

Figure 5.2: Stress-deformation of the samples shown in Figure (5.1), solid line: 10% and dashed line: 15%.

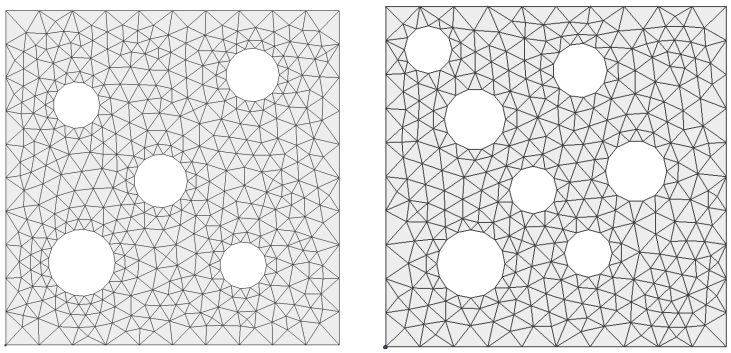

(a) (b)

Figure 5.3: Second morphologies of the samples with size of $20\mu m$ and volume fraction of inclusions equal to (a): 10% and (b): 15%.

solution and determine which size is enough for a specific micro-structure with different levels of IVF to be representative, a statistical analysis is performed in Section 5.4. Two criteria are proposed for determination of the size of RVE.

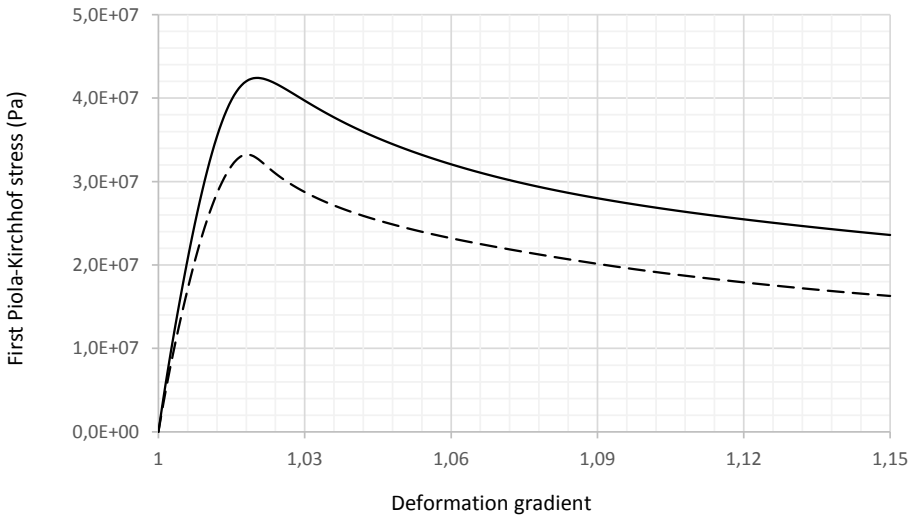

Figure 5.4: Stress-deformation of the samples shown in Figure (5.3), solid line: 10% and dashed line: 15%

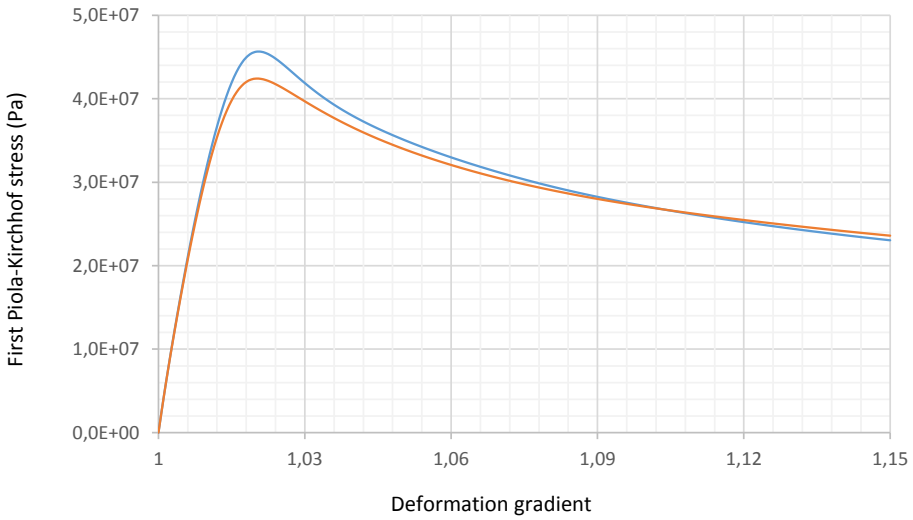

Figure 5.5: Stress-deformation of the samples shown in Figures (5.1a) and (5.3a), both with IVF equal to 10%.

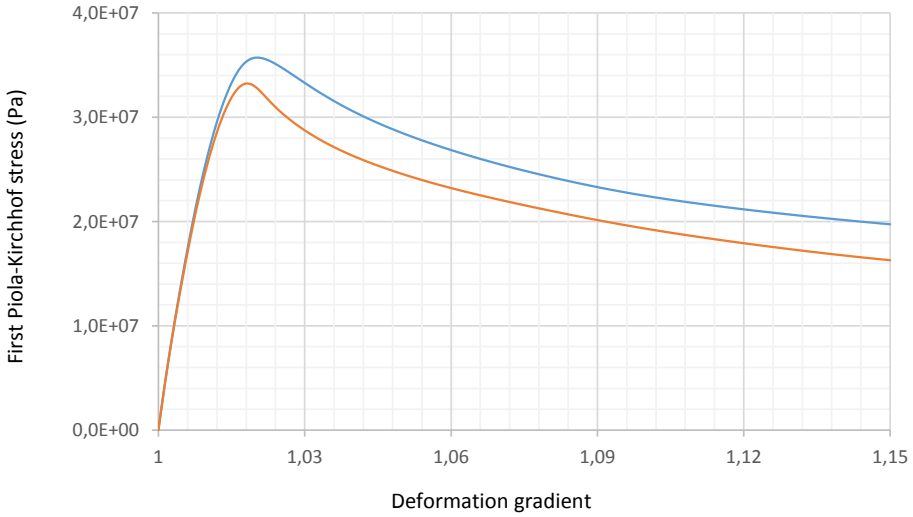

Figure 5.6: Stress-deformation of the samples shown in Figures (5.1b) and (5.3b), both with IVF equal to 15%.

5.4 RVE size

As mentioned before, working with a coupled multi-scale model requires the user to define the RVE. Hence, it is necessary to obtain the RVE size (RVES) such that the definition of the RVE is satisfied. During the last two decades, there have been different methods employed by the scientific community to determine the RVES mainly from image processing approach [Grimal et al. (2011), Shan and Gokhale (2002), Graham and Yang (2003)], experimental-image processing methods [Romero and Masad (2001)], analytical approaches [Drugan and Willis (1996), Sebsadji and Chouicha (2012)] and statistical-numerical methods [Kanit et al. (2003), Kanit et al. (2006) Pelissou et al. (2009), Skarzynski and Tejchman (2012), Gitman et al. (2007), Stroeven et al. (2004)].
Grimal et al. (2011) have derived the field of elastic coefficients from one acoustic microscopy image of a human femur cortical bone sample with an overall porosity of 8.5%. They have also used FEM to obtain the homogenized properties of the RVEs. Shan and Gokhale (2002) have introduced a methodology involving image analysis techniques for determination of the RVES for Ceramic Matrix Composites (CMC) with different fiber sizes. Graham and Yang (2003) determined the

RVES for HY-100 steel using image analysis of the polished cross section of the material. Romero and Masad (2001) have obtained the RVES for an asphalt concrete specimen utilizing an image analysis approach and they have verified their results with some mechanical tests. Drugan and Willis (1996) employed a variational formulation to derive a nonlocal constitutive equation for a class of random linear elastic composite materials. They have estimated the RVES by comparing the magnitude of the non-local term and the portion of the equation that relates ensemble average stresses and strains through a constant "overall" modulus tensor. Sebsadji and Chouicha (2012) have proposed an analytical approach, using fractal analysis, to obtain the RVES for concrete mixtures. Kanit et al. (2003) have performed a statistical analysis of the numerical examples in order to quantify the RVES for two-phase three-dimensional Voronoii mosaic in case of linear elasticity and thermal conductivity. Kanit et al. (2006) have extended the statistical-numerical approach introduced in the other work by Kanit et al. (2003) to the case of real microstructures of two materials from food industry for RVES determination. Pelissou et al. (2009) have started from the work by Kanit et al. (2003) and introduced a new approach for RVES determination for a metal matrix composite with randomly distributed aligned brittle inclusions. Skarzynski and Tejchman (2012) have used two different approaches, within a statistical analysis, to determine RVES for softening quasi brittle materials. The first approach, failure zone averaging approach, was previously introduced by Nguyen et al. (2010). Gitman et al. (2007) investigated RVE existence in different stages of loading, elastic-hardening-softening, and also proposed a method to determine the RVES for random three-phase (matrix, inclusion and ITZ) heterogeneous materials. Stroeven et al. (2004) have used different criteria, (peak load, dissipated energy, strain concentration factor) within a statistical-numerical framework to determine RVES for materials with particles in a matrix material.

In this section, the main contribution of this chapter, which is the statistical procedure of the numerical examples to determine the RVES, is presented. The samples are analyzed using FEM and the constitutive model described in Chapter 3. The quadratic (6-noded) triangular element with 3 Gauss integration points is used for the spatial discretization of samples. Periodic boundary condition, explained in Cection 5.2.1, is applied to the boundaries of the analyzed samples.

Rubber Toughened Polystyrene (RT-PS) is considered for the numerical examples. Two different volume fraction of inclusions are considered namely 10% and 15%. The initial Volume Element Size (VES) is assumed to be $20\mu m$ and the Inclusion Size Range (ISR) is from $1.4\mu m$ to $2\mu m$. The material properties of the matrix material are provided in Table (3.1) of chapter 3.
The process for RVES determination is done as follows. First, different distribution of one VES and IVF are generated. Then, the samples are loaded numerically and the stress-deformation graphs are extracted. Two criteria are introduced in order to determine the RVES:

1. The standard deviation of the deformation behavior should not be more than a predefined percentage of average deformation behavior.

2. The average behavior of all the realisations of the same VES is within a desirable predefined error with the average response of the next VES.

The next stage is to check the first criterion to see whether it is satisfied. If the first criterion is satisfied, different distributions of the next VES with the same IVF are to be generated and analyzed and the second criterion is checked. In case the second criterion is satisfied as well, the previous VES is RVES. If the first criterion is not satisfied, the next VES would be considered as the initial VES and the same process, as mentioned above, would be done. This procedure is represented in the Figure (5.7). Numerical examples are performed on different micro-structural samples in order to determine the RVES for two different IVFs. For IVF equal to 10% the VES starts from $20\mu m$ and goes to $40\mu m$. For each VES, five different realizations are generated.

5.4.1 RT-PS with 10% of rubbery particles

Five different morphologies for IVF equal to 10% and VES equal to $20\mu m$ are shown in Figure (5.8). Figure (5.9) shows stress-deformation curves for different realizations of samples with IVF equal to 10% and VES equal to $20\mu m$. In order to proceed with the determination of the RVES, it is required to check whether or not the first criterion is satisfied. Figure (5.10), shows the average response of the samples shown on Figure (5.8) together with upper and lower bounds

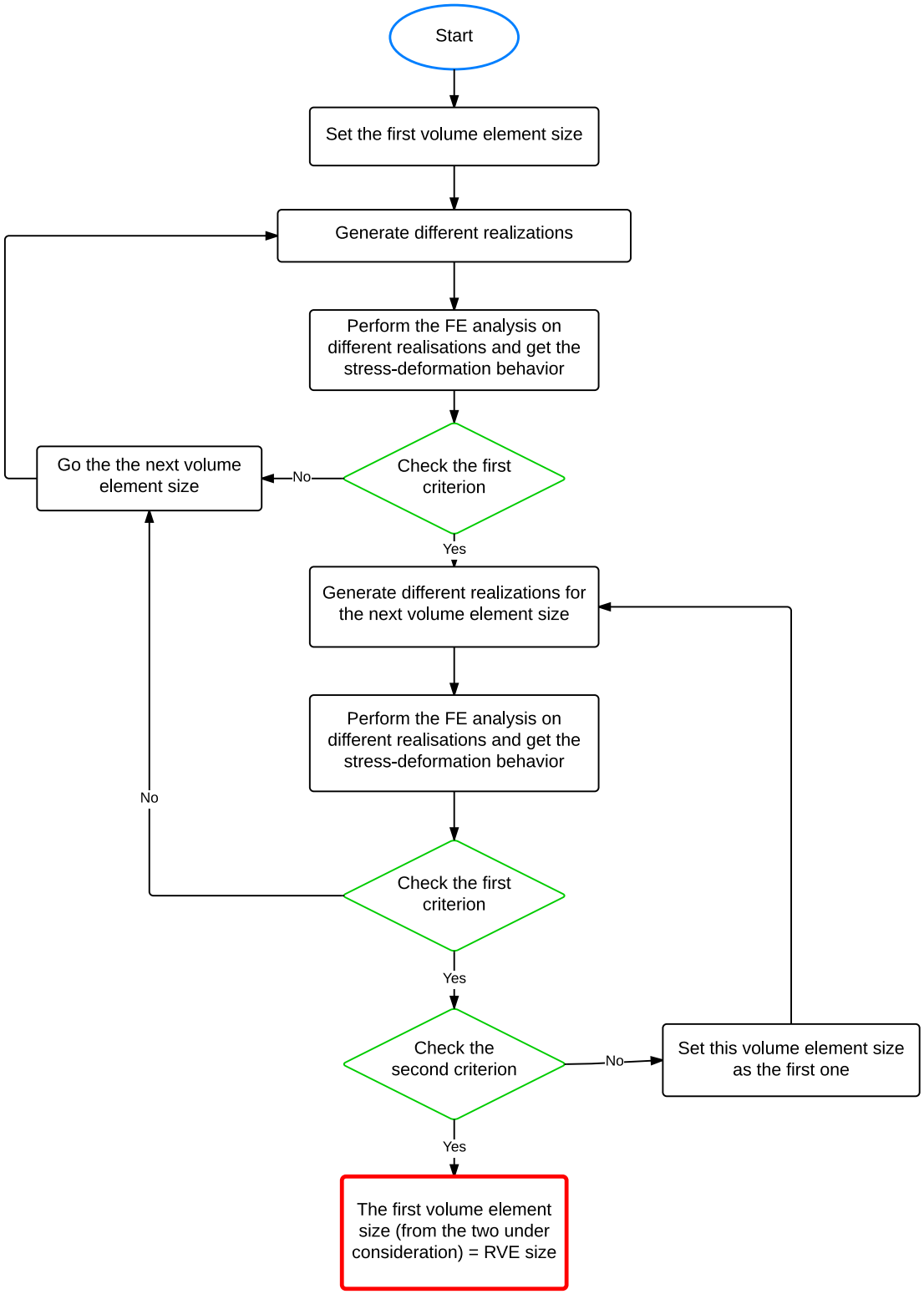

Figure 5.7: Flow chart for RVES determination.

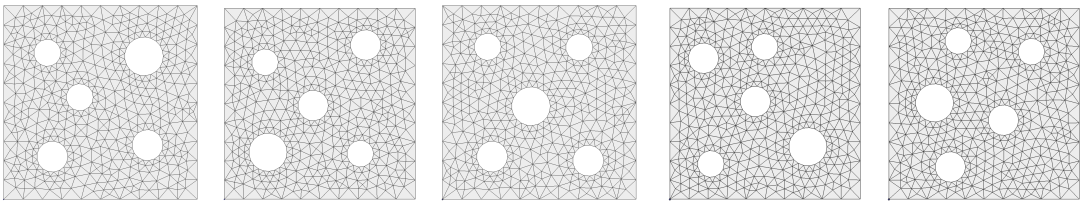

(a) (b) (c) (d) (e)

Figure 5.8: Different realizations for IVF equal to 10% and VES equal to 20μm.

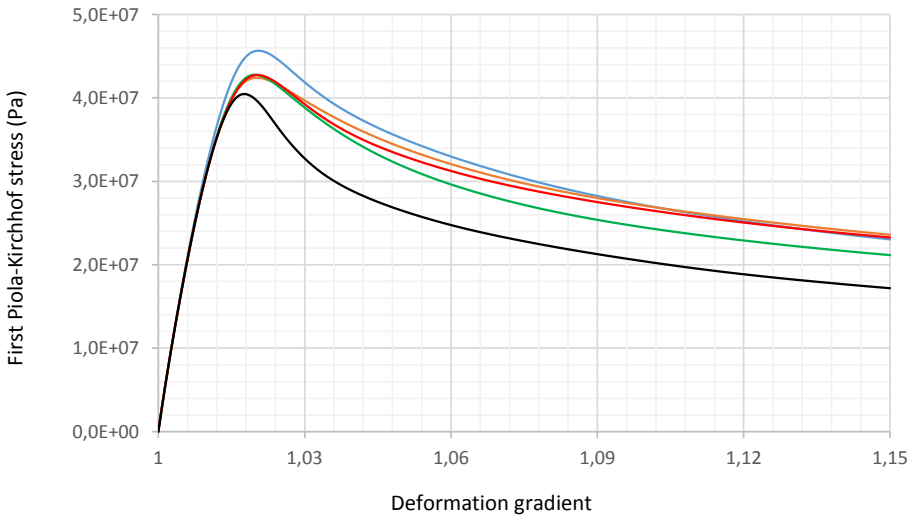

Figure 5.9: Stress-deformation of the samples shown in Figure (5.8).

of standard deviation. In this study, the allowed percentage of average for the standard deviation is considered as 5%. In other words, if the standard deviation of the deformation behaviour, through the whole deformation, is less than 5% of the average deformation behaviour, the first criterion is satisfied. For the first series of samples, IVF equal to 10% and VES equal to 20μm, the first criterion is not satisfied [see Figure (5.10)]. It means that for the whole deformation process, the standard deviation is not less than 5% of the average deformation behaviour. So according to the proposed algorithm, shown in Figure (5.7), the next step is to generate samples with the same IVF and a bigger size.

Five different morphologies for IVF equal to 10% and VES equal to 30μm are shown in Figure (5.11). Stress-deformation curves for different realizations of

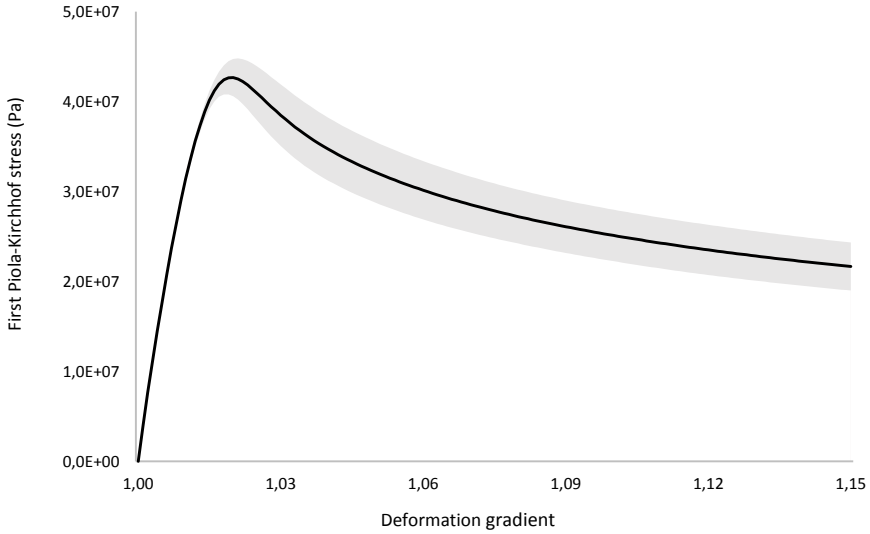

Figure 5.10: Average stress-deformation of the samples shown in Figure (5.8) with shaded bounds of standard deviation.

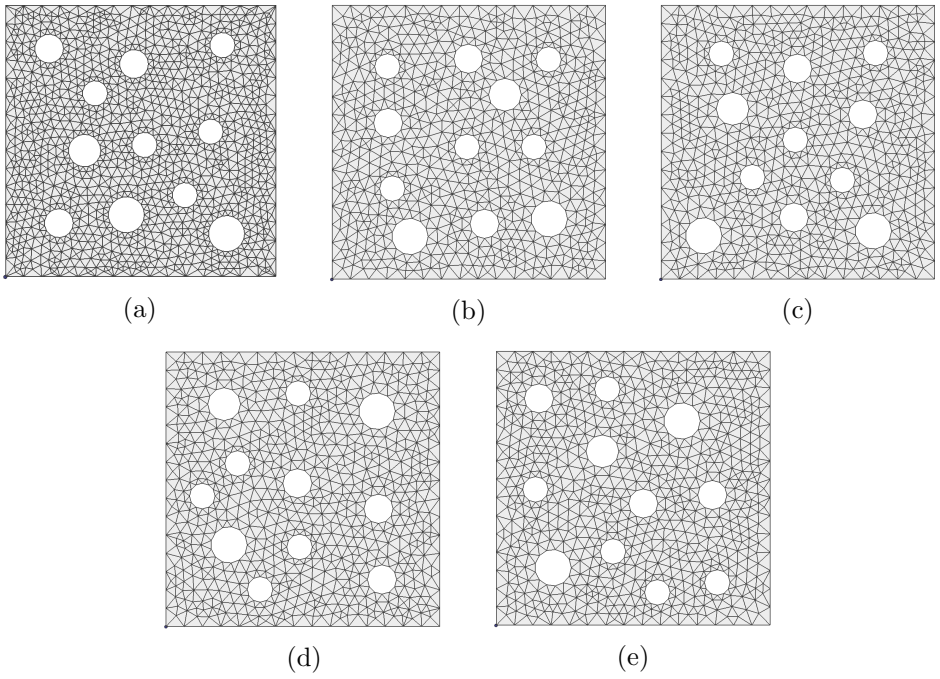

Figure 5.11: Different realizations for IVF equal to 10% and VES equal to $30\mu m$.

samples with IVF equal to 10% and VES equal to $30\mu m$ are given in Figure (5.12). Figure (5.13) shows the average response of the samples depicted in Figure (5.11)

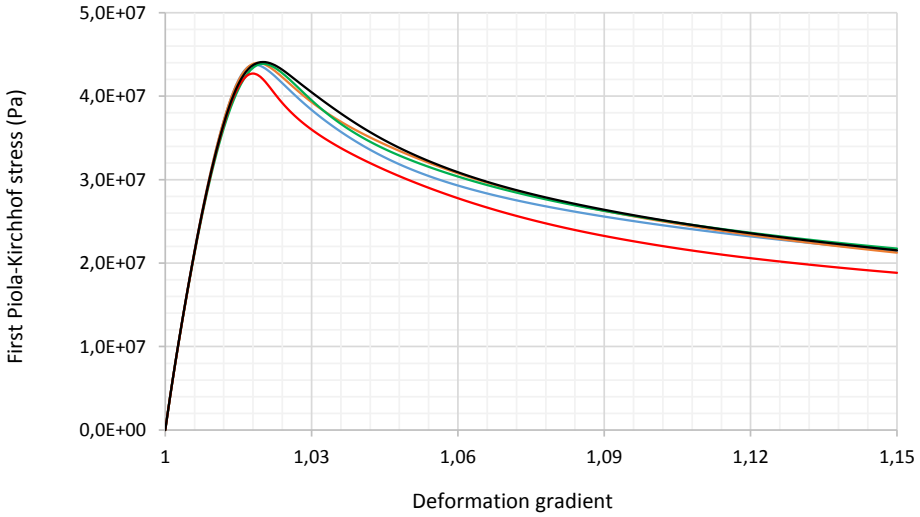

Figure 5.12: Stress-deformation of the samples shown in Figure (5.11).

with the upper and lower bounds of standard deviation. As expected, making a

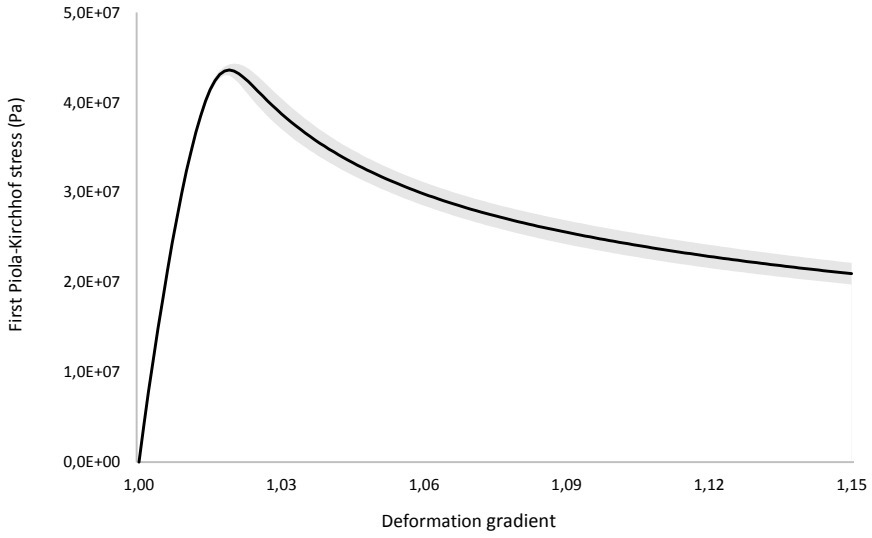

Figure 5.13: Average stress-deformation of the samples shown in Figure (5.11) with shaded bounds of standard deviation.

comparison between Figures (5.9) and (5.12) and also between Figures (5.10) and (5.13) shows that by increasing the VES from $20\mu m$ to $30\mu m$, the deformation behaviour of different realizations are closer to each other.

Considering the average deformation stress-deformation behaviour of the samples with 10% of IVF and VES equal to $30\mu m$, shown in Figure (5.13), the first criterion is satisfied i.e. the values of the standard deviation during deformation is less than 5% of the average behaviour. The next stage is generating bigger samples in order to proceed with the determination of the RVES.
Five different realizations for IVF equal to 10% and VES equal to $40\mu m$ are shown in Figure (5.14). Figure (5.15) depicts the stress-deformation behavior

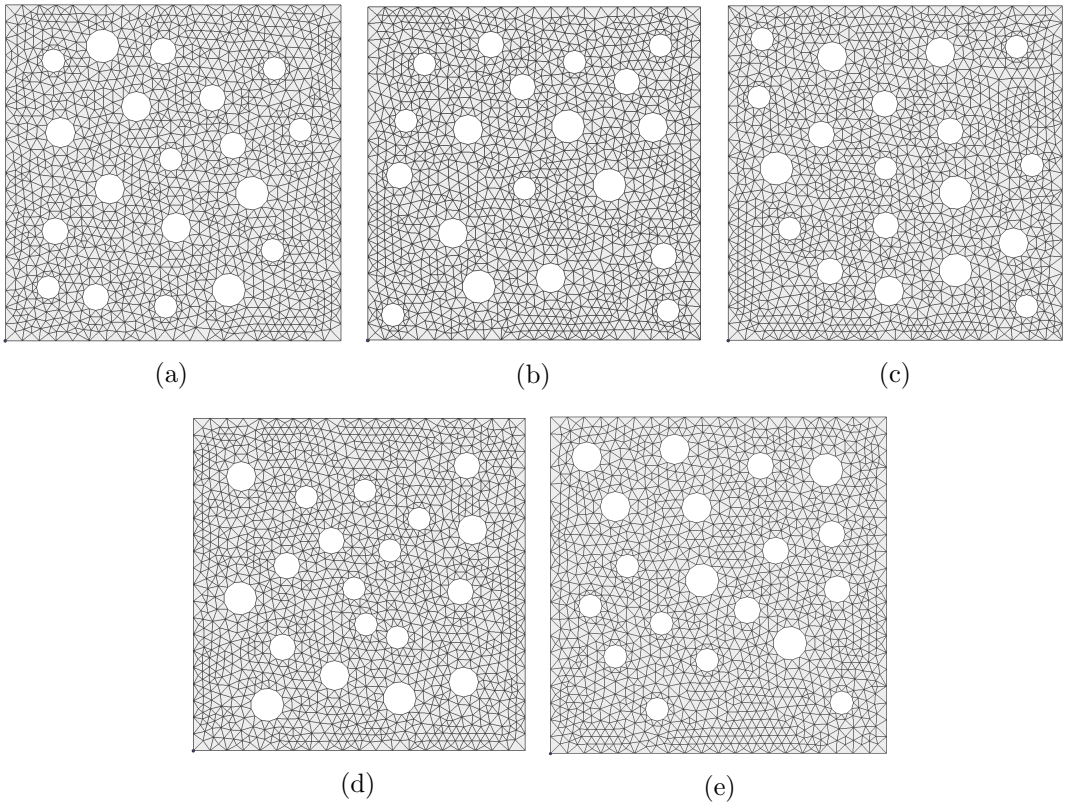

Figure 5.14: Different realizations for IVF equal to 10% and VES equal to $40\mu m$.

of samples shown in Figure (5.14). It is required to check if the first criterion is satisfied for the samples with IVF equal to 10% and VES equal to $40\mu m$. The average response of the samples shown in Figure (5.14) with the bounds of standard deviation are given in Figure (5.16). The values of standard deviation are within the bounds defined, 5% of the average. Hence, the second criterion should be checked. In this study, 10% difference between the average behaviour

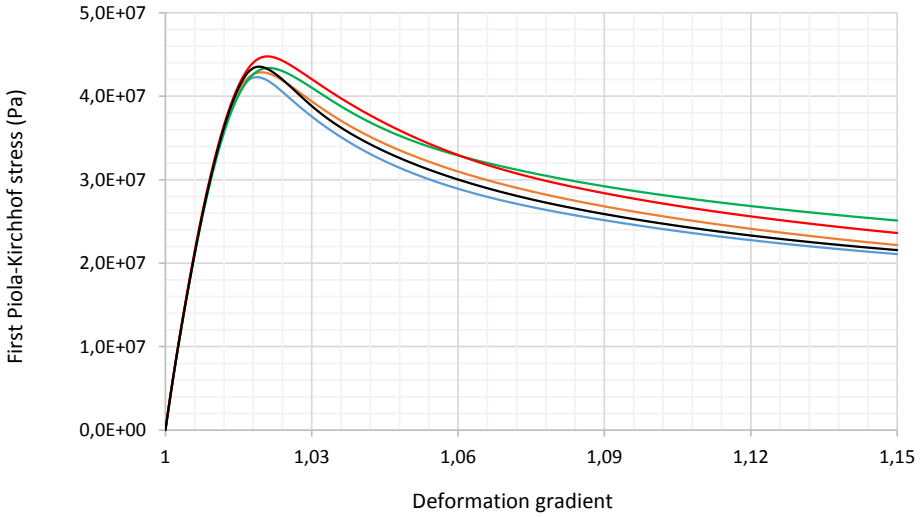

Figure 5.15: Stress-deformation of the samples shown in Figure (5.14).

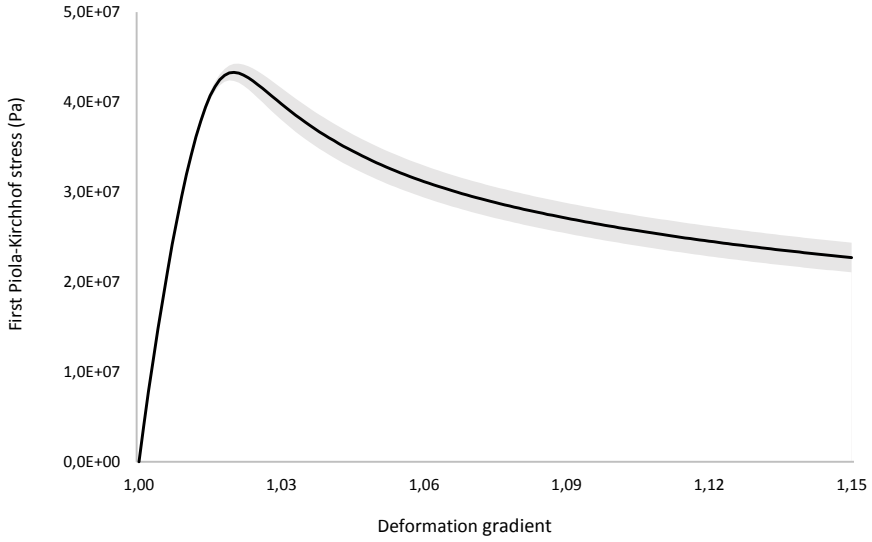

Figure 5.16: Average stress-deformation of the samples shown in Figure (5.14) with shaded bounds of standard deviation.

of two VES is allowed. In other words, if the average behaviour of samples with 10% of Inclusion Volume Fraction and $30\mu m$ of Volume Element Size, shown in Figure (5.11), are within 10% difference to the average behavior of samples with 10% of Inclusion Volume Fraction and $40\mu m$ of Volume Element Size, the second

criterion is satisfied too. Figure (5.17) shows the average responses of both series of samples. According to the values of the average deformation behaviours of the

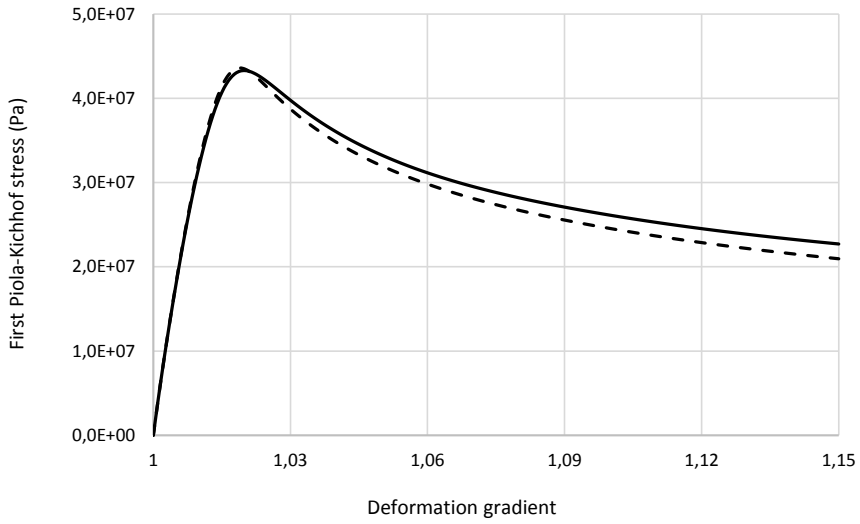

Figure 5.17: Average stress-deformation of the samples shown in Figures (5.11) and (5.14). Solid line: VES=40μm and dashed line: VES=30μm.

two series of samples and also the defined criteria and algorithm in this chapter, it can be concluded that for Rubber Toughened Polystyrene (RT-PS) with 10% of rubbery particles, the the size of the Representative Volume Element (RVES) could be considered as 30μm.

5.4.2 RT-PS with 15% of rubbery particles

The next volume fraction of rubbery particles to be considered is 15%. Figure (5.18) shows five different realizations for IVF equal to 15% and VES equal to 20μm. The stress-deformation curves for samples shown in Figure (5.18), are given in Figure (5.19). In order to check the first criterion, if the standard deviation is within the 5% of the average response, Figure (5.20) presents the average response of the samples given in Figure (5.18) together with the bounds of standard deviation of the samples responses. The criterion is checked and it is not satisfied. The next stage is to generate samples with the same IVF and a bigger size. Figure (5.21) shows five different morphologies for IVF equal to 15% and

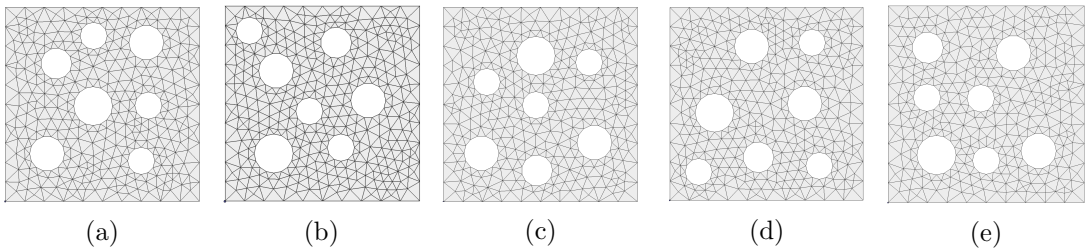

(a) (b) (c) (d) (e)

Figure 5.18: Different realizations for IVF equal to 15% and VES equal to 20μm.

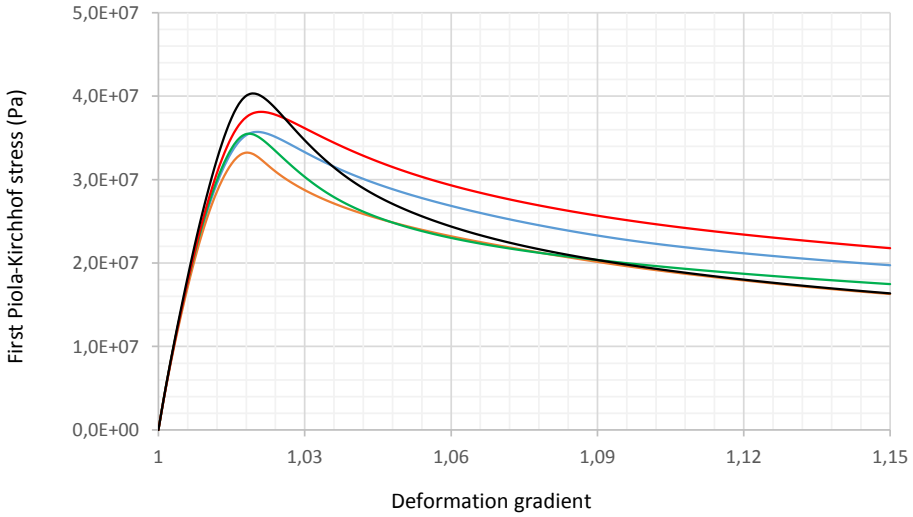

Figure 5.19: Stress-deformation of the samples shown in Figure (5.18).

VES equal to 30μm. Figure (5.22) depicts stress-deformation curves for different realizations of samples with IVF equal to 15% and VES equal to 30μm. The average response of the samples presented in Figure (5.21) with the bounds of standard deviation is given in Figure (5.23). The standard deviation of the behaviour of the samples is within the defined 5% of the average. Samples with VES equal to 40μm and IVF equal to 15% are to be generated in order to check the first and second criterion. Five different morphologies for IVF equal to 15% and VES equal to 40μm are shown in Figure (5.24).

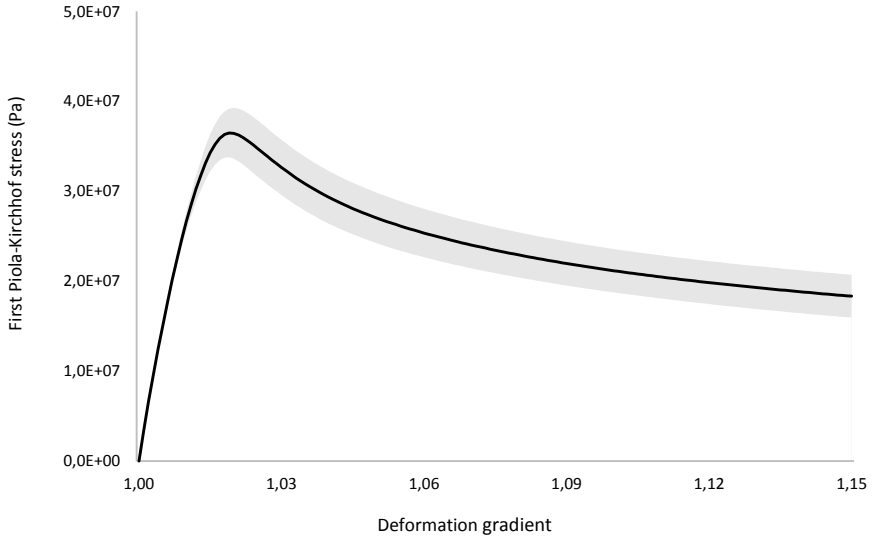

Figure 5.20: Average stress-deformation of the samples shown in Figure (5.18) with shaded bounds of standard deviation.

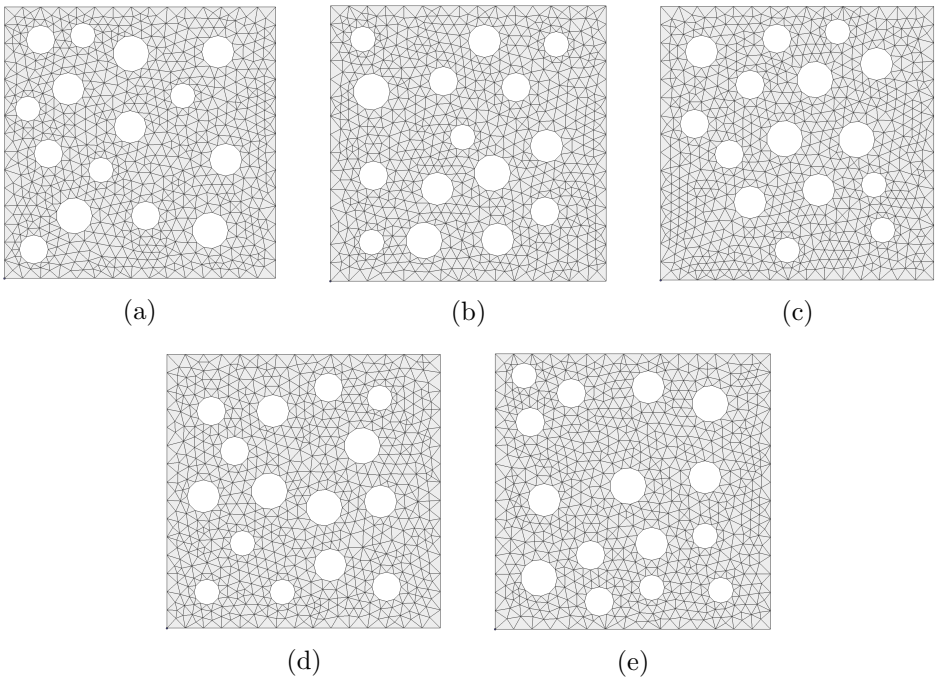

Figure 5.21: Different realizations for IVF equal to 15% and VES equal to $30\mu m$.

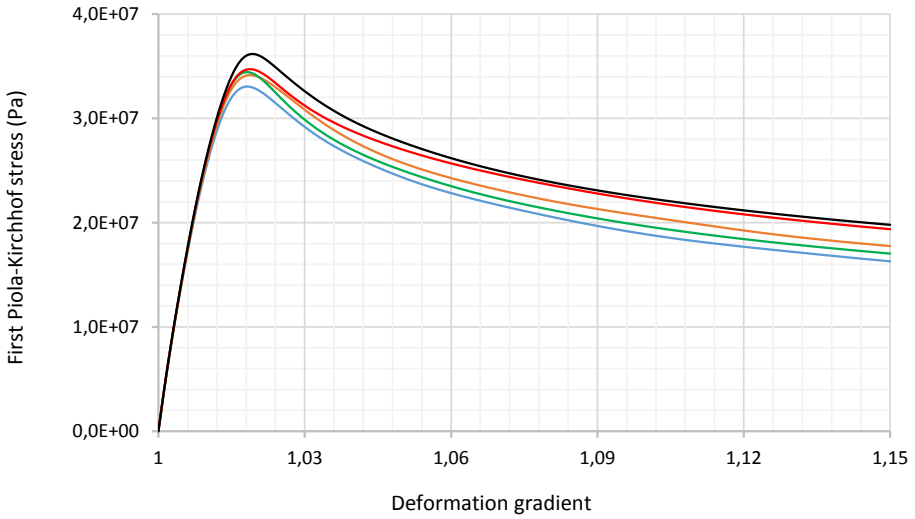

Figure 5.22: Stress-deformation of the samples shown in Figure (5.21).

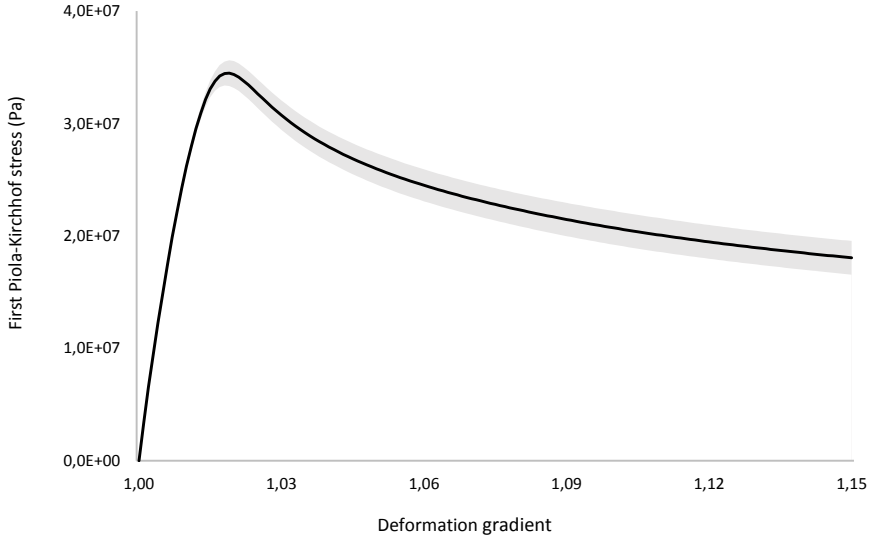

Figure 5.23: Average stress-deformation of the samples shown in Figure (5.21) with shaded bounds of standard deviation.

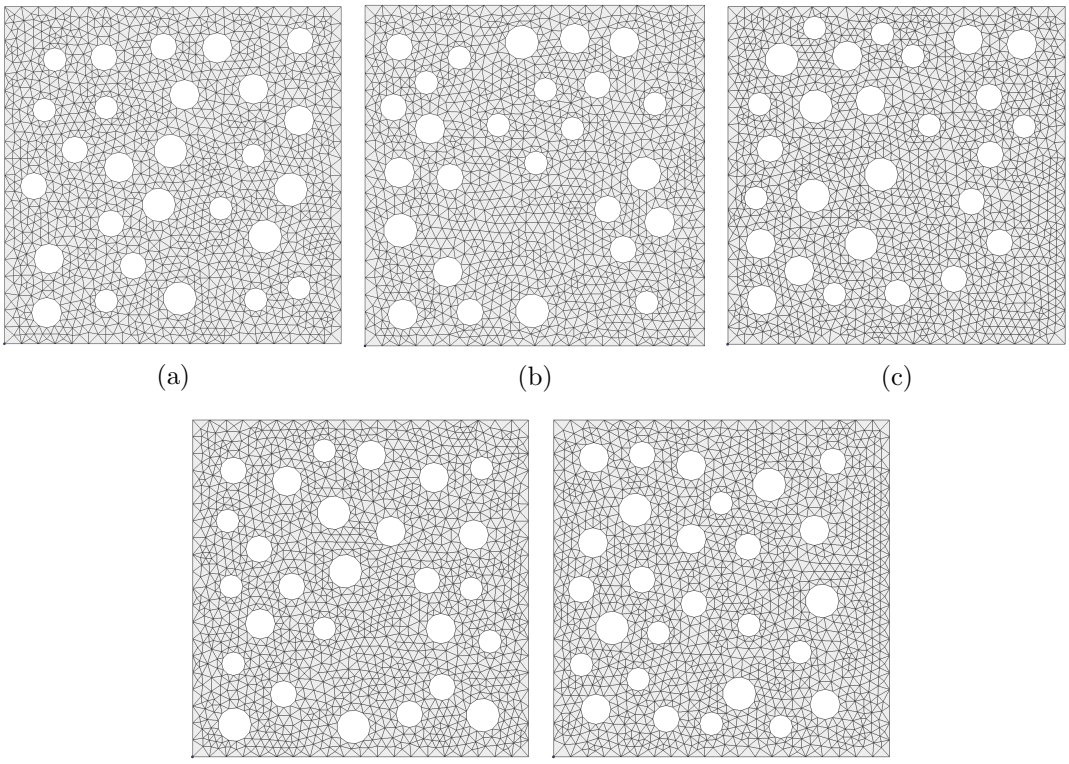

Figure 5.24: Different realizations for IVF equal to 15% and VES equal to $40\mu m$.

Figure (5.25) depicts stress-deformation curves for different realizations of samples with IVF equal to 15% and VES equal to $40\mu m$

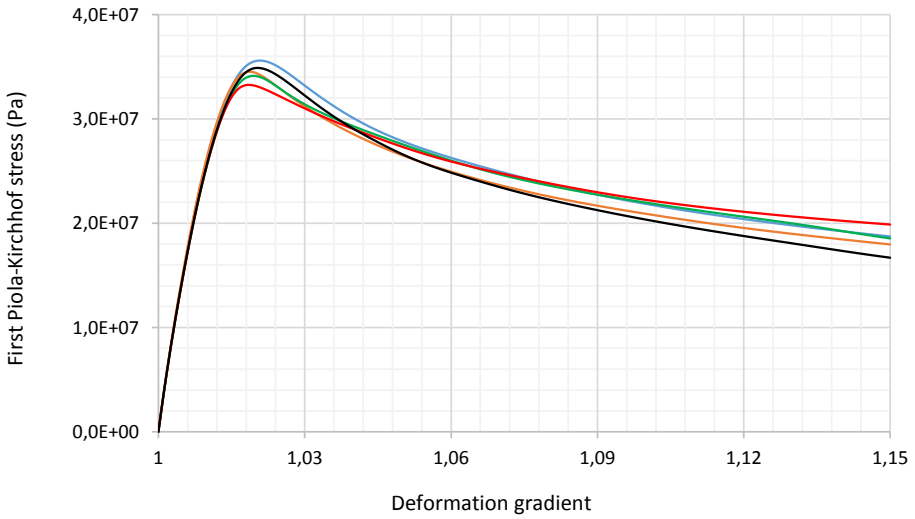

Figure 5.25: Stress-deformation of the samples shown in Figure (5.24).

Figure (5.26) shows the average response of the samples presented in Figure (5.24) with the bounds of standard deviation.

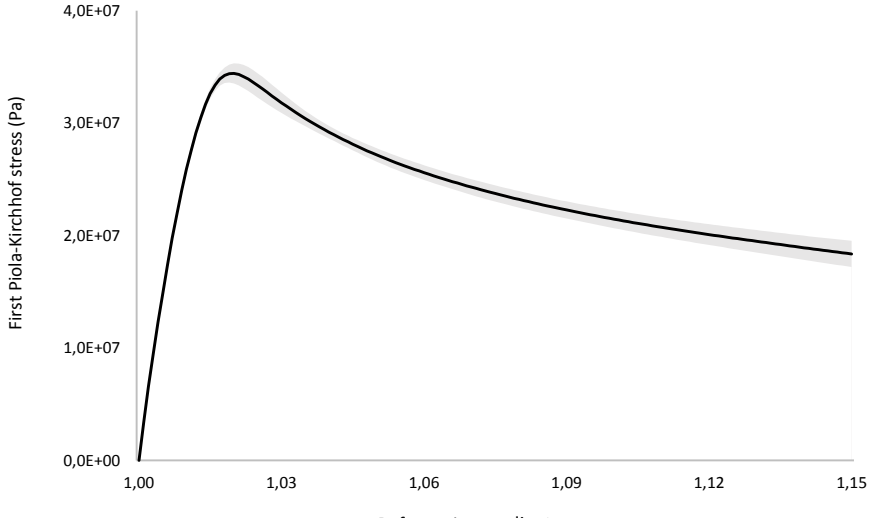

Figure 5.26: Average stress-deformation of the samples shown in Figure (5.24) with shaded bounds of standard deviation.

The first criterion is satisfied for this series of samples too. The second criterion should be checked. Figure (5.27) depicts the average response of the samples

shown in Figures (5.21) and (5.24).

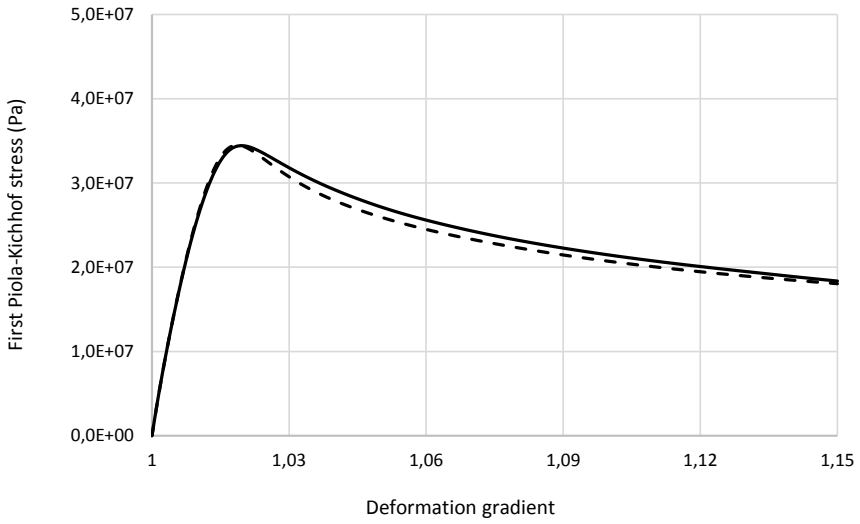

Figure 5.27: Average stress-deformation of the samples shown in Figures (5.11) and (5.14). Solid line: VES=40μm and dashed line: VES=30μm.

Based on the defined factors for determination of the RVES and also considering the values of the average deformation behaviours of the two series of samples, the RVES for Rubber Toughened Polystyrene (RT-PS) with 15% of rubbery particles could be chosen as 30μm.

5.5 Conclusions

In this chapter, the kinematics of microstructural problem was presented. Some numerical examples on Rubber Toughened Polystyrene (RT-PS), with two different levels of Inclusion Volume Fraction, were given. Having different morphologies showed the necessity of determination of the RVE Size. Due to strong post-yield softening behaviour of the material, determination of a minimum size for the microstructural samples is of great importance. This fact was shown by increasing the size of the micro-structural samples and observing the difference. According to the factors, commonly used in the definition of the RVE, two criteria were

introduced for determination of the RVES. It is worth emphasizing that in case of non-softening materials, determination of the RVES would be much easier due to the fact that softening behavior causes localization of the deformation and this deformation localization greatly affects the overal deformation behaviour of the material. It was concluded that for both cases of IVF equal to 10% and 15% the RVES could be considered $30\mu m$. It should be emphasized that in order to have more accurate result for the RVES, it would be beneficial to expand this statistical analysis and generate larger number of samples for each VES. Using automatic algorithms and developed codes for generation of micro-structural samples and also meshing the generated samples, would facilitate this study.

Chapter 6

Continuum and coupled multi-scale modelling of porous polymers

To characterize a polymeric material, it is essential to understand the properties of a material system across several length scales, from nanoscopic to macroscopic dimensions. One way to study the properties and behavior of complex materials, such as polymers, is through computer modeling and simulation. Computer simulations can provide information not accessible experimentally, reducing expensive and time-consuming trial-and-error approaches, and are particularly effective in exploring the physical and mechanical properties of new materials [Araujo et al. (2014)].

One of the main goals of computational materials science is to increase the speed and accuracy of the prediction of properties and features of new materials, which cannot be achieved with traditional simulation methods at a single length and time scale. Since no single model is capable of covering the enormous length and time scales associated with polymeric materials, a multi-scale approach can provide a deeper physical insight and has the potential to better predict the macroscopic properties.

In this chapter, two different approaches will be used in order to characterize the deformation behaviour of porous polymers. A continuum level constitutive model is developed in order to predict the behaviour of heterogeneous polymeric

materials. In contrast to homogeneous polymers, such as the ones discussed in Chapters 3 and 4, where the plastic deformation of the material is assumed incompressible, the plastic deformation of heterogeneous polymers can have both deviatoric and volumetric contributions. In other words, the flow rule of homogeneous material is usually totally deviatoric but for porous polymeric materials, the plastic deformation has both volumetric and deviatoric contributions. The continuum constitutive model uses a flow potential representing both deviatoric and volumetric plastic deformations. To this end, the model developed in Chapter 3 is extended with the Gurson yield surface to modify the flow rule of the model in order to account for the porosity effect on the overall deformation behaviour. In addition to continuum constitutive modelling, coupled multi-scale approach is also used to characterize the deformation behaviour of porous polymers. The Leonov based model, presented in Chapter 3, is used for the polymeric matrix material.

6.1 Introduction

One of the existing approaches to improve the mechanical properties of materials consists in modifying the microstructure of the material, see e.g. [van der Sanden (1993)]. There are different approaches to characterize the behavior of materials with heterogeneous microstructures, see [Geers (1997), Ghosh et al. (1996), Smit et al. (1998) and Danielsson et al. (2007)]. Different homogenization techniques are used by different authors in order to model the mechanical behavior of heterogeneous materials. Van der sluis et al. (2000) used a homogenization procedure to determine the apparent properties for Perzyna constitutive law. Van der sluis et al. (2001) developed a numerical homogenization method to characterize the behavior of elasto-viscoplastic heterogeneous materials at finite strains. Love and Batra (2006) determined the effective thermo-mechanical properties of a composite comprising two different constituents. Yong and Chiang (2007) used phase field microelasticity (PFM) within a homogenization process to find the elastic properties of a three dimensional heterogeneous material. The reader is referred to [Charalambakis (2010)] for a review of homogenization techniques. Glassy Polymers show brittleness under specific conditions. PS and PMMA,

among other glassy polymers, are considered brittle since they show brittle failure under low stress triaxiality such as uniaxial tension [Danielsson et al. (2007)]. Nowadays, Polymers are being increasingly used in different industries in areas already dominated by other metals, which requires development of polymeric materials with enhanced properties including improved mechanical properties. A well-known technique in order to deal with the undesired characteristic of glassy polymers, brittleness, is rubber toughening which is basically dispersing rubbery particles into the polymeric matrix [Danielsson et al. (2007), Smit (1998)]. Due to the successful increase in the toughness of glassy polymers by blending rubbery particles with glassy polymers, this technique has been applied to most of commercial glassy polymers. It is known that in rubber modified glassy polymers, by increasing the level of deformation, damage mechanisms might take place. Internal cavitation of rubbery particles and crazing in the matrix are commonly observed damage mechanisms in rubber-toughened glassy polymers. Due to the mentioned damages, the constitutive models typically used for neat polymeric materials, which do not take into account the phenomena, could not be used for characterizing the behaviour of rubber modified polymers. In this chapter, a continuum level constitutive model is developed using the model presented in Chapter 3 and Gurson yield function. The Leonov based model in Chapter 3 uses a purely deviatoric flow potential, i.e. the plastic deformation of the material is considered volume preserving which is, to a great extent, what is happening is reality. Gurson micromechanical potential is used to modify the flow potential of the Leonov based phenomenological constitutive model in order to take into account the effect of rubbery particles in the deformation behaviour. It should be mentioned that due to the deformation induced cavitation early during deformation, the rubbery particles are modelled as voids. Hence, the model should account for porosity effect on the deformation behaviour.

This chapter is structured as follows:

Section 6.2 describes a continuum level constitutive model for heterogeneous polymers: Section 6.2.1 presents the formulation of the constitutive model for porous polymers. The integration algorithm of the model for the Finite Element implementation in an implicit Finite Element code, including the state update procedure and consistent tangent operator, is given in Section 6.2.2. Section 6.2.3 gives

some numerical examples through which the evolution of stress and porosity are shown for materials with different percentage of initial porosity. Some benchmark problems are also simulated in Section 6.2.3.
Section 6.3 describes coupled multi-scale approach for analysing heterogeneous polymers: In Section 6.3.1, a brief summary of application of coupled multi-scale to polymeric materials will be given. Section 6.3.2 presents some numerical examples for RT-PS with 10% of rubbery particles. The Leonov based model, presented in Chapter 3, is used for the polymeric matrix material. Some comparison are made with homogeneous material.
Section 6.4 provides some comparisons between the two previously introduced approaches and gives some suggestions for extending the study for the sake of better agreement between the results. Finally, Section 6.5 summarizes the main contribution and conclusions of this chapter.

6.2 Continuum modelling

This section introduces a macroscopic constitutive model for rubber toughened glassy polymers (modelled as porous due to internal cavitation of rubbery particles) based on both phenomenological (Leonov based model) and micro-mechanical (Gurson model) considerations. It is well established that rubber toughening change the behaviour of glassy polymers in certain ways as given below [Danielsson et al. (2007)]:

- The material stiffness is decreased due to void-like behavior of rubbery particles. This effect should be clearly observed in the initial elastic regime of the stress strain curves and also force-displacement curves.

- Porosity evolves during deformation and thus in spite of plastically incompressible matrix, the rubber toughened polymer deformed volumetrically throughout the deformation. Hence, the plastic flow rule should include a volumetric component in addition to originally existing deviatoric contribution.

- In the limit case of zero initial void volume fraction, the original model, presented in Chapter 3, should be recovered both in theory and in terms of results of the implemented algorithm.

According to the Leonov based model (presented in Chapter 3) the inelastic behaviour of the matrix material is governed by a fully deviatoric flow potential. It is worth emphasizing that since the model does explicitly not use a yield surface, both elastic and inelastic contributions to strain and also the rate of them are non-zero in all stages of deformation.

6.2.1 Formulation

The flow rule of the porous polymeric based material is assumed and additively composed of deviatoric and hydrostatic contributions [Zairi et al. (2008)]:

$$\mathbf{d}_M^p = \mathbf{d}_d^p + d_h^p \mathbf{I} \tag{6.1}$$

In this study, a rate sensitive form of the Gurson model [Gurson (1977)], introduced by Pan et al. [Pan et al. (1983)], is used to be coupled with the elasto-viscoplastic model presented in Chapter 3 based on single mode Leonov model [Timmermans (1998), Govaert et al. (2000)]. In the mentioned model, the flow rule is totally deviatoric and, as a result, the plastic flow is incompressible. For the porous material, due to volumetric deformation of voids during deformation, a modified version of the model to account for porosity within the material, is developed. According to [Pan et al. (1983)], the flow rule could be postulated with the following form:

$$\mathbf{d}_M^p = \Lambda \frac{\partial \Phi}{\partial \boldsymbol{\tau}_M}. \tag{6.2}$$

Where, Λ is a proportionality factor which will be determined by the equivalence between macroscopic plastic work and microscopic plastic dissipation. The second order tensor $\boldsymbol{\tau}_M$ is the macroscopic Kirchhof stress and Φ is the yield function. It should be emphasized that due to the assumption of associativity of the elasto-viscoplastic model, the dissipation potential, Ψ, is assumed for the yield function i.e. $\Phi = \Psi$. The macroscopic plastic work is given by:

$$\dot{W}_M = \boldsymbol{\tau}_M : \mathbf{d}_M^p = \boldsymbol{\tau}_M : \Lambda \frac{\partial \Phi}{\partial \boldsymbol{\tau}_M}. \tag{6.3}$$

The microscopic plastic dissipation is given by:

$$\dot{W}_m = (1-f)\tau_m^{eq}\dot{\gamma}_m^{eq}, \tag{6.4}$$

where,f is void volume fraction given by:

$$f = \frac{V_v}{V_{RVE}}, \tag{6.5}$$

where, V_v is the volume of the voids and V_{RVE} is the volume of the RVE. τ_m^{eq} is an equivalent stress of the matrix material which is given by:

$$\tau_m^{eq} = \sqrt{\frac{1}{2}\mathbf{s}_m : \mathbf{s}_m}, \tag{6.6}$$

where, $\mathbf{s}_m$ is the deviatoric stress of the matrix:

$$\mathbf{s}_m = \boldsymbol{\tau}_m + p_m\mathbf{I}, \tag{6.7}$$

where, $\boldsymbol{\tau}_m$ is the Kirchhof stress of the matrix material and p_m is the hydrostatic stress of the matrix given by:

$$p_m = -\frac{1}{3}tr(\boldsymbol{\tau}_m) = -\frac{1}{3}(\tau_m(xx) + \tau_m(yy) + \tau_m(zz)). \tag{6.8}$$

In relation (6.4), $\dot{\gamma}_m^{eq}$ is the rate of equivalent shear strain of the matrix:

$$\dot{\gamma}_m^{eq} = \sqrt{2\mathbf{d}_m^p : \mathbf{d}_m^p}, \tag{6.9}$$

where, $\mathbf{d}_m^p$ is the dissipation potential of the matrix material given by:

$$\mathbf{d}_m^p = \frac{\mathbf{s}_m}{2\eta}, \tag{6.10}$$

where, the parameter η is the viscosity function given by:

$$\eta = A_0 \exp\left[\frac{\Delta H}{RT} + \frac{\mu P}{\tau_0} - D_\infty + D_\infty \exp\left(\frac{-h\sqrt{3}\ \bar{\varepsilon}^p}{\sqrt{2}D_\infty}\right)\right]$$
$$\left[\tau^{eq}/\sinh\left(\frac{\tau^{eq}}{\tau_0}\right)\right]. \tag{6.11}$$

From the equivalence between relations (6.3) and (6.4), the proportionality factor, Λ, is obtained:

$$\Lambda = \frac{(1-f)\tau_m^{eq}\dot{\gamma}_m^{eq}}{\boldsymbol{\tau}_M : \frac{\partial \Phi}{\partial \boldsymbol{\tau}_M}}. \tag{6.12}$$

Initially, the Gurson yield function is assumed for the dissipation potential of the porous polymeric material. The Gurson yield function is given by [Gurson (1977)]:

$$\Phi = \frac{(\tau_M^{eq})^2}{\tau_{M0}^2} + 2f\cosh\left(\frac{tr\,(\boldsymbol{\tau}_M)}{2\tau_{M0}}\right) - (1+f^2) = 0. \tag{6.13}$$

Where, the parameter τ_{M0} is the equivalent tensile flow strength of the matrix material and the von-Mises equivalent stress, τ_M^{eq}, is given by:

$$\tau_M^{eq} = \sqrt{\frac{3}{2}\mathbf{s}_M : \mathbf{s}_M}. \tag{6.14}$$

Where, $\mathbf{s}_M$ is macroscopic deviatoric stress:

$$\mathbf{s}_M = \boldsymbol{\tau}_M + p_M\mathbf{I}, \tag{6.15}$$

where, $\boldsymbol{\tau}_M$ is the macroscopic Kirchhof stress and p_M is the macroscopic hydrostatic stress:

$$p_M = -\frac{1}{3}tr(\boldsymbol{\tau}_M) = -\frac{1}{3}(\tau_M(xx) + \tau_M(yy) + \tau_M(zz)). \tag{6.16}$$

The Gurson yield function, relation (6.13), could be rewritten as follows:

$$\Phi = (\tau_M^{eq})^2 + 2f\,(\tau_{M0})^2\cosh\left(\frac{tr\,(\boldsymbol{\tau}_M)}{2\tau_{M0}}\right) - (\tau_{M0})^2\,(1+f^2) = 0. \tag{6.17}$$

As mentioned before, the model presented in Chapter 3 does not use an explicit yield function and thus, we do not use any explicit value for the tensile flow strength of the matrix material. Hence instead of using τ_{M0}, the equivalent stress of the matrix material is used in the definition of the yield function. Consequently, the Gurson yield function considered for the present study is given by:

$$\Phi = (\tau_M^{eq})^2 + 2f(\tau_m^{eq})^2\cosh\left(\frac{tr\,(\boldsymbol{\tau}_M)}{2(\tau_m^{eq})}\right) - (\tau_m^{eq})^2(1+f^2) = 0. \tag{6.18}$$

where, $\boldsymbol{\tau}_M$ is macroscopic Kirchhof stress and τ_M^{eq} is a macroscopic effective stress:

$$\tau_M^{eq} = \sqrt{\frac{1}{2}\mathbf{s}_M : \mathbf{s}_M}. \tag{6.19}$$

where, $\mathbf{s}_M$ is the deviatoric part of the Kirchhof stress.

The yield function, relation (6.13), was originally proposed by Gurson [Gurson (1977)] and extended by Tvergaard and Needleman [Tvergaard and Needleman (1984)]. Zairi et al. [Zairi et al. (2008)] used the yield function to extend BP (Bodner and Partom model [Bonder and Partom (1975)]) for porous material. It should be emphasized that in relation (6.18), effective stress at the matrix and macroscopic effective stress are correspondingly defined by relations (6.6) and (6.19).

In order to obtain the flow potential of the porous material, $\mathbf{d}_M^p$, the derivative of the dissipation potential, Φ, in order to macroscopic Kirchhof stress should be computed:

$$\frac{\partial \Phi}{\partial \boldsymbol{\tau}_M} = \frac{\partial}{\partial \boldsymbol{\tau}_M}\left[(\tau_M^{eq})^2 + 2f(\tau_m^{eq})^2 \cosh\left(\frac{tr\,(\boldsymbol{\tau}_M)}{2\tau_m^{eq}}\right) - (\tau_m^{eq})^2(1+f^2)\right]. \tag{6.20}$$

It could be expressed as:

$$\frac{\partial \Phi}{\partial \boldsymbol{\tau}_M} = \mathbf{s}_M + \frac{f}{3}\tau_m^{eq} \sinh\left(\frac{tr\,(\boldsymbol{\tau}_M)}{2\tau_m^{eq}}\right)\mathbf{I}. \tag{6.21}$$

Using relations (6.2),(6.6),(6.9),(6.10),(6.12) and (6.21), the flow rule of the porous polymeric material is obtained:

$$\mathbf{d}_M^p = (1-f)(\frac{1}{\eta})(\tau_m^{eq})^2 \left[\mathbf{s}_M : \mathbf{s}_M + \frac{f}{3}\tau_m^{eq} \sinh\left(\frac{tr\,(\boldsymbol{\tau}_M)}{2\tau_m^{eq}}\right)\boldsymbol{\tau}_M : \mathbf{I}\right]^{-1}$$
$$\left[\mathbf{s}_M + \frac{f}{3}\tau_m^{eq} \sinh\left(\frac{tr\,(\boldsymbol{\tau}_M)}{2\tau_m^{eq}}\right)\mathbf{I}\right] \tag{6.22}$$

For a neat (undamaged) glassy polymer, $f = 0$, the flow potential of porous material (equation (6.22)) is reduced to the dissipation potential of the solid ligaments between voids (relation (6.10)). According to relations (6.1) and (6.22), the deviatoric and hydrostatic terms of the flow rule of the porous materials are given by:

$$\mathbf{d}_d^p = (1-f)(\frac{1}{\eta})(\tau_m^{eq})^2 \left[\mathbf{s}_M : \mathbf{s}_M + \frac{f}{3}\tau_m^{eq} \sinh\left(\frac{tr\,(\boldsymbol{\tau}_M)}{2\tau_m^{eq}}\right)\boldsymbol{\tau}_M : \mathbf{I}\right]^{-1} \mathbf{s}_M, \tag{6.23}$$

$$d_h^p = (1-f)(\frac{1}{\eta})(\tau_m^{eq})^2 \left[\mathbf{s}_M : \mathbf{s}_M + \frac{f}{3}\tau_m^{eq} \sinh\left(\frac{tr\left(\boldsymbol{\tau}_M\right)}{2\tau_m^{eq}}\right)\boldsymbol{\tau}_M : \mathbf{I}\right]^{-1} \left[\frac{f}{3}\tau_m^{eq} \sinh\left(\frac{tr\left(\boldsymbol{\tau}_M\right)}{2\tau_m^{eq}}\right)\right]. \tag{6.24}$$

As mentioned before, due to deformation induced cavitation early during deformation, the rubbery particles are considered as voids. Many researchers devoted their research to internal cavitation of rubbery particles, see e.g. [Dompas and Groeninckx (1994)] and [Lazzeri and Bucknall (1995)]. During last decades, a lot of researchers tried to predict the growth of voids in metals, see e.g. [Pardoen and Hutchinson (2000)] and [Wen et al. (2005)] for some recent ones. Recent studies prove that the classical micro-mechanical models describing void growth process in metals, could be used for growth of voids in rubber toughened glassy polymers as well [Zairi et al. (2008)]. Assuming no nucleation of voids, the rate of change in the void volume fraction, $\dot{f}$, is equal to the growth rate of existing voids, $\dot{f}_g$. Considering plastic incompressibility of the matrix material and according to mass conservation law, the growth rate of existing voids is given by:

$$\dot{f}_g = 3(1-f)d_h^p. \tag{6.25}$$

The elastic behaviour, for both homogeneous and heterogeneous materials, is assumed isotropic and then two elastic properties (e.g. Young modulus and Poissons ratio or shear modulus and bulk modulus) characterize the elastic behaviour. If G_1 and K_1 are the shear modulus and bulk modulus of the homogeneous polymer, then it is required to obtain the effective elastic properties of the rubber toughened polymer. The effective elastic properties of void-containing matrix are studied by different authors, see e.g. [Budiansky (1965)]. Mori and Tanaka (1973) proposed the following relations for the shear and bulk modulus of porous material based on the elastic properties of the matrix material and also the level of porosity.

$$G = \frac{G_1\left(1-f\right)}{1+6f\left(\frac{K_1+2G_1}{9K_1+8G_1}\right)} \tag{6.26}$$

$$K = \frac{4(1-f)}{\frac{4}{K_1}+\frac{3f}{G_1}} \tag{6.27}$$

It is worth noting that the development of the constitutive model was done exclusively at the material level, i.e. the kinematics of the deformation was not mentioned. The kinematical relations of the Leonov based model in Chapter 3, relation (3.1) to (3.11), are considered for this porosity dependent model.

6.2.2 Integration algorithm

In order to implement the model within an implicit finite element code, derivation of state update and also consistent tangent operator are needed. It should be mentioned that similarly to the integration algorithms of the models presented in Chapters 3 and 4, the derivation of the state update procedure and consistent tangent operator will be performed on the small strain format of the constitutive equations and they will be extended to finite strain counterparts with the finite strain extension explained in Chapter 3.

6.2.2.1 State update

For derivation of the state update procedure, the small strain counterpart of relation (6.22) is used:

$$\dot{\boldsymbol{\varepsilon}}^p_M = (1-f)(\frac{1}{\eta})(\tau^{eq}_m)^2 \left[\mathbf{s}_M : \mathbf{s}_M + \frac{f}{3}\tau^{eq}_m \sinh\left(\frac{tr\left(\boldsymbol{\tau}_M\right)}{2\tau^{eq}_m}\right)\boldsymbol{\tau}_M : \mathbf{I}\right]^{-1}$$

$$\left[\mathbf{s}_M + \frac{f}{3}\tau^{eq}_m \sinh\left(\frac{tr\left(\boldsymbol{\tau}_M\right)}{2\tau^{eq}_m}\right)\mathbf{I}\right]. \tag{6.28}$$

Integrating both sides of relation (6.28) between time steps t_n and t_{n+1} results in:

$$\boldsymbol{\varepsilon}^p_{M,n+1} - \boldsymbol{\varepsilon}^p_{M,n} = X_{n+1}\Delta t, \tag{6.29}$$

where, Δt is the time interval between t_n and t_{n+1} and X_{n+1} is given by:

$$X_{n+1} = (1-f_{n+1})(\frac{1}{\eta_{n+1}})(\tau^{eq}_{m,n+1})^2$$

$$\left[\mathbf{s}_{M,n+1} : \mathbf{s}_{M,n+1} + \frac{f_{n+1}}{3}\tau^{eq}_{m,n+1} \sinh\left(\frac{tr\left(\boldsymbol{\tau}_{M,n+1}\right)}{2\tau^{eq}_{m,n+1}}\right)\boldsymbol{\tau}_{M,n+1} : \mathbf{I}\right]^{-1}$$

$$\left[\mathbf{s}_{M,n+1} + \frac{f_{n+1}}{3}\tau^{eq}_{m,n+1}\sinh\left(\frac{tr\left(\boldsymbol{\tau}_{M,n+1}\right)}{2\tau^{eq}_{m,n+1}}\right)\mathbf{I}\right]. \tag{6.30}$$

In a generic three dimensional case, relation (6.29) includes 6 non-linear algebraic equations. The unknowns of the six equations are $\varepsilon^{p}_{M,n+1}(xx)$, $\varepsilon^{p}_{M,n+1}(yy)$, $\varepsilon^{p}_{M,n+1}(zz)$, $\varepsilon^{p}_{M,n+1}(xy)$, $\varepsilon^{p}_{M,n+1}(xz)$, $\varepsilon^{p}_{M,n+1}(yz)$, f_{n+1}, η_{n+1} and $\tau^{eq}_{m,n+1}$. Hence, for the system of six equations, there are nine unknown to be determined. The seventh equation of the system of equations is the discretized version of equation (6.25).

$$f_{n+1} = 1 - (1 - f_n)\exp(-3d^{p}_{h,n+1}\Delta t), \tag{6.31}$$

where, $d^{p}_{h,n+1}$ is discretized hydrostatic part of flow rule of the porous material given by:

$$d^{p}_{h,n+1} = (1 - f_{n+1})(\frac{1}{\eta_{n+1}})(\tau^{eq}_{m,n+1})^2$$

$$\left[\mathbf{s}_{M,n+1} : \mathbf{s}_{M,n+1} + \frac{f_{n+1}}{3}\tau^{eq}_{m,n+1}\sinh\left(\frac{tr\left(\boldsymbol{\tau}_{M,n+1}\right)}{2\tau^{eq}_{m,n+1}}\right)\boldsymbol{\tau}_{M,n+1} : \mathbf{I}\right]^{-1}$$

$$\left[\frac{f_{n+1}}{3}\tau^{eq}_{m,n+1}\sinh\left(\frac{tr\left(\boldsymbol{\tau}_{M,n+1}\right)}{2\tau^{eq}_{m,n+1}}\right)\right]. \tag{6.32}$$

The eighth equation is the time discretized version of viscosity function, relation (6.11), as given below:

$$\eta_{n+1} = A_0\exp\left[\frac{\Delta H}{RT} + \frac{\mu P_{m,n+1}}{\tau_0} - D_\infty + D_\infty\exp\left(\frac{-h\sqrt{3}\,\bar{\varepsilon}^{p}_{m,n+1}}{\sqrt{2}D_\infty}\right)\right]$$

$$\left[\tau^{eq}_{m,n+1}/\sinh\left(\frac{\tau^{eq}_{m,n+1}}{\tau_0}\right)\right]. \tag{6.33}$$

The final equation is discretized version of Gurson yield function given by relation (6.18).

$$\Phi_{n+1} = \left(\tau^{eq}_{M,n+1}\right)^2 + 2f(\tau^{eq}_{m,n+1})^2\cosh\left(\frac{tr\left(\boldsymbol{\tau}_{M,n+1}\right)}{2(\tau^{eq}_{m,n+1})}\right)$$

$$-(\tau^{eq}_{m,n+1})^2(1 + f^2_{n+1}) = 0. \tag{6.34}$$

Consequently, relations (6.29), (6.31), (6.33) together with equation (6.34) make the system of nine non-linear equations to be solved simultaneously for three

dimensional problems. In order to solve the system of nine non-linear equations, the well-known Newton-Raphson method is used in an iterative fashion. Since, the plastic strain at time step t_n is known, the unknowns of the equation (6.29) are considered the incremental plastic strain.

$$(\Delta\boldsymbol{\varepsilon})^{p}_{M,n+1} = \boldsymbol{\varepsilon}^{p}_{M,n+1} - \boldsymbol{\varepsilon}^{p}_{M,n}. \tag{6.35}$$

The other unknowns to be determined are porosity, f_{n+1}, viscosity, η_{n+1} and effective stress at matrix material, $\tau^{eq}_{m,n+1}$. For notational convenience, the unknowns are referred to u_1, u_2, ... , u_9. If the unknowns are considered as a vector, the Newton-Raphson method implies that:

$$\mathbf{u}^{k} = \mathbf{u}^{k-1} + (\delta\mathbf{u})^{k}. \tag{6.36}$$

Where $k-1$ and k are two consecutive iterations of Newton-Raphson, $(\delta\mathbf{u})^{k}$ is incremental unknowns which is obtained from:

$$\left[\mathbf{R}_{i,j}\right]^{k-1}\left[\delta\mathbf{u}_{j}\right]^{k} = -\left[\mathbf{R}_{i}\right]^{k-1}. \tag{6.37}$$

Where,

$$\mathbf{R}_{i,j} = \frac{\partial\mathbf{R}_{i}}{\partial\mathbf{u}_{j}}. \tag{6.38}$$

For the reader convenience, Equation (6.37) is expanded for two dimensional implementation in Appendix D and the components of the first right hand side matrix will also be given in Appendix D. Having the Newton-Raphson iterations on linearised system of equations, presented in relation (6.37), converged, the components of the elastic strain tensor and also the stresses should be updated. The elastic strain is obtained by:

$$\boldsymbol{\varepsilon}^{e}_{M,n+1} = \boldsymbol{\varepsilon}^{e,trial}_{M,n+1} - (\Delta\boldsymbol{\varepsilon})^{p}_{M,n+1}, \tag{6.39}$$

where, $\boldsymbol{\varepsilon}^{e,trial}_{M,n+1}$ is the elastic trial strain. When the elastic strain tensor is obtained, the deviatoric stress the hydrostatic pressure are simply computed by:

$$\mathbf{s}_{M,n+1} = 2G\boldsymbol{\varepsilon}^{e}_{M,d,n+1}, \tag{6.40}$$

$$p_{M,n+1} = -Ktr\left(\boldsymbol{\varepsilon}^{e}_{M,n+1}\right). \tag{6.41}$$

It should be mentioned that shear modulus and bulk modulus in relations (6.40) and (6.41) are the updated shear and bulk modulus with relations (6.26) and (6.27) using the converged value for current void volume fraction. Hence, the elastic properties of the material are not constant during deformation and they change as the current porosity of the material changes.

6.2.2.2 Tangent operator

As mentioned before, the consistent tangent operator needs to be obtained for the sake of completing the numerical treatment of the model within an implicit quasi-static integration scheme. The global tangent stiffness matrix is assembled using the tangent operators, which are derived by consistently linearizing the integration scheme [De Souza Neto et al. (2008)]. The tangent operator is given by:

$$\mathsf{D} = \frac{d\boldsymbol{\tau}_{M,n+1}}{d\boldsymbol{\varepsilon}^{e,trial}_{M,n+1}} = \frac{d\boldsymbol{\tau}_{M,n+1}}{d\boldsymbol{\varepsilon}_{M,n+1}}, \tag{6.42}$$

or equivalently,

$$\mathsf{D} = \frac{d}{d\boldsymbol{\varepsilon}_{M,n+1}}\left(\mathbf{s}_{M,n+1} - p_{M,n+1}\mathbf{I}\right) = \frac{d\mathbf{s}_{M,n+1}}{d\boldsymbol{\varepsilon}_{M,n+1}} - \frac{dp_{M,n+1}}{d\boldsymbol{\varepsilon}_{M,n+1}}\mathbf{I}. \tag{6.43}$$

The stress deviator, $\mathbf{s}_{M,n+1}$, and the hydrostatic stress, $p_{M,n+1}$, are given by relations (6.40) and (6.41), respectively. The deviatoric elastic strain, $\boldsymbol{\varepsilon}_{M,d,n+1}$, is obtained by:

$$\boldsymbol{\varepsilon}^{e}_{M,d,n+1} = \mathsf{I}_d : \boldsymbol{\varepsilon}^{e}_{M,n+1}, \tag{6.44}$$

where, the elastic strain, $\boldsymbol{\varepsilon}^{e}_{M,n+1}$, is given by relation (6.39). The first term in relation (6.43) which is the derivative of stress deviator in order to strain is obtained as:

$$\frac{d\mathbf{s}_{M,n+1}}{d\boldsymbol{\varepsilon}_{M,n+1}} = 2G\mathsf{I}_d - 2G\frac{d}{d\boldsymbol{\varepsilon}_{M,n+1}}\left[(\Delta\boldsymbol{\varepsilon})^{p}_{M,d,n+1}\cdot\right], \tag{6.45}$$

where, the deviatoric part of incremental plastic strain is given by:

$$(\Delta\boldsymbol{\varepsilon})^{p}_{M,d,n+1} = \mathsf{I}_d : (\Delta\boldsymbol{\varepsilon})^{p}_{M,n+1}\,. \tag{6.46}$$

The derivative of hydrostatic stress in order to strain, the second part of relation (6.43), is obtained as:

$$\frac{dp_{M,n+1}}{d\boldsymbol{\varepsilon}_{M,n+1}} = K \frac{d}{d\boldsymbol{\varepsilon}_{M,n+1}} \left[tr\left(\Delta\boldsymbol{\varepsilon}\right)^{p}_{M,n+1} \right] \tag{6.47}$$

Considering relations (6.45) and (6.47), in order to obtain the tangent operator, it is required to calculate the derivatives of the components of incremental plastic strain with respect to strain. The following matrix relation could be written:

$$\left[-\left(\partial \mathbf{R}_i / \partial \boldsymbol{\varepsilon}_{M,n+1}\right) : d\boldsymbol{\varepsilon}_{M,n+1} \right] = \left[\mathbf{R}_{i,j} \right] \left[d\mathbf{u}_i \right] . \tag{6.48}$$

Matrix relation (6.48) could be rewritten as:

$$\left[d\mathbf{u}_i \right] = \left[\mathbf{R}_{i,j} \right]^{-1} \left[-\left(\partial \mathbf{R}_i / \partial \boldsymbol{\varepsilon}_{M,n+1}\right) : d\boldsymbol{\varepsilon}_{M,n+1} \right] \tag{6.49}$$

The expanded versions of relations (6.48) and (6.49) are given in Appendix E. The components of first matrix in the right hand side of relation (6.49) were already introduced and as mentioned before they are given in Appendix D. The derivatives of the residuals in order to strain, which are the components of the second matrix in the right hand side of relation (6.49), together with mathematical manipulations for tangent operator are given in Appendix E.

6.2.3 Numerical examples

In the previous sections of this chapter, a constitutive model was developed for characterizing the behaviour of rubber toughened (modelled as porous) amorphous polymers and the integration algorithm of the model for the Finite Element implementation was derived. In this section, some numerical examples will be given through which the capability of the model to predict the deformation behaviour of porous amorphous polymers will be evaluated. The following features are expected to be observed in the deformation behaviour of rubber toughened amorphous polymers by increasing the volume fraction of rubbery particles.

- The slope of the elastic deformation will decrease.
- The yield stress will decrease.

- The slope of the post-yield softening and hardening will decrease.

In addition to the aforementioned features, it is also expected that by introducing no volume fraction of rubbery inclusions (zero porosity), the results of the original model are recovered since the nucleation of voids is neglected. The material is Rubber Toughened Polystyrene (RT-PS). Different volume fraction of rubbery inclusions are considered. First, some numerical examples will be conducted through which the effects of porosity on the stress-strain curve under different strain rates and also the evolution of porosity will be evaluated. In addition, the capability of the model to characterize the expected features will be assessed. Then, a benchmark problem will be provided and the effect of rubber toughening on the deformation behaviour of the material will be investigated.

6.2.3.1 Evolution of stress and porosity

In this section, tensile simulations are performed on RT-PS, considering different volume fractions of rubbery particles and under four different strain rates, namely $\dot{\varepsilon} = 0.0001(1/s)$, $\dot{\varepsilon} = 0.0005(1/s)$, $\dot{\varepsilon} = 0.001(1/s)$ and $\dot{\varepsilon} = 0.005(1/s)$. With the simulations in this section, it is intended to check if the developed model is capable of characterizing the stress-strain behaviour of rubber toughened polymers and the expected features are captured.
In Figure (6.1), the evolution of stress and porosity against strain is shown for RT-PS with different initial porosity levels and under strain rate of $\dot{\varepsilon} = 0.0001(1/s)$. As can be seen in Figure (6.1), the evolution of the porosity starts after the elastic domain for all different initial porosities. Since, the nucleation of voids is neglected, for the case of zero initial void void fraction, Figure (6.1a), there is no evolution of porosity and as expected for that case, the response of the homogeneous material is obtained. The stress-strain curves for RT-PS with different initial porosity and at different strain rates are shown in Figure (6.2). The reduction in the yield stress by increasing the initial porosity could be obviously observed in Figure (6.2) for different strain rates. Figure (6.3) shows the expected decrease in the softening and also hardening slope by the introduction of rubbery particles into the polymeric matrix. The stress-strain curves are for PS and RT-PS 20% initial void volume fraction at strain rate $\dot{\varepsilon} = 0.0005(1/s)$. Figure (6.3)

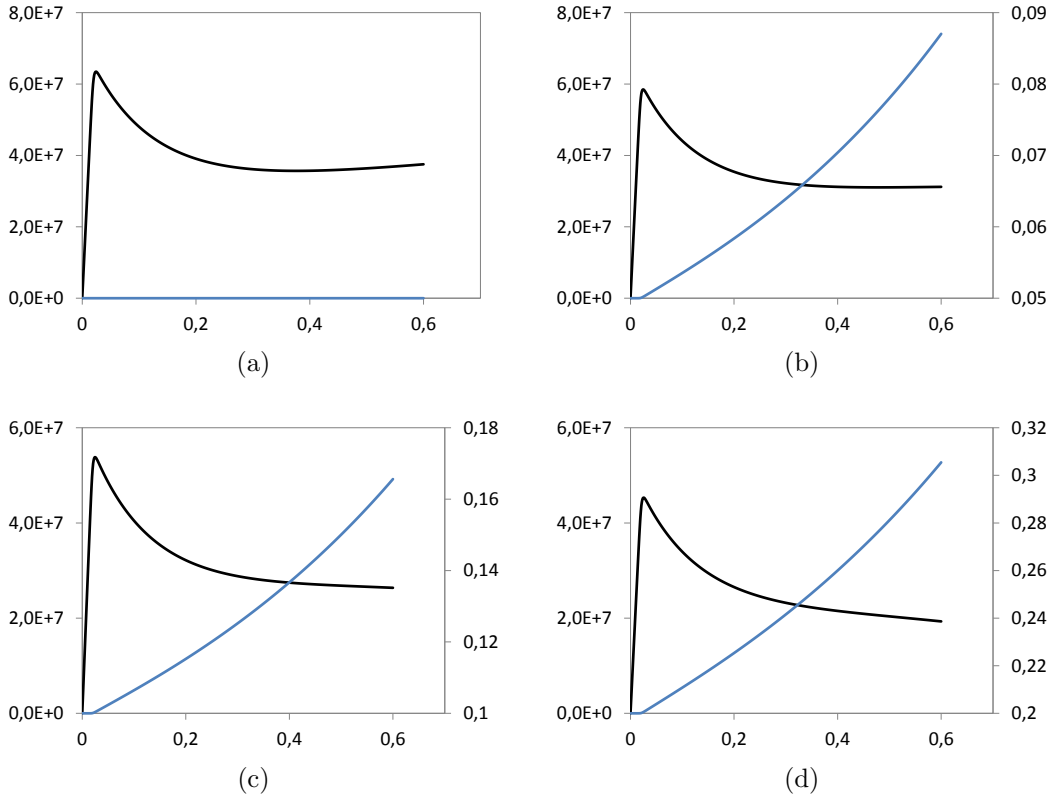

Figure 6.1: Evolution of stress and porosity against strain for RT-PS at strain rate equal to $\dot{\varepsilon} = 0.0001(1/s)$, right vertical axis: stress (Pa); horizontal axis: strain; right vertical axis: porosity; black line: evolution of stress; blue line: evolution of viscosity; (a): $f_0 = 0$; (b): $f_0 = 5\%$; (c): $f_0 = 10\%$; (d): $f_0 = 20\%$.

also shows the reduction in the elastic modulus of porous material compared to the homogeneous material. Figure (6.4) shows the evolution of volumetric strain against axial strain, under different strain rates and considering different volume fraction of rubbery inclusions. As expected, for the homogeneous material, the volumetric strain remains almost unchanged after the elastic domain of the deformation. On the other hand, increasing the level of rubbery particles causes remarkable plastic volumetric deformation.

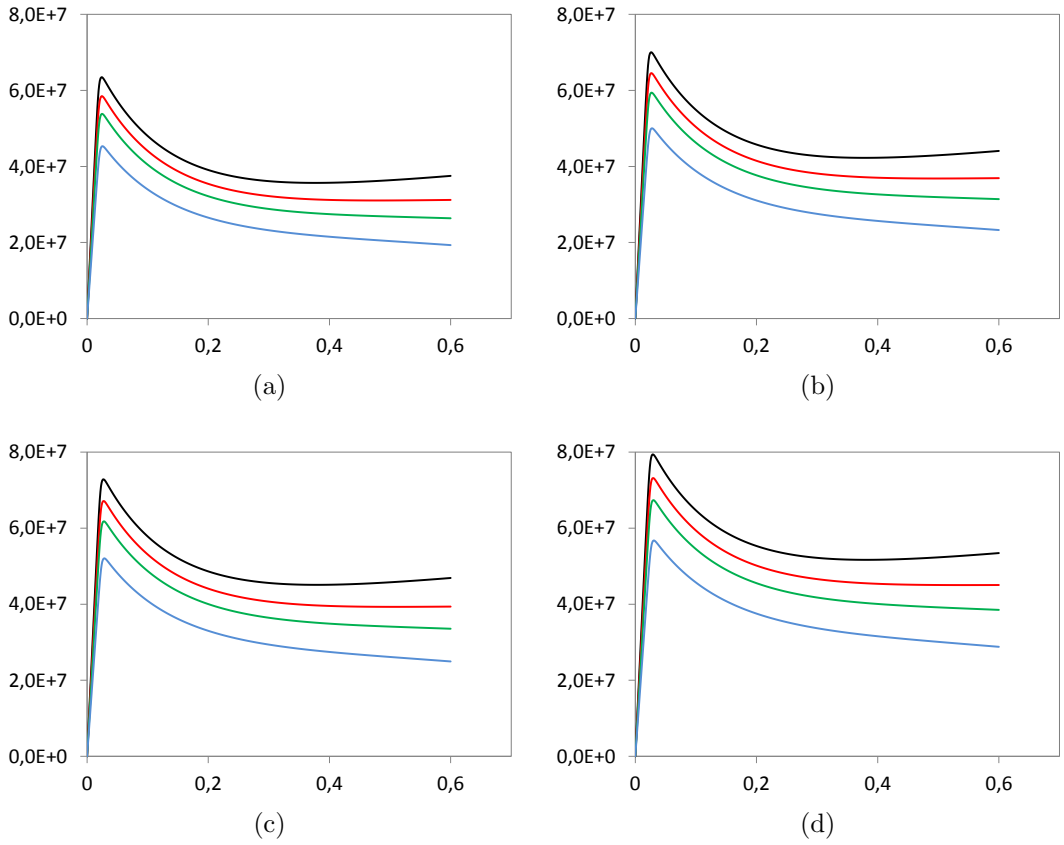

Figure 6.2: Stress-strain curves of RT-PS under different strain rates, vertical axis: stress (Pa); horizontal axis: strain; (a): $\dot{\varepsilon} = 0.0001(1/s)$; (b): $\dot{\varepsilon} = 0.0005(1/s)$; (c): $\dot{\varepsilon} = 0.001(1/s)$; (d): $\dot{\varepsilon} = 0.005(1/s)$; black line: $f_0 = 0$; red line: $f_0 = 5\%$; green line: $f_0 = 15\%$; blue line: $f_0 = 20\%$.

6.2.3.2 Boundary value problem

In this section, the effect of rubber toughening on the deformation behaviour of a dog-bone specimen under uniaxial tensile loading will be examined. The simulation is performed under axisymmetric conditions. The mesh of the simulation is given in Figure (6.5) again. Total displacement of $u = 1.5\ mm$ is applied within 100 increments and under displacement rate equal to $\dot{u} = 0.75\ mm/min$. Figure (6.6) depict the contour plots of void volume fraction for the dog-bone specimen made from RT-PS with different values of initial void volume fraction.

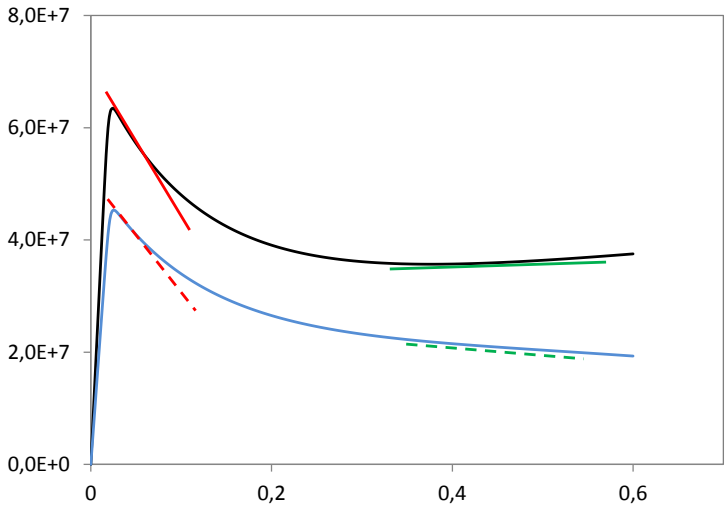

Figure 6.3: Comparison of the post-yield softening and hardening of PS and RT-PS with initial 20% of porosity.

6.3 Coupled Multi-scale

The macroscale behavior of a specimen, regardless of the material from which the specimen is made, is dependent on the nano and micro structure. In order to take into account the effects of these scales on the overall macro scale behavior of different structures, the coupled multiscale approach has become an interesting tool despite its expensive simulation cost. A material can be considered homogeneous at macro scale but, once gone deep into the microstructure, we will probably find some heterogeneities such as inclusions and voids. It can be said that every material is heterogeneous at one or more scales. In order to take into account the effects of significant heterogeneities at the micro structure on the observable structure behavior, we need to have a representative part of the micro structure. Hill (1963) proposed a representative sub-region of the micro structure named Representative Volume Element (RVE) which is statistically representative. In other words, the RVE should include the most possible effects of the micro structure such that if the distribution of the micro heterogeneities changes, the overall response of the RVE would not be remarkably changed. A schematic presentation of an RVE is provided in Figure (6.7). The size of the RVE, l, should be much smaller than the size of the structure at macro scale, L, and the size of the

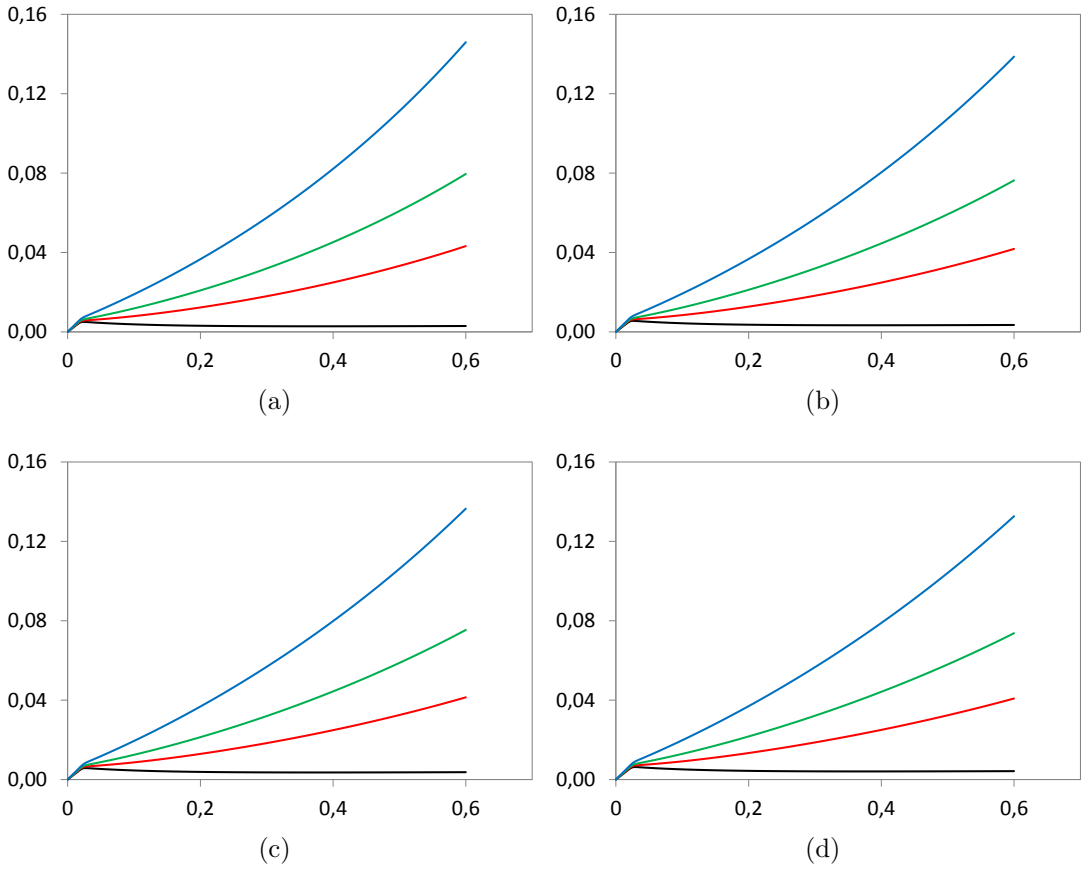

Figure 6.4: The evolution of volumetric strain versus axial strain for RT-PS under different strain rates, vertical axis: volumetric strain; horizontal axis: axial strain; (a): $\dot{\varepsilon} = 0.0001(1/s)$; (b): $\dot{\varepsilon} = 0.0005(1/s)$; (c): $\dot{\varepsilon} = 0.001(1/s)$; (d): $\dot{\varepsilon} = 0.005(1/s)$; black line: $f_0 = 0$; red line: $f_0 = 5\%$; green line: $f_0 = 15\%$; blue line: $f_0 = 20\%$.

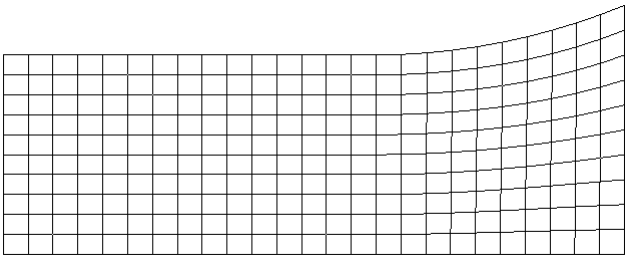

Figure 6.5: Mesh of the dog-bone specimen.

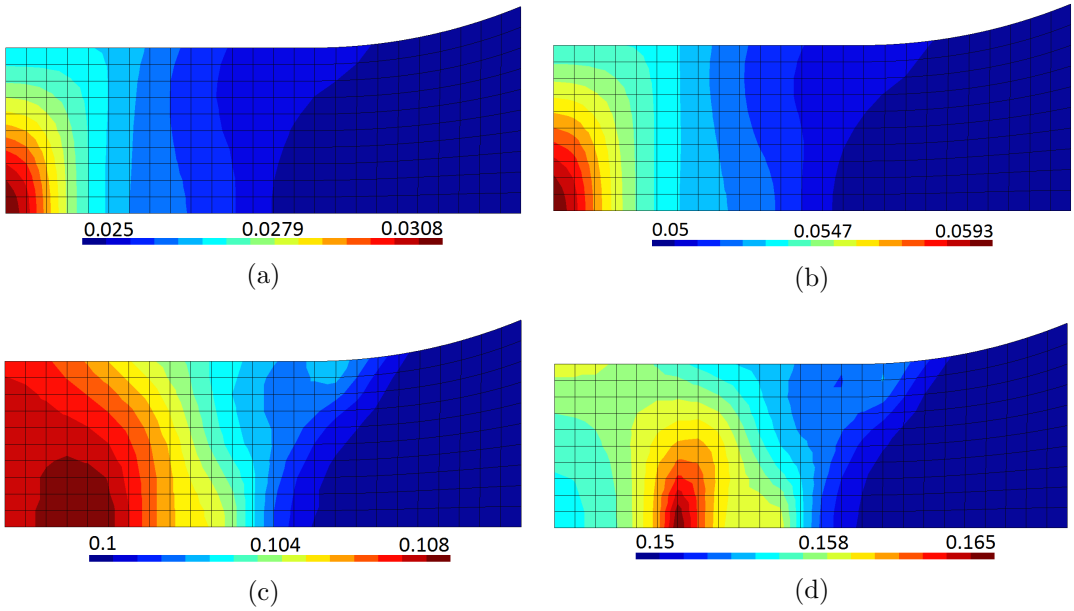

Figure 6.6: The level of porosity in the dog-bone specimen after deformation considering different levels of initial porosity (a): 2.5%; (b):5%; (c):10% and (d): 15%.

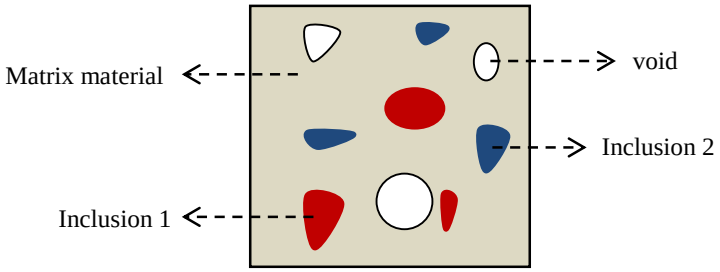

Figure 6.7: Schematic representation of an RVE

heterogeneities at the micro scale, d, should be very small compared to the RVE size. The above mentioned relations between the sizes of the macro body, RVE size, and micro heterogeneities, can be explained by the following inequality:

$$d \ll l \ll L, \tag{6.50}$$

where, d is the size of inclusions, l is the size of the RVE and L is the size of the body at macro level. This relation is called separation of scales [Hashin (1983)]. In the coupled multi-scale finite element approach, each integration

Gauss point of the macro structure mesh will be associated to one RVE. It means that for each Gauss point, we assume the RVE as the micro structure of the material. Separation of scales is illustrated in Figure (6.8). The history of coupled

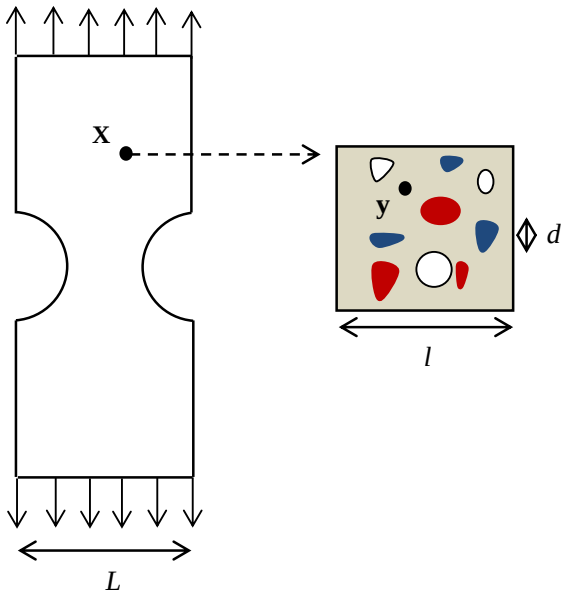

Figure 6.8: Separation of scales

multi-scale model dates back to 1980's and 1990's when the basic ideas behind the multi-scale theory were introduced by Suquet (1985), Guedes and Kikuchi (1990), Terada and Kikuchi (1995), Ghosh et al. (1995) and Ghosh et al. (1996). The modeling approach introduces a stress-strain relationship at each macroscopic point as the homogenization of stresses and strains of microscopic points (transitional or RVE level) associated to the macroscopic point under study. Using the finite element approximation to continuum mechanics, coupled multi-scale approach solves two boundary value problems, namely macroscopic and microscopic, at the same time. The microscopic, or transitional or RVE, problem is actually solved for each macroscopic integration Gauss point. The procedure of coupled multi-scale problem is schematically shown in Figure (6.9). This approach has the following advantages:

- At the RVE level, arbitrary geometries can be used;
- Time dependent and non-linear problems could be solved;

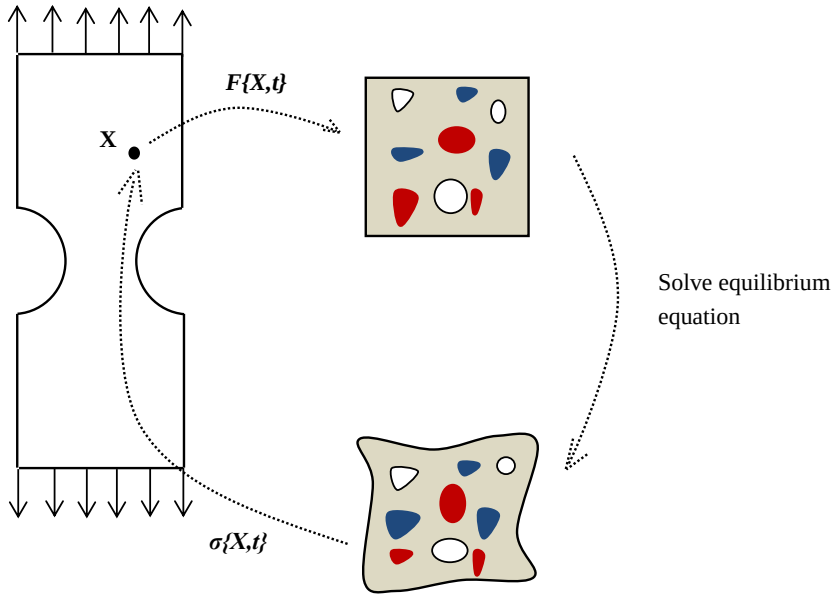

Figure 6.9: Schematic representation of coupled multi-scale problem

- The possible interactions between different constituents and other eventual phenomena such as phase transformation could be modelled using appropriate algorithms [Kouznetsova and Geers (2008)];
- Large deformations are applicable at both macro and micro level;
- In case just the behaviour of the material at macro scale is of interest, regardless of RVE behaviour, it is possible to consider only the macro structure behaviour which is a consequence of the RVE characteristics.

6.3.1 Coupled Multi-scale for polymers

Polymeric materials have become the reference material for high reliability and performance applications. However, their performance in service conditions is difficult to predict, due in large part to their inherent complex morphology, which leads to non-linear and anisotropic behaviour, highly dependent on the thermo-mechanical environment under which it is processed [Araujo et al. (2014)]. In order to improve the mechanical properties of polymers, microstructural adaptations are common procedures. For example, suitable scattering of low modulus

rubber particles into the microstructure of amorphous and semi-crystalline polymers remarkably improves toughness and impact resistance [Smit (1998)]. Performing experimental studies has been a way to observe the behaviour of different materials including polymeric materials. There is a large number of experimental studies conducted on polymers in order to understand different features and aspects of deformation behaviour of polymers such as mechanical behaviour e.g. Raha and Bowden (1972), Boyce and Arruda (1990), Diez (2010) to name a few. In order to avoid expensive, time wise and cost wise, experimental procedures, powerful simulation tools in order to characterize the behaviour of polymers are required.

Semi-crystalline polymers often have spherulitic structure which consists of radial assembly of crystalline lamellae separated by amorphous layers [Ghorbel (2008)]. In view of existing different phases into the structure of these materials, using multi-scale approach seems really useful and applicable. Parks and Azhi (1990), Dahoun (1992), lee et al. (1993) and van Dommelin et al. (2003) proposed multi-scale models to describe the behaviour of semi-crystalline polymers at large strains. Modelling small deformation of semi-crystalline polymers using multi-scale approach has been accomplished by some authors e.g. Nikolov and Doghri (2000), Nikolov et al. (2002), Drozdov and Gupta (2003) and Drozdov and Christiansen (2003). Contrary to semi-crystalline polymers, no crystalline phase in observed in the structure of amorphous polymers. Smit et al. (1998) used multi-level finite element modelling (coupled multi-scale) in order to predict the deformation behaviour of heterogeneous polymeric materials. One may consider the work as one of the first applications of coupled multi-scale approach for polymeric materials available in the open literature. Smit et al. (1999) predicted the mechanical behaviour of voided polycarbonate by spatial discretization of the microstructure of the material. They used the Leonov model for characterizing the behaviour of the glassy matrix material. Smit et al. (2000) performed coupled multi-scale simulations on rubber modified notched and hour-glass-shaped polycarbonate and polystyrene tensile specimen with different volume fraction of rubbery particles.

6.3.2 Numerical examples

In this section, some numerical examples are presented using coupled multi-scale analysis for heterogeneous polymers. As mentioned before, rubber toughening is a process applied to polymeric material in order to deal with brittleness of the material. In this chapter, RT-PS is considered for the numerical examples. The rubbery particles are considered to occupy 10% of the total volume faction of the material. A flat grooved specimen under uniaxial loading is simulated. The finite element mesh of the macro structure and also the micro-structural sample associated to each integration Gauss point of the macro structure is shown in Figure (6.10). The macro structure is descritized with 30 eight noded quadrilate-

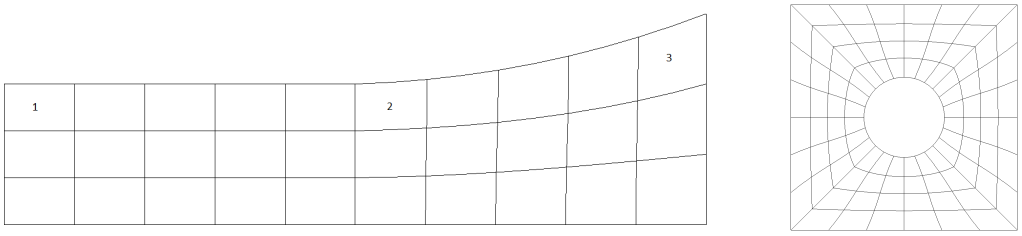

(a) (b)

Figure 6.10: Finite element discretization of the coupled multi-scale simulation of a flat grooved specimen; (a): spatial discretization of the macro structure; (b): Spatial discretization of the micro-structural sample.

rial elements with reduced four integration Gauss points. The mesh of the micro structural sample includes 96 eight noded quadrilateral elements with reduced integration. The element numbered $1, 2$ and 3 in the macro-structure mesh are the elements for which the evolution of effective stress at micro level will be given in Figures (6.14) and (6.15), respectively. Total displacement of $u = 0.5mm$ is applied and the deformation speed is considered $\dot{u} = 0.75mm/min$. It is expected that by introduction of porosity into a homogeneous material (Practically dispersing rubbery particles into homogeneous polymer), some changes in the deformation behaviour will be observed. First of all, due to the reduction in the stiffness of the material, the slope of the elastic regime is expected to be reduced. Reduced yield behaviour and also decreased softening behaviour are two more expected changes. In order to check if the mentioned changes are captured using

the coupled multi-scale analysis, the simulation is performed at macro scale, using the finite element mesh shown in Figure (6.10a), as well. Figure (6.11) shows the force displacement curve for both homogeneous and heterogeneous materials. It

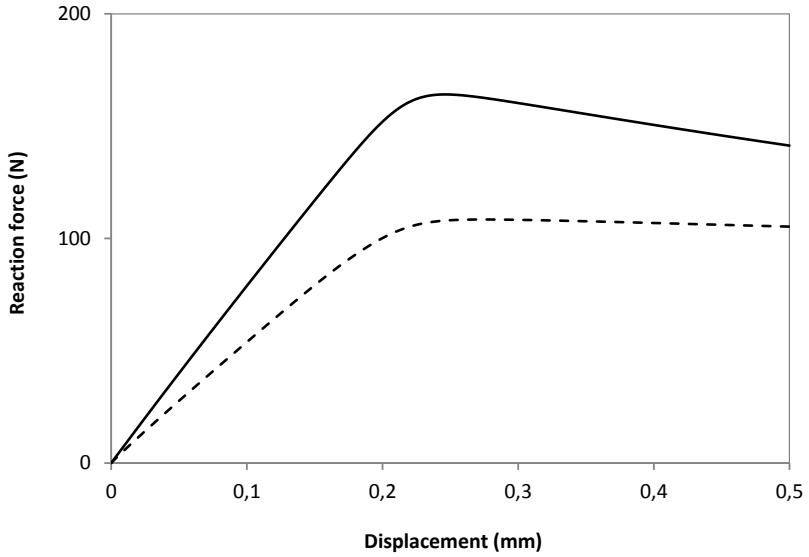

Figure 6.11: The force-displacement curves for heterogeneous and homogeneous material, solid line: homogeneous material and dashed line: heterogeneous material.

can be clearly observe that, using coupled multi-scale analysis, it was possible to capture the expected changes in the mechanical behaviour of RT-PS compared to PS at macro scale. For the sake of comparison between the RT-PS and PS, the contour plots of distribution of effective stress at two different stages of the deformation are shown in Figures (6.12) and (6.13). As expected, it can be seen in Figure (6.12) that although the same pattern of distribution of effective stress is observed for both neat (undamaged) and rubber modified (damaged) materials, the level of stress in the rubber modified material is less than homogeneous one. This is consistent with the force-displacement curves depicted in Figure (6.11). In other words, when the polymeric material is rubber modified, the resistance to load decreases and it is because of the reduction in the stiffness of the material. Similarly to Figure (6.12), it can be seen that when the load is completely applied, Figure (6.13), the pattern of deformation is almost the same for both materials

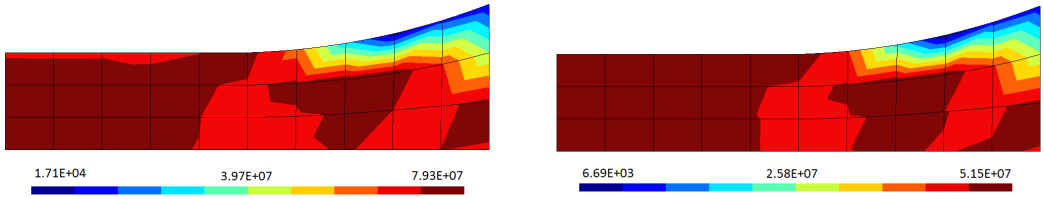

(a) (b)

Figure 6.12: The contour plot of the effective stress at macro level using macro and coupled analyses when $u = 0.25mm$, (a):macro analysis; (b): coupled analysis.

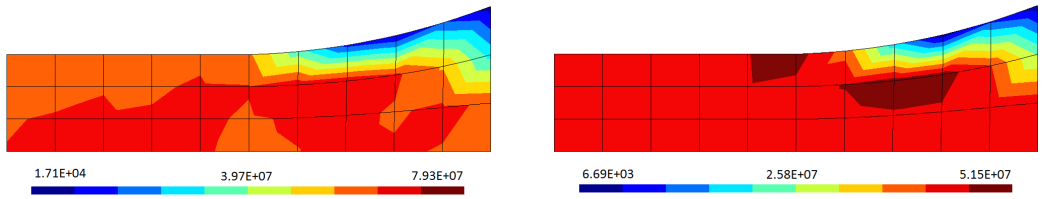

(a) (b)

Figure 6.13: The contour plot of the effective stress at macro level using macro and coupled analyses when $u = 0.5mm$, (a):macro analysis; (b): coupled analysis.

with reduced level of load tolerant for heterogeneous material compared to the undamaged material.

In order to observe how simultaneously macro structure and micro structure deformation proceeds, the contour plots of effective stress at both macro structure and micro structure are given. Figure (6.14) shows contour plots at macro structure and also micro structural level at three different regions of the specimen when displacement of $u = 0.25mm$ is applied. As mentioned before, one of the advantages of using coupled multi-scale simulations is that the evolution of different parameters such as effective stress at both macro structure and micro structure could be monitored simultaneously. In order to observe the evolution of effective stress, the contour plots of effective stress at both levels will be given when $u = 0.5mm$, total deformation, is applied in Figure (6.15).

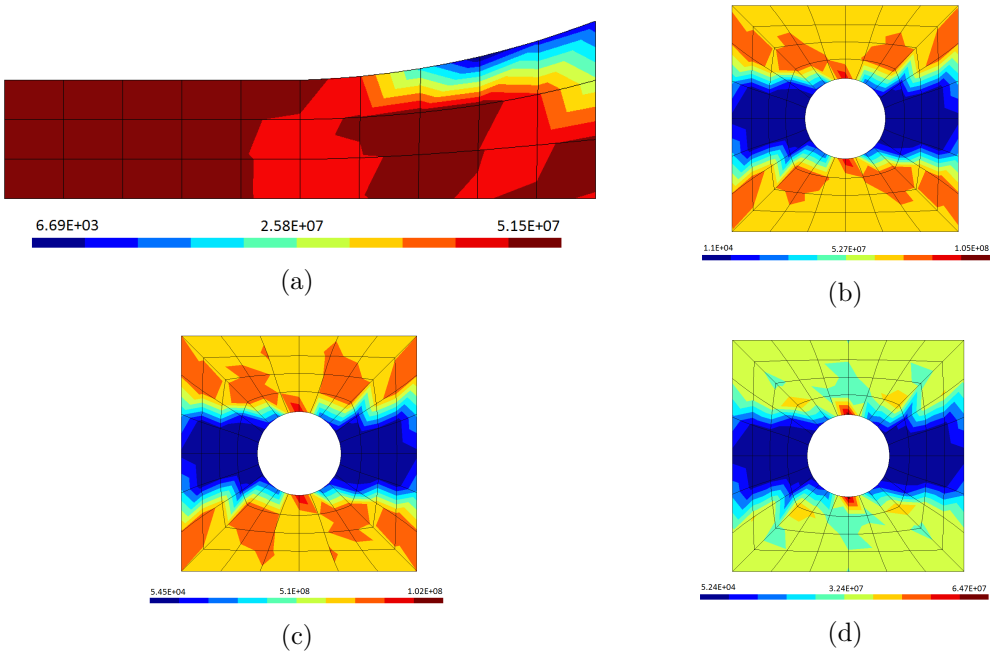

Figure 6.14: The contour plot of the effective stress at both macro level and micro level when $u = 0.25mm$, (a):macro structure; (b): micro-structural sample (1); (c):micro-structural sample (2) and (d): micro-structural sample (3).

6.4 Comparison

In this section, the results of both approaches, namely continuum modelling and coupled multi-scale analysis of porous polymers, are compared. Figure (6.16) shows the force-displacement curves for the tensile test on the flat grooved specimen for which the spatial discretization was given in Figure (6.10a). Considering Figures (6.11) and (6.16), it is obviously realized that the expected changes in the deformation behaviour of Polystyrene by rubber toughening are captured with both approaches. Nevertheless, it can be seen in Figure (6.16) that the yield behaviour in the force-displacement curve is overestimated by the continuum model compared to coupled multi-scale analysis. Besides, the post yield softening is also overestimated by the continuum model. This differences in the predictions could be attributed to the followings:

- The issue of RVE size was not addressed when the micro-structural sample was created. In other words, if the micro-structural sample was defined so

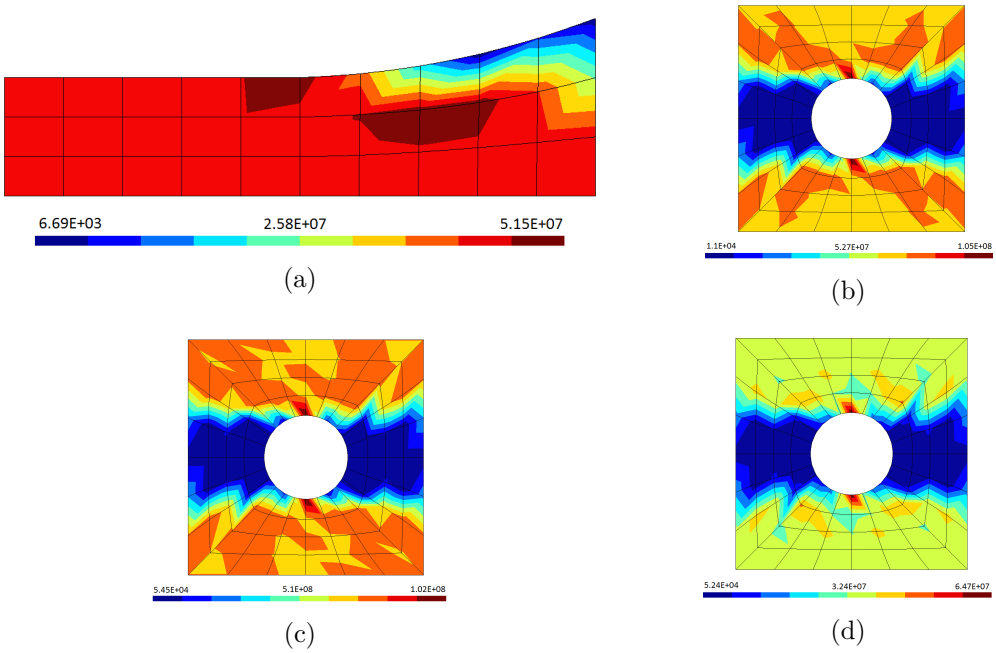

Figure 6.15: The contour plot of the effective stress at both macro level and micro level when $u = 0.5mm$, (a):macro structure; (b): micro-structural sample (1); (c):micro-structural sample (2) and (d): micro-structural sample (3).

that it could be statistically representative, it would be expected to observe smaller differences in the predictions of two approaches;

- Considering plane strain conditions at the RVE level implies that the rubbery inclusions are like unidirectional fibres inside the polymeric matrix, but actually they are more like spheres dispersed in the matrix. Hence, in order to have more realistic coupled analysis, it is required to create three dimensional micro structural samples with dispersed spheric rubbery particles;

- The first order coupled multi-scale approach, which is used in this study, is not capable of characterizing the softening and strain localization properly. Using second order coupled multi-scale or non-local approach would provide more accurate predictions;

- In addition to the aforementioned issues, the appropriateness of periodic

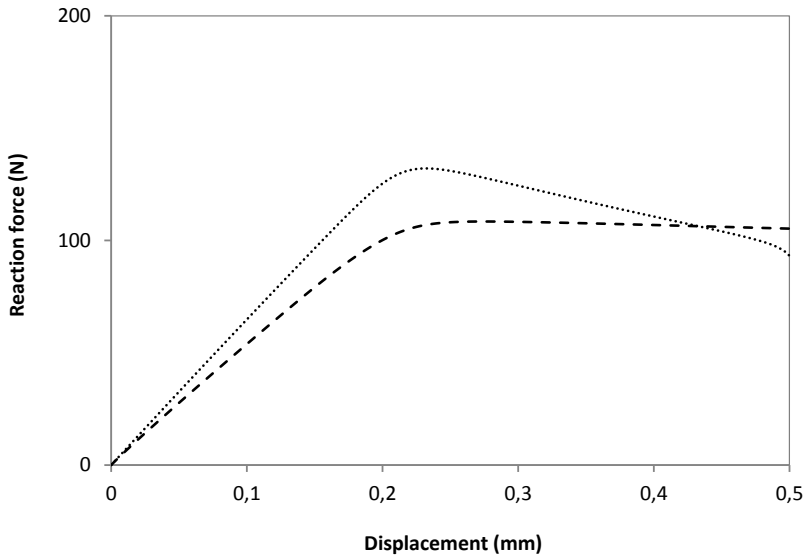

Figure 6.16: The force-displacement curves for Rubber Toughened Polystyrene (RT-PS), dotted line: continuum model; dashed line: coupled multi-scale.

boundary conditions at the RVE level and its capability to lead to realistic results should be investigated.

In order to see the stress distribution through the specimen with both approaches, the contour plots of effective stress with both approaches when half of the deformation is applied will be given. Figures (6.17) depicts the contour plots of effective stress when $u = 0.25mm$. Figure shows that both continuum modelling

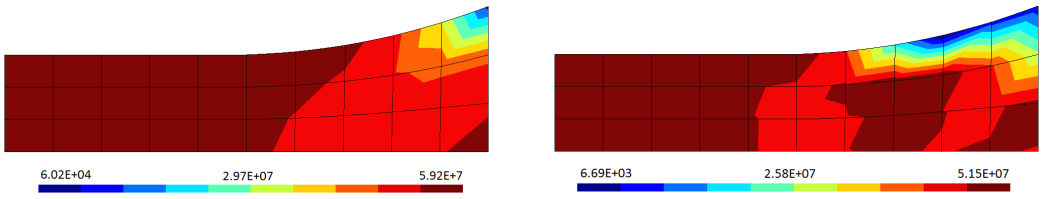

(a) (b)

Figure 6.17: The contour plot of the effective stress for RT-PS at macro level using continuum model and coupled analyses when $u = 0.25mm$, (a):continuum model; (b): coupled analysis.

approach and coupled multi-scale give almost the same deformation pattern with

some differences in the values. Again, in order to have closer simulations with both approaches, the previously mentioned issues should be taken care of.

6.5 Conclusions

Brittle failure phenomena happens when homogeneous amorphous polymers are under severe stress states. As mentioned before, in order to improve the ductility of this kind of materials, rubber toughening, which is basically blending rubber particles into the material, is used. In order to predict the deformation behaviour of rubber toughened amorphous polymers, a possible approach, among other possibilities, is to develop a constitutive model capable of taking into account the effects of rubbery particles on the overal deformation behaviour. In this chapter, a continuum level constitutive model was developed using the Leonov based model, presented in Chapter 3, and Gurson model. The rubbery particles were characterized as voids and the nucleation of voids was neglected. Furthermore, the derivation of integration algorithm including state update and consistent tangent operator was given. Using the developed model, the plastic deformation is not incompressible any more and due to volumetric changes of voids during plastic deformation, the flow potential has both hydrostatic and deviatoric terms. Considering the well-known effects of additive rubbery particles on the deformation behaviour of amorphous polymers and also the results provided in this chapter, it could be concluded that the model is capable to predict the overall deformation behaviour of rubber toughened amorphous polymers qualitatively.
Besides, coupled multi-scale approach was used for simulating the deformation behaviour of RT-PS. A micro-structural sample with 10% of porosity was considered as the RVE of the analysis. It is known that dispersing rubbery particles affect the deformation behaviour of polymeric material in certain ways, namely reduction in the stiffness, yield reduction and also reduced post yield softening. Comparing force-displacement curves obtained from coupled multi-scale analysis for heterogeneous material and macro-scale analysis for homogeneous material showed that changes in the deformation pattern are captured. Contour plots of effective stress of the homogeneous materials and heterogeneous material show the differences in the deformation pattern of different parts of the specimen.

Since one of the main advantages of the coupled multi-scale is analysing macro-structure and micro-structure simultaneously, some contour plots of the effective stress at both levels showed the evolution of deformation.
Finally, by making some comparisons between two approaches (continuum constitutive modelling of porous polymers and also coupled multi-scale analysis), it was realized that in order to have more reliable simulations, some issues such as addressing the RVE size, generating three dimensional micro-structural samples and investigating appropriateness of boundary conditions at the RVE level should be addressed.

Chapter 7

Conclusions and suggestions

In this chapter, the main goals of this thesis and the conclusions drawn from different parts of the work are reviewed. Then, based on the results and achievements of different sections, some suggestions are given for future work.

7.1 Objectives and achievements

The ultimate goal of this thesis was addressing the topic of modelling and analysis of the behaviour of polymeric materials at multiple scales, more specifically amorphous polymers, at different scales. After explaining the typical behaviour of polymeric materials, classification of polymers, reviewing different modelling approaches, motivation of this work and outline of the thesis in Chapter 1, the non-linear continuum mechanics theory and finite element method were reviewed in Chapter 2. Chapter 3 presented an elasto-viscoplastic model, including the formulation together with integration algorithm and implementation within an implicit FE code, capable of predicting the behaviour of not only amorphous polymers but also crystalline and semi-crystalline polymeric materials. In addition to thermoplastics, the mentioned model is capable of predicting the mechanical behaviour of thermosetting polymers. Characterizing the behaviour of polymers under different stress states is addressed in Chapter 4. Some modifications, using lode angle parameter, were introduced in Chapter 4 in order to improve the predictions of the Leonov based model, presented in Chapter 3. It is worth emphasizing that, to the author‘s knowledge, there is no prior work in polymer constitutive

modelling which addresses the topic of different stress states using stress invariants to modify the constitutive equations. In Chapter 5, microstructure analysis with different levels of porosity were presented. Based on the results obtained and the definition of Representative Volume Element, two criteria for determination of RVE size and an associated algorithm were proposed. Chapter 6 presented a continuum level constitutive model, which is basically a combination of the model presented in Chapter 3 and Gurson micro-mechanical model, in order to model the mechanical behaviour of rubber toughened polymeric materials. The derivation of the state update algorithm and consistent tangent operator were included. Chapter 6 also presented some coupled multi-scale analysis for porous amorphous polymers. The achievements of the different chapters are detailed in what follows.

Chapter 3

A three dimensional finite strain elasto-viscoplastic constitutive model which is capable of characterizing the behaviour of polymeric materials was formulated and presented in this chapter. The model was developed based on the single mode compressible Leonov model [Timmermans (1998), Govaert et al. (2000)]. The numerical integration algorithm for the model was reduced to the solution of only one equation return mapping procedure. The operator split methodology and the Newton-Raphson method are used to derive the state update algorithm and to obtain the numerical solution of the discretized evolution equations. Exact linearization of the discretized evolution equations resulted in a closed form formula for the corresponding consistent tangent operator. Through some numerical examples, the capability of the model to characterize the deformation behaviour of polymeric materials and the numerical efficiency were investigated.

Chapter 4

The model, introduced in Chapter 3, was modified to improve the prediction of the mechanical behaviour of polymers under different stress states. A specific constitutive model may, most likely, not provide good prediction of a specific polymer under different stress states with just one set of material properties. In other words, it is probably required to calibrate the material properties separately for different loading conditions in order to have good agreement between

simulations and experimental results under different loading conditions. Some experimental results, for a commercial grade of Polycarbonate, called Makrolon 2607, under three different stress states were taken from [Diez (2010)]. The required material properties were determined and calibrated using uniaxial compression experiments. According to the initial simulations, some modifications in the constitutive relations, mainly for softening evolution function and hardening stress, were proposed using the lode angle parameter. The results with the modified model showed remarkable improvements in the predictions of the model under different loading conditions.

Chapter 5

Some micro-structural analyses, on samples with Polystyrene (PS) as the matrix material and rubbery particles as inclusions (Rubber Toughened Polystyrene or RT-PS) with two different fractions of rubbery particles under periodic boundary condition, were presented. Performing preliminary analysis on different realizations for the same sample size (VES) and the same volume fraction of inclusions (IVF), leaded to the conclusion that the issue of RVE size should be addressed in order to have the micro-structural sample representative. Based on the definition of the RVE, two criteria were introduced in order for determination of the RVE size. For IVF equal to 10% and also 15%, the statistical analysis were performed and based on the proposed criteria and the associated algorithm, the RVE size was obtained.

Chapter 6

Rubber toughening is a procedure to increase the fracture toughness of polymeric materials. This chapter presented a continuum level constitutive model in order to characterize the behaviour of heterogeneous polymeric materials. In contrast to the models presented in Chapters 3 and 4, the assumption of plastic incompressibility does not hold. In other words, while assuming homogeneous material, the plastic flow is totally deviatoric but for porous material the plastic dissipation is considered both volumetric and deviatoric. The model presented in this chapter is essentially incorporation of Gurson‘s yield function into the model presented in Chapter 3. The formulation of the model was derived and

then the integration algorithm, including the state update procedure and also the derivation of consistent tangent operator was presented. RT-PS with different levels of rubbery particles was considered. The stress-strain curves, together with evolution of the porosity were given. This chapter also presented coupled multi-scale (micro-macro) analysis of rubber toughened Polystyrene (RT-PS) in order to characterize the behaviour of RT-PS and observe how the mechanical behaviour changes compared to the homogeneous material without rubbery particles. The force-displacement curves of a tensile test on a flat grooved specimen for homogeneous and heterogeneous materials are compared and the expected changes in the deformation behaviour were observed. Besides, the effective stress of the macro-structure as well as micro-structure were shown through the deformation. Some concluding comparisons between the two approaches were given as well.

7.2 Suggestions for future research

In the final section of this thesis, some suggestions for future research, based on the results and achievements of this work, will be given. According to the work in different chapters of this thesis, the suggestions are provided in the following:

- As presented in Chapter 4, experimental results available for Makrolon 2607 were for cylinder upsetting, cube compression and tensile test on a dumbbell shape specimen. For the aforementioned cases, it was shown that the modified model was capable of providing reasonable predictions. In order to check the capability of the model under more complex stress states, it seems necessary to perform some other experiments, specifically experiments on the butterfly specimen, and make some comparisons between simulations and experimental results. Performing such experiments would reveal if there would be more enhancements and modifications required to be applied in order for the model to capture a wider range of stress states. Besides, to check if the model could characterize adequately other polymeric materials, it would be interesting to check other polymers for which there are at least

two or more stress states available in the literature.

- For the micro-structural analysis and RVES determination, there are different issues to be studied in more detail. Since only one Inclusion Size Range (ISR) was used in this study, it could be of further interest to study the effect of having larger or smaller ISR on the RVES. A comparison between regularly distributed inclusions and irregularly distributed ones, in terms of obtained RVES, can be performed. Determination of the RVES for other loading conditions could be interesting too. The question of the effect of employed boundary condition on the RVES could also be answered by using the other boundary conditions. Performing an optimization procedure in order to optimize the IVF with respect to different factors e.g. maximum stress at failure or maximum strain at failure seems attractive. Moreover, having some RVE analysis and RVES determination in 3D will eventually provide the opportunity to realize how different are the results in 2D from 3D.

- For the model developed for continuum modelling of porous polymers, making some comparisons with the experiments mentioned in the previous item could give an idea how quantitatively accurate is the model. If the comparisons are not good, there should be some improvements in the model to make it more accurate. First, the nucleation of voids was neglected. Hence, adding the nucleation of voids to void growth rate might help to improve the predictions. In addition, using GTN model instead of original Gurson model might also provide better and improved predictions of the model.

- For coupled multi-scale analysis, developing 3D micro-structural samples seems necessary. This is due to the fact that, with 2D micro-structural samples, it is in fact assumed that the inclusions are as unidirectional fibres while in reality, the inclusions are more similar to spherical particles

dispersed in the matrix material. After generating 3D micro-structural samples, mentioned before, addressing the RVE size is of importance as well in order to be sure about the representativeness and also the accuracy of the results. Performing some experiments on a neat polymeric material provides the opportunity to obtain the material properties required for the model. Then, having some experiments conducted on rubber toughened class of the same material, will help to evaluate the results of the coupled analysis. Making comparisons between coupled simulations and experiments might also provide the opportunity to check which kind of boundary conditions at micro level will give better predictions of experiments.

Appendix A

Softening evolution function for Leonov based model

In this Appendix, the algebraic manipulations for softening evolution and consequently to derive relation (3.39) for the viscosity are provided. By substituting relation (3.33) in relation (3.31) we obtain:

$$\eta = A_0 \exp\left[\frac{\Delta H}{RT} + \frac{\mu P}{\tau_0} - D\right]\left[\frac{\tau^{eq}}{\sinh\left(\tau^{eq}/\tau_0\right)}\right]. \tag{A.1}$$

Rearranging the equation (3.37) results in:

$$\dot{\overline{\gamma}}^p = \left(\frac{D_\infty}{h(D_\infty - D)}\right)\dot{D}. \tag{A.2}$$

Then, we integrate both sides of the above relation through the time step $[0, t]$:

$$\int_0^t \dot{\overline{\gamma}}^p dt = \int_0^t \left(\frac{D_\infty}{h(D_\infty - D)}\right)\dot{D}dt. \tag{A.3}$$

From relation (A.3) we can write:

$$\overline{\gamma}^p|_0^t = \left(-\frac{D_\infty}{h}\right)\ln\left(D_\infty - D\right)|_0^t. \tag{A.4}$$

Applying the initial conditions $\overline{\gamma}^p = 0$ and $D = 0$ at $t = 0$ and some final rearrangements gives:

$$D = D_\infty\left[1 - \exp\left(\frac{-h\overline{\gamma}^p}{D_\infty}\right)\right]. \tag{A.5}$$

Or equivalently,

$$D = D_\infty \left[1 - \exp\left(\frac{-h\sqrt{3}\bar{\varepsilon}^p}{\sqrt{2}D_\infty} \right) \right]. \tag{A.6}$$

Where, $\bar{\varepsilon}^p$ is accumulated plastic strain rate. The rate of accumulated plastic strain rate is given by:

$$\dot{\bar{\varepsilon}}^p = \sqrt{\frac{2}{3}\mathbf{d}^p : \mathbf{d}^p}. \tag{A.7}$$

Substituting relation (A.6) in relation (A.1) results in relation (3.39) for the viscosity.

Appendix B

Derivation of tangent operator for Leonov based model

In this appendix, exact linearization of the state update relations is presented in order to show how to derive relation (3.88) for the plastic consistent tangent operator. Tangent operator is obtained as the derivative of stress in order to strain:

$$\mathsf{D} = \frac{d\boldsymbol{\tau}_{n+1}}{d\boldsymbol{\varepsilon}_{n+1}}. \tag{B.1}$$

According to equation (3.41), we have:

$$d\boldsymbol{\tau}_{n+1} = d\boldsymbol{\tau}_{n+1}^{driving} + d\boldsymbol{\tau}_{n+1}^{hardening}. \tag{B.2}$$

Thus, the relation (B.1) is rewritten as follows:

$$\mathsf{D} = \frac{d\left(\boldsymbol{\tau}_{n+1}^{driving} + \boldsymbol{\tau}_{n+1}^{hardening}\right)}{d\boldsymbol{\varepsilon}_{n+1}}. \tag{B.3}$$

First, we compute the first term in the above relation, $d\boldsymbol{\tau}_{n+1}^{driving}/d\boldsymbol{\varepsilon}_{n+1}$. Driving stress tensor is given by:

$$\boldsymbol{\tau}_{n+1}^{driving} = \mathbf{s}_{n+1} - p_{n+1}\mathbf{I} \tag{B.4}$$

Differentiation of the above relation gives:

$$d\boldsymbol{\tau}_{n+1}^{driving} = d\mathbf{s}_{n+1} - dp_{n+1}\mathbf{I}. \tag{B.5}$$

The first term of the above relation, in more detail, is:

$$d\mathbf{s}_{n+1} = d\left[\frac{\eta_{n+1}}{\eta_{n+1} + \Delta t\ G}\ \mathbf{s}_{n+1}^{trial}\right] \tag{B.6}$$

or equivalently, broken down to,

$$d\mathbf{s}_{n+1} = d\left(\frac{\eta_{n+1}}{\eta_{n+1} + \Delta t\ G}\right)\mathbf{s}_{n+1}^{trial} + \left(\frac{\eta_{n+1}}{\eta_{n+1} + \Delta t\ G}\right)d\mathbf{s}_{n+1}^{trial}. \tag{B.7}$$

We have:

$$d\mathbf{s}_{n+1}^{trial} = d(2G\boldsymbol{\varepsilon}_{d\ n+1}^{e\ trial}) = d(2G\boldsymbol{\varepsilon}_{d\ n+1}) = 2G\left[\mathsf{I}_s - \frac{1}{3}(\mathbf{I}\otimes\mathbf{I})\right] : d\boldsymbol{\varepsilon}_{n+1}. \tag{B.8}$$

In order to complete the first term in relation (B.5), we have to compute the following:

$$d\left(\frac{\eta_{n+1}}{\eta_{n+1} + \Delta t\ G}\right) = \frac{\Delta t\ G\ d\eta_{n+1}}{(\eta_{n+1} + \Delta t\ G)^2}. \tag{B.9}$$

Consequently and based on relations (B.5) and (B.9), we need to compute the terms $d\eta_{n+1}$ and dp_{n+1} in order to obtain $d\boldsymbol{\tau}_{n+1}^{driving}$. Two relations are considered to compute the mentioned terms. In order to be consistent with the state update algorithm, the first relation is the residual equation, used in state update algorithm and introduced in relation (3.70). The second equation is the following:

$$p_{n+1} + K\mathbf{I} : \varepsilon_{n+1} = 0. \tag{B.10}$$

Therefore, we can write the following system of two equations.

$$\begin{cases} R_1(\eta_{n+1}, p_{n+1}) = \eta_{n+1} - (C_1\ C_2/C_3) = 0 \\ R_2(\eta_{n+1}, p_{n+1}) = p_{n+1} + K\mathbf{I} : \boldsymbol{\varepsilon}_{n+1} = 0 \end{cases} \tag{B.11}$$

According to the above system of equations, we can write:

$$\begin{bmatrix} (\partial R_1/\partial\eta_{n+1}) & (\partial R_1/\partial p_{n+1}) \\ (\partial R_2/\partial\eta_{n+1}) & (\partial R_2/\partial p_{n+1}) \end{bmatrix} \begin{bmatrix} d\eta_{n+1} \\ dp_{n+1} \end{bmatrix} =$$

$$\begin{bmatrix} -(\partial R_1/\partial \boldsymbol{\varepsilon}_{n+1}) : d\boldsymbol{\varepsilon}_{n+1} \\ -(\partial R_2/\partial \boldsymbol{\varepsilon}_{n+1}) : d\boldsymbol{\varepsilon}_{n+1} \end{bmatrix}. \tag{B.12}$$

Now, it is required to compute the derivatives of the two equations in order to η_{n+1}, p_{n+1} and $\boldsymbol{\varepsilon}_{n+1}$. the first term, $(\partial R_1/\partial \eta_{n+1})$, is already computed and presented in relation (4.23).

$$\frac{\partial R_1}{\partial p_{n+1}} = -\frac{C_1\ C_2\ \mu}{C_3\ \tau_0} \tag{B.13}$$

$$\frac{\partial R_2}{\partial \eta_{n+1}} = 0 \tag{B.14}$$

$$\frac{\partial R_2}{\partial p_{n+1}} = 1 \tag{B.15}$$

The derivatives of the equations in order to strain, $\boldsymbol{\varepsilon}_{n+1}$, are the followings:

$$-\frac{\partial R_1}{\partial \boldsymbol{\varepsilon}_{n+1}} = F_1[1 - F_2 - F_3](\mathbf{I}_d : \mathbf{s}^{trial}_{n+1}) - \frac{C_1 \mu K}{\tau_0 C_3}\mathbf{I}$$

$$= F_1[1 - F_2 - F_3]\mathbf{s}^{trial}_{n+1} - \frac{C_1 \mu K}{\tau_0 C_3}\mathbf{I}, \tag{B.16}$$

$$-\frac{\partial R_2}{\partial \boldsymbol{\varepsilon}_{n+1}} = -K\mathbf{I}, \tag{B.17}$$

where, the factors F_1, F_2 and F_3 are introduced in relations (B.18)-(B.20).

$$F_1 = \frac{\sqrt{2}GC_1\eta_{n+1}}{C_3\,(\eta_{n+1} + \Delta G)\,||\mathbf{s}^{trial}_{n+1}||} \tag{B.18}$$

$$F_2 = \frac{C_2 h \Delta t}{\eta_{n+1}} \exp\left(\frac{-h\sqrt{3}C_4}{D_\infty}\right) \tag{B.19}$$

$$F_3 = \frac{C_2}{C_3\tau_0} \cosh\left(\frac{C_2}{\tau_0}\right) \tag{B.20}$$

Having determined the components of relation (B.12), we can write:

$$\begin{bmatrix} d\eta_{n+1} \\ dp_{n+1} \end{bmatrix} = \begin{bmatrix} (\partial R_1/\partial \eta_{n+1}) & (\partial R_1/\partial p_{n+1}) \\ (\partial R_2/\partial \eta_{n+1}) & (\partial R_2/\partial p_{n+1}) \end{bmatrix}^{-1} \tag{B.21}$$

$$\begin{bmatrix} -\left(\partial R_1/\partial \boldsymbol{\varepsilon}_{n+1}\right) : d\boldsymbol{\varepsilon}_{n+1} \\ -\left(\partial R_2/\partial \boldsymbol{\varepsilon}_{n+1}\right) : d\boldsymbol{\varepsilon}_{n+1} \end{bmatrix}. \tag{B.22}$$

By computing the aforementioned invert matrix and performing some straight forward algebric manipulations, we can acheive the follwoing relations:

$$d\eta_{n+1} = \left(\frac{1}{X}\right)\left(F_1\left[1 - F_2 - F_3\right]\mathbf{s}_{n+1}^{trial} - \frac{C_1\mu K}{\tau_0 C_3}\mathbf{I}\right) : d\boldsymbol{\varepsilon}_{n+1} \tag{B.23}$$

$$-\left(\frac{C_1 C_2 \mu}{C_3 \tau_0 X}\right)\left(K\mathbf{I} : d\boldsymbol{\varepsilon}_{n+1}\right) \tag{B.24}$$

$$dp_{n+1} = -K\mathbf{I} : d\boldsymbol{\varepsilon}_{n+1} \tag{B.25}$$

Using relations (B.3),(B.5),(B.7),(B.8),(B.9), (B.24) and (B.25), the driving part of the consistent tangent operator is obtained. In order to complete the relation, we need to add the hardening contribution to the tangent operator, $d\boldsymbol{\tau}_{n+1}^{hardening}/d\boldsymbol{\varepsilon}_{n+1}$. The hardening part of the tangent operator is the following:

$$\frac{d\boldsymbol{\tau}_{n+1}^{hardening}}{d\boldsymbol{\varepsilon}_{n+1}} = H\left[\mathsf{I}_s - \frac{1}{3}(\mathbf{I}\otimes\mathbf{I})\right] \tag{B.26}$$

Appendix C

Tangent operator for different stress states model

As mentioned in Chapter 4, the tangent operator for different stress states model is given by:

$$\mathsf{D}^p = K\left(\mathbf{I}\otimes\mathbf{I}\right) + \left(F_1 + F_5\right)\mathsf{I}_d + F_2\left(\mathbf{s}_{n+1}\otimes\mathbf{I}\right) + F_3\left(\mathbf{s}_{n+1}\otimes\mathbf{z}_{n+1}\right) + F_4\left(\mathbf{s}_{n+1}\otimes\mathbf{s}_{n+1}\right) +$$

$$F_6\left(\boldsymbol{\varepsilon}_{d\ n+1}^{tot}\otimes\mathbf{z}_{n+1}\right) + F_7\left(\boldsymbol{\varepsilon}_{d\ n+1}^{tot}\otimes\mathbf{s}_{n+1}\right) + F_8\left(\boldsymbol{\varepsilon}_{d\ n+1}^{tot}\otimes\mathbf{I}\right). \tag{C.1}$$

The components of tensor $\mathbf{z}_{n+1}$ in 2D space (for plane strain and axisymmetric simulations) are given by:

$$\mathbf{z}_{n+1}(xx) = \frac{1}{3}\left[(EF - AB - BC) + 2(AC)\right], \tag{C.2}$$

$$\mathbf{z}_{n+1}(yy) = \frac{1}{3}\left[(EF - AC - BC) + 2(AB)\right], \tag{C.3}$$

$$\mathbf{z}_{n+1}(zz) = \frac{1}{3}\left[(-AB - AC) + 2\left(BC - EF\right)\right], \tag{C.4}$$

$$\mathbf{z}_{n+1}(xy) = \mathbf{z}_{n+1}(yx) = -\frac{1}{2}D\left(E + F\right), \tag{C.5}$$

$$\mathbf{z}_{n+1}(xz) = \mathbf{z}_{n+1}(zx) = \mathbf{z}_{n+1}(yz) = \mathbf{z}_{n+1}(zy) = 0, \tag{C.6}$$

where, the factors A, B, C, D, E, F are given by:

$$A = \boldsymbol{\varepsilon}_{n+1}^{e\ trial}(zz) - \frac{1}{3}\left(\boldsymbol{\varepsilon}_{n+1}^{e\ trial}(xx) + \boldsymbol{\varepsilon}_{n+1}^{e\ trial}(yy) + \boldsymbol{\varepsilon}_{n+1}^{e\ trial}(zz)\right),$$

$$B = \boldsymbol{\varepsilon}_{n+1}^{e\ trial}(xx) - \frac{1}{3}\left(\boldsymbol{\varepsilon}_{n+1}^{e\ trial}(xx) + \boldsymbol{\varepsilon}_{n+1}^{e\ trial}(yy) + \boldsymbol{\varepsilon}_{n+1}^{e\ trial}(zz)\right), \tag{C.7}$$

$$C = \boldsymbol{\varepsilon}_{n+1}^{e\ trial}(yy) - \frac{1}{3}\left(\boldsymbol{\varepsilon}_{n+1}^{e\ trial}(xx) + \boldsymbol{\varepsilon}_{n+1}^{e\ trial}(yy) + \boldsymbol{\varepsilon}_{n+1}^{e\ trial}(zz)\right), \tag{C.8}$$

$$E = F = \frac{1}{2}\boldsymbol{\varepsilon}_{n+1}^{e\ trial}(xy) = \frac{1}{2}\boldsymbol{\varepsilon}_{n+1}^{e\ trial}(yx). \tag{C.9}$$

In a generic case of 3D simulation, the components of the tensor $\mathbf{z}_{n+1}$ are given by:

$$\mathbf{z}_{n+1}(xx) = \frac{1}{3}\left[2\left(BC - EE\right) - A\left(B + C\right) + D^2 + F^2\right], \tag{C.10}$$

$$\mathbf{z}_{n+1}(yy) = \frac{1}{3}\left[-\left(BC - EE\right) - A\left(B + 2C\right) + D^2 - 2F^2\right], \tag{C.11}$$

$$\mathbf{z}_{n+1}(zz) = \frac{1}{3}\left[-\left(BC - EE\right) + A\left(2B - C\right) - 2D^2 + F^2\right], \tag{C.12}$$

$$\mathbf{z}_{n+1}(xy) = EF - DC, \tag{C.13}$$

$$\mathbf{z}_{n+1}(yz) = DF - AE, \tag{C.14}$$

$$\mathbf{z}_{n+1}(xz) = DE - BF, \tag{C.15}$$

where, the factors A, B, C, D, E, F are, in 3D case, given by:

$$A = \boldsymbol{\varepsilon}_{n+1}^{e\ trial}(xx) - \frac{1}{3}\left(\boldsymbol{\varepsilon}_{n+1}^{e\ trial}(xx) + \boldsymbol{\varepsilon}_{n+1}^{e\ trial}(yy) + \boldsymbol{\varepsilon}_{n+1}^{e\ trial}(zz)\right), \tag{C.16}$$

$$B = \boldsymbol{\varepsilon}_{n+1}^{e\ trial}(yy) - \frac{1}{3}\left(\boldsymbol{\varepsilon}_{n+1}^{e\ trial}(xx) + \boldsymbol{\varepsilon}_{n+1}^{e\ trial}(yy) + \boldsymbol{\varepsilon}_{n+1}^{e\ trial}(zz)\right), \tag{C.17}$$

$$C = \boldsymbol{\varepsilon}_{n+1}^{e\ trial}(zz) - \frac{1}{3}\left(\boldsymbol{\varepsilon}_{n+1}^{e\ trial}(xx) + \boldsymbol{\varepsilon}_{n+1}^{e\ trial}(yy) + \boldsymbol{\varepsilon}_{n+1}^{e\ trial}(zz)\right), \tag{C.18}$$

$$D = \frac{1}{2}\boldsymbol{\varepsilon}_{n+1}^{e\ trial}(xy), \tag{C.19}$$

$$E = \frac{1}{2}\boldsymbol{\varepsilon}_{n+1}^{e\ trial}(yz), \tag{C.20}$$

$$E = \frac{1}{2}\boldsymbol{\varepsilon}_{n+1}^{e\ trial}(xz). \tag{C.21}$$

The factors F_1-F_4 in relation (C.1) are given by:

$$F_1 = \frac{2G\eta_{n+1}}{\eta_{n+1} + \Delta tG} \tag{C.22}$$

$$F_2 = \frac{\Delta tG}{\eta_{n+1}\left(\eta_{n+1} + \Delta tG\right)}\left(F_9F_{10} - KF_{11}\right) \tag{C.23}$$

$$F_3 = \frac{\Delta tG}{\eta_{n+1}\left(\eta_{n+1} + \Delta tG\right)}\left(F_9F_{12}\right) \tag{C.24}$$

$$F_4 = \frac{\Delta tG}{\eta_{n+1}^2}\left(F_9F_{13}\right) \tag{C.25}$$

In relations (C.22)-(C.25), the factors F_9-F_{13} are given by relations (C.26)-(C.30).

$$F_9 = \frac{1}{1 - \left[\frac{N_1M_2}{M_3} + M_1\left(\frac{N_2M_3 - N_3M_2}{M_3^2}\right)\right]}. \tag{C.26}$$

$$F_{10} = -\frac{M_2M_1\mu K}{\tau_0} \tag{C.27}$$

$$F_{11} = \frac{\frac{M_1M_2\mu}{M_3\tau_0}}{1 - \left[\frac{N_1M_2}{M_3} + M_1\left(\frac{N_2M_3 - N_3M_2}{M_3^2}\right)\right]}. \tag{C.28}$$

$$F_{12} = -\frac{18hM_2M_6M_1\overline{\theta}_{n+1}\exp\left(M_5\right)}{\pi M_3\sqrt{1-\xi_{n+1}^2}}\left(\frac{2G}{||\mathbf{s}_{n+1}^{trial}||}\right)^3 \tag{C.29}$$

$$F_{13} = \left(\frac{M_2}{M_3}\right)\left[\frac{108M_1\exp\left(M_5\right)hM_6\overline{\theta}_{n+1}G\det\left(\mathbf{s}_{n+1}^{trial}\right)}{\pi\sqrt{1-\xi_{n+1}^2}}\right]\left(\frac{1}{||\mathbf{s}_{n+1}^{trial}||}\right)^5 -$$

$$\left(\frac{M_2}{M_3}\right)\left[\frac{M_1\exp\left(M_5\right)Gh\Delta t\left(1+\overline{\theta}_{n+1}^2\right)}{2\left(\eta_{n+1}+\Delta tG\right)||\mathbf{s}_{n+1}^{trial}||}\right]+\left(\frac{M_1}{M_3}\right)\left[\frac{\sqrt{2}G\eta_{n+1}}{\left(\eta_{n+1}+\Delta tG\right)||\mathbf{s}_{n+1}^{trial}||}\right]-$$

$$\left(\frac{M_1M_2}{M_3^2}\right)\left[\frac{\sqrt{2}G\eta_{n+1}}{\tau_0\left(\eta_{n+1}+\Delta tG\right)||\mathbf{s}_{n+1}^{trial}||}\right]\cosh\left(\frac{M_2}{\tau_0}\right) \tag{C.30}$$

The factors in relation (C.1), which are not introduced yet (F_5-F_8), are provided below.

$$F_5=\frac{1}{4}aH_{ini}\left(\overline{\theta}_{n+1}+5\right)\left[\overline{\varepsilon}_n^p+\frac{\Delta t}{3\left(\eta_{n+1}+\Delta tG\right)}\sqrt{3/2}||\mathbf{s}_{n+1}^{trial}||\right] \tag{C.31}$$

$$F_6=F_{14}-F_{15}F_{16} \tag{C.32}$$

where,

$$F_{14}=\frac{18aH_{ini}\overline{\boldsymbol{\varepsilon}}_{n+1}^p}{4\sqrt{3/2}\pi\sqrt{1-\xi_{n+1}^2}}\left(\frac{2G}{||\mathbf{s}_{n+1}^{trial}||}\right)^3 \tag{C.33}$$

$$F_{15}=\frac{\sqrt{3/2}aH_{ini}\Delta t||\mathbf{s}_{n+1}^{trial}||\left(\overline{\theta}_{n+1}+5\right)}{12\left(\eta_{n+1}+\Delta tG\right)^2} \tag{C.34}$$

$$F_{16}=-\left(\frac{M_1M_2D_\infty\exp\left(M_5\right)}{M_3}\right)\left[\frac{1}{1-\left[\frac{N_1M_2}{M_3}+M_1\left(\frac{N_2M_3-N_3M_2}{M_3^2}\right)\right]}\right]*$$

$$\frac{18\sqrt{3}h\overline{\theta}_{n+1}M_6}{\sqrt{2}\pi D_\infty\sqrt{1-\xi_{n+1}^2}}\left(\frac{2G}{||\mathbf{s}_{n+1}^{trial}||}\right)^3 \tag{C.35}$$

$$F_7=F_{17}+F_{18}-F_{19}F_{20}\left(F_{21}+F_{22}-F_{23}\right), \tag{C.36}$$

where,

$$F_{17}=-\frac{108GaH_{ini}\overline{\boldsymbol{\varepsilon}}_{n+1}^p\det\left(\mathbf{s}_{n+1}^{trial}\right)}{4\sqrt{3/2}\pi\sqrt{1-\xi_{n+1}^2}\left(||\mathbf{s}_{n+1}^{trial}||\right)^5} \tag{C.37}$$

$$F_{18}=\frac{2\sqrt{3/2}GaH_{ini}\Delta t\left(\overline{\theta}_{n+1}+5\right)}{4\left(\eta_{n+1}+\Delta tG\right)||\mathbf{s}_{n+1}^{trial}||} \tag{C.38}$$

$$F_{19}=\frac{\sqrt{3/2}aH_{ini}\Delta t||\mathbf{s}_{n+1}^{trial}||\left(\overline{\theta}_{n+1}+5\right)}{12\left(\eta_{n+1}+\Delta tG\right)^2} \tag{C.39}$$

$$F_{20} = \frac{1}{1 - \left[\frac{N_1 M_2}{M_3} + M_1 \left(\frac{N_2 M_3 - N_3 M_2}{M_3^2}\right)\right]} \tag{C.40}$$

$$F_{21} = \frac{108 M_1 M_2 M_6 \exp\left(M_5\right) h G \overline{\theta}_{n+1} \det\left(\mathbf{s}_{n+1}^{trial}\right)}{\pi \sqrt{1 - \xi_{n+1}^2} ||\mathbf{s}_{n+1}^{trial}||^5} + \frac{M_1 M_2 \exp\left(M_5\right) h G \Delta t \left(1 + \overline{\theta}_{n+1}^2\right)}{2\left(\eta_{n+1} + \Delta t G\right) ||\mathbf{s}_{n+1}^{trial}||} \tag{C.41}$$

$$F_{22} = \frac{\sqrt{2} M_1 G \eta_{n+1}}{\left(\eta_{n+1} + \Delta t G\right) ||\mathbf{s}_{n+1}^{trial}||} \tag{C.42}$$

$$F_{23} = \frac{\sqrt{2} M_1 M_2 G \eta_{n+1}}{\tau_0 M_3^2 \left(\eta_{n+1} + \Delta t G\right) ||\mathbf{s}_{n+1}^{trial}||} \cosh\left(\frac{M_2}{\tau_0}\right) \tag{C.43}$$

The final factor in the closed form tangent operator is given in the following.

$$F_8 = K F_{15} F_{24} \tag{C.44}$$

where,

$$F_{24} = \frac{\mu M_1 M_2}{M_3 \tau_0 \left[1 - \left[\frac{N_1 M_2}{M_3} + M_1 \left(\frac{N_2 M_3 - N_3 M_2}{M_3^2}\right)\right]\right]} \tag{C.45}$$

Appendix D

Details of the state update for Porous model

In this appendix, some details with regard to state update procedure of model presented in Chapter 6 will be given.
In two dimensional implementation of the model presented in Chapter 6, there are seven unknown to be determined. If the unknowns are considered as a vector:

$$\mathbf{u} = \begin{bmatrix} u_1 \\ u_2 \\ u_3 \\ u_4 \\ u_5 \\ u_6 \\ u_7 \end{bmatrix}, \tag{D.1}$$

The expanded version of relation (6.37) reads:

$$\begin{bmatrix} R_{1,1} & R_{1,2} & R_{1,3} & R_{1,4} & R_{1,5} & R_{1,6} & R_{1,7} \\ R_{2,1} & R_{2,2} & R_{2,3} & R_{2,4} & R_{2,5} & R_{2,6} & R_{2,7} \\ R_{3,1} & R_{3,2} & R_{3,3} & R_{3,4} & R_{3,5} & R_{3,6} & R_{3,7} \\ R_{4,1} & R_{4,2} & R_{4,3} & R_{4,4} & R_{4,5} & R_{4,6} & R_{4,7} \\ R_{5,1} & R_{5,2} & R_{5,3} & R_{5,4} & R_{5,5} & R_{5,6} & R_{5,7} \\ R_{6,1} & R_{6,2} & R_{6,3} & R_{6,4} & R_{6,5} & R_{6,6} & R_{6,7} \\ R_{7,1} & R_{7,2} & R_{7,3} & R_{7,4} & R_{7,5} & R_{7,6} & R_{7,7} \end{bmatrix}^{k-1} \begin{bmatrix} \delta u_1 \\ \delta u_2 \\ \delta u_3 \\ \delta u_4 \\ \delta u_5 \\ \delta u_6 \\ \delta u_7 \end{bmatrix}^{k} = - \begin{bmatrix} R_1 \\ R_2 \\ R_3 \\ R_4 \\ R_5 \\ R_6 \\ R_7 \end{bmatrix}^{k-1} . \tag{D.2}$$

Where, R_1, ... , R_7 refer to the seven residual equations. In this following, the derivatives of the residual functions for the porous model presented in Chapter 6 which are required by relation (D.2) are given.
In order to have the derivatives in a more compact form, first, some variables are introduced and then the derivatives will be given using the introduced variables.

$$V_1 = \mathbf{s}_{M,n+1} : \mathbf{s}_{M,n+1} + \left(\frac{f_{n+1}\tau^{eq}_{m,n+1}}{3}\right)(\boldsymbol{\sigma}_{M,n+1} : \mathbf{I}) \sinh\left(\frac{tr\left(\boldsymbol{\sigma}_{M,n+1}\right)}{2\tau^{eq}_{m,n+1}}\right), \tag{D.3}$$

$$V_2 = \left(\frac{f_{n+1}\tau^{eq}_{m,n+1}}{3}\right) \sinh\left(\frac{tr\left(\boldsymbol{\sigma}_{M,n+1}\right)}{2\tau^{eq}_{m,n+1}}\right), \tag{D.4}$$

$$V_3 = (1 - f_{n+1})\left(\frac{1}{\eta_{n+1}}\right)\left(\tau^{eq}_{m,n+1}\right)^2, \tag{D.5}$$

$$V_4 = 4G^2\left[-\frac{4}{3}\boldsymbol{\varepsilon}^e_{d,M,n+1}(xx) + \frac{2}{3}\boldsymbol{\varepsilon}^e_{d,M,n+1}(yy) + \frac{2}{3}\boldsymbol{\varepsilon}^e_{d,M,n+1}(zz)\right] \tag{D.6}$$

$$V_5 = 4G^2\left[\frac{2}{3}\boldsymbol{\varepsilon}^e_{d,M,n+1}(xx) - \frac{4}{3}\boldsymbol{\varepsilon}^e_{d,M,n+1}(yy) + \frac{2}{3}\boldsymbol{\varepsilon}^e_{d,M,n+1}(zz)\right] \tag{D.7}$$

$$V_6 = 4G^2\left[\frac{2}{3}\boldsymbol{\varepsilon}^e_{d,M,n+1}(xx) + \frac{2}{3}\boldsymbol{\varepsilon}^e_{d,M,n+1}(yy) - \frac{4}{3}\boldsymbol{\varepsilon}^e_{d,M,n+1}(zz)\right] \tag{D.8}$$

$$V_7 = \cosh\left(\frac{tr\left(\boldsymbol{\sigma}_{M,n+1}\right)}{2\tau^{eq}_{m,n+1}}\right)\left(-\frac{3K}{2\tau^{eq}_{m,n+1}}\right) \tag{D.9}$$

$$V_8 = -\left(\frac{f_{n+1}\tau^{eq}_{m,n+1}}{3}\right)\left(\frac{3K}{2\tau^{eq}_{m,n+1}}\right)\cosh\left(\frac{tr\left(\boldsymbol{\sigma}_{M,n+1}\right)}{2\tau^{eq}_{m,n+1}}\right) \tag{D.10}$$

$$V_9 = \frac{\tau^{eq}_{m,n+1}\boldsymbol{\sigma}_{M,n+1} : \mathbf{I}}{3} \sinh\left(\frac{tr\left(\boldsymbol{\sigma}_{M,n+1}\right)}{2\tau^{eq}_{m,n+1}}\right) \tag{D.11}$$

$$V_{10} = \frac{\tau^{eq}_{m,n+1}}{3} \sinh\left(\frac{tr\left(\boldsymbol{\sigma}_{M,n+1}\right)}{2\tau^{eq}_{m,n+1}}\right) \tag{D.12}$$

$$V_{11} = -\frac{\left(\tau^{eq}_{m,n+1}\right)^2}{\eta_{n+1}} \tag{D.13}$$

$$V_{12} = -\left(1 - f_{n+1}\right)\left(\frac{\tau^{eq}_{m,n+1}}{\eta_{n+1}}\right)^2 \tag{D.14}$$

$$V_{13} = \sinh\left(\frac{tr\left(\boldsymbol{\sigma}_{M,n+1}\right)}{2\tau^{eq}_{m,n+1}}\right) - \frac{tr\left(\boldsymbol{\sigma}_{M,n+1}\right)}{2\tau^{eq}_{m,n+1}}\cosh\left(\frac{tr\left(\boldsymbol{\sigma}_{M,n+1}\right)}{2\tau^{eq}_{m,n+1}}\right) \tag{D.15}$$

$$V_{14} = 2\left(1 - f_{n+1}\right)\left(\frac{1}{\eta_{n+1}}\right)\tau^{eq}_{m,n+1} \tag{D.16}$$

$$V_{15} = -\frac{h\Delta t}{\sqrt{2}\eta_{n+1}}\exp\left[\frac{h\sqrt{3}\left(\overline{\varepsilon}^p_n + \frac{\sqrt{3}\Delta t}{3\eta_{n+1}}\tau^{eq}_{m,n+1}\right)}{\sqrt{2}D_\infty}\right] \tag{D.17}$$

$$V_{16} = \left[\frac{\Delta H}{RT} + \frac{\mu P_{m,n+1}}{\tau_0} - D_\infty + D_\infty \exp\left(\frac{-h\sqrt{3}\left(\overline{\varepsilon}^p_n + \frac{\sqrt{3}\Delta t}{3\eta_{n+1}}\tau^{eq}_{m,n+1}\right)}{\sqrt{2}D_\infty}\right)\right] \tag{D.18}$$

$$V_{17} = V_7\left(\boldsymbol{\sigma}_{M,n+1} : \mathbf{I}\right) + \sinh\left(\frac{tr\left(\boldsymbol{\sigma}_{M,n+1}\right)}{2\tau^{eq}_{m,n+1}}\right)(-3K) \tag{D.19}$$

$$V_{18} = V_4 + \left(\frac{f_{n+1}\tau^{eq}_{m,n+1}}{3}\right)V_{17} \tag{D.20}$$

$$V_{19} = V_5 + \left(\frac{f_{n+1}\tau^{eq}_{m,n+1}}{3}\right)V_{17} \tag{D.21}$$

$$V_{20} = V_6 + \left(\frac{f_{n+1}\tau^{eq}_{m,n+1}}{3}\right)V_{17} \tag{D.22}$$

$$V_{21} = \frac{f_{n+1}\boldsymbol{\sigma}_{M,n+1} : \mathbf{I}}{3}V_{13} \tag{D.23}$$

$$V_{22} = \frac{f_{n+1}}{3}V_{13} \tag{D.24}$$

$$V_{23} = \left(\frac{f_{n+1}\tau^{eq}_{m,n+1}}{3}\right)V_7 \tag{D.25}$$

Using the The above mentioned variables, the derivatives of the residual equations in order to unknowns are given in the following.

Derivatives of the first residual equation

$$R_{1,1} = \frac{\partial R_1}{\partial u_1} = 1 - \Delta t \left[\frac{V_3}{V_1^2} \left(\frac{2G}{3} V_1 - V_{18} \mathbf{s}_{M,n+1}(xx) + V_8 V_1 - V_{18} V_2 \right) \right] \quad \text{(D.26)}$$

$$R_{1,2} = \frac{\partial R_1}{\partial u_2} = -\Delta t \left[\frac{V_3}{V_1^2} \left(\frac{2G}{3} V_1 - V_{19} \mathbf{s}_{M,n+1}(xx) + V_{23} V_1 - V_{19} V_2 \right) \right] \quad \text{(D.27)}$$

$$R_{1,3} = \frac{\partial R_1}{\partial u_3} = 0 \quad \text{(D.28)}$$

$$R_{1,4} = \frac{\partial R_1}{\partial u_4} = -\Delta t \left[\frac{V_3}{V_1^2} \left(\frac{2G}{3} V_1 - V_{20} \mathbf{s}_{M,n+1}(xx) + V_{23} V_2 - V_{20} V_2 \right) \right] \quad \text{(D.29)}$$

$$R_{1,5} = \frac{\partial R_1}{\partial u_5} = -\Delta t \left[\mathbf{s}_{M,n+1}(xx) \left(\frac{V_{11} V_1 - V_9 V_3}{V_1^2} \right) + \left[\frac{V_1 \left(V_{11} V_2 + V_3 V_{10} \right) - V_9 V_3 V_2}{V_1^2} \right] \right] \quad \text{(D.30)}$$

$$R_{1,6} = \frac{\partial R_1}{\partial u_6} = -\Delta t \left[\mathbf{s}_{M,n+1}(xx) \left(\frac{V_{12} V_1 - V_{10} V_3}{V_1^2} \right) + \left[\frac{V_1 V_{12} V_2 - V_{10} V_3 V_2}{V_1^2} \right] \right] \quad \text{(D.31)}$$

$$R_{1,7} = \frac{\partial R_1}{\partial u_7} = -\Delta t \left[\mathbf{s}_{M,n+1}(xx) \left(\frac{V_{14} V_1 - V_{21} V_3}{V_1^2} \right) + V_2 \left[\frac{V_{14} V_1 - V_{21} V_3}{V_1^2} \right] + \left(\frac{V_3 V_{22}}{V_1} \right) \right] \quad \text{(D.32)}$$

Derivatives of the second residual equation

$$R_{2,1} = \frac{\partial R_2}{\partial u_1} = -\Delta t \left[\frac{V_3}{V_1^2} \left(\frac{2G}{3} V_1 - V_{18} \mathbf{s}_{M,n+1}(yy) + V_8 V_1 - V_{18} V_2 \right) \right] \quad \text{(D.33)}$$

$$R_{2,2} = \frac{\partial R_2}{\partial u_2} = 1 - \Delta t \left[\frac{V_3}{V_1^2} \left(\frac{2G}{3} V_1 - V_{19} \mathbf{s}_{M,n+1}(yy) + V_{23} V_1 - V_{19} V_2 \right) \right] \quad \text{(D.34)}$$

$$R_{2,3} = \frac{\partial R_2}{\partial u_3} = 0 \quad \text{(D.35)}$$

$$R_{2,4} = \frac{\partial R_2}{\partial u_4} = -\Delta t \left[\frac{V_3}{V_1^2} \left(\frac{2G}{3} V_1 - V_{20} \mathbf{s}_{M,n+1}(yy) + V_{23} V_2 - V_{20} V_2 \right) \right] \quad \text{(D.36)}$$

$$R_{2,5} = \frac{\partial R_1}{\partial u_5} = -\Delta t \Bigg[\mathbf{s}_{M,n+1}(yy) \left(\frac{V_{11} V_1 - V_9 V_3}{V_1^2} \right) + \left[\frac{V_1 \left(V_{11} V_2 + V_3 V_{10} \right) - V_9 V_3 V_2}{V_1^2} \right] \Bigg] \quad \text{(D.37)}$$

$$R_{2,6} = \frac{\partial R_1}{\partial u_6} = -\Delta t \Bigg[\mathbf{s}_{M,n+1}(yy) \left(\frac{V_{12} V_1 - V_{10} V_3}{V_1^2} \right) + \left[\frac{V_1 V_{12} V_2 - V_{10} V_3 V_2}{V_1^2} \right] \Bigg] \quad \text{(D.38)}$$

$$R_{2,7} = \frac{\partial R_1}{\partial u_7} = -\Delta t \Bigg[\mathbf{s}_{M,n+1}(yy) \left(\frac{V_{14} V_1 - V_{21} V_3}{V_1^2} \right) + V_2 \left[\frac{V_{14} V_1 - V_{21} V_3}{V_1^2} \right] + \left(\frac{V_3 V_{22}}{V_1} \right) \Bigg] \quad \text{(D.39)}$$

Derivatives of the third residual equation

$$R_{3,1} = \frac{\partial R_3}{\partial u_1} = \Delta t \left[\mathbf{s}_{M,n+1}(xy) \frac{V_3 V_{18}}{V_1^2} \right] \quad \text{(D.40)}$$

$$R_{3,2} = \frac{\partial R_3}{\partial u_2} = \Delta t \left[\mathbf{s}_{M,n+1}(xy) \frac{V_3 V_{19}}{V_1^2} \right] \quad \text{(D.41)}$$

$$R_{3,3} = \frac{\partial R_3}{\partial u_3} = 1 + \Delta t \left(\frac{G V_3}{V_1} \right) \quad \text{(D.42)}$$

$$R_{3,4} = \frac{\partial R_3}{\partial u_4} = \Delta t \left[\mathbf{s}_{M,n+1}(xy) \frac{V_3 V_{20}}{V_1^2} \right] \tag{D.43}$$

$$R_{3,5} = \frac{\partial R_3}{\partial u_5} = \Delta t \left[\mathbf{s}_{M,n+1}(xy) \left(\frac{V_1 V_{11} - V_3 V_9}{V_1^2} \right) \right] \tag{D.44}$$

$$R_{3,6} = \frac{\partial R_3}{\partial u_6} = \Delta t \left[\mathbf{s}_{M,n+1}(xy) \left(\frac{V_1 V_{12} - V_3 V_{10}}{V_1^2} \right) \right] \tag{D.45}$$

$$R_{3,7} = \frac{\partial R_3}{\partial u_7} = \Delta t \left[\mathbf{s}_{M,n+1}(xy) \left(\frac{V_1 V_{14} - V_3 V_{21}}{V_1^2} \right) \right] \tag{D.46}$$

Derivatives of the fourth residual equation

$$R_{4,1} = \frac{\partial R_4}{\partial u_1} = -\Delta t \left[\frac{V_3}{V_1^2} \left(\frac{2G}{3} V_1 - V_{18} \mathbf{s}_{M,n+1}(zz) + V_8 V_1 - V_{18} V_2 \right) \right] \tag{D.47}$$

$$R_{4,2} = \frac{\partial R_4}{\partial u_2} = -\Delta t \left[\frac{V_3}{V_1^2} \left(\frac{2G}{3} V_1 - V_{19} \mathbf{s}_{M,n+1}(zz) + V_{23} V_1 - V_{19} V_2 \right) \right] \tag{D.48}$$

$$R_{4,3} = \frac{\partial R_3}{\partial u_3} = 0 \tag{D.49}$$

$$R_{4,4} = \frac{\partial R_4}{\partial u_4} = 1 - \Delta t \left[\frac{V_3}{V_1^2} \left(\frac{2G}{3} V_1 - V_{20} \mathbf{s}_{M,n+1}(zz) + V_{23} V_2 - V_{20} V_2 \right) \right] \tag{D.50}$$

$$R_{4,5} = \frac{\partial R_4}{\partial u_5} = -\Delta t \left[\mathbf{s}_{M,n+1}(zz) \left(\frac{V_{11} V_1 - V_9 V_3}{V_1^2} \right) + \left[\frac{V_1 \left(V_{11} V_2 + V_3 V_{10} \right) - V_9 V_3 V_2}{V_1^2} \right] \right] \tag{D.51}$$

$$R_{4,6} = \frac{\partial R_4}{\partial u_6} = -\Delta t \left[\mathbf{s}_{M,n+1}(zz) \left(\frac{V_{12} V_1 - V_{10} V_3}{V_1^2} \right) + \left[\frac{V_1 V_{12} V_2 - V_{10} V_3 V_2}{V_1^2} \right] \right] \tag{D.52}$$

$$R_{4,7} = \frac{\partial R_4}{\partial u_7} = -\Delta t \Bigg[\mathbf{s}_{M,n+1}(zz) \left(\frac{V_{14}V_1 - V_{21}V_3}{V_1^2} \right) + V_2 \left[\frac{V_{14}V_1 - V_{21}V_3}{V_1^2} \right] + \left(\frac{V_3 V_{22}}{V_1} \right) \Bigg] \tag{D.53}$$

Derivatives of the fifth residual equation

$$R_{5,1} = \frac{\partial R_5}{\partial u_1} = -3V_3\Delta t\,(1 - f_n) \left(\frac{V_8V_1 - V_{18}V_2}{V_1^2} \right) \exp\left(-\frac{3V_7V_8}{V_6}\Delta t \right) \tag{D.54}$$

$$R_{5,2} = \frac{\partial R_5}{\partial u_2} = -3V_3\Delta t\,(1 - f_n) \left(\frac{V_{23}V_1 - V_{19}V_2}{V_1^2} \right) \exp\left(-\frac{3V_7V_8}{V_6}\Delta t \right) \tag{D.55}$$

$$R_{5,3} = \frac{\partial R_5}{\partial u_3} = 0 \tag{D.56}$$

$$R_{5,4} = \frac{\partial R_5}{\partial u_4} = -3V_3\Delta t\,(1 - f_n) \left(\frac{V_{23}V_1 - V_{20}V_2}{V_1^2} \right) \exp\left(-\frac{3V_7V_8}{V_6}\Delta t \right) \tag{D.57}$$

$$R_{5,5} = \frac{\partial R_5}{\partial u_5} = 1 - 3\Delta t\,(1 - f_n) \left[\frac{V_1\left(V_{11}V_2 + V_3V_{10}\right) - V_9V_3V_2}{V_1^2} \right] \exp\left(-\frac{3V_7V_8}{V_6}\Delta t \right) \tag{D.58}$$

$$R_{5,6} = \frac{\partial R_5}{\partial u_6} = -3\Delta t\,(1 - f_n) \left[\frac{V_1V_{12}V_2 - V_3V_{10}V_2}{V_1^2} \right] \exp\left(-\frac{3V_7V_8}{V_6}\Delta t \right) \tag{D.59}$$

$$R_{5,7} = \frac{\partial R_5}{\partial u_7} = -3\Delta t\,(1 - f_n) \left[V_2 \left(\frac{V_{14}V_1 - V_{21}V_3}{V_1^2} \right) + \left(\frac{V_3V_{22}}{V_1} \right) \right] \exp\left(-\frac{3V_7V_8}{V_6}\Delta t \right) \tag{D.60}$$

Derivatives of the sixth residual equation

$$R_{6,1} = \frac{\partial R_6}{\partial u_1} = 0 \tag{D.61}$$

$$R_{6,2} = \frac{\partial R_6}{\partial u_2} = 0 \tag{D.62}$$

$$R_{6,3} = \frac{\partial R_6}{\partial u_3} = 0 \tag{D.63}$$

$$R_{6,4} = \frac{\partial R_6}{\partial u_4} = 0 \tag{D.64}$$

$$R_{6,5} = \frac{\partial R_6}{\partial u_5} = 0 \tag{D.65}$$

$$R_{6,6} = \frac{\partial R_6}{\partial u_6} = 1 - A_0 \exp\left(V_9\right) \left(\overline{\varepsilon}_n^p + \frac{\sqrt{3}\Delta t}{3\eta_{n+1}} \tau_{m,n+1}^{eq} \right) \left[\frac{\tau_{m,n+1}^{eq}}{\sinh\left(\tau_{m,n+1}^{eq}/\tau_0\right)} \right] \tag{D.66}$$

$$R_{6,7} = \frac{\partial R_6}{\partial u_7} = -A_0 \left[\frac{\exp\left(V_{16}\right)}{\sinh\left(\tau_{m,n+1}^{eq}/\tau_0\right)} + \right. \tag{D.67}$$

$$\left. \tau_{m,n+1}^{eq} \exp\left(V_{16}\right) \left[\frac{\sinh\left(\tau_{m,n+1}^{eq}/\tau_0\right) V_{15} - \cosh\left(\tau_{m,n+1}^{eq}/\tau_0\right) \left(1/\tau_0\right)}{\left(\sinh\left(\tau_{m,n+1}^{eq}/\tau_0\right)\right)^2} \right] \right] \tag{D.68}$$

Derivatives of the last residual equation

$$R_{7,1} = \frac{\partial R_7}{\partial u_1} = \frac{1}{2} V_4 - 3K\tau_{m,n+1}^{eq} f_{n+1} \sinh\left(\frac{tr\left(\boldsymbol{\sigma}_{M,n+1}\right)}{2\tau_{m,n+1}^{eq}} \right) \tag{D.69}$$

$$R_{7,2} = \frac{\partial R_7}{\partial u_2} = \frac{1}{2} V_5 - 3K\tau_{m,n+1}^{eq} f_{n+1} \sinh\left(\frac{tr\left(\boldsymbol{\sigma}_{M,n+1}\right)}{2\tau_{m,n+1}^{eq}} \right) \tag{D.70}$$

$$R_{7,3} = \frac{\partial R_7}{\partial u_3} = 0 \tag{D.71}$$

$$R_{7,4} = \frac{\partial R_7}{\partial u_4} = \frac{1}{2}V_6 - 3K\tau^{eq}_{m,n+1} f_{n+1} \sinh\left(\frac{tr\left(\boldsymbol{\sigma}_{M,n+1}\right)}{2\tau^{eq}_{m,n+1}}\right) \tag{D.72}$$

$$R_{7,5} = \frac{\partial R_7}{\partial u_5} = 2\left(\tau^{eq}_{m,n+1}\right)^2 \cosh\left(\frac{tr\left(\boldsymbol{\sigma}_{M,n+1}\right)}{2\tau^{eq}_{m,n+1}}\right) - \left(\tau^{eq}_{m,n+1}\right)^2 \tag{D.73}$$

$$R_{7,6} = \frac{\partial R_7}{\partial u_6} = 0 \tag{D.74}$$

$$R_{7,7} = \frac{\partial R_7}{\partial u_7} = 2f_{n+1}\left[2\tau^{eq}_{m,n+1}\cosh\left(\frac{tr\left(\boldsymbol{\sigma}_{M,n+1}\right)}{2\tau^{eq}_{m,n+1}}\right)\right.$$
$$\left. - \left(\frac{tr\left(\boldsymbol{\sigma}_{M,n+1}\right)}{2}\right)\sinh\left(\frac{tr\left(\boldsymbol{\sigma}_{M,n+1}\right)}{2\tau^{eq}_{m,n+1}}\right)\right] - 2\tau^{eq}_{m,n+1}\left(1 + f^2_{n+1}\right) \tag{D.75}$$

Appendix E

Tangent operator for the Porous model

As mentioned in Chapter 6, for the sake of completeness of the numerical treatment of the developed model for heterogeneous polymers, it is needed to derive the tangent operator consistent with the state update. The expanded version of relation (6.48) reads:

$$\begin{bmatrix} -\left(\partial R_1/\partial \boldsymbol{\varepsilon}_{M,n+1}\right) : d\boldsymbol{\varepsilon}_{M,n+1} \\ -\left(\partial R_2/\partial \boldsymbol{\varepsilon}_{M,n+1}\right) : d\boldsymbol{\varepsilon}_{M,n+1} \\ -\left(\partial R_3/\partial \boldsymbol{\varepsilon}_{M,n+1}\right) : d\boldsymbol{\varepsilon}_{M,n+1} \\ -\left(\partial R_4/\partial \boldsymbol{\varepsilon}_{M,n+1}\right) : d\boldsymbol{\varepsilon}_{M,n+1} \\ -\left(\partial R_5/\partial \boldsymbol{\varepsilon}_{M,n+1}\right) : d\boldsymbol{\varepsilon}_{M,n+1} \\ -\left(\partial R_6/\partial \boldsymbol{\varepsilon}_{M,n+1}\right) : d\boldsymbol{\varepsilon}_{M,n+1} \\ -\left(\partial R_7/\partial \boldsymbol{\varepsilon}_{M,n+1}\right) : d\boldsymbol{\varepsilon}_{M,n+1} \end{bmatrix} =$$

$$\begin{bmatrix} R_{1,1} & R_{1,2} & R_{1,3} & R_{1,4} & R_{1,5} & R_{1,6} & R_{1,7} \\ R_{2,1} & R_{2,2} & R_{2,3} & R_{2,4} & R_{2,5} & R_{2,6} & R_{2,7} \\ R_{3,1} & R_{3,2} & R_{3,3} & R_{3,4} & R_{3,5} & R_{3,6} & R_{3,7} \\ R_{4,1} & R_{4,2} & R_{4,3} & R_{4,4} & R_{4,5} & R_{4,6} & R_{4,7} \\ R_{5,1} & R_{5,2} & R_{5,3} & R_{5,4} & R_{5,5} & R_{5,6} & R_{5,7} \\ R_{6,1} & R_{6,2} & R_{6,3} & R_{6,4} & R_{6,5} & R_{6,6} & R_{6,7} \\ R_{7,1} & R_{7,2} & R_{7,3} & R_{7,4} & R_{7,5} & R_{7,6} & R_{7,7} \end{bmatrix} \begin{bmatrix} du_1 \\ du_2 \\ du_3 \\ du_4 \\ du_5 \\ du_6 \\ du_7 \end{bmatrix} . \tag{E.1}$$

Relation E.1 could be conveniently rearranged as:

$$\begin{bmatrix} du_1 \\ du_2 \\ du_3 \\ du_4 \\ du_5 \\ du_6 \\ du_7 \end{bmatrix} = \begin{bmatrix} R_{1,1} & R_{1,2} & R_{1,3} & R_{1,4} & R_{1,5} & R_{1,6} & R_{1,7} \\ R_{2,1} & R_{2,2} & R_{2,3} & R_{2,4} & R_{2,5} & R_{2,6} & R_{2,7} \\ R_{3,1} & R_{3,2} & R_{3,3} & R_{3,4} & R_{3,5} & R_{3,6} & R_{3,7} \\ R_{4,1} & R_{4,2} & R_{4,3} & R_{4,4} & R_{4,5} & R_{4,6} & R_{4,7} \\ R_{5,1} & R_{5,2} & R_{5,3} & R_{5,4} & R_{5,5} & R_{5,6} & R_{5,7} \\ R_{6,1} & R_{6,2} & R_{6,3} & R_{6,4} & R_{6,5} & R_{6,6} & R_{6,7} \\ R_{7,1} & R_{7,2} & R_{7,3} & R_{7,4} & R_{7,5} & R_{7,6} & R_{7,7} \end{bmatrix}^{-1}$$

$$\begin{bmatrix} -\left(\partial R_1/\partial \boldsymbol{\varepsilon}_{M,n+1}\right) : d\boldsymbol{\varepsilon}_{M,n+1} \\ -\left(\partial R_2/\partial \boldsymbol{\varepsilon}_{M,n+1}\right) : d\boldsymbol{\varepsilon}_{M,n+1} \\ -\left(\partial R_3/\partial \boldsymbol{\varepsilon}_{M,n+1}\right) : d\boldsymbol{\varepsilon}_{M,n+1} \\ -\left(\partial R_4/\partial \boldsymbol{\varepsilon}_{M,n+1}\right) : d\boldsymbol{\varepsilon}_{M,n+1} \\ -\left(\partial R_5/\partial \boldsymbol{\varepsilon}_{M,n+1}\right) : d\boldsymbol{\varepsilon}_{M,n+1} \\ -\left(\partial R_6/\partial \boldsymbol{\varepsilon}_{M,n+1}\right) : d\boldsymbol{\varepsilon}_{M,n+1} \\ -\left(\partial R_7/\partial \boldsymbol{\varepsilon}_{M,n+1}\right) : d\boldsymbol{\varepsilon}_{M,n+1} \end{bmatrix}. \tag{E.2}$$

As indicated by relation (E.2), it is required to have the derivatives of the residual equations in order to strain. They are given in the following.

First some second order tensors are introduced and then, using the introduced tensors, the derivatives of the residuals in order to strain will be given.

$$\mathbf{Q}_1 = 8G^2\boldsymbol{\varepsilon}^e_{d,M,n+1}(xx)\begin{bmatrix} 2/3 \\ -1/3 \\ 0 \\ -1/3 \end{bmatrix} + 8G^2\boldsymbol{\varepsilon}^e_{d,M,n+1}(yy)\begin{bmatrix} 1/3 \\ 2/3 \\ 0 \\ -1/3 \end{bmatrix} +$$

$$16G^2\boldsymbol{\varepsilon}^e_{d,M,n+1}(xy)\begin{bmatrix} 0 \\ 0 \\ 1/2 \\ 0 \end{bmatrix} + 8G^2\boldsymbol{\varepsilon}^e_{d,M,n+1}(zz)\begin{bmatrix} -1/3 \\ -1/3 \\ 0 \\ 2/3 \end{bmatrix} \tag{E.3}$$

$$\mathbf{Q}_2 = 3K\mathbf{I} \tag{E.4}$$

$$\mathbf{Q}_3 = -\frac{\mu K}{\tau_0}\mathbf{I} \tag{E.5}$$

$$\mathbf{Q}_4 = 2G\begin{bmatrix} 2/3 \\ -1/3 \\ 0 \\ -1/3 \end{bmatrix} \tag{E.6}$$

$$\mathbf{Q}_5 = 2G \begin{bmatrix} -1/3 \\ 2/3 \\ 0 \\ -1/3 \end{bmatrix} \tag{E.7}$$

$$\mathbf{Q}_6 = 2G \begin{bmatrix} 0 \\ 0 \\ 1/2 \\ 0 \end{bmatrix} \tag{E.8}$$

$$\mathbf{Q}_7 = 2G \begin{bmatrix} -1/3 \\ -1/3 \\ 0 \\ 2/3 \end{bmatrix} \tag{E.9}$$

$$\mathbf{Q}_8 = \left(\frac{1}{2\tau^{eq}_{m,n+1}} \right) \cosh \left(\frac{tr\left(\boldsymbol{\sigma}_{M,n+1}\right)}{2\tau^{eq}_{m,n+1}} \right) \mathbf{Q}_2 \tag{E.10}$$

$$\mathbf{Q}_9 = \left(\boldsymbol{\sigma}_{M,n+1} : \mathbf{I}\right) \mathbf{Q}_8 + \sinh \left(\frac{tr\left(\boldsymbol{\sigma}_{M,n+1}\right)}{2\tau^{eq}_{m,n+1}} \right) \mathbf{Q}_2 \tag{E.11}$$

$$\mathbf{Q}_{10} = \frac{f_{n+1}\tau^{eq}_{m,n+1}}{3} \mathbf{Q}_5 \tag{E.12}$$

$$\mathbf{Q}_{11} = \mathbf{Q}_1 + \frac{f_{n+1}\tau^{eq}_{m,n+1}}{3} \mathbf{Q}_9 \tag{E.13}$$

$$\mathbf{Q}_{12} = \frac{V_1 \mathbf{Q}_4 - \mathbf{s}_{M,n+1}(xx)\mathbf{Q}_{11}}{V_1^2} \tag{E.14}$$

It should be mentioned that the V scalar parameters used in this Appendix, are already given in Appendix D.

$$\mathbf{Q}_{13} = \frac{V_1 \mathbf{Q}_4 - V_7 \mathbf{Q}_{11}}{V_1^2} \tag{E.15}$$

$$\mathbf{Q}_{14} = \frac{V_1 \mathbf{Q}_5 - \mathbf{s}_{M,n+1}(yy)\mathbf{Q}_{11}}{V_1^2} \tag{E.16}$$

$$\mathbf{Q}_{15} = \frac{V_1 \mathbf{Q}_6 - \mathbf{s}_{M,n+1}(xy)\mathbf{Q}_{11}}{V_1^2} \tag{E.17}$$

$$\mathbf{Q}_{16} = \frac{V_1 \mathbf{Q}_7 - \mathbf{s}_{M,n+1}(zz)\mathbf{Q}_{11}}{V_1^2} \tag{E.18}$$

$$\mathbf{Q}_{17} = \left(\frac{1}{2\tau^{eq}_{m,n+1}}\right) \sinh\left(\frac{tr\left(\boldsymbol{\sigma}_{M,n+1}\right)}{2\tau^{eq}_{m,n+1}}\right) \mathbf{Q}_2 \tag{E.19}$$

Using the above given tensors, the derivatives of the residual equations in order to strain could be given as follows.

$$\frac{\partial R_1}{\partial \boldsymbol{\varepsilon}_{n+1}} = -\Delta t V_3 \left(\mathbf{Q}_{12} + \mathbf{Q}_{13}\right) \tag{E.20}$$

$$\frac{\partial R_2}{\partial \boldsymbol{\varepsilon}_{n+1}} = -\Delta t V_3 \left(\mathbf{Q}_{13} + \mathbf{Q}_{14}\right) \tag{E.21}$$

$$\frac{\partial R_3}{\partial \boldsymbol{\varepsilon}_{n+1}} = -\Delta t V_3 \mathbf{Q}_{15} \tag{E.22}$$

$$\frac{\partial R_4}{\partial \boldsymbol{\varepsilon}_{n+1}} = -\Delta t V_3 \left(\mathbf{Q}_{13} + \mathbf{Q}_{16}\right) \tag{E.23}$$

$$\frac{\partial R_5}{\partial \boldsymbol{\varepsilon}_{n+1}} = -3\Delta t \left(1 - f_n\right) \exp\left(-\frac{3V_2 V_3 \Delta t}{V_1}\right) \left(V_3 \mathbf{Q}_{13}\right) \tag{E.24}$$

$$\frac{\partial R_6}{\partial \boldsymbol{\varepsilon}_{n+1}} = -A_0 \left[\frac{\tau^{eq}_{m,n+1}}{\sinh\left(\tau^{eq}_{m,n+1}/\tau_0\right)}\right] \exp(V_{16}) \mathbf{Q}_3 \tag{E.25}$$

$$\frac{\partial R_7}{\partial \boldsymbol{\varepsilon}_{n+1}} = \frac{1}{2}\mathbf{Q}_1 + 2 f_{n+1} \left(\tau^{eq}_{m,n+1}\right)^2 \mathbf{Q}_{17} \tag{E.26}$$

Appendix F

Relevant publications

Journal papers

- Alexandre Correia, S. Mohsen Valashani, Francisco Pires, Ricardo simões, (2013). Modelling the Mechanical Behavior of Polymer-Based Nanocomposites. Materials Science Forum Vols. 730-732, 543-548.
- M. Carvalho Araujo, J. P. Martins, S.M.Mirkhalaf, Senentxu Lanceros-Mendez, F.M. Andrade Pires, Ricardo simões, (2014). Predicting the mechanical behavior of amorphous polymer-based materials under strain through multi-scale modeling and simulation. Applied Surface Science 306, 37-46.
- S.M.Mirkhalaf, F.Pires, R.simões. An elasto-viscoplastic constitutive model for polymers at finite strain: formulation and computational aspects (submitted).
- S.M.Mirkhalaf, F.Pires, R.simões. Determination of the size of Representative Volume Element (RVE) for heterogeneous amorphous polymers at finite strain (in preparation).
- S.M.Mirkhalaf, F.Pires, R.simões. An elasto-viscoplastic constitutive model for polymers under different stress states: formulation and computational aspects (in preparation).

- S.M.Mirkhalaf, F.Pires, R.simões. Heterogeneous polymeric materials: continuum and coupled multi-scale modelling (in preparation).

- S.M.Mirkhalaf, F.Macedo, N.Bahramsari, F.Pires. A BPA based elasto-viscoplastic constitutive model: formulation and integration algorithm (in preparation).

- S.M.Mirkhalaf, N.Correia. Modeling the mechanical behavior and forming process of unidirectional (UD) polymer matrix composites: A review (in preparation).

Conference proceedings and presentations

- S.M.Mirkhalaf, F.Pires, R.simões, (2011), An efficient numerical integration algorithm for the single mode compressible Leonov model. 11^{th} International Conference on Computational Plasticity (COMPLAS XI), Barcelona.

- S.M.Mirkhalaf, F.Pires, R.simões, (2012), Prediction of the stress-strain behavior of heterogeneous amorphous polymers using micro-scale finite element analysis. 10^{th} World Conference on Computational Mechanics (WCCM X), São Paulo.

- S.M.Mirkhalaf, F.Pires, R.simões, (2014). Constitutive description of yield properties for heterogeneous polymers. 17^{th} International Conference on Advances and Trends in Engineering Materials and their Applications (ATEMA XVII), Montreal.

- S.M.Mirkhalaf, F.Pires, R.simões, (2014). An improved elasto-viscoplastic constitutive model for polymers under different stress states. 14^{th} European Mechanics of Materials Conference (EMMC XIV), Gothenburg

- F.Pires, S.M.Mirkhalaf, R.simões, (2016). Continuum modelling of heterogeneous polymers. PLASTICITY, DAMAGE & FRACTURE 2016, Hawaii.

References

Araujo, M.C., Martins, J.P., Mirkhalaf, S.M., Lanceros-Mendez, S., Pires, F.M.A., Simoes, R., 2014. Predicting the mechanical behavior of amorphous polymeric materials under strain through multi-scale simulation. Applied Surface Science 306, 37-46. xii, 8, 10, 128, 149

Arruda, E.M., Boyce, M.C., 1993. Evolution of plastic anisotropy in amorphous polymers during finite straining. International Journal of Plasticity 9, 697-720. 58, 68, 89

Argon, A.S., 1973. A theory for the low temperature plastic deformation of glassy polymers. Philosophical Magazine 28, 839-865.

Bai, Y., Wierzbicki, T., 2007. A new model of metal plasticity and fracture with pressure and Lode dependence. International Journal of Plasticity 24, 1071-1096. 74

Balieu, R., Lauro, F., Bennani, B., Delille, R., Matsumoto, T., Mottola, E., 2013. A fully coupled elastoviscoplastic damage model at finite strains for mineral filled semi-crystalline polymer. International Journal of Plasticity 51, 241-270. xiv, 68, 79, 87, 88

Bodner, S.R., Partom, Y., 1975. Constitutive equations for elastic-viscoplastic strain-hardening materials. Journal of Applied Mechanics 42, 385-389. 9

Boyce, M.C., Parks, D.M., Argon, A.S., 1988. Large inelastic deformation of glassy polymers, Part I: Rate dependent constitutive model. Mechanics of Materials 7, 15-33. 135

Baaijens, F.P.T., 1991. Calculation of residual stresses in injection molded products. Rheological Acta 30, 284-299 4, 68

Bertram, A., 2005. Elasticity and plasticity of large deformations. An introduction. Springer-Verlag, Berlin, Germany. 5, 38

Bonet, J. and Wood, R.D., 2008. Nonlinear continuum mechanics for finite element analysis. Cambridge University Press, 2 edition. 15

Boyce, M.C., Weber, G.G., Parks, D.M., 1989. On the kinematics of finite strain plasticity. Journal of the Mechanics and Physics of Solids 37, 647-665. 15

Boyce, M.C., and Arruda, E.M., 1990. An experimental and analytical investigation of the large strain compressive and tensile response of glassy polymers. Polymer Engineering and Science 30, 1288-1298. 41

Borbely, A., Biermann, H., Hartmann, O., 2001. FE investigation of the effect of particle distribution on the uniaxial stress-strain behaviour of particulate reinforced metal-matrix composites. Materials Science and Engineering: A 313, 34-45. 9, 74, 150

Bowden, P.B., Jukes, J.A., 1972. The plastic flow of isotropic polymers. Journal of Materials Science 7, 5263.

Buckley, C.P., Jones, D.C., Jones, D.P., 1996. Hot-drawing of poly(ethylene terephthalate) under biaxial stress: application of a three-dimensional glass?rubber constitutive model. Polymer 37, 2403-2414. 68

Budiansky, B., 1965. On the elastic moduli of some heterogeneous materials. Journal of the Mechanics and Physics of Solids 13, 223227. 9
136

Coenen, E.W.C., Kouznetsova, V.G., Geers., M.G.D., 2010. Computational homogenization for heterogeneous thin sheets. International Journal for Numerical Methods in Engineering 83,1180-1205. 7

Charalambakis, N., 2010. Homogenization Techniques and Micromechanics. A Survey and Perspectives. Applied Mechanics Reviews 63, 030803-1. 129

Criesfield, M.A., 2000. Non-linear finite element analysis of solids and structures, Vol 1, Essentials. John Wiley, UK. 48

Criesfield, M.A., 1997. Non-linear finite element analysis of solids and structures, Vol 2, Advanced topic. John Wiley, UK. 15

Dahoun, A., 1992. Comportement plastique et textures de deformation des polyme 'res semi-cristallins en traction uniaxiale et en cisaillement simple. Ph.D. Dissertation, Institut National Polytechnique de Lorraine, France. 8, 150

Danielsson, M., Parks, D.M., Boyce, M.C., 2007. Micromechanics, macromechanics and constitutive modeling of the elasto-viscoplastic deformation of rubber-toughened glassy polymers. Journal of the Mechanics and Physics of Solids 55, 533-561. 129, 130, 131

Drozdov, A.D., Gupta, R.K., 2003. Non-linear viscoelasticity and viscoplasticity of isotactic polypropylene. International Journal of Engineering Science 41, 2335-2361. 8, 150

Drozdov, A.D., Christiansen, J., 2003. Modelling the viscoplastic response of polyethylene in uniaxial loadingunloading tests. Mechanics Research Communication 30, 431-442. 8, 9, 150

Drugan, W.J., Willis, J.R., 1996. A micromechanics-based nonlocal constitutive equation and estimates of representative volume element size for elastic composites. Journal of the Mechanics and Physics of Solids 44, 497-524. 100, 111, 112

De Souza Neto, E.A., Peric, D.J., Owen, D.R.J., 2008. Computational methods for plasticity: Theory and applications. John Wiley, UK. xii, 11, 16, 18, 19, 28, 29, 38, 48, 49, 55, 140

De Souza Neto, E.A., Peric, D.J., Owen, D.R.J., 1994. A model for elastoplastic damage at finite strains: algorithmic issues and applications. Engineering computations 11, 257-281. 48

Diez, J.M., 2010. Thermoviscoplasticity of Glassy Polymers: Experimental Characterization, Parameter Identification and Model Validation. Ph.D. thesis, University of Stuttgart, Stuttgart, Germany. 9, 12, 57, 58, 69, 70, 150, 161

Dompas, D., Groeninckx, G., 1994. Toughening behaviour of rubber-modified thermoplastic polymers involving very small rubber particles: 1. A Criterion for internal rubber cavitation. Polymer 35, 4743-4749. 136

Dupaix, R.B., Boyce, M.C., 2005. Finite Strain Behaviour of Poly(ethylene terephthalate) (PET) and Poly(ethylene terephthalate)-glycol (PETG). Polymer 46, 4827-4838. 9

Del Piero, G., Pampolini, G., 2012. The influence of viscosity on the response of open-cell polymeric foams in uniaxial compression: experiments and theoretical model. Continuum Mechanics and Thermodynamics 24, 181-199.

Eyring, H., 1936. Viscosity, plasticity, and diffusion as examples of absolute reaction rates. Journal of Chemical Physics 4, 283-295. 9
4

Evesque, P., 2000. Fluctuations, correlations and representative elementary volume (REV) in granular materials. Poudres and Grains 11, 6-17. 101

Epee, A.F., Lauro, F., Bennani, B., Bourel, B., 2011. Constitutive model for a semi-crystalline polymer under dynamic loading. International Journal of Solids and Structures 48, 15901599. 68

Fasce, L.A., Pettarin, V., Marano, C., Rink, M., Frontini, P.M., 2008. Biaxial yielding of polypropylene/elastomeric polyolefin blends: effect of elastomer content and thermal annealing. Polymer Engineering and Science 48, 14141423. 68

Farrokh, B., Khan, A.S., 2010. A strain rate dependent yield criterion for isotropic polymers: low to high rates of loading. European Journal of Mechanics A/Solids 29, 274282. 68

Freudenthal, A.M., 1950. The Inelastic Behavior of Engineering Materials and Structures, Wiley. 101

Feyel, F., Chaboche, J.L., 2000. FE^2 multiscale approach for modelling the elastovis-coplastic behaviour of long fiber SiC/Ti composite materials. Computer Methods in Applied Mechanics and Engineering 183, 309-330. 7

Geers, M., 1997. Experimental Analysis and Computational Modelling of Damage and Fracture. Ph.D. thesis, Eindhoven University Of Technology, Eindhoven, The Netherlands. 129

Ghanbari, J., Naghdabadi, R., 2009. Nonlinear hierarchical multiscale modeling of cortical bone considering its nanoscale microstructure. Journal of Biomechanics, 42, 1560-1565. 7

Ghorbel, E., 2008. A viscoplastic constitutive model for polymeric materials. International Journal of Plasticity 24, 2032-2058. 8, 47, 48, 68, 150

Ghosh, S., Lee, K., Moorthy S., 1995. Multiple scale analysis of heterogeneous elastic structures using homogenisation theory and voronoi cell finite element method. International Journal of Solids and Structures 32, 27-62. 4, 6, 148

Ghosh, S., Lee, K., Moorthy S., 1996. Two scale analysis of heterogeneous elastic-plastic materials with asymptotic homogenisation and voronoi cell finite element model. Computer Methods in Applied Mechanics and Engineering 132, 63-116. 4, 6, 129, 148

Ghosh, S., Lee, K., Raghavan, P., 2001. A multi-level computational model for multi-scale damage analysis in composite and porous materials. International Journal of Solids and Structures 38, 2335-2385. 7

Ghoniem, N.M., Busso, E.P., Kioussis, N., Huang, H., 2003. Multiscale modelling of nanomechanics and micromechanics: an overview. Philosophical Magazine 83, 3475-3528. 5

Gitman, I.M., Askes, H., Aifantis, E.C., 2005. The Representative Volume Size in Static and Dynamic Micro-Macro Transitions. International Journal of Fracture 135, L3-L9.

Gitman, I.M., Askes, H., Sluys, L.J., 2007. Representative volume: Existence and size determination. Engineering Fracture Mechanics 74, 2518-2534. 111, 112

Gitman, I.M., Askes, H., Sluys, L.J., 2008. Coupled-volume multi-scale modelling of quasi-brittle material. European Journal of Mechanics - A/Solids 27, 302-327.

Gitman, I.M., Gitman, M.B., Askes, H., 2005. Quantification of stochastically stable representative volumes for random heterogeneous materials. Archive of Applied Mechanics 75, 79-92.

Graham, S., Yang, N., 2003. Representative volumes of materials based on microstructural statistics. Scripta Materialia 48, 269-274. 111

Grimal, Q., Raum, K., Gerisch, A., Laugier, P., 2011. A determination of the minimum sizes of representative volume elements for the prediction of cortical bone elastic properties. Biomechanics and modeling in mechanobiology 10, 925-937. 111

Govaert, L., Timmermans, P., Brekelmans, W., 2000. The influence of intrinsic strain softening on strain localization in polycarbonate: modelling and experimental validation. Journal of Engineering Materials and Technology 122, 177-185. 5, 11, 38, 46, 88, 132, 160

Guedes, J.M., Kikuchi, N., 1990. Preprocessing and postoprocessing for materials based on the homogenization method with adaptative finite element methods. Computer Methods in Applied Mechanics and Engineering 83, 143-198. 4, 6, 148

Gurson, A.L., 1977. Continuum theory of ductile rupture by void nucleation and growth: Part I-Yield criteria and flow rules for porous ductile media. Journal of Engineering Materials and Technology, Transaction of ASME 99, 2-15. 4, 132, 134, 135

Guo, T.F., Faleskog, J., Shih, C.F., 2008. Continuum modeling of a porous solid with pressure-sensitive dilatant matrix. Journal of the Mechanics and Physics of Solids 56, 2188-2212.

Hasan O.A., Boyce M.C., Li X.S., Berko, S., 1993. An investigation of the yield and postyield behaviour and corresponding structure of poly(methyl methacrylate). Journal of Polymer Science Part B: Polymer Physics 31, 185-197. 46

Haward, R.N., Thackray, G., 1968. The use of mathematical model to describe isothermal stress-strain curves in glassy polymers, Proceedings of the Royal Society, A 302, 453-472. 4, 74

Haward, R.N., 1987. The application of simplified model for the stress-strain curves of polymers. Polymer 28, 1485-1488. 73

Hachour, K., Zairi, F., Nait-Abdelaziz, M., Gloaguen, J.M., Aberkane, M., Lefebvre, J.M., 2014. Experiments and modeling of high-crystalline polyethylene yielding under different stress states. International Journal of Plasticity 54, 1-18. 9, 68, 80

Hall, C., 1989. Polymer Materials, an introduction for technologists and scientists. Wiley. 1, 2

Harper, L.T., Qian, C., Turner, T.A., Li, S., Warrior, N.A., 2012. Representative volume elements for discontinuous carbon fibre composites - Part 1: Boundary conditions. Composites Science and Technology 72, 225-234.

Harper, L.T., Qian, C., Turner, T.A., Li, S., Warrior, N.A., 2012. Representative volume elements for discontinuous carbon fibre composites - Part 2: Determining the critical size. Composites Science and Technology 72, 204-210.

Hashin, Z., 1983. Analysis of composite materials - a survey. Journal of Applied Mechanics 50, 481-505. 100, 147

Hettich, T, Hund, A., Ramm, E., 2008. Modeling of failure in composites by X-FEM and level sets within a multiscale framework. Computer Methods in Applied Mechanics and Engineering 197, 414-424. 7

Hencky, H., 1924. Zur theorie der plastischer deformationen und der dafur im Material hervorgerufenen Nachspannungen. Zeitschrift fur Angewandte Mathematik und Mechanik 4, 323-334. 4

Holzapfel, G.A., 2000. Nonlinear solid mechanics: a continuum approach for engineering. John Wiley and Sons, Chichester. 15

Hill, R., 1963. Elastic properties of reinforced solids: some theoreticel principles. Journal of the Mechanics and Physics of Solids 11, 357-372. 100, 145

Huber, M.T., 2004. Specific work of strain as a measure of material effort. Archives of Mechanics 56, 173-190. Translation from the original paper in Polish published in 1904. 4

Kaczmarczyk, L., Pearce, C.J., Bicanic, N., 2010. Studies of microstructural size effect and higher-order deformation in second-order computational homogenization. Computers and Structures 88, 1383-1390.

Kanit, T., Forest, S., Galliet, I., Mounoury, V., Jeulin, D., 2003. Determination of the size of the representative volume element for random composites: statistical and numerical approach. International Journal of Solids and Structures 40, 3647-3679. 111, 112

Kanit, T., N'Guyen, F., Forest, S., Jeulin, D., Reed, M., Singleton, S., 2006. Apparent and effective physical properties of heterogeneous materials: Representativity of samples of two materials from food industry. Computer Methods in Applied Mechanics and Engineering 195, 3960-3982. 111, 112

Khdir, Y.K., Kanit, T., Zairi, F., Nait-Abdelaziz, M., 2013. Computational homogenization of elastic-plastic composites. International Journal of Solids and Structures 50, 2829-2835.

Kouznetsova, V.G., Geers., M.G.D., 2008. A multi-scale model of martensitic trans-formation plasticity. Mechanics of Materials 40, 641-657. 6, 149

Kouznetsova, V.G., Geers., M.G.D., Brekelmans, W.A.M., 2004. Multi-scale second-order computational homogenization of multi-phase materials: a nested finite element solution strategy. Computer Methods in Applied Mechanics and Engineering 193, 5525-5550. 7

Khan, F., 2002. The deformation behavior of solid polymers and modeling with the viscoplasticity theory based overstress. Ph.D. Thesis, Rensselaer Polytechnic Institute, New York. 9

Khan, A., Zhang, H., 2001. Finite deformation of a polymer: experiments and modeling. International journal of Plasticity 17, 1167-1188. 9

Lazzeri, A., Bucknall, C.B., 1995. Applications of a dilatational yielding model to rubber-toughened polymers. Polymer 36, 2895-2902. 136

Lee, B.J., Parks, D.M., Ahzi, S., 1993. Micromechanical modeling of large plastic deformation and texture evolution in semi-crystalline polymers. Journal of Mechanics and Physics of Solids 41, 1651-1687. 8, 150

Lee, E.H., 1969. Elastic-plastic Deformation at Finite Strains. Journal of Applied Mechanics 36, 16. 19, 40

Leonov, A., 1976. Non-equilibrium thermodynamics and rheology of viscoelastic polymer media. Rheological Acta 15, 85-98. 38

Li, Y., Abberton, B., Kroger, M., Liu, W., 2013. Challenges in Multiscale Modeling of Polymer Dynamics. Polymers 5, 751-832.

Li, Y., Abberton, B., Krger, M., Liu, W., 2013. Challenges in Multiscale Modeling of Polymer Dynamics. Polymers 5, 751-832. xii, 9

Liu, S., Su, W., 2009. Effective couple-stress continuum model of cellular solids and size effects analysis. International Journal of Solids and Structures 46, 2787-2799.

Liu, Y., Zhou, J., Ling, X., 2010. Impact of grain size distribution on the multiscale mechanical behavior of nanocrystalline materials. Materials Science and Engineering: A 527, 1719-1729.

Love, B.M., Batra, R.C., 2006. Determination of effective thermo-mechanical parameters of a mixture of two elastothermoviscoplastic constituents. International Journal of Plasticity 22, 1026-1061. 129

Matsui, K., Terada, K., Yuge, K., 2004. Two-scale finite element analysis of heteroge-neous solids with periodic microstructures. Computers and Structures 82, 593-606. 7

Malcher, L., 2012. Continuum Modelling and Numerical Simulation of Damage for Ductile Materials. Ph.D. thesis, University of Porto, Porto, Portugal. xiv, 80

Mackerle, J., 1997. Finite element analysis and simulation of polymers: a bibliography (1976-1996). Modelling and Simulation in Materials Science and Engineering 5, 615-650. 5, 37

Mackerle, J., 2003. Finite element anlysis and simulation of polymers an addendum: a bibliography (1996-2002). Modelling and Simulation in Materials Science and Engineering 11, 195-231. 1, 2, 3, 5, 37

Mercatoris, B.C.N., Bouillard, Ph., Massart, T.J., 2009. Multi-scale detection of failure in planar masonry thin shells using computational homogenisation. Engineering Fracture Mechanics 79, 479-499. 7

Miehe, C., Schotte, J. Schroder, J., 1999. Computational micro-macro transitions and overall moduli in the analysis of polycrystals at large strains. Computational Materials Science 16, 372-382. 7

Miehe, C., Koch, A., 2002. Computational micro-to-macro transitions of discretized microstructures undergoing small strains. Archive of Applied Mechanics 72, 300-317. 7

Mooney, M., 1940. A theory of large elastic deformation. Journal of Applied Physics 11, 582. 4

Mori, T., Tanaka, K., 1973. Average stress in matrix and average elastic energy of materials with misfitting inclusions. Acta Metallurgica 21, 571-574. 136

Mathiesen, D., Vogtmann, D., Dupaix, R.B., 2014. Characterization and constitutive modeling of stress-relaxation behavior of Poly(methyl methacrylate) (PMMA) across the glass transition temperature. Mechanics of Materials 71, 74-84. 9, 68

Nguyen, V.P., Valls, O.L., Stroeven, M., Sluys, L.J., 2010. On the existence of representative volumes for softening quasi-brittle materials A failure zone averaging scheme. Computer Methods in Applied Mechanics and Engineering 45-48, 3028-3038. 112

Nikolov, S., Doghri, I., 2000. A micro/macro constitutive model for the small-deformation behavior of polyethylene. Polymer 41, 18831891. 8, 150

Nikolov, S., Doghri, I., Pierard, O., Zealouk, L., Goldberg, A., 2002. Multi-scale constitutive modeling of the small deformation of semi-crystalline polymers. Journal of Mechanics and Physics of Solids 50, 2275-2302. 8, 150

Ostoja-Starzewski, M., 2002. Microstructural randomness versus representative volume element in thermomechanics. Journal of Applied Mechanics 69, 25-35. 101

Ozdemir, I., Brekelmans, W.A.M., Geers., M.G.D., 2008. FE computational homogenization for the thermo-mechanical analysis of heterogeneous solids. Computer Methods in Applied Mechanics and Engineering 198, 602-613.

Ozdemir, I., Brekelmans, W.A.M., Geers., M.G.D., 2008. Computational homogenization for heat conduction in heterogeneous solids. International Journal for Numerical Methods in Engineering 73, 185204. 7

Ortiz, M., Pinsky, P.M., Taylor, R.L., 1983. Operator split methods for the numerical solution of the elastoplastic dynamic problem. Computer Methods in Applied Mechanics and Engineering 39, 137-157. 38

Owen, D.R.J., Hinton. E., 1980. Finite Elements in Plasticity: Theory and Practice. Pineridge Press, Swansea, UK. 38

Pardoen, T., Hutchinson, J.W., 2000. An extended model for void growth and coalescence. Journal of the Mechanics and Physics of Solids 48, 2467-2512. 136

Parks, D.M., Azhi, S., 1990. Polycrystalline plastic deformation and texture evolution for crystals lacking five independent slip systems. Journal of Mechanics and Physics of Solids 38, 701-724. 8, 150

Pan, J., Saje, M., Needleman, A., 1983. Localization of deformation in rate sensitive porous plastic solids. International journal of fracture 21, 261-278. 132

Peric, D.J., Owen, D.R.J., Honnor, M.E., 1992. A model for finite strain elasto-plasticity based on logarithmic strains: Computational issues. Computer Methods in Applied Mechanics and Engineering 94, 35-61. 48

Pelissou, C., Baccou, J., Monerie, Y., Perales, F., 2009. Determination of the size of the representative volume element for random quasi-brittle composites. International Journal of Solids and Structures 46, 2842-2855. 111, 112

Raha, S., Bowden, P.B., 1972. Birefringence of plastically deformed poly(methyl methacrylate). Polymer 13, 174-183. 9, 150

Raghava, R.S., Caddell, R.M., Yeh, G.S.Y., 1973. The macroscopic yield behaviour of polymers. Journal of Materials Science 8, 225232. 68

Rojek, J., Onate, E., Chiumenti, M., Mariela, L., Zarate, F., Fruitos, O., Ferriz, A., SOller, S.J., 2004. Economical exploitation of polymer coated steel sheet in large-scale production of new can types by the European can industry. International Center for Numerical Methods in Engineering (CIMNE). 5

Rosato, D., Rosato, D., 2003. Plastics engineered product design. Elsevier, UK. 2

Reis, F.J.P., 2014. Multi-scale modelling and analysis of heterogeneous solids at finite strains. Ph.D. thesis, University of Porto, Porto, Portugal.

Romero, P., Masad, E., 2001. Relationship between the representative volume element and mechanical properties of asphalt concrete. Journal of Materials in Civil Engineering 193, 77-84. 111, 112

Rouinia, M., Peric, D.J., 1998. A computational model for elasto-viscoplatic solids at finite strain with reference to thin shell applications. International Journal for Numerical Methods in Engineering 42, 289-311.

Sebsadji, S.K., Chouicha, K., 2012. Determining periodic representative volumes of concrete mixtures based on the fractal analysis. International Journal of Solids and Structures 49, 2941-2950. 48

Shan, Z., Gokhale, A.M., 2002. Representative volume element for non-uniform micro-structure. Computational Materials Science 24, 361-379. 111, 112

Simo, J.C., Hughes, T.J.R., 1998. Computational Inelasticity. Springer-Verlag, New York, US. 111
38, 48

Simo, J.C., Kennedy, J.G., Govindjee, S., 1998. Non-smooth multisurface plasticity and viscoplasticity. Loading/unloading conditions and numerical algorithms. International Journal for Numerical Methods in Engineering 26, 2161-2185. 38

Smit, R., Brekelmans, W., Meijer, H.E.H., 2000. Predictive modelling of the properties and toughness of polymeric materials, part I: Why is polystyrene brittle and polycarbonate tough? Journal of Materials Science 35, 2855-2867. 38

Smit, R., Brekelmans W., Meijer, H.E.H., 1999. Prediction of the large-strain mechanical response of heterogeneous polymer systems: local and global deformation behaviour of a representative volume element of voided polycarbonate. Journal of the Mechanics and Physics of Solids 47, 201-221. 8, 38, 150

Smit, R., Brekelmans, W., Meijer, H.E.H., 2000. Predictive modelling of the properties and toughness of polymeric materials, part III: Simultaneous prediction of micro- and macro-structural deformation of rubber-modified polymers. Journal of Materials Science 35, 2881-2892. 8, 38, 150

Smit, R., Brekelmans, W., Meijer, H.E.H., 1998. Prediction of the mechanical behavior of nonlinear heterogeneous systems by multi-level finite element modeling. Computer Methods in Applied Mechanics and Engineering 155, 181-192. 8, 129, 150

Smit, R., 1998. Toughness of Heterogeneous Polymeric Systems: a modeling approach. Ph.D. thesis, Eindhoven University of Technology, Eindhoven, The Netherlands. 9, 130, 150

Shabana, A.A., 2008. Computational continuum mechanics. Cambridge University Press. 15

Skarzynski, L., Tejchman, J., 2012. Determination of representative volume element in concrete under tensile deformation. Computers and Concrete 9, 35-50. 111, 112

Speirs, D.C.D., De Souza Neto, E.A., Peric, D.J., 2008. An approach to the mechanical constitutive modelling of arterial tissue based on homogenization and optimization. Journal of Biomechanics 41, 2673-2680. 7

Stroeven, M., Askes, H., Sluys, L.J., 2004. Numerical determination of representative volumes for granular materials. Computer Methods in Applied Mechanics and Engineering 193, 3221-3238. 111, 112

Suquet, P.M., 1985. Local and global aspects in the mathematical theory of plasticity. In Sawczuk, A. and Bianchi, G. editors, Plasticity today: modelling, methods and applications, pages 279-310. Elsevier Applied Science Publishers. 4, 6, 148

Srivastava, V., Chester, S.A., Ames, N.M., Anand, L., 2010. A thermo-mechanically-coupled large-deformation theory for amorphous polymers in a temperature range which spans their glass transition. International Journal of Plasticity 26, 1138-1182. 9

Senden, D.J.A., Peters, G.W.M., Govaert, L.E., Van Dommelen, J.A.W., 2013. Anisotropic yielding of injection molded polyethylene: Experiments and modeling. Polymer 54, 5899-5908. 9, 68

Takano, N., Fukasawa, K., Nishiyabu, K., 2010. Structural strength predic-tion for porous titanium based on micro-stress concentration by micro-CT image-based multiscale simulation. International Journal of Mechanical Sciences 52, 229-235. 7

Terada, K., Kikuchi, N., 1995. Nonlinear homogenization method for practical application. In Ghosh, S. and Ostoja-Starzewski, M. editors, Proceedings of 1995 ASME International Mechanical Engineering Congress and Exposition, volume 212, pages 116. 4, 6, 148

Tresca, M.H., 1864. Mmoire sur lecoulement des corps solides soumis a de fortes pressions. Comptes Rendus Hebdomadaires des Seances de lAcademie des Sciences 59, 754-758. 4

Trias, D., Costa, J., Turon, A., Hurtado, J., 2006. Determination of the critical size of a statistical representative volume element (SRVE) for carbon reinforced polymers. Acta Materialia 54, 3471-3484.

Tervoort, T., 1996. Constitutive modelling of polymer glasses: finite, nonlinear viscoelastic Behaviour of Polycarbonate. Ph.D. thesis, Eindhoven University of Technology, Eindhoven, The Netherlands. 38, 43, 68, 71, 75

Tervoort, T., Smit, R., Brekelmans, W., Govaert, L., 1998. A constitutive equation for the elasto-viscoplastic deformation of glassy polymers. Mechanics of Time-Dependent Materials 1, 269-291. 5

Timmermans, P.H.M., 1997. Evaluation of a constitutive model for solid polymeric materials: model selection and parameter quantification. Ph.D. thesis, Eindhoven University of Technology, Eindhoven, The Netherlands. 11, 38, 41, 46, 56, 73, 75, 88, 132, 160

Tvergaard, V., Needleman, A., 1984. Analysis of the cup-cone fracture in a round tensile bar. Acta Metallurgica 32, 157-169. 135

van Breemen, L.C.A., Engels, T.A.P., Klompen, E.T.J., Senden, D.J.A., Govaert, L.E., 2012. Rate- and temperature-dependent strain softening in solid polymers. Journal of Polymer Science Part B: Polymer Physics 50, 1757-1771. 88

Van der Aa, M.A.H., 1999. Wall ironing of polymer coated sheet metal. Ph.D. thesis, Eindhoven University of Technology, Eindhoven, The Netherlands. 38, 56

Van Melic, H.G.H., Govaert, L.E., Meijer, H.E.H., 2003. Localisation phenomena in glassy polymers: influence of thermal and mechanical history. Polymer 44, 3579-3591. 56, 60

Van der sluis, O., Schreurs, P.J.G., Brekelmans, W.A.M., Meijer, H.E.M., 2000. Overall behavior of heterogeneous elastoviscoplastic materials: effect of microstructural modelling. Mechanics of Materials 32, 449-462. 129

Van der sluis, O., Schreurs, P.J.G., Meijer, H.E.M., 2001. Homogenization of structured elastoviscoplastic solids at finite strains. Mechanics of Materials 33, 499-522. 129

van Breemen, L.C.A., Engels, T.A.P., Klompen, E.T.J., Senden, D.J.A., Govaert, L.E., 2012. Rate- and temperature-dependent strain softening in solid polymers. Journal of Polymer Science Part B: Polymer Physics 50, 1757-1771.

van der Sanden, M.C.M., 1993. Ultimate toughness of amorphous polymers. Ph.D. thesis, Eindhoven University of Technology, Eindhoven, The Netherlands. 129

van Dommelin, J.A.W., Parks, D.M., Boyce, M.C., Brekelmans, W.A.M., Baaijens, F.P.T., 2003. Microme-chanical modeling of elasto-viscoplastic behavior of semi-crystalline polymers. Journal of Mechanics and Physics of Solids 51, 519-541. 8, 150

van Breemen, L.C.A., Engels, T.A.P., Klompen, E.T.J., Senden, D.J.A., Govaert, L.E., 2012. Rate- and temperature-dependent strain softening in solid polymers. Journal of Polymer Science Part B: Polymer Physics 50, 1757-1771.

van Melick, H.G.H., Govaert, L.E., Meijer, H.E.H., 2003. Localisation phenomena in glassy polymers: influence of thermal and mechanical history. Polymer 44, 3579-3591.

van Mier J.G.M., 1996. Fracture processes of concrete. CRC Press, USA. 100

von Mises, R., 1913. Mechanik der festen Korper im plastisch-deformablen Zustand. Nachrichten von der Gesellschaft der Wissenschaften zu Gottingen, mathematisch-physikalische Klasse 1, 582-592. 4

Wen, J., Huang, Y., Hwang, K.C., Liu, C., Li, M., 2005. The modified Gurson model accounting for the void size effect. International Journal of Plasticity 21, 381-395. 136

Wu, P.D., van der Giessen, E., 1994. Analysis of shear band propagation in amorphous glassy polymers. International Journal of Solids and Structures 31, 1493-1517.

Wu, J.J., Buckley, C.P., 2004. Plastic deformation of glassy polystyrene: a unified model of yield and the role of chain length. Journal of Polymer Science Part B 42, 2027-2040. 9

Yong, N., Chiang, Y.M., 2007. Prediction of elastic properties of heterogeneous materials with complex microstructures. Journal of the Mechanics and Physics of Solids 55, 517-532. 129

Zairi, F., Nait-Abdelaziz, M., Gloaguen, J.M., Lefebvre, J.M., 2008. Modelling of the elasto-viscoplastic damage behaviour of glassy polymers. International Journal of Plasticity 24, 945-965. 132, 135, 136

Zairi, F., Nait-Abdelaziz, M., Gloaguen, J.M., Lefebvre, J.M., 2011. A physically-based constitutive model for anisotropic damage in rubber-toughened glassy polymers during finite deformation. International Journal of Plasticity 27, 25-51.

Zienkiewicz, O.C., Taylor, R.L., 1991. The Finite Element Method, Vol 2: Solid and Fluid Mechanics, Dynamics and Non-Linearity. McGraw-Hill, London, UK. 38